LITHIUM INSERTION IN CARBONACEOUS MATERIALS CONTAINING SILICON

by

Alfred M. Wilson

B.Sc., University of Waterloo, 1992

THESIS SUBMITTED IN PARTIAL FULFILLMENT OF
THE REQUIREMENTS FOR THE DEGREE OF
DOCTOR OF PHILOSOPHY

in the Department of Physics

SIMON FRASER UNIVERSITY
March 1997

National Library
of Canada

Acquisitions and
Bibliographic Services

395 Wellington Street
Ottawa ON K1A 0N4
Canada

Bibliothèque nationale
du Canada

Acquisitions et
services bibliographiques

395, rue Wellington
Ottawa ON K1A 0N4
Canada

Your file Votre référence

Our file Notre référence

0-612-24364-8

APPROVAL

Name: Alfred MacDonald Wilson
Degree: Doctor of Philosophy
Title of Thesis: Lithium Insertion in Carbonaceous Materials Containing Silicon

Examining Committee:
Chair: Dr. Michael Plischke

Dr. Jeffrey Raymond Dahn
Senior Supervisor
Professor of Physics and Chemistry
Dalhousie University

Dr. Albert Curzon
Professor

Dr. Simon Watkins
Associate Professor

Dr. Steven Holdcroft
Internal Examiner
Associate Professor
Department of Chemistry, Simon Fraser University

Dr. Linda Nazar
External Examiner
Associate Professor
Department of Chemistry, University of Waterloo

Date Approved: 25 March 1997

ABSTRACT

Three different series of silicon-containing carbonaceous materials were synthesized for use as anodes in lithium ion cells. Disordered (or pregraphitic) carbons containing nanodispersed silicon were prepared by the chemical vapour deposition (CVD) of various chlorosilanes ($SiCl_4$, $(CH_3)_2Cl_2Si$, and $(CH_3)_3ClSi$) with benzene in two different apparatuses. Silicon oxycarbide glasses were synthesized by the pyrolysis of over 50 silicon-containing polymers at various temperatures, although the principal materials in the study were prepared at 1000°C. Finally, materials which we believe to be similar to disordered carbons containing nanodispersed silicon were prepared by the pyrolysis of various blends of pitches with polysilanes.

Powder X-ray diffraction was used to learn about the structure of all the materials made. Thermal gravimetric analysis was used to determine the silicon content in the CVD materials and, when coupled to a residual gas analyzer, to study the decomposition process of the polymers. Near edge X-ray absorption spectroscopy measurements of the silicon *L*- and *K*-edges of CVD materials and the silicon *K*-edges of silicon oxycarbides were used to learn about local chemical environments of the silicon atoms.

Lithium metal electrochemical test cells of the silicon-containing CVD materials showed larger capacities (up to 500 mAh/g) than pure carbons prepared in the same way (~300 mAh/g). The additional capacity was observed to be centered near 0.4 V on charge, the average voltage observed for the removal of lithium from a silicon-lithium alloy.

Chemical analysis showed that the stoichiometries of materials made by polymer pyrolysis were distributed over a well-defined region in the Si-O-C Gibbs phase diagram. An interesting series of materials is found near the line in the Si-O-C Gibbs triangle connecting carbon to $SiO_{1.3}$.

Lithium metal electrochemical test cells made using all the silicon oxycarbides synthesized showed that a stoichiometry of about $Si_{.25}C_{.45}O_{.30}$ gave the maximum reversible capacity (about 900 mAh/g). However, materials near this stoichiometry exhibit large irreversible capacities (>350 mAh/g) and significant hysteresis (the voltage difference between charge and discharge) in the voltage profile (~0.8 V).

In an attempt to reduce the oxygen content in one of the silicon oxycarbide glasses, a sample was washed in a dilute solution of hydrofluoric acid (HF) for times ranging from 2 minutes to 24 hours. The material lost, at most, 40 percent of its initial mass, although there was only a small change in its stoichiometry. In addition to the techniques mentioned above, small angle X-ray scattering and BET surface area measurements were used to study the microscopic pore network that was created by the HF washing.

Lithium metal electrochemical test cells made using the product of pyrolysing pitch-polysilane blends showed that the capacity increased with silicon content from 340 mAh/g for pure carbon to a maximum of 600 mAh/g for samples with about 15 atomic % silicon ($Si_{.14}O_{.09}C_{.77}$). The capacity then decreased to near zero as the composition approached SiC. These materials contain oxygen which is correlated to irreversible capacity loss.

Because of the expense it is highly unlikely that any material synthesized by CVD would be used in industrial lithium-ion cell production. Although the silicon oxycarbides can be made by the considerably less expensive pyrolysis of polysiloxanes, detailed investigations into the nature of the irreversible capacity and hysteresis would be required before they could be considered for use in commercial cells. However, materials similar to the first disordered carbons containing nanodispersed silicon were made by the pyrolysis of pitch-polysilane blends. These materials may find application in lithium-ion batteries, if the oxygen content can be reduced.

All of this work has contributed not only to the greater understanding of high capacity lithium-ion anode materials, but also to the understanding of silicon oxycarbide glasses and the novel disordered carbons containing nanodispersed silicon.

QUOTATION

What we do as scientists, as scholars, as advocates, has consequences, just as our refusal to speak or act has definite consequences. We cannot escape this condition in a society based on concentration of power and privilege. There is a heavy responsibility that the scientist or scholar would not have to bear in a decent society, in which individuals would not relegate to authorities decisions over their lives or their beliefs.

NOAM CHOMSKY

in The Chomsky Reader, p. 202, Pantheon Books (New York, 1987)
(from "Equality," an essay written in 1976)

ACKNOWLEDGMENTS

My first thanks must go to my supervisor, Dr. Jeff Dahn, without whose guidance and consistent encouragement this work would certainly have been less extensive and, likely, have taken longer. I am grateful for the many opportunities which Jeff gave me to present at conferences, quite literally, around the world.

During my time working in Jeff's lab I have met many talented and interesting individuals. I would like to thank the following people (roughly in order of appearance) for their support and for making my graduate studies a more enjoyable time: Dr. Brian Way, Brad Hughes, Wolfgang Weydanz, Eric Fuller, Dr. Hang Shi, Dr. Wu Li, Oliver Schilling, Dr. Tao Zheng, Monique Richard, Dr. Yuan Gao, Dr. Meijie Zhang, Dr. Weibing Xing, Immo Koetschau, Ian Courtney, and Mark Obrovac. Special thanks are owed to Dr. Weibing Xing for making and testing almost all of the electrochemical cells for the materials discussed in Chapters 8 and 9. Also, thanks go to Dr. Gregg Zank and Dr. Katz Eguchi of Dow Corning Asia for a successful and enjoyable collaboration.

I would like to acknowledge the financial support of Simon Fraser University and the British Columbia Science Council and also Moli Energy (1990) Ltd. of Maple Ridge, B.C. for the use of equipment.

On a more personal note, I would like to thank Megan Fairbanks for her love and constant support throughout the long hours of writing this thesis. The very fact that I have survived this writing process is a testament to the patience of both my roommates, Kevin and Megan. Thanks for your support.

Finally, thanks to my parents, not only for having me but also for their constant encouragement, even when they were unsure exactly what it was they were encouraging.

TABLE OF CONTENTS

LIST OF TABLES

LIST OF FIGURES

PREFACE

I began my graduate studies with Jeff Dahn rather serendipitously. I had expected to be working as a bachelor scientist in a large corporate lab (which will go nameless) when they suddenly engaged in what is now considered routine: a hiring freeze. I did not have a scholarship nor particularly good grades, which acted to greatly narrow my search for a graduate school. Ironically, this was to my advantage. After one 20 minute meeting with Jeff I had decided to move from southern Ontario and come to SFU, with the hopes of working with him on energy storage materials for use in electric vehicles (EVs).

I have been concerned with the state of the planet, and it's self appointed 'care-takers' (politicians and CEOs, in the name of their shareholders), for much of my life. I started working with Jeff with the hope of contributing to the research of technologies applicable to electric (more specifically, battery powdered) vehicles. I hoped to contribute to developing more "environmentally friendly" science. Since then I have come to realize that it is the politics of society that shape how scientific research will be used. Science is a tool and can provide ways of understanding. Alone it can neither solve nor create problems.

I have also come to realize that the greatest barrier to the mass production of electric vehicles is a lack of funding for research and development. The amount of money spent on internal combustion engine research still dwarfs all zero emission vehicle (ZEV) research combined. This is a product of our political and economic structure and it will take enormous pressure from knowledgeable people to accelerate the development of cost-effective ZEVs. This has happened in California, where legislation was enacted that a minimum percentage of the automobiles sold in the state must be ZEV. This legislation was met with huge protest from the American automobile manufacturers, which also have interests in the petroleum industry.

With the recent announcements from automobile manufacturers of EVs which will provide performance near that of gasoline powered cars, I have a renewed hope that the work presented in this thesis may indeed make a contribution to EV battery research.

Currently, lithium-ion batteries find scores of applications in portable consumer electronics, displacing the less than "environmentally friendly" nickel-cadmium cells. Lithium, however, is not a renewable resource, although the strip mining of lithium continues to produce enormous swimming pools for future generations to enjoy. Lithium-ion batteries do represent a more environmentally benign technology, but they have obvious short comings.

The solution, in my opinion, is to put fewer vehicles on the road, to live closer to work, and to invest in more efficient public transit. Such solutions are far beyond the bounds of any 'scientific' research. However, it is important to recognize that the privilege of being part of an educated elite must be weighted with the responsibility to use that knowledge wisely. Indeed, with an estimated petroleum resource of only 30 years, interesting changes are to be witnessed over the next few decades. Whatever the outcome, my work in this field has been and promises to continue to be fascinating and exciting. I have been fortunate to be in the position to do this work.

CHAPTER 1

AN INTRODUCTION TO LITHIUM ION CELLS AND THIS THESIS

The market for portable consumer electronics is booming throughout the G7 nations. Computers more powerful than any university could procure ten years ago now weigh less than ten pounds, fit inside a small briefcase or shoulder bag and carry a price tag which even many small companies and individuals can afford. Many want more powerful, lighter, and smaller portable computers which will operate under their own power for longer. Those who use them would like smaller and lighter cellular phones and cam-corders.

Beyond consumer electronics, there is the desire by many, including the author, to have vehicles which do not pollute during their operation and have the performance which matches that of automobiles in use today. Many of the states in the USA with urban pollution problems stand poised to enact legislation following California's, which requires that a certain percentage of all automobiles sold by manufacturers in that state be zero emission vehicles (ZEV; i.e. not emit CO_x, NO_x, or SO_x).

The main obstacle to be overcome in all these cases is the energy storage device. For consumer electronics, the battery is the energy storage device. Further miniaturization of portable electronics requires batteries which can store more energy, take up less space and weigh less. That is, they must have higher energy density in both volume and mass. Nickel cadmium (Ni-Cd) cells are presently the most popular rechargeable batteries for consumer electronics. Ni-Cd cells are marketed as 'environmentally friendly,' despite the fact that they contain toxic metals and an infrastructure for proper disposal of spent cells does not yet exist.

For vehicles, the most common energy storage devices are gasoline and diesel fuel tanks. In a ZEV the gas tank and internal combustion engine can be replaced with a battery or a hydrogen gas storage device and fuel cell system and an electric motor. Both the lack of a hydrogen fueling infrastructure and the apparent danger associated with carrying around hydrogen impede the use of fuel cell powered vehicles. Ballard Power Systems (a company in South Burnaby) is making strides to develop a *direct methanol fuel cell* product using methanol (instead of H_2) as a fuel which is fed directly into the cell. They have measured CO_2 as the only gaseous emission above 5 to 10 ppm (i.e. no measurable NO_x, CO, or SO_x [Colbow, 1997]). Since the California legislation does not count CO_2 as a pollutant (nor does the BC lower mainland's Air Care) direct methanol fuel cells could legally be used in ZEVs. However, there are still issues of cost (Colbow, 1997).

Electric vehicle (EV) progress is still hampered by the lack of a suitable battery and so great strides have and must be made to develop lighter, smaller, safer, and cheaper batteries. Invented over 140 years ago (Sinstead, 1854), lead acid batteries are being used in the electric vehicles currently under production in North America, such as General Motor's 1997 *Impact* (Whitney, 1996) and Bombardier's *Neighborhood Electric Vehicle* (NEV). The lead acid system has also been used for years by many Japanese EV manufacturers. However, the use of lead acid batteries is undesirable because of the inherent performance limitations and the obvious environmental concerns with lead.

Amongst the newer technologies, the nickel metal hydride (Ni-MH [Ovshinsky, 1993]) and lithium-ion systems are being developed for EV use. Both are presently used in laptop computers and fulfill many of the USABC (United States Advanced Battery Consortium) requirements for an EV battery. However, the 1995 cost of Ni-MH cells needs to be reduced by a factor of about ten in order for them to comply with the USABC cost requirement. There are also concerns that nickel is a carcinogen. Still, several Japanese auto manufacturers have recently displayed EVs using both these systems. The Honda EV Plus uses Ni-MH batteries and will be available in May of 1997 (EVAA, 1997). Toyota has demonstrated two EVs; the *RAV4* which uses Ni-MH batteries, and the

Table 1-1. A summary of the characteristics of various rechargeable battery technologies. The energy densities are given as ranges (compiled from the references).*

SYSTEM	VOLTAGE (V)	GRAVIMETRIC ENERGY DENSITY (Wh/kg)	VOLUMETRIC ENERGY DENSITY (Wh/l)	CYCLE LIFE
Pb-acid	2	20 - 40	70 - 90	~500**
Ni-Cd	1.2	20 - 60	40 - 170	> 500
Ni-MH	1.2	50 - 65	175 - 200	~ 500
Alkaline (Zn-Mn)	1.5	85	250	> 50
Li-metal	~3	55 - 155	135 - 325	~ 200
Li-ion (i.e. C-Li_xCoO_2)	3.5 - 4.0	70 - 135	185 - 300	> 500

*Data compiled from: Linden, 1995; Bennet, 1995; Tadiran, 1997; Sanyo, 1997

** some specially designed systems (traction, deep cycle) can achieve >1000 cycles.

FCEV which uses fuel cells with lead acid batteries (EVAA, 1996a). Nissan and Sony have announced plans to release a test fleet of 30 electric vehicles equipped with lithium-ion batteries in California in 1998, with retail sales starting as early as 2000 (EVAA, 1996b). They claim that their EV will have the acceleration performance of a typical gas powered car and a range of over 120 miles (EVAA, 1996b).

An inspection of Table 1-1, which compares several rechargeable battery systems, shows that the lithium systems are superior in all categories shown. Lithium ion (Li-ion) cells have about three, two, and 1.5 times the energy density of lead acid, Ni-Cd, and Ni-MH cells, respectively. Although lithium metal (Li-metal) cells have higher energy densities than Li-ion cells, the Li-metal system has been shown to be unsafe due to the extreme reactivity of the lithium metal anode. The Li-metal and Li-ion systems are discussed next.

1.1 LI-METAL AND LI-ION CELLS

Illustrated in Figure 1-1, a Li-metal cell consists of a lithium metal anode and a transition metal oxide (TMO) cathode. The electrolyte is a lithium salt (i.e. $LiPF_6$) dissolved in a nonaqueous solvent (i.e. propylene carbonate and ethylene carbonate). In a practical cell, the electrodes are electrically isolated by an insulating microporous polymer film (the separator) which allows the passage of electrolyte molecules and lithium ions, but not electrons. In button and coin cells, a cathode / separator / lithium metal stack is pressed together.

The voltage of the cell is a direct result of the difference between the chemical potential of lithium in the anode (μ_{anode}) and cathode ($\mu_{cathode}$). Figure 1-2 shows the chemical potential (in eV) of lithium atoms in many lithium intercalation compounds relative to that of lithium metal. As will be discussed in greater detail in Section 6.1.1, the voltage of a cell can be calculated from

$$V = -\frac{\mu_{cathode} - \mu_{anode}}{e} \tag{1-1}$$

where V is the cell voltage, e is the magnitude of the charge of one electron. Since the potential for lithium in metallic lithium is constant and zero, μ_{anode} for a Li-metal cell can be set to zero. Referring to Figure 1-2 the voltage of a Li-metal cell using a $LiCoO_2$ cathode would be about 4 V.

The lithium button and coin cells which are commonly used in watches and cameras are designed to be used for only one discharge. These *primary* cells are typically *anode limited*. They contain slightly less lithium than the TMO can react with so that after complete discharge there is no lithium metal left in the anode. However, the chemical reaction in the TMO has the potential of being reversed.

Intercalation is the process by which guest atoms or molecules (intercalants) are inserted into a host by a reversible reaction which does not cause a significant structural change in the host. The TMOs used in rechargeable (*secondary*) lithium cells are lithium intercalation hosts. A secondary Li-metal cell is *cathode limited* (there is excess

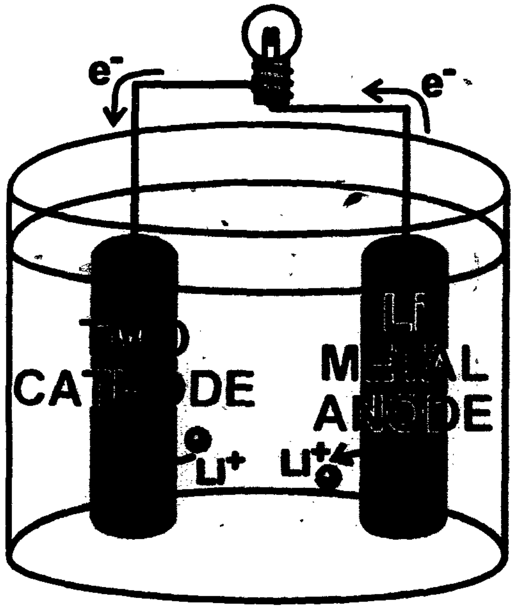

Figure 1-1. A schematic representation of a lithium metal cell. The cathode is labeled as a transition metal oxide.

lithium in the anode), which means that after complete reaction at the cathode there is still lithium metal in the anode. A voltage can be applied to the cell to move electrons from the cathode to the anode, increasing the potential inside the cell until lithium ions are forced from the cathode, into the electrolyte, and finally to the anode where they can then plate onto the existing lithium metal. There are, however, some complications with the use of lithium metal.

Lithium metal reacts with all the known electrolytes used in cells. When lithium metal reacts with the electrolyte it forms an insoluble, passivating, ionically conducting film known as the *solid electrolyte interphase* (SEI; Peled, 1979). The film grows, covering all available surfaces, until it reaches a thickness which prevents further reaction.

Lithium metal has a tendency to form dendrites during electrochemical plating, and so upon repeated cycling (charging and discharging) of these cells, the surface area of the lithium metal increases dramatically. Additionally, dendrites can reach from the anode through the separator to the cathode causing an internal short in the cell leading to rapid

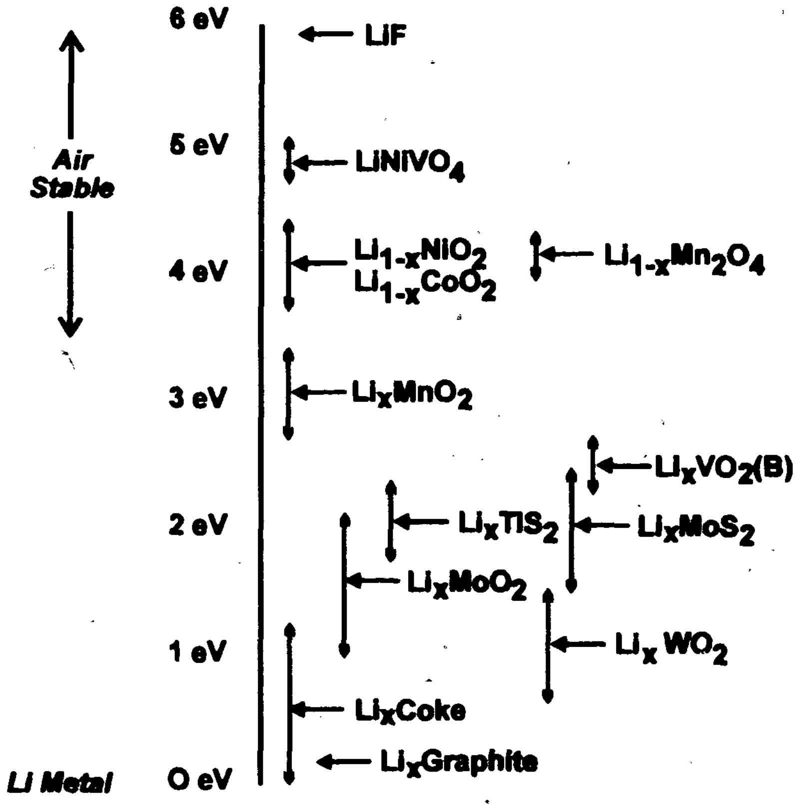

Figure 1-2. The binding energy (referenced to Li metal) of various lithium intercalation compounds.

self discharge and an increase in cell temperature. If the reacting surface area is sufficiently large this can cause self-heating which can melt the lithium and result in a runaway exothermic reaction.

One Li-metal cell released by Moli Energy Ltd. "vented with flame" while inside a cellular phone being used, injuring the individual using the phone (See: 'For Example' in references). This signaled what appeared to be the end for commercial production of secondary Li-metal cells. Like the 'new' company, Moli Energy (1990) Ltd., most manufacturers of secondary lithium batteries now produce Li-ion cells which contain no metallic lithium. However, many research groups are still investigating ways of inhibiting dendritic growth on the lithium metal surface and solid polymer electrolytes which should not react with the lithium. At least one company (Tadiran) has cells on the market which contain metallic lithium (Tadiran, 1997). It is the opinion of the author, and many others, that the commercial production of cells containing lithium metal is unwise.

In a lithium-ion cell, another intercalation compound (graphite) replaces lithium metal as the anode material. Figure 1-2 shows that graphite intercalates lithium at a voltage well below 1 V. Many lithium-ion cells currently being produced (i.e. by Moli Energy and AT Battery) use graphite as the anode material. In such a cell, the lithium ions shuttle back and forth between the two electrodes.

A reaction can occur on the surface of a carbon forming a passivating film similar to the SEI which forms on lithium metal. However, the surface area of the graphite can be controlled and there is no dendrite formation when lithium intercalates into carbon. Thus, the surface area remains essentially constant during cycling so that a carbon which is initially safe will remain so, regardless of the cycling conditions.

In a practical cell, the anode and cathode materials are coated onto metallic backings. In the *jelly roll* configuration, a cathode / separator / anode / separator stack is made, rolled up, placed into a cell can, electrolyte is added and the can is sealed. In the *prismatic* configuration, the cell stack is rolled onto a flat mandrel so that it can fit into a flat rectangular case. Cells are assembled with the lithium in the cathode material because the *lithiated* ('filled' with lithium) TMOs used are air stable whereas lithiated carbons are not.

Thus, cells are assembled in a discharged state and first need to be charged. Upon the application of a voltage, electrons are forced out of the cathode and into the anode. When the potential exceeds the binding energy for lithium in the cathode, lithium ions are forced into the electrolyte and diffuse across the separator to the graphite where they recombine with electrons and are intercalated (Figure 1-3).

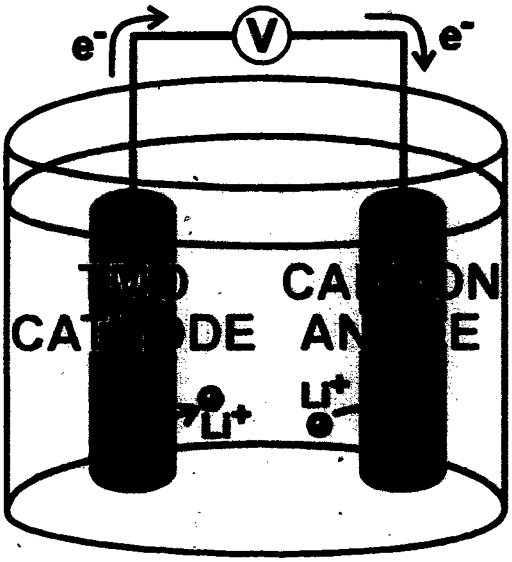

Figure 1-3. A schematic representation of a lithium metal cell. The cathode is labeled as a transition metal oxide.

The voltage of these cells is dependent on the chemical potential of lithium in the anode and cathode which both change during operation (Equation 1-1). For example, as a cell is discharged the lithium atoms will move from the lower binding energy states in the graphite to the higher binding energy states in the TMO. As more graphite sites become emptied the chemical potential inside the graphite will increase. Simultaneously, the chemical potential in the TMO will decrease as available sites are filled. Both add to a decrease in cell voltage, making results more difficult to interpret than in a Li-metal cell.

During discharge (to the right) or charge (to the left), the reactions which occur at the graphite anode and cathode are, respectively,

$$Li_xC_6 \Leftrightarrow Li_{x-y}C_6 + ye^- + yLi^+$$

and

$$Li_zMO + ye^- + yLi^+ \Leftrightarrow Li_{z+y}MO$$

where $Li_{z+y}MO$ is the lithiated metal oxide and Li_xC_6 is the lithiated graphite. Combining both equations the overall cell reaction is

$$Li_xC_6 + Li_zMO \Leftrightarrow Li_{x-y}C_6 + Li_{z+y}MO.$$

Lithium cobalt oxide is currently used in several commercial Li-ion cells. Lithium manganese oxides are advantageous because they are less expensive than cobalt oxides and have a comparable capacity. They are now used in commercial Nippon Moli Energy cells.

Presently, the only anode materials used in commercial lithium ion cells are various synthetic and natural graphites. There are, however, virtually countless different carbons which could be tried. The performance of any carbon is strongly correlated to its structure and, as will be discussed in the next chapter, there have been recent reports of various high capacity disordered carbons. Other recent research has focused on carbonaceous materials containing different 'additive' elements (Way, 1992; Weydanz, 1994).

This technology is still in its infancy and there are opportunities to make many improvements in electrolytes and electrode materials.

1.2 THIS THESIS

This section explains the main motivation behind this work and gives a chronological overview of the work done. The last section provides a basic outline of the thesis.

1.2.1 Motivation and Goals

The principal motivation of this thesis is to increase our knowledge by investigating novel anode materials which might have application in Li-ion batteries.

In this work we investigated alternative materials to replace the carbon anode with carbonaceous materials containing silicon. We investigated silicon because of the large alloying capacity of silicon for lithium (an order of magnitude larger than the intercalation capacity of graphite) at low average voltage (less than 0.5V [Huggins, 1987]). However, the alloying process is not sufficiently reversible for the direct replacement of the anode with pure silicon. It was our desire to synthesize materials which combined the reversibility of a carbon with the high capacity of silicon. The silicon must be available to form bonds with lithium atoms, unlike silicon carbide. Also, silicon will not form sp^2 hybrid bonds to bond substitutionally in a graphene sheet. So the silicon must exist within a carbon matrix in a manner inconsistent with silicon carbide. This will be more clearly defined in Section 2.4.

1.2.2 The Condensed Story of this Work

A chronological summary of this thesis is included here because it explains the motivations behind the series of projects done and forms the basis for the structure of the results and discussion chapters of the thesis.

Our initial attempts to make carbonaceous materials containing silicon were done using chemical vapour deposition (CVD), a technique useful in synthesizing novel materials. As will be presented, our initial attempts proved successful in making a material which had a capacity for reversible lithium insertion exceeding that of graphite. These materials consisted of a pregraphitic or disordered carbon which contained small clusters of (or possibly individual) silicon atoms at concentrations up to 11 atomic % silicon (Wilson, 1995a; Wilson, 1995b). We found no reports of materials similar to these *disordered carbons containing nanodispersed silicon*. This led us to design and build a second CVD apparatus in which more controlled experiments could be performed. With this apparatus a greater understanding of the nanodispersed materials was gained, although we were not successful in synthesizing materials with further increases in capacity (Wilson, 1995c). However, while the second CVD apparatus was being built, we attempted another approach.

CVD is a notoriously expensive process with which to make materials on an industrial scale. Materials requiring a CVD synthesis route would, thus, never be economically viable in the Li-ion battery market. We hoped to discover an alternate synthesis route to these materials by experimenting with the pyrolysis of siloxane polymers (Wilson, 1994a). However, the materials made were networked glasses containing carbon, silicon, and oxygen. It was therefore surprising to us when these *silicon oxycarbide glasses* exhibited capacities in excess of the CVD materials.

Once the second series of CVD experiments did not produce the materials we had hoped for, we focused our attention on materials synthesis by polymer pyrolysis and started a collaboration with Dr. Gregg Zank of Dow Corning. We could recommend final compositions and Dr. Zank was able to synthesize polymers which would give the desired stoichiometries after pyrolysis to ceramic. With Dr. Zank synthesizing polymers at Dow

Corning, a large volume of work was possible and, so, Weibing Xing (a post-doctoral research assistant) joined the project. By the pyrolysis of over 50 polymers we learned about the effects of various chemical compositions on the electrochemical properties and determined which regions in stoichiometry produced materials with the highest capacities. The maximum reversible capacity of about 900 mAh/g was for a material with the stoichiometry of $Si_{.25}C_{.45}O_{.30}$ (Wilson, 1996a; Xing, 1996a). As part of this project we also studied the decomposition of these polymers (Wilson, 1996b). In a failed attempt to remove the oxygen from one of the silicon oxycarbide glasses by washing it in a solution of hydrofluoric acid, we learned about micropore creation (Wilson, 1996c). Although our focus was on the synthesis of ceramics containing carbon, silicon, and oxygen, an alternative synthesis route to the nanodispersed silicon materials was realized.

By blending silicon-containing polymers with pitches (commonly used in the synthesis of graphites and disordered carbons) we were able to synthesize materials which we believe are similar to the disordered carbons containing nanodispersed silicon which we had first made by CVD (Xing, 1996b). These materials performed well and were synthesized by a method which is considerably simpler and less expensive than CVD.

1.2.3 The Organization of this Thesis

This chapter and the next provide background information to assist the reader in understanding the work done in this thesis. Chapter 2 describes lithium intercalation in carbons and briefly touches on lithium alloying with silicon.

The following four chapters (3, 4, 5, and 6) detail the experimental techniques used to synthesize and characterize the materials made. Chapter 3 explains how CVD was used to make the nanodispersed silicon in both apparatus used. Chapter 4 details how the silicon oxycarbides were synthesized from silicon-containing polymers and includes a section on the synthesis of the polymer-pitch blended materials. Chapter 5 describes all of the non-electrochemical experimental techniques used to characterize the materials made. The electrochemical testing procedure from cell assembly to charge and discharge data analysis is described in Chapter 6.

Chapters 7, 8, and 9 present the results and discussions concerning the CVD, silicon oxycarbide, and pitch-blend materials, respectively.

Finally, conclusions, recommendations, and a summary of the contributions made by this thesis are provided in Chapter 10.

CHAPTER 2

LITHIUM INTERCALATION IN CARBONS AND ALLOYING IN SILICON

To discuss intercalation in carbons, one must first understand the structure of carbon. This thesis deals with two main types of materials: disordered carbons containing silicon and silicon oxycarbide glasses. An understanding of disordered carbon structures is necessary to understand the disordered carbons which contain silicon.

Section 2.5 provides a brief introduction to lithium-silicon alloying and the proposed structure of the disordered carbons containing nanodispersed silicon. The structure of the silicon oxycarbide glasses will be discussed in Chapter 8.

2.1 THE STRUCTURE OF CARBONS

Carbon has three basic forms, each with different types of carbon-carbon bonds. The structures of diamond and graphite have long been well known, while buckminsterfullerenes have existed for billions of years but, with the isolation and identification of C_{60}, were only recently discovered. The diamond structure consists of two overlapping face-centered cubic (fcc) lattices separated by 1/4 the length of the cube diagonal. The tetrahedral sp^3 bonds form a three dimensional network which is not easily broken, making it one of the hardest materials known. Graphite is a layered crystal. It and other disordered forms are of the most interest to this thesis and will be discussed in detail below.

Buckminsterfullerenes form a number of structures, the first reported being C_{60}. The structure is analogous to a Buckminsterfuller geodesic sphere or, more commonly seen, a soccer ball. The 60 carbon atoms sit at the points of pentagons and hexagons which bond to form a closed surface. Crystals of these C_{60} molecules form the face-centered cubic structure. Also included in the Buckminsterfüllerene family are similar, but larger, molecules such as C_{70}, other geodesic spheres, and the still larger carbon nano-tubes, which consist of distorted graphene sheets which are rolled to form tubes. The ends of these tubes are sometimes capped with hemispheres of C_{60}, C_{70}, and so on.

Within these idealized forms, there exist varying degrees of disorder. For graphite-like carbons, there are polycrystalline and quasi-crystalline forms ranging from the highly crystalline graphitic state to nearly amorphous states.

Carbons can be synthesized in many micro- and macroscopic forms with various applications. Powdered graphite is used as a dry lubricant (usually for low temperature applications). Mesocarbon microbeads are small spheres of graphite crystallites. Carbon fibers are used in lightweight composites to reinforce the structure of items such as squash racquets and Indy race cars. These fibers (which have been tested in lithium-ion batteries) can be synthesized with the graphene sheets oriented radially (similar to the spokes of a wheel) or cylindrically with the graphene sheets distorted and arranged as cylinders. Carbon felt (matted carbon fibers) can also be synthesized.

2.1.1 Graphite

As mentioned above, graphite is a layered crystal. The carbon atoms form planar,

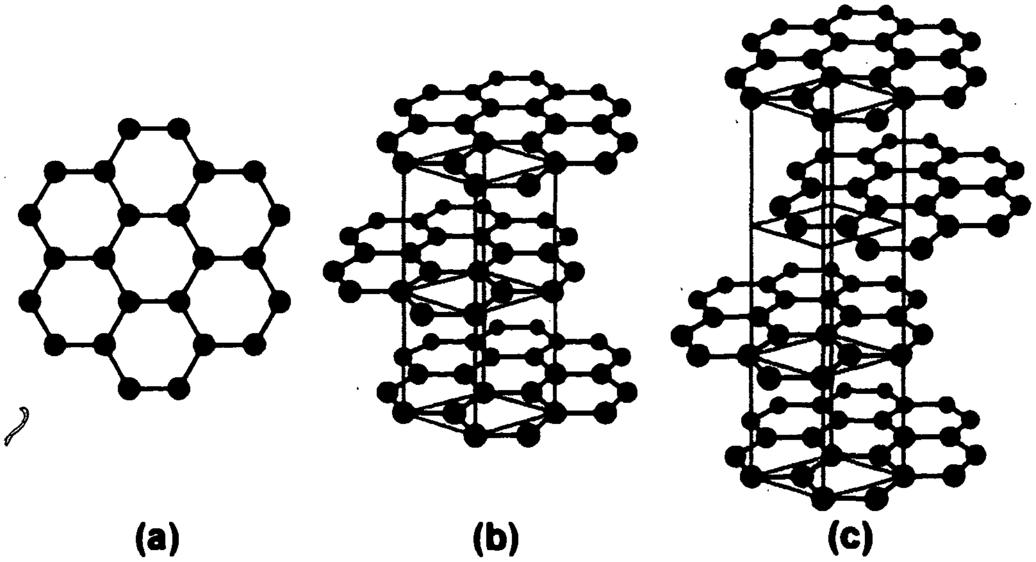

Figure 2-1. (a) A section of a graphene sheet and the structures of (b) 2H graphite and (c) 3R graphite.

trigonal sp^2 hybrid bonds (σ bonding), forming 2-dimensional hexagonal, honeycomb *graphene* sheets. A section of one is pictured in Figure 2-1a. Each carbon atom has one other bonding p-orbital aligned perpendicular to the sheet which forms π-bonds. These atoms also experience weaker van der Waal's (induced dipole-dipole) forces between the sheets which hold them together in a registered formation. The in-plane lattice constant, a, is approximately 2.45Å and the stacking distance (d_{002}), along the c, direction, is about 3.55Å. Natural graphite has two different forms with different stacking along the c direction. The most commonly found form is 2H, with hexagonal or ABABAB... stacking, shown in Figure 2-1b. Here the B layers are shifted by 1/3 of the unit cell along the (110) direction with respect to the A layers. Less common is the 3R form, with rhombohedral or ABCABCABC... stacking, shown in 2-1c. In 3R, the B and C layers are respectively shifted by 1/3 and 2/3 of a unit cell along the (110) direction. Shown schematically in Figure 2-2, natural and synthetic graphites tend to have a significant amount of stacking disorder, with both random stackings and 3R intergrowths in a predominantly 2H structure (Haering, 1958).

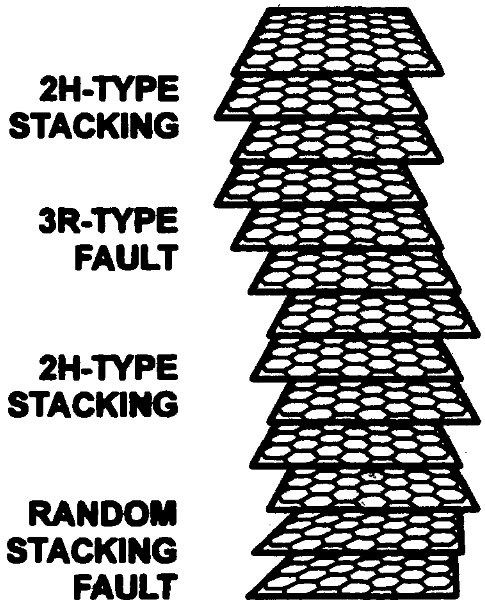

Figure 2-2. Schematic representation of a 3R intergrowth and a random stacking fault in a graphitic carbon.

The next section discusses disordered carbon structures, but some of these defects (i.e. stacking disorders, and lack of registered stacking) also apply to graphite.

2.1.2 Disordered Carbons

Carbons such as those prepared from polymers and petroleum pitches (Ashland, Crowley, etc.) by 'low' temperature pyrolysis (900 to 1300°C), have a disordered carbon structure. These are sometimes called *pregraphitic carbons*, although this may be a misnomer, as will be pointed out later. The graphene sheets may be bent, buckled or very small and the number of parallel stacked layers may average around as little as 2 to 3 or as many as 5 to 10. Some hard carbons consist almost entirely of single graphene layers (Liu, 1996). Figure 2-3 shows schematic representations of cross-sections of two different disordered carbons. The lines represent graphene sheets. The lateral layer extent, L_a, and the extent of the stacks, L_c, are much smaller than in graphite. There is strain in the stacking of the layers and there is a large probability (essentially 1) that adjacent graphene sheets are randomly stacked. There are both random rotations and lateral shifts between adjacent layers, leading to a loss of registry, referred to as *turbostratic disorder* (Warren, 1941; Franklin, 1951). Turbostratic disorder is a defect which can be observed in graphitic carbon. For pyrolytic graphites (synthetic), turbostratic disorder is complete at 2000°C and decreases with increasing pyrolysis temperature until about 3000°C, where it is eliminated (Zheng, 1996b).

Upon pyrolysis at higher temperatures (2000 to 3000°C) some of these disordered carbons form synthetic graphites. These are *soft carbons* and their disordered precursors may correctly be called *pregraphitic carbons*, because they are graphite precursors. However, other precursors do not form graphite after high temperature pyrolysis. These are *hard* or *non-graphitizable carbons*, and their precursors include highly crosslinked synthetic polymers. Many of the crosslinks in these polymers are not broken during pyrolysis, resulting in bonds between graphene layers which prevent proper registry.

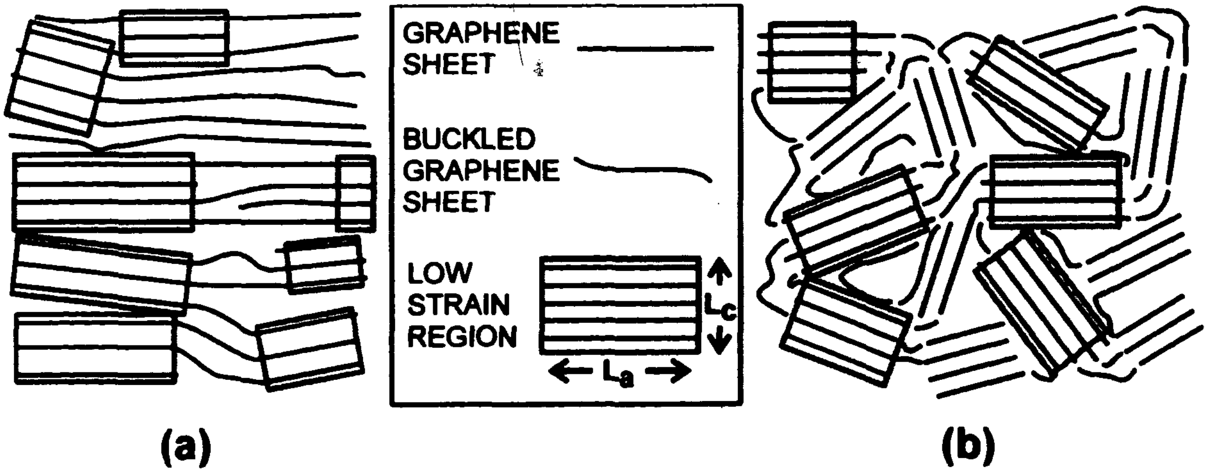

Figure 2-3. Schematics of (a) soft or pregraphitic carbon and (b) a hard or non-graphitizable carbon.

Figures 2-3a and 2-3b respectively show schematic representations of a soft and a hard carbon.

The powder X-ray diffraction profiles of disordered carbons can be difficult to interpret because there are only a few broad peaks. By using the Scherrer equation, one can estimate the average crystallite dimensions L_a and L_c. The in-plane carbon lattice constant a and the average layer spacing d_{002} can be estimated using Bragg's law. Some disordered carbons have L_a and L_c as small as 10Å with surface areas estimated by gas adsorption (BET) to be less than 1 m^2/g (Dahn, 1993). But, if the crystallite dimensions determine the particle size the observed surface area would be much larger. A simple calculation assuming a square particle of 10Å on a side and a graphite density of 2 g/cm^3 gives a surface area of 3000 m^2/g. Thus, the crystallite dimensions do not reflect the particle sizes. L_a and L_c represent the dimensions of regions, or correlation lengths, which scatter X-rays coherently. These regions of *organized carbon* (regions of low strain) are labeled in Figure 2-3. Franklin proposed that the organized regions were separated by regions of *unorganized carbon*, which consist of strained tetrahedrally bonded carbon and buckled graphene sheets (Franklin, 1951). The schematic in Figure 2-3b is similar to that proposed by Franklin. Note that the unorganized regions contain many atomic sized voids.

In order to better understand the structure of disordered carbons, a model based on these concepts can be developed. The important parameters are:

P - the probability that adjacent layers are randomly stacked
P_t - the probability of having 3R-type stacking
$1-P-P_t$ - the probability of having 2H-type stacking
g - the fraction of carbon that is made up of organized regions

and schematic representation of them is shown in Figure 2-4. The probability P_t is only relevant within organized regions. In unorganized regions, $P=1$.

Hang Shi *et al.* developed a structure refinement program which minimizes the difference between a measured powder diffraction profile and a calculated pattern based on the above parameters (Shi, 1993b). By using this program, one can determine accurate values of these parameters for many carbons of varying degrees of disorder. This program was used to determine the structure of some silicon-containing carbons (Chapter 7). The use of these parameters in understanding intercalation into disordered carbons will be discussed in Section 2.3.1.

However, some hard carbons consist almost entirely of unorganized carbon, where most of the carbon exists in single graphene sheets which are arranged more or less like a "house of cards" (Dahn, 1995; Liu, 1996). Because of the large population of voids, or *pores*, between the graphene sheets, these carbons have been called *microporous hard carbons*. The electrochemical interaction of lithium with these materials is discussed in Section 2.3.3.

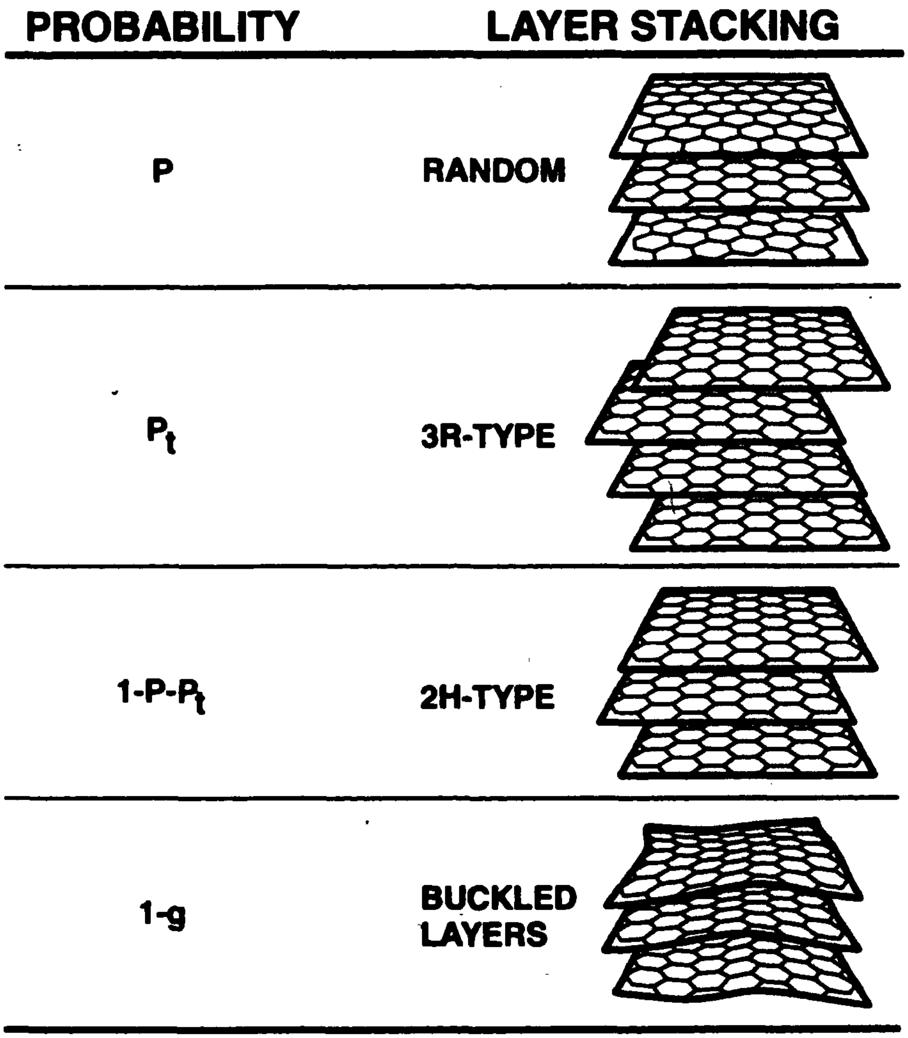

Figure 2-4. Schematic representations of the probabilities P, P_t, $1-P-P_t$, and $1-g$.

2.2 INTERCALATION

Intercalation is defined by McKinnon and Haering as "the reversible insertion of guest atoms into host solids such that the structure of the host is not significantly altered" (McKinnon, 1983). The *intercalants* (McKinnon and Haering's "guest atoms") should also include molecules. Here, a "significant" change involves a reordering of the host structure. The 'insignificant' change in intercalation typically involves an expansion of the host structure, but not a reordering of the atoms. Hosts typically have either a layered or tunnel structure. In this thesis, lithium is the only intercalant and disordered carbons are the only intercalation hosts of concern. The next section discusses lithium intercalation into various types of carbons.

2.3 LITHIUM INTERCALATION INTO CARBONS - 3 IMPORTANT REGIONS

The insertion of lithium into carbons is critically dependent on the structure of the carbon (Dahn, 1993; Noguchi, 1992). The structure of the carbon has been shown to be

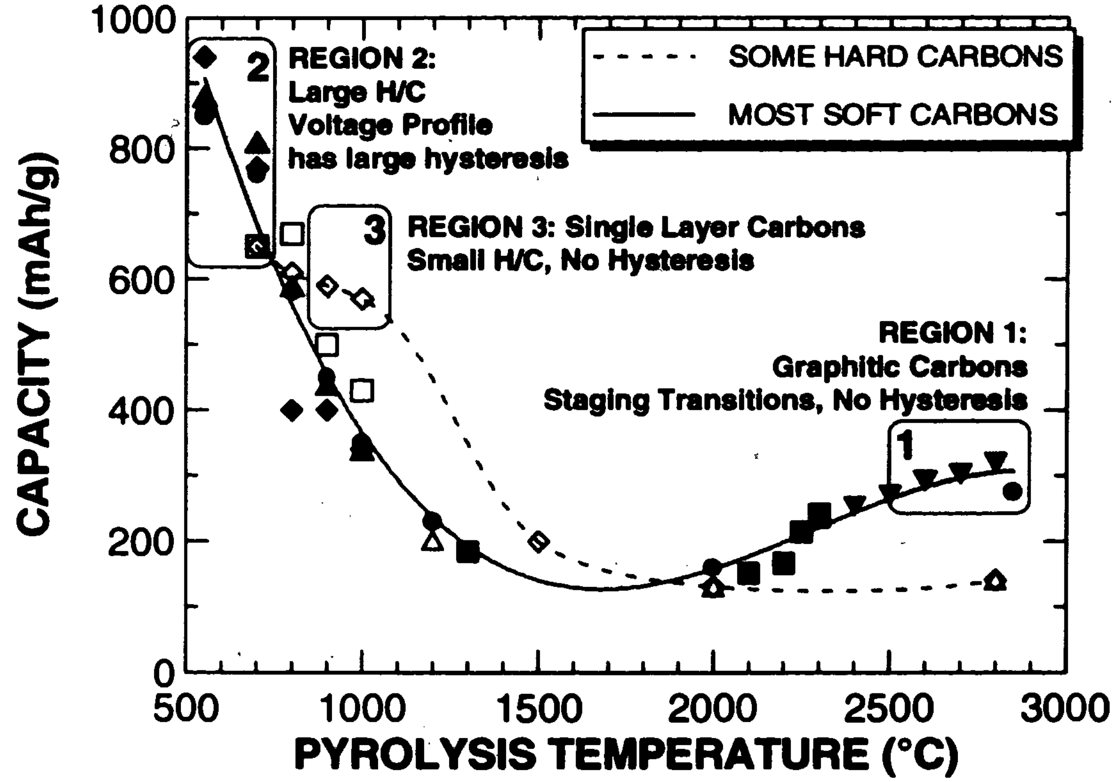

Figure 2-5. (From Dahn, 1995) The capacity versus pyrolysis temperature for carbons prepared from a variety of carbon precursors. Solid and open symbols respectively represent soft and hard carbons. H/C refers to the hydrogen to carbon ratio.

influenced greatly by pyrolysis temperature and precursor (Dahn, 1993; Qiu, 1993). Thus it makes sense to separate the discussion of electrochemical insertion of lithium into synthetic carbons into three regions, as done by Dahn *et al.* (Dahn, 1995). The regions are determined by three principal pyrolytic carbon groups determined by precursors and pyrolysis temperatures. Figure 2-5 (based on Dahn, 1995) shows the three regions of interest on the *master graph.* Region 1 contains graphitic carbons prepared by the pyrolysis of soft carbon precursors at temperatures above 2400°C (Zheng, 1995b; Zheng, 1996b). Region 2 contains carbons prepared by the pyrolysis of both soft and hard carbon precursors at temperatures between 500 and 800°C which contain significant amounts of hydrogen (Zheng, 1995c; Zheng, 1996c). Region 3 contains carbons prepared by the pyrolysis of hard carbon precursors to temperatures between 900 and 1200°C which are made up primarily of single graphene layers arranged in a manner analogous to a house of cards (Zheng, 1995d; Liu, 1996).

Lithium intercalates to different capacities at different voltages in materials from each of these regions. Figure 2-6 (based on Dahn, 1995) shows sample voltage profiles for electrochemical cells made of representative materials from each of these regions. The

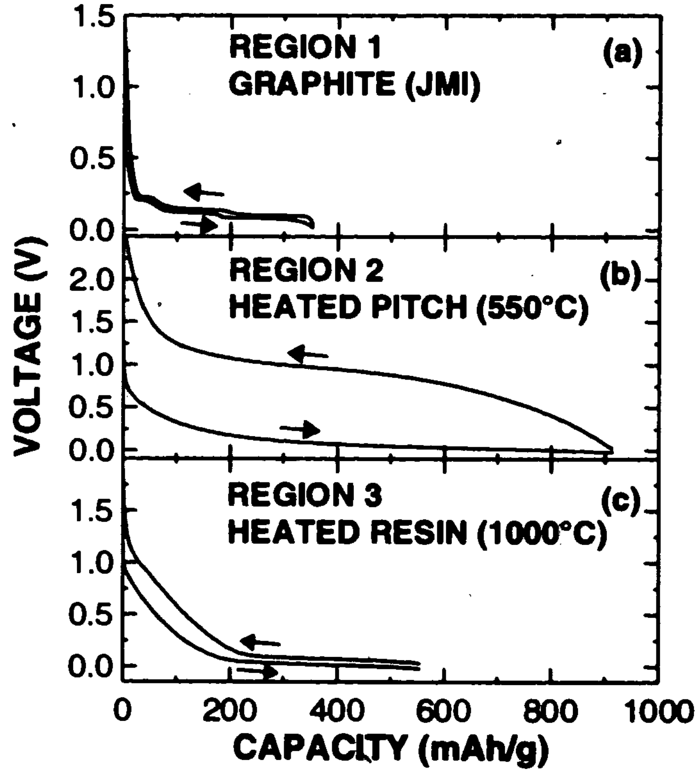

Figure 2-6. (From Dahn, 1995) Panels (a), (b), and (c) respectively show voltage profiles of cells made from materials representative of regions 1, 2, and 3.

next sections touch briefly on how lithium intercalates into each of these varied carbon structures and how this is observed in the voltage profiles.

2.3.1 Region 1 - Graphitic Carbons

The structure of graphite was discussed in Section 2.1.1. The insertion of lithium into graphite structures has been the subject of extensive study by many (Kambe, 1979; McKinnon, 1983; Fischer, 1987; Boehm, 1992; Ohzuku, 1993; Dahn, 1995; Zheng, 1995a to d; Zheng, 1996a to d; etc.). Lithium is inserted between the graphene layers which expand in the stacking direction and shift slightly along the in-plane direction. The lithium atoms reside between the layers aligned with the centres of carbon hexagons (Kambe, 1979). Thus, in the regions which accommodate the lithium atoms the layers expand along the c-axis direction and shift along the (110) direction, losing their 2H or 3R registry, stacking in an AAA... fashion (Boehm, 1992). This is shown schematically in Figure 2-7. Lithium can be intercalated into graphite at ambient pressure and temperature to a theoretical maximum of LiC_6 (Fischer, 1987). This corresponds to each lithium occupying the centre of a hexagon where each adjacent hexagon is empty.

It has been known since 1955 that graphite intercalation compounds exhibit staging (Herold, 1955). In 1980, Safran concluded that the staging arises from a competition

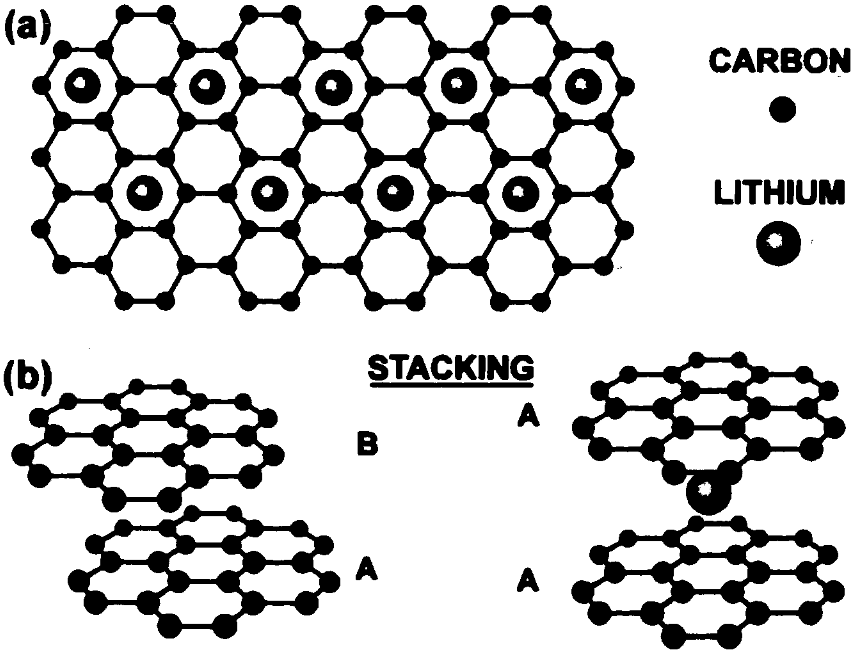

Figure 2-7. Schematic representations of lithium intercalated graphite (a) A basal view of LiC_6 (b) 2H graphite, before and after lithium insertion.

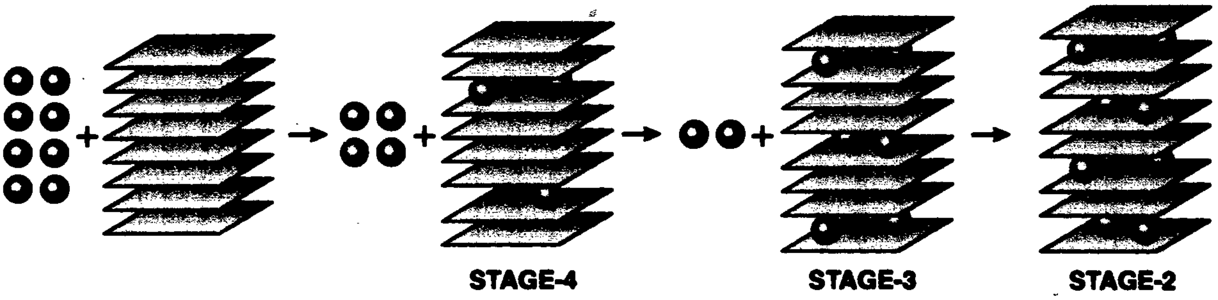

Figure 2-8. A schematic representation of staging in a layered host.

between inter-layer repulsive forces and in-plane attractive forces (Safran, 1980). Stage-*n* is defined such that there are *n* graphene sheets between each intercalated layer, as shown schematically in Figure 2-8. The final stage of graphite, fully intercalated to LiC_6, is stage-1 graphite. The transitions between stages appear as plateaus in the voltage profiles of graphitic carbons, which can be seen in Figure 2-6a.

If the stages in graphite appeared as long rigid sheets, the conversion between observed stages would be difficult. For example, if in stage-3 the space between every fourth graphene sheet had to be completely filled with lithium, and none of the other spacings contained any lithium, the conversion from stage-3 to stage-2 would be extremely unlikely. The lithium atoms would first have to deintercalate and then re-enter the appropriate layers, or else tunnel through layers. To understate the obvious, neither is likely to happen. The domain model proposed by Daumas and Herold (Daumas, 1969) explains these stage transformations. Here there are domains which are all stage-*n* and upon further intercalation, the conversion to stage-*(n-1)* is achieved by lithium atoms sliding to different domains while staying between the graphene sheets. A possible stage-2 under the Daumas and Herold domain model is shown in Figure 2-9.

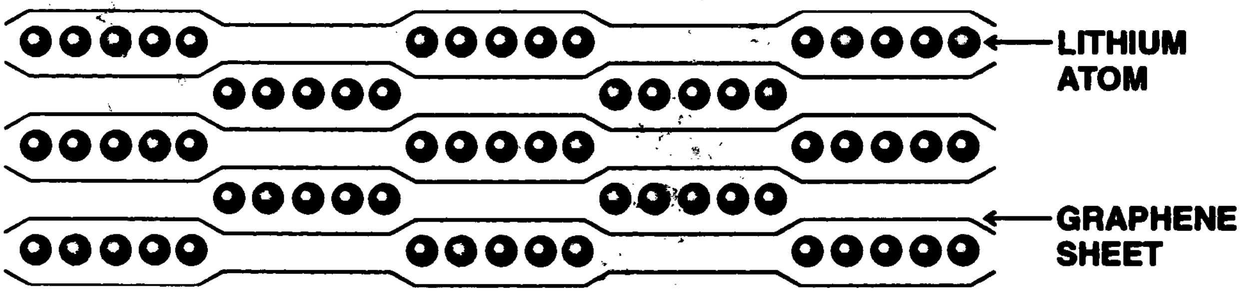

Figure 2-9. A schematic representation of stage-2 in the Daumas and Herold domain model for staging.

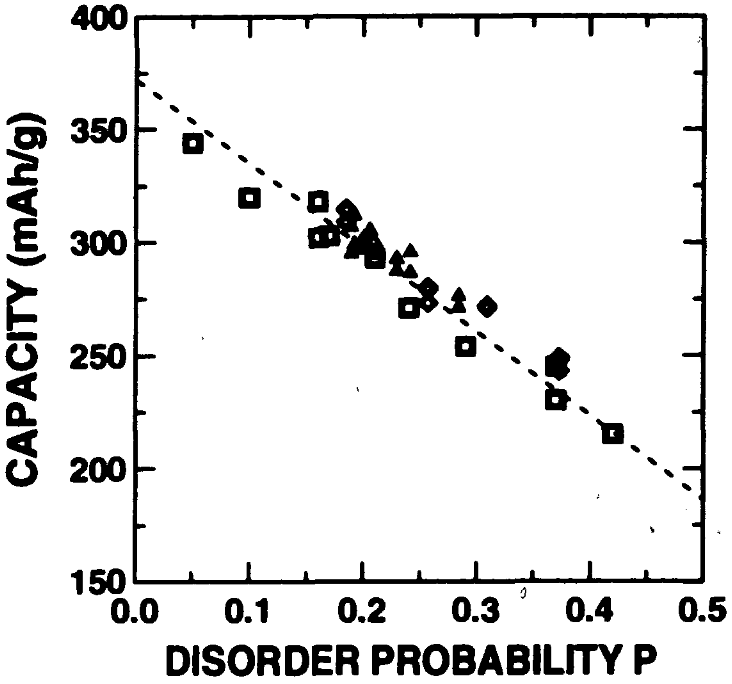

Figure 2-10. (From Zheng, 1995b.) Reversible capacity versus P, for soft carbons heated above 2200°C.

Graphites can contain differing amounts of disorder, as discussed in Section 2.1.2. Turbostratic disorder in a graphite can prevent the insertion of significant amounts of lithium into the material, and thus reduces the capacity from the theoretical maximum of LiC_6, which corresponds to 372 mAh/g of capacity. Figure 2-10 shows the capacity, in mAh/g, of various graphites to intercalate lithium versus the probability, *P*, of finding a turbostratic shift between graphene sheets (Zheng, 1995b). This suggests that little or no lithium can intercalate between randomly stacked layers (Dahn, 1993).

2.3.2 Region 2 - Hydrogen-Containing Carbons

These carbons are made from both hard and soft carbon precursors pyrolysed to temperatures between 700 and 900°C. When organic precursors are heated to near 700°C, they partially decompose leaving graphene sheets (and sheet fragments) with hydrogen-terminated edges. Depending on the precursor, there may be other impurities in these materials, including oxygen, nitrogen, and sulfur, although carbon and hydrogen make up the bulk of the material (Zheng, 1996d). Pyrolysis to temperatures above 700°C begins to drive off the hydrogen, and by 1000 to 1100°C, essentially all of the hydrogen is gone (Yata, 1994; Mabuchi, 1994; Sato, 1994; Zheng, 1996a).

These materials show large capacities with a difference in voltage between charge and discharge (*charge-discharge hysteresis*) of about 1 V, as in Figure 2-6b. Figure 2-11 (Zheng, 1996a) shows the capacity during charging of the 1 V plateau versus the hydrogen to carbon atomic ratio (H/C) for lithium metal electrochemical cells made from these materials (Figure 6-20 in Zheng, 1996a). Clearly, there is a correlation between the amount of hydrogen in the material and the capacity of the 1 V plateau. However, the structure of the carbon is also correlated to the pyrolysis temperature and this has led to some controversy.

Scientists at Osaka Gas Co., Ltd. feel that the hydrogen is merely a spectator, and that it is the structure of these carbons which is responsible for the capacity of the 1 V plateau (Mabuchi, 1994; Yata, 1994; Matsumura, 1995; Tokumitsu, 1996). Many of these arguments are also applied to the region 3 carbons, which are discussed in the next section. The models which disregard the role of the hydrogen are not consistent with all of the experimental evidence which has been presented.

Zheng *et al.* have shown that for some hard carbon precursors, while hydrogen is lost,

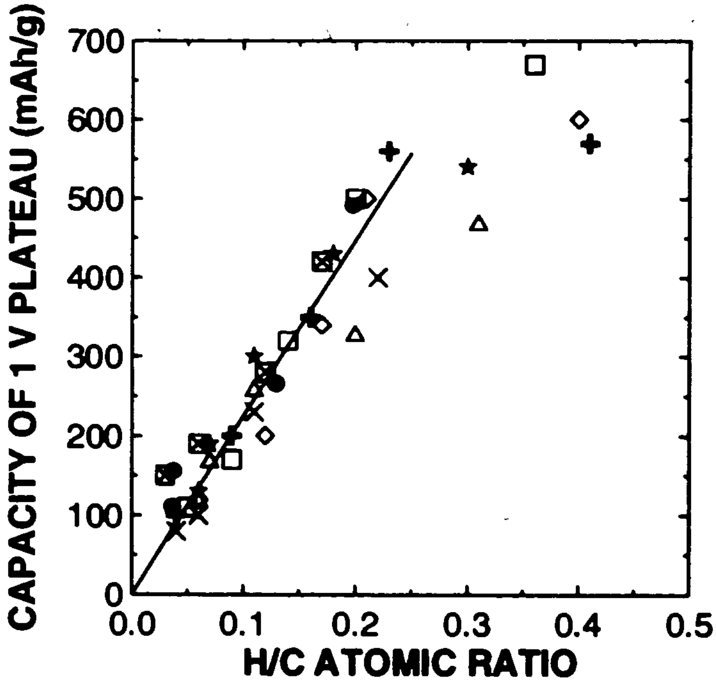

Figure 2-11. (From Zheng, 1996a) The capacity of the one volt plateau measured during the second cycle of several series of samples versus the atomic ratio of hydrogen to carbon (H/C) in the samples. The solid line suggests that there is a hydrogen atom for each lithium atom binding. Note that the solid circles represent data from Mabuchi et al., 1994.

there is little structural change upon heating and the 1 V charging plateau essentially vanishes (Zheng, 1996a). Figure 2-11 shows that many carbons with different structures all prepared at low temperatures from various precursors all exhibit the same correlation between the hydrogen content and the capacity of the 1 V plateau.

To explain this, Zheng *et al.* present a model suggesting that the hysteresis results from the activated process of lithium atoms bonding near carbon atoms which are also bonded to hydrogen atoms (Zheng, 1996c). Referencing work by Papanek *et al.*, they suggest that the lithium which bonds to the edges of hydrogen-terminated hexagonal carbon fragments may have local geometries analogous to the organolithium molecule $C_2H_2Li_2$ (Zheng, 1996c). The model agrees well with the electrochemical behaviour of these materials when cycled in test cells at higher temperatures. Their model also agrees with the experimental data presented by many others (Mabuchi, 1994; Yata, 1994; Matsumura, 1995; Tokumitsu, 1996).

2.3.3 Region 3 - Microporous Hard Carbons

These carbons consist mostly of single graphene sheets arranged like a house of cards as shown schematically in Figure 2-12a. They are prepared at temperatures above 900°C, so that there is a negligible amount of hydrogen. Figure 2-6c shows a typical voltage profile for a carbon from region 3 (Zheng, 1996d). There have been several reports of carbons with similar voltage profiles (Omaru, 1992; Takahashi, 1994; Sonobe, 1994; Liu,

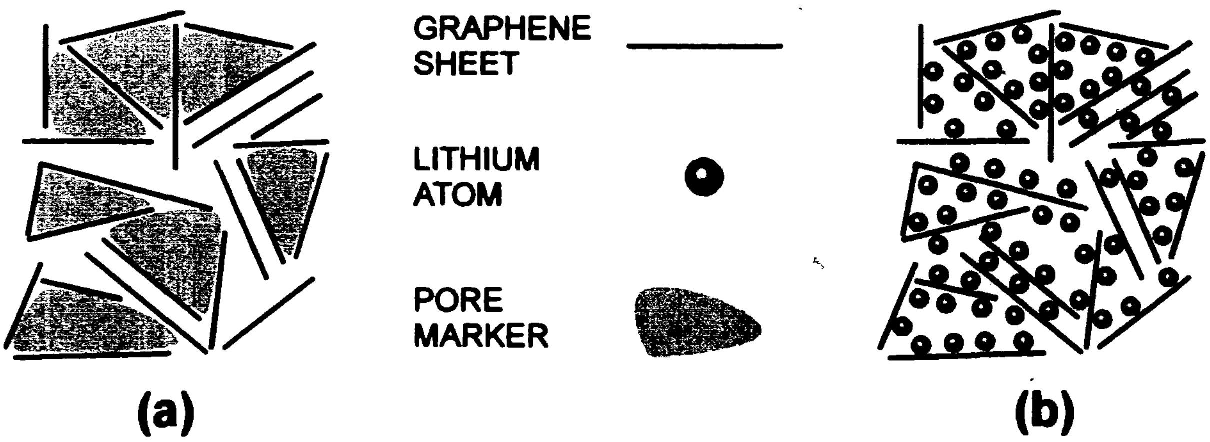

Figure 2-12. The schematic view of a microporous hard carbon (Zheng, 1996d) (a) before reaction with lithium (examples of pores formed by graphene sheets are marked by grey shading) and (b) after the adsorption of lithium onto the internal surfaces of the nanopores.

1996). At the time of writing, the mechanism by which these carbons intercalate lithium was another area of contention, although the models presented by Zheng *et al.* (Zheng, 1996d) and Matsumura (Matsumura, 1995) agree and are the most reasonable.

Others have suggested that the lithium is somehow being inserted between graphene layers to a concentration greater than LiC_6 (Mabuchi, 1994). This model, however, ignores the X-ray diffraction data which clearly shows very little parallel stacking of graphene sheets. Also, studies by Nalimova *et al.* suggest that the only way to make the saturated compound LiC_2 with graphite is under a pressure of 50 to 60 kbar at a temperature of 280°C (Nalimova, 1995). They made LiC_2 and LiC_4 and observed that it decomposed to a 'stable' step in the decomposition process to LiC_6. The 'stable' compound was identified as $LiC_{2.67}$ and was kept at ambient pressure and temperature for one year without decomposing to LiC_6 (Nalimova, 1995). However, it has not been demonstrated that LiC_2 or $LiC_{2.67}$ can be made from graphite at ambient conditions by electrochemical or any other means.

More realistic is that the lithium is being adsorbed on the walls of micropores in the hard carbon (Liu, 1996; Zheng, 1996d). These micropores (or nanopores) are created by the graphene sheets arranged like a house of cards (Figure 2-12a). Figure 2-12b shows a schematic of how the lithium is inserted into the pores (based on Figure 7-1 in Zheng, 1996d). The lithium atoms bond to the faces of the graphene sheets (Matsumura, 1996; Zheng, 1996d; Liu 1996). Most of the lithium atoms in the pores are not bonded between graphene sheets so many graphene sheets can accommodate lithium on both sides. This increases the total amount of lithium intercalated beyond the composition of LiC_6. Some region 3 carbons contain small numbers of graphene sheets stacked with disorder in a parallel manner. Due to the disorder, lithium atoms which intercalate between these graphene sheets are bound at many different potentials. This can be observed as the sloping voltage (absence of staging) in Figure 2-6c. The long plateau near 0 V is thought to be a result of the bonding of lithium to the surface of graphene sheets. The lithium is not bound tightly and thus has a low voltage with respect to lithium metal.

The next section discusses lithium alloys and their relevance to this work.

2.4 LITHIUM ALLOYS

Lithium will form alloys with a number of different elements. Table 2-1 presents the stoichiometry range, the average voltage, and the theoretical maximum capacity (in mAh per gram of starting material) for lithium alloys created by electrochemical reactions (Besenhard, 1996, Wang, 1986, Huggins, 1987). For comparison purposes, graphite (an intercalation compound) is included in this list (Kambe, 1979). The alloying process is not sufficiently reversible for the direct replacement of the carbonaceous electrode materials, in spite of the greater capacity of the alloys for lithium (Besenhard, 1986). It was our idea that the benefits of the alloys could be combined with the reversibility of the carbonaceous hosts if the alloying atoms could be dispersed throughout a disordered carbon host.

Of the lithium alloys shown, silicon has, by far, the largest capacity. The average silicon-lithium alloying potential is less than one volt (Besenhard, 1986), which is advantageous for lithium-ion battery applications, as discussed in Chapter 1. For these reasons and also because it is chemically similar to carbon, silicon was chosen as the alloying element for our studies. The next section discusses some of the difficulties associated with direct replacement of the carbon anode materials with silicon.

2.4.1 Silicon-lithium Alloys

When silicon alloys with lithium, there is a radical change in the structure of the silicon atoms (Boukamp, 1981). Boukamp *et al.* showed that, after alloying to the maximum

Table 2-1. A summary of various lithium alloys (ambient temperature and pressure).

Material	Range of x	Calculated Specific Capacity* (mAh/g)	Reference
Li_xSn	0.4 - 4.4	901	Besenhard, 1996
Li_xAl	0.0 - 1.0	993	Wang, 1986
Li_xCd	1.0 - 3.0	477	Huggins, 1987
Li_xPb	1.0 - 4.4	440	Huggins, 1987
Li_xSi	0.0 - 4.4	4196	Huggins, 1987
Li_xC_6**	0.0 - 1.0	372	Kambe, 1979

* the specific capacities of the alloys are calculated from the stoichiometries given using Equation 6-1 (Section 6.1.2.1), multiplied by the total Δx with y set to 1.

** lithiated graphite is an intercalation compound (not an alloy) lithium concentration ($Li_{4.4}Si$) the silicon atoms completely rearranged (from cubic to orthorhombic crystal structures) and the crystal volume per silicon atom increased by more than 300% (Boukamp, 1981). Upon removal of the lithium the material shrinks and breaks apart. Maintaining electrical contact to the shrinking and crumbling material poses serious difficulties. Since electrical contact cannot be maintained, electrons cannot be supplied to (or removed from) the silicon to allow lithium ions to come out of (or dissolve into) the electrolyte. This makes it virtually impossible to make a secondary lithium-ion cell using pure silicon as an anode material. However, research investigating lithium alloys as anodes for lithium ion cells continues. Besenhard *et al.* are attempting to compensate for the expansion and contraction of alloys by making electrodes which consist of fine-grained and slightly porous deposits of composite alloys on copper substrates (Besenhard, 1996). The composites cycle reasonably well, although there are other considerations involved with making electrodes of small reactive particles.

2.4.2 Silicon in Disordered Carbons

Figure 2-13a shows a schematic of a disordered carbon. We sought to synthesize a material where the regions of unorganized carbon contained silicon, as shown in Figure 2-13b. The silicon contained within the disordered carbon matrix may consist of individual atoms or as clusters small enough to allow reversible reaction with lithium. The organized

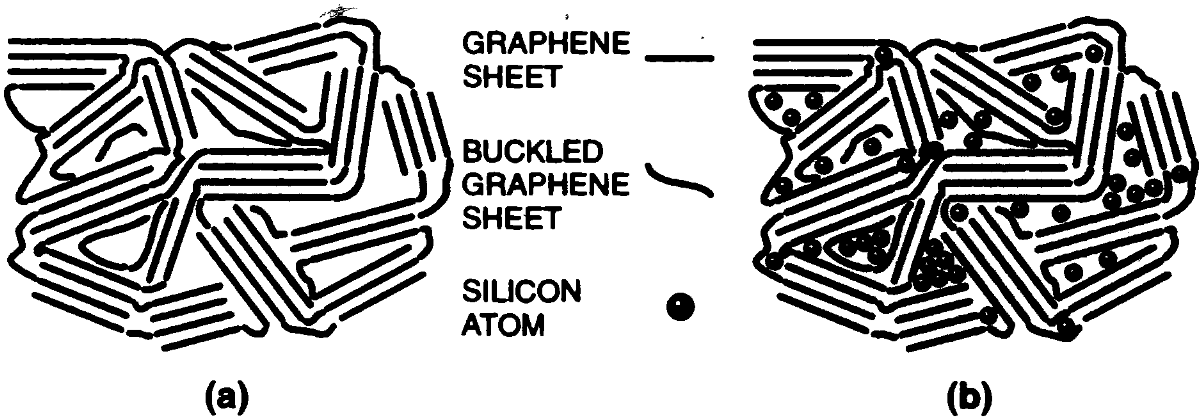

Figure 2-13. (a) A disordered carbon and (b) a disordered carbon containing nanodispersed silicon atoms. The silicon atoms occupy the unorganized carbon regions.

carbon provides a pathway for the lithium to the alloying atoms while it remains available to intercalate lithium reversibly. The structure shown in Figure 2-13b is presumably metastable, since such compounds are not found in the silicon-carbon phase diagram (Moffat, 1990).

This thesis shows that we were successful in making materials like those shown in Figure 2-13b by two different synthesis routes and that they performed in the desired way in electrochemical cells. Chapters 3 and 4 discuss two different ways these materials were made and Chapters 7 and 9 discuss their properties.

CHAPTER 3

EXPERIMENTAL I: SYNTHESIS OF THE CVD MATERIALS

Chemical vapour deposition (CVD) is a convenient method commonly used to prepare novel materials. Since silicon- and carbon-containing gas sources are readily available, we adopted a CVD method for synthesizing these materials.

3.1 INTRODUCTION TO CHEMICAL VAPOUR DEPOSITION

Hitchman and Jensen define CVD in the following way:

> Chemical Vapor deposition (CVD) is a process whereby a thin solid film is synthesized from the gaseous phase by a chemical reaction. It is this reactive process which distinguishes CVD from physical deposition processes, such as evaporation, sputtering and sublimation. (Hitchman, 1993)

However, in the context of the rest of the introductory chapter, the deposition of powders, such as carbon black, is also considered a CVD process. That is, the nucleation of reactants in the gas stream to form particles which do not deposit as a film is also considered CVD. This is specifically pointed out, because it is the synthesis of powders which make up the bulk of the CVD work in this thesis.

3.1.1 A Brief History of CVD

Chemical vapour deposition has been practiced for a long time. In an overview, Hitchman and Jensen point out that CVD development has been closely linked to the practical needs of society (Hitchman, 1993). They claim that the oldest example of a material deposited by CVD was probably pyrolytic carbon, since (they reference Blocher

(1966)) "some prehistoric art was done on cave walls with soot condensed from incomplete oxidation of wood" (Hitchman, 1993). While this may seem to be stretching the definition of CVD, it was indeed a similar procedure which was used commercially (the patent was issued to John Howarth) for the preparation of carbon black as a pigment. The next major application of CVD was the emerging electric lamp industry to make improvements to fragile carbon filaments.

According to Hitchman and Jensen, the first records of silicon made by CVD describe the hydrogen reduction of silicon tetrachloride by Pring and Fielding in 1909. Just after World War II this was used to make silicon for photo cells and rectifiers.

Work on CVD increased during the 1960's and 70's. During the 1980's, CVD literature experienced exponential growth (Hitchman, 1993).

3.1.2 Deposition Parameters

Hitchman and Jensen write an overview of the important factors for CVD processes. The principal factors, arguably of equal importance, are categorized as reactor design, energy input method, and materials (substrates and precursors).

The energy input method is treated separately because most of the chemical reactions employed in CVD are thermodynamically endothermic and/or have an energy of activation associated with them. The most obvious method of inputting energy into the reaction is by thermal means. That is, either by heating the entire reaction area (as is done with a hot wall reactor) or by heating the substrate (the material on which you want to deposit the reaction products). Other methods of inputting energy into the system are through the use of plasmas, higher frequency radiation (photo CVD), and sound waves (acoustic CVD). In this thesis, the CVD reactions were all performed in a hot wall reactor.

Reactor design includes such rudimentary factors as the pressure of the reaction and the design of the energy input method (i.e. hot wall reactor versus a heated substrate). The reactor shape affects fluid flow, transport phenomenon, and reaction kinetics. In order to make smooth well adhered deposits, gas-phase nucleation should be avoided. Special attention should be paid to the fluid flow in order to make even deposits over the entire substrates.

Considering all of these factors, a clear understanding of the kinetics of many CVD reactions is an exceedingly difficult task. Thus, it is only in recent years that there has been a noticeable attempt to move away from the empirical approach in CVD.

The choice of precursors and substrates is entirely dependent on the application. The precursors must be carefully selected so that the chemical reaction will produce the desired product without the interference of 'waste' products (the byproducts of the reaction). Similar care must be taken in choosing a substrate.

Since we were not especially interested in making films and due to constraints on the equipment at hand, we used a hot walled CVD reactor at ambient pressure. Therefore, the areas of concern within this work were sources, vapour flow rates, temperature, and substrate.

3.2 PREVIOUS CVD STUDIES

Carbon and silicon are two of the most abundant elements on the planet. They have been used together in ways too numerous to mention. Despite this, at the time of writing there were no reports (by others) of materials similar to that shown in Figure 2-13 (nanodispersed silicon in disordered carbons).

CVD methods have been commonly employed to make carbon-doped silicon (Herremans, 1992; Rübel, 1993; Shufflebotham, 1987; Wang, 1991) and silicon carbides (Grow, 1993; Waki, 1989). Some studies of carbons with silicon impurities have been reported (Gat, 1993; Ibraham, 1989; Dorfman, 1992; Marinkovíc, 1984). None of these appear to describe a material similar to that shown in Figure 2-13.

Of the studies of carbons with silicon impurities, the review by Marinkovíc of silicon solid solubility in carbon is specifically of interest. In this review, materials which contain small silicon concentrations in pyrolytic carbons (made by CVD of $SiCl_4$ and CH_4 with H_2) show evidence that the silicon exists as silicon carbide or possibly in other forms, about which the author does not speculate. Some of the materials in the review by Marinkovíc may have contained regions similar to the material shown in Figure 2-13. However, the existence of these regions was not reported, and it is unlikely that they were detected.

The greatest value of these studies to this thesis was in suggesting criteria for the *avoidance* of byproducts during the synthesis of materials like that shown in Figure 2-13.

3.3 CVD WITH APPARATUS I

Two apparatuses were employed to make silicon nanodispersions in pregraphitic carbons. In this section the first apparatus (CVD Apparatus I) is discussed. Materials made using it are referenced throughout the thesis as CVD-I materials. It was used to evaluate whether the synthesis of these materials was possible, before expending the effort to design and construct CVD Apparatus II, discussed in Section 3.4.

3.3.1 Description of CVD Apparatus I

Figure 3-1 shows a schematic representation of CVD Apparatus I. The deposition takes place inside a 4-ft-long, 2-in.-diam., quartz reaction tube located inside a Lindberg tube furnace. In order to collect material deposited where the temperature is best known, a 1-ft-long, 1.5-in.-diam., quartz, tubular insert is placed inside the reaction tube at the centre of the 18-in.-long hot zone. The thermocouple which measures the temperature of the furnace is located at the centre of the hot zone. Quartz was selected as the material for

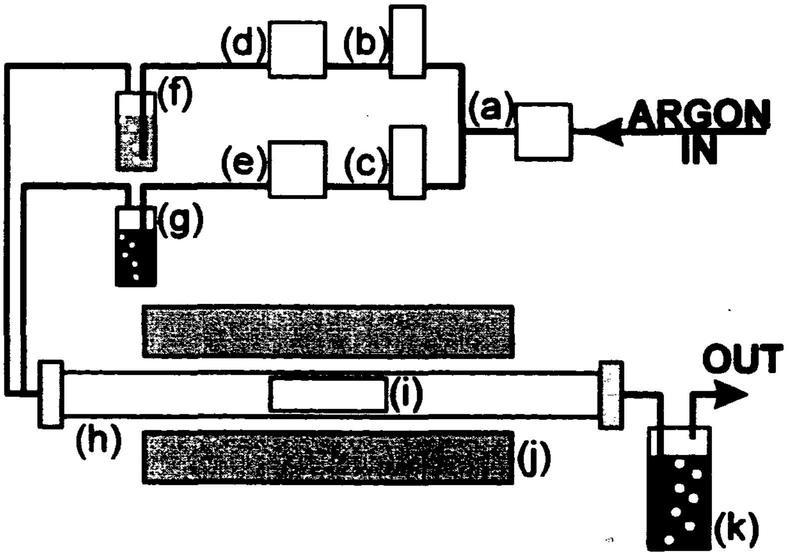

***Figure 3-1.** A schematic representation of the CVD apparatus where (a) is the automatic flow controller; (b) and (c) are manual flow controllers; (d) and (e) are digital flow meters; (f) and (g) are stainless-steel source bottles; (h) is the reaction tube; (i) is the tubular insert, aligned to the furnace hot zone; (j) is the furnace; and (k) is the oil bubbler.*

the reaction tube and tubular insert because it was not likely to react with our source vapours or the reaction products of these vapours and could withstand temperatures up to 1150°C.

The sources are held in Teflon-lined stainless steel bottles which are connected to the deposition tube via Teflon-lined stainless-steel hoses. The two source vapours mix at the reaction tube end cap.

Argon, used as a carrier gas, is supplied to the source bottles after passing through a series of flow controllers and meters. A Sierra Side-Trak™ automatic flow controller regulates the total argon flow, which is then split between two manual Matheson flow controllers, allowing the ratio of the flows to be controlled. The flow rates of argon via each path were measured by Sierra Top-Trak™ digital flow meters. The flow rate is measured by the Top-Trak™ by diverting a small percentage of the carrier gas through an alternate path and measuring the temperature difference between temperature sensors placed upstream and downstream of a heater coil. The Side-Trak™ controller employs the same method to measure the flow rate and automatically adjusts a piston to keep the flow rate to the constant, calibrated value selected. The Model 860 Side-Trak™ mass flow controller has a rated error 1% of full scale, which is 200 SCCM (cm^3/min under standard conditions).

Flow through the manual Matheson flow controllers is adjusted by manual adjustment of a piston which partially blocks the gas flow. The resulting flow is then measured by reading a plastic ball which is lifted by the gas stream inside a glass column. The ball travels upward in the column until the force of gravity on the ball is equal to the net force exerted by the gas flowing up past the ball. A flow reading can be taken from the ball to graduated markings printed on the outside of the glass column. Calibration curves for these flow controllers could not be located so a manual calibration was performed. A one litre Erlenmeyer flask was filled with water and inverted in a tray of water. Argon was supplied to fill the bottle through a flow controller adjusted to read a specific number on the scale. The time to fill the container was measured and used to calculate the flow rate.

This was done for various settings for each flow controller and the results were plotted as a calibration curve. As discussed next, highly accurate flow rates were not required.

The flow rates of the source vapours were estimated from the vapour pressure for the source and the flow rate of the argon through the bottle, assuming that the source had sufficient time to saturate the carrier gas. Because the gases partially decompose along the reactor tube walls, the absolute ratio of source vapours in the hot zone is not known. Thus, highly precise knowledge of flow rates would not have been useful. The total flow rate was kept below 200 cm^3/min. The carrier gas flow rate ranged from 37 to 74 cm^3/min for benzene, and 20 to 60 cm^3/min for the silicon sources.

Gases leave the system via an oil bubbler (to prevent any possible backwash from the outside) attached to a fume hood line.

3.3.2 Synthesis of Materials with CVD Apparatus I

3.3.2.1 Chemical Sources

Reagent grade benzene (Caledon Labs, Ltd. ACS spectrograde) was used as the carbon source. It has been frequently used by other members of this group as a carbon source for CVD work. Benzene is quite stable and will not decompose in an inert atmosphere at temperatures below 800°C. We believed that it was fairly unlikely that benzene would react with the silicon sources to form silicon carbide at temperatures in our range of interest.

Semiconductor grade $SiCl_4$ (Aldrich Chemical Company, Inc. 99.999%) and research grade $(CH_3)_2Cl_2Si$ (DOW-Corning Chemical) were used as silicon sources. These chemicals were selected mainly for safety reasons. SiH_4 might have been used as a silicon source, as it is in the semiconductor industry, but being pyrophoric it was felt that organochlorosilanes, such as those used here, might be more appropriate. The chemistry appeared to be favourable and less exothermic. It was suspected that SiH_4, through an exothermic decomposition, might react with benzene to produce silicon carbide, an undesired product.

All liquids were used as received. Ultrahigh-purity argon (Linde, 99.999%) was used as a carrier gas.

3.3.2.2 Temperature

The goal was to incorporate silicon into a pregraphitic carbon, without producing silicon carbide. The upper temperature limit of the Lindberg furnace was in the lower range of temperatures at which silicon carbide may be produced by CVD (Marinkovíc, 1984). Since benzene will not completely decompose below 800°C, the range of 850°C to 1050°C was selected.

3.3.2.3 Substrate

The only substrate used for deposition of materials in this thesis was quartz. Since most of the materials studied were deposited onto a quartz tubular insert for later removal and study, it made sense to also deposit films and powders onto quartz substrates. The films deposited on the quartz substrate could be studied without removal from the substrate. However, it was the powders and not the films which were of principal interest.

3.3.2.4 General Deposition Method

To ensure that there are no leaks in the system, the far end of the reaction tube is sealed. Argon is then supplied to pressurize the system to 10 psi. A mixture of water and detergent (Snoop™) is then applied to all joints in the system. Bubbles appear where there are significant leaks. This type of leak checking is only performed after sections of the system, other than end-caps, were opened (i.e. when source bottles were refilled).

The tubular insert, with optional substrates, is placed in the centre of the reaction tube, which is placed, centered, in the tube furnace. To check for leaks, a very small gas flow of approximately 6 cm^3/min is allowed into the tube. The oil bubbler is then inspected to ensure that the gas is forcing the argon through the bubbler. At such low flow rates any leaks of consequence would allow the argon to escape and no bubbles would be observed in the oil.

The furnace is then raised to the temperature which is desired for the deposition. While this is proceeding, the system is then flushed with a volume of argon sufficient to fill the reaction tube 10 times.

Argon carrying the source vapours is then allowed to enter the tube. The total flow rate was kept below 200 cm^3/min. The carrier gas flow rate ranged from 37 to 74 cm^3/min for benzene and 20 to 60 cm^3/min for the silicon sources. The estimated flow rate ratio of $SiCl_4$ to benzene for the CVD-I samples was controlled between 2:3 and 2:1. The estimated flow rate ratio of $(CH_3)_2Cl_2Si$ to benzene for the CVD-I sample presented here was 1:1. Benzene was deposited alone, at a carrier gas flow rate of 37 cm^3/min.

After a deposition and subsequent sample reclamation the reaction tube and tubular insert were cleaned. First the reaction tube with insert inside is burned out in the furnace. The sealed tube is supplied house air with gases exiting through the oil bubbler and out the fume hood line. The tube is heated to 1050°C until it is clear that no further oxidation of the contents will continue. After removing and cooling, the reaction tube and insert are both scrubbed with detergent and well rinsed. They are then dried in the furnace, ready for the next deposition.

3.4 CVD WITH APPARATUS II

This section describes the second CVD apparatus used. Materials made using it are referenced throughout the thesis as CVD-II materials.

3.4.1 Description of CVD Apparatus II

This apparatus was designed to allow greater and more accurate control of source vapour pressures and to allow injection of the mixed vapours into different regions in the tube. Figure 3-2 shows a schematic representation of CVD Apparatus II.

As in CVD Apparatus I (Section 3.3.1), deposition takes place inside a similar quartz reaction tube with a tubular insert holding quartz substrates.

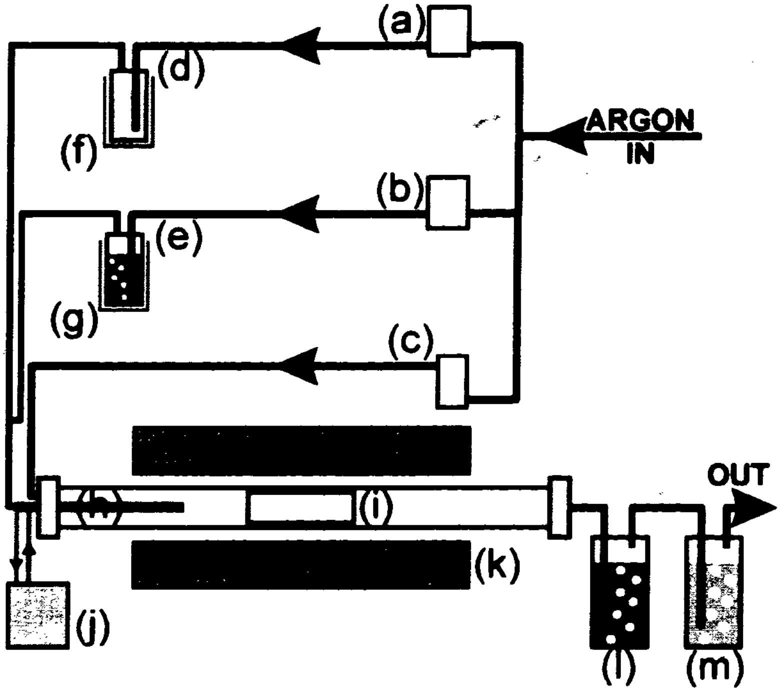

***Figure 3-2.** A schematic of the CVD apparatus where (a) and (b) are automatic flow controllers; (c) is the flushing manual flow controller; (d) and (e) are the source bottles; (f) and (g) are the heated copper sleeves; (h) is the injection rod; (i) is the tubular insert; (j) is the circulating bath; (k) is the furnace; (l) is the oil bubbler; and (m) is the water bubbler.*

The sources are stored in vacuum-passivated, stainless steel bottles which are kept at constant temperatures by heated copper sleeves, controlled by Omega temperature controllers. A resistance temperature device (RTD) temperature sensor (Omega 1 Pt 100 K 20 15) is located approximately 1/2 way up the copper sleeve, in good thermal contact with the source bottle and copper sleeve. The RTD consists of a very thin coil of Pt wire embedded in a ceramic sleeve. As the temperature of the RTD changes, so does the resistance of the Pt wire. This is sensed by the Omega temperature controller which is calibrated to convert this to a temperature. The base of the copper sleeve, a 1/4-in-thick sheet of copper metal is placed on a hot plate. The Omega temperature controller reads the RTD and maintains a roughly constant temperature inside the source bottle by turning the hot-plate on and off.

The source bottles are connected to an 'injection rod' via Teflon-lined, stainless-steel hoses. The hoses are kept above 50°C by heating tape, which was connected to a Variac.

The 'injection rod' is a custom, 3-ft-long, stainless-steel, double-walled tube which is kept at a constant temperature. A circulating bath (VWR Scientific 1157) flushes ethylene glycol through the outer chamber of the injection rod, maintaining it at a temperature of 48°C. This particular circulating bath will only cool fluids when they are below 50°C, so it determined the maximum temperature of the injection rod, and thus the maximum temperature of the source bottles. The injection rod must be maintained at a temperature equal to or higher than the temperature inside the source bottles or the source vapours will condense inside the injection rod.

The injection rod is attached to the deposition tube end cap by means of Ultra-Torr fittings which allow injection into various positions of the deposition tube. The Ultra-Torr fitting may be loosened to allow the injection rod to slide, into or out of the tube, to another position and then be tightened to provide a seal.

Argon, used as a carrier gas, is supplied to each source bottle after passing through a Sierra Model 860 Side-Trak™ automatic flow controller. The details of how these controllers operate is described in Section 3.3.1. The flow controllers are individually controlled by a Sierra 920C Flow Controller. The Model 860 Side-Trak™ mass flow controllers have a rated error 1% of full scale, which is 200 SCCM (cm^3/min under standard conditions).

To flush the system, argon is supplied to the deposition tube end cap after passing through a manual Matheson flow controller. The details of how these types of manual flow controllers work is described in Section 3.3.1.

Each source bottle was equipped with 3 valves which acted as a bypass system for the carrier gas. When set to bypass, the carrier gas passes over the input and output valves of the source bottle, which remains sealed. This allows for complete flushing of all hoses, and the establishment of steady carrier gas flow rates prior to opening the source bottles and deposition.

The flow rates of the source gases are calculated from the vapour pressure of the source (determined from the temperature of the source bottle) and the flow rate of argon through the bottle, assuming argon saturation. The assumption that the source had sufficient time to saturate the carrier gas is reasonable if sufficiently low flow rates are maintained. The total flow rate was kept below 60 cm^3/min. The carrier gas flow rates ranged from 5 to 25 cm^3/min.

Gases leave the system via an oil bubbler followed by a water bubbler attached to a fume hood line. The oil bubbler prevents air or water vapour from the water bubbler from entering the reaction tube. The water bubbler reacts with any residual organochlorosilane gas.

3.4.2 Synthesis of Materials with CVD Apparatus II

3.4.2.1 Chemical Sources

As with CVD Apparatus I, reagent grade benzene (Caledon Labs, Ltd. ACS spectrograde) was used as the carbon source. Research grade $(CH_3)_2Cl_2Si$ (DOW-Corning Chemical) and $(CH_3)_3ClSi$ (DOW-Corning Chemical) were used as silicon sources. All liquids were used as received. Ultrahigh-purity argon (Linde, 99.999%) was used as a carrier gas. We tried $(CH_3)_3ClSi$ as a silicon source in these experiments because it was related to $(CH_3)_2Cl_2Si$, which produced better materials than $SiCl_4$ in CVD Apparatus I. The reason for using the other sources was discussed in Section 3.3.2.1.

3.4.2.2 Temperature

For the reasons stated in Section 3.3.2.2 and based on results from experiments performed with CVD Apparatus I, a temperature of 950°C was used to prepare all the CVD-II samples described in this thesis.

3.4.2.3 Substrate

As discussed in Section 3.3.2.3, quartz was used as a substrate.

3.4.2.4 General Deposition Method

The leak checking procedure for CVD Apparatus I (Section 3.3.2.4) was also used to check for leaks in CVD Apparatus II.

The tubular insert, with optional substrates, is placed in the centre of the reaction tube, which is placed, centered, in the tube furnace. As discussed in Section 3.3.2.4, a very small gas flow is allowed into the tube to check for leaks.

Once the system has been leak checked, temperature stabilization and gas flushing commences. The Omega temperature controllers are set to the desired temperature and begin heating the source bottles. The Variac is turned on to heat the source vapour hoses (which connect the source bottles to the injection rod) to approximately 100°C. The circulating bath is turned on and set to maintain the injection rod temperature at 48°C. The flow controllers are set to flush all the lines and reaction tube. The tube furnace is then raised to the desired deposition temperature.

Once the tube furnace has reached the desired deposition temperature and the reaction tube has been flushed with enough carrier gas to fill the tube at least 10 times, the source vapour flow controllers are set to the flow rates desired for that deposition. The manual flow controller (flush) is reduced to approximately 10 cm^3/min. When the temperature of the source bottles has stabilized then deposition can begin. The bypass valves on the source bottles are switched to bubble carrier gas through the source. The pressure in the source bottles will have increased slightly, due to the increase in temperature. To avoid backwash of the source into the flow controllers the output valve for each source bottle is slowly opened before the input valve.

When the desired time for deposition has elapsed (usually 1 hour) the source bottle valves are switched to bypass. The flow rate through the manual flow controller (flush) is increased. After at least 10 minutes, the furnace is set to return to 100°C. Before opening the reaction tube, the system may be flushed for several hours to remove some of the vapours which are released by the tar-like partially decomposed species which collect in the lower temperature end sections of the tube. The amount of flushing was determined by the competing factors of 'tar' quantity and the urgency of the experiment.

The materials made by CVD are discussed in Chapter 7. The next chapter details the synthesis and pyrolysis of the silicon-containing polymers and pitch-polysilane blends.

CHAPTER 4

EXPERIMENTAL II: SILICON OXYCARBIDE GLASS SYNTHESIS

In an effort to find a less expensive route to silicon-containing carbonaceous materials than the CVD technique, we turned to the pyrolysis of silicon-containing polymers. Our early work on these materials (Wilson, 1994a) led us to conclude that silicon oxycarbide glasses warranted further investigation. Xue *et al.* investigated the effect of changing the silicon and oxygen content by using an epoxy-silane technique (Xue, 1995a). This method had a limited control of the stoichiometry and so we started a collaboration with Dr. Gregg Zank, who synthesized polymers for a more extensive study (Dahn, 1996a through 1996d; Xing, 1996a; Wilson, 1996a and b). During the course of this collaboration, we also investigated mixtures of silicon-containing polymers and petroleum pitches as pyrolytic precursors (Xing, 1996b), which (as will be discussed in Chapter 9) provided an alternate route to the nanodispersions previously made by CVD. This is explained in context and more detail in Chapter 1.

This chapter summarizes the synthesis of the materials we made by pyrolysis. The materials synthesis for the early work (Wilson, 1994a) is explained in Section 4.3. Section 4.4 describes the synthesis procedure for the samples used in the main silicon oxycarbide study (Dahn, 1996a; Xing, 1996a). Section 4.5 explains the synthesis of the polysilane-pitch blends (Dahn, 1996b and c; Xing, 1996b). Section 4.6 details the pyrolysis method. But first, the next section presents some definitions to act as an introduction to polymers and facilitate the discussion which follows. Section 4.2 presents a selection from the vast amount of previous work done by others on the pyrolysis of silicon-containing polymers.

No previous work done tested the electrochemical behaviour of these materials with lithium.

4.1 AN INTRODUCTION TO POLYMER NOMENCLATURE

We have used silicon-containing polymers as precursors to silicon oxycarbide glasses. The following is adapted from information in 'Contemporary Polymer Chemistry' by Allcock and Lampe (Allcock, 1990).

Monomers are substances which can be converted to a polymeric chain, and typically represent one polymer repeating unit. Monomer polymerization often occurs sequentially, first forming a *dimer* from two monomers. Then another monomer is added to form a *trimer*, then a *tetramer* and *pentamer* and so on. All low-molecular-weight polymeric chains are known as *oligomers*. Thus, polymers are high-molecular-weight substances which have many repeating units. Figure 4-1 shows schematic representations of three silicon-containing polymers.

A *linear polymer* consists of a long chain of skeletal atoms, or *backbone*, which has

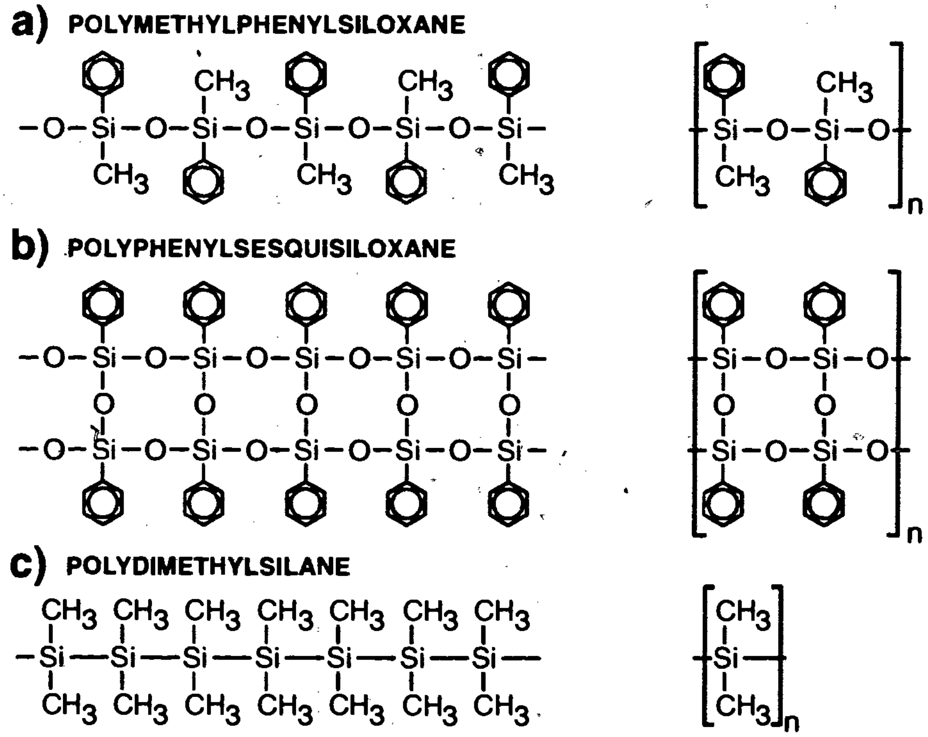

Figure 4-1. Schematic representations of a) polymethylphenylsiloxane (linear polymer), b) polyphenylsesquisiloxane (ladder polymer) and c) polydimethylsilane (linear polymer).

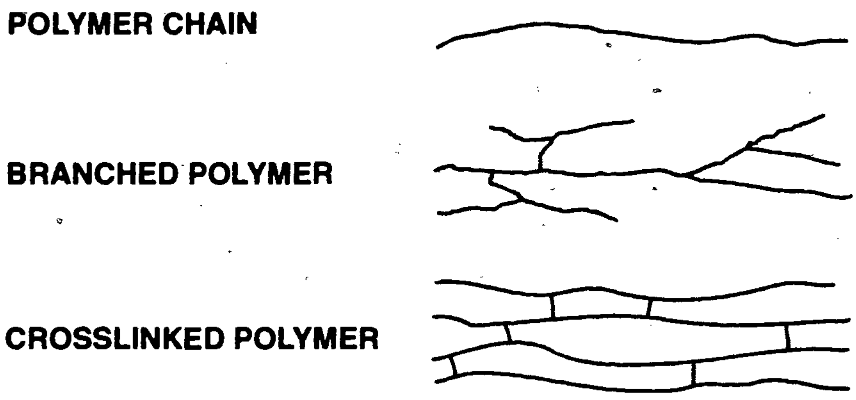

***Figure 4-2.** A schematic illustrating the difference between branched and crosslinked polymers.*

attached substituent groups. Figures 4-1a and 4-1c respectively show linear polymers with *siloxane* (silicon-oxygen bonding) and *silane* (silicon-silicon bonding) backbones. *Branched polymers* are linear polymers where some of the substituent groups have been replaced by a polymer chain the same as the main. *Crosslinked polymers* (also called *network polymers*) have chemical linkages between the chains. Figure 4-2 illustrates the difference between branched and crosslinked polymers. The degree of crosslinking in such a polymer determines the flexibility, melting point, and other physical attributes of the polymer. The more crosslinking a polymer has, the more rigid it is. *Ladder polymers* consist of linear polymers which have regular crosslinking between the backbones. Figure 4-1b shows a ladder polymer with a siloxane backbone (because of the stoichiometry it is more specifically a *sesquisiloxane* backbone).

Copolymers are made from two or more different monomers. The three types of sequencing arrangements commonly found are *random copolymers*, where there is no definite sequence of monomer units, *regular copolymers*, which contain a regular alternating sequence of two monomer units, and *block polymers*, which contain blocks of

RANDOM COPOLYMER	...-A-B-B-A-A-A-B-A-B-B-A-A-B-A-A-B-B-B-B-...
REGULAR COPOLYMER	...-A-B-A-B-A-B-A-B-A-B-A-B-A-B-A-B-A-B-A-...
BLOCK COPOLYMER	...-A-A-A-A-A-A-A-A-A-A-A-B-B-B-B-B-B-B-B-...

***Figure 4-3.** Schematic representations of random, regular, and block copolymers. A and B represent two different monomers.*

one polymer attached to a block of another. Figure 4-3 shows schematic representations of copolymers with only two different monomers, represented by A and B. *Terpolymers* contain three different monomer units and can be sequenced randomly or in blocks.

Most of the siloxane and silane polymers used in this thesis were highly crosslinked random polymers.

4.2 PREVIOUS WORK

Silane and siloxane polymers are commonly used in the production of silicon carbide (Abu-eid, 1992; Allcock, 1990; Burns, 1992; Hurwitz, 1991) and silicon oxycarbide glasses (Babonneau, 1994; Hurwitz, 1987 and 1989; Renuld, 1991). Polyorganosiloxanes, such as polymethylphenylsiloxane and polyphenylsesquisiloxane (pictured in Figures 4-1a and 4-1b), can be reduced to silicon oxycarbide glasses or silicon carbides upon pyrolysis in inert gas (Wilson, 1994a). Polysilanes, such as polydimethylsilane (pictured in Figure 4-1c), contain no silicon-oxygen bonds and are commonly used as precursors to silicon carbide (Allcock, 1990: 206). Thus, depending on the material desired, one chooses appropriate polymer composition and pyrolysis parameters. Typically, silicon carbide will be produced from most polysiloxanes by pyrolysis to sufficiently high temperatures (Burns, 1992; Abu-eid, 1992; Wilson, 1994a).

Certain polysiloxanes and polysilanes have been used as precursors to ceramics because of their minimal loss in mass upon conversion by pyrolysis to a ceramic (Burns, 1992; Hurwitz, 1989 and 1987). This low mass loss, or high *ceramic yield*, usually means minimal volume contraction. These materials are then useful as binders, which should experience the least volume change upon pyrolysis, in the making of shaped ceramics (Burns, 1992; Hurwitz, 1989). Use of appropriate sesquisiloxanes allowed Hurwitz *et al.* to make complex-shaped and flaw-tolerant ceramic composite parts through low temperature processing (Hurwitz, 1987). Other factors that make these precursors desirable include resistance to crystallization and oxidation at temperatures above 1000°C (Renuld, 1991).

Until our preliminary study (Wilson, 1994a), there were no reports of others testing the electrochemical behaviour of these materials with lithium. This work was followed up by Xue *et al.* who used an epoxy-silane technique to control the silicon and oxygen concentration with respect to the carbon content (Xue, 1995a).

4.3 PRELIMINARY WORK

For our initial investigation into pyrolysed silicon-containing polymers, we chose two readily available polysiloxanes. Polymethylphenylsiloxane (PMPS) (Dow 710 fluid) was obtained from Aldrich and used as received. Polyphenylsesquisiloxane (PPSS) was obtained from United Chemical Technologies Inc. (Bristol, Pa., USA) and used as received. Their structures are shown in Figure 4-1.

The polymers were pyrolysed in a tube furnace inside a quartz tube under flowing UHP grade argon (Linde, 99.999). Polymer samples were weighed and placed in alumina boats. The boats were put in the quartz tube which was sealed from the room atmosphere and well flushed with argon. The samples were heated at a constant ramp rate (which varied, depending on the sample) to the maximum pyrolysis temperature and held at this temperature for one hour. Gases leave the system via an oil bubbler attached to a fume hood line. Samples were typically cooled to 100°C by turning off the furnace heaters. This resulted in an average cooling rate of about 4°C/min. Samples were prepared at maximum pyrolysis temperatures ranging from 600 to 1100°C.

Samples of PMPS pyrolysed at 1100°C were further pyrolysed at 1300 and 1500°C, using a Centorr series 10 graphite element tube furnace. The 1 g samples were heated under UHP argon and were weighed prior to and after heating. To show that there were no air leaks into the furnace a sample of graphite powder was heated to 1500°C under identical conditions. It showed no weight loss proving that there were no air leaks.

The results and discussion of the study of these polymers is presented in Chapter 8, and has been published elsewhere (Wilson, 1994a). These materials showed great promise for use in lithium-ion cells, as did the materials made by Xue *et al.* (Xue, 1995a), so a more extensive study was done in collaboration with Dr. Gregg Zank. The next section outlines the synthesis of the polymers used in that extensive study.

4.4 POLYMER SYNTHESIS

Because the synthesis of polysiloxanes and polysilanes was beyond the abilities of anyone in our group, all polymer synthesis was performed by Gregg Zank of Dow-Corning. Through this close collaboration we were able to choose stoichiometries of interest, based on previous experiments, and Dr. Zank could then synthesize the appropriate polymer precursors. This section details the synthesis of the polymers and, although this work was not done by the author, it is included here for completeness.

The next sections each detail the various synthesis routes for the polysiloxanes studied. The work on these materials has been published elsewhere (Wilson, 1996a to c; Xing 1996a).

Our goal was to synthesize a wide array of siloxane polymers from the following generic structure (Burns, 1992):

$$(R^1R^2R^3SiO_{0.5})_w\,(R^4R^5SiO)_x\,(R^6SiO_{1.5})_y\,(SiO_{4/2})_z \qquad [4\text{-}1],$$

where R^1, R^2, R^3, R^4, R^5, and R^6 are groups consisting of hydrogen or hydrocarbons and w, x, y, and z are molar ratios with $w + x + y + z = 1$. The hydrocarbons can include alkyls such as methyl (Me), ethyl, propyl, butyl, etc., alkenyls such as vinyl (Vi), allyl, etc., and aryls such as phenyl (Ph). The units in Equation 4-1, ($R^1R^2R^3SiO_{0.5}$), (R^4R^5SiO), ($R^6SiO_{1.5}$), and ($SiO_{4/2}$), are often referred to as M, D, T, and Q units, respectively (Burns, 1992). The *M*, *D*, *T*, and *Q* units respectively correspond to silicon bonding to one, two, three, and four oxygens (alternately, silicon:oxygen ratios of 2, 1, 2/3 and 1/2). By selecting the appropriate polymer structure, one can begin to control the ceramic composition. In general, for branched silicon-based polymers, the backbone elements remain in the ceramic. Therefore, a change in precursor (M, D, T, or Q) will change the Si to O atomic ratio in the ceramic. There are many ways to synthesize these types of materials.

The following sections detail the typical procedures which were used to prepare the specified siloxane polymers. The final samples made with these polymers are assigned sample numbers in Chapter 8 which are mentioned below as a reference. Although this section is not required for an understanding of the final ceramics made, it is included here for completeness. Table 4-1, at the end of this section, details all the precursors made.

4.4.1 MT Materials Cured by Peroxides

The precursors to samples 13 through 18 and 34 through 41 were prepared using this technique (Dahn, 1996a). The following is a specific description for the preparation of the polymer pyrolysed to make sample 37. Phenyltrimethoxysilane (77.0g, 0.39mol), methyltrimethoxysilane (742g, 5.46mol), 1,1,3,3-tetramethyl-1,3-divinyldisiloxane (192g, 1.03mol), trifluoromethanesulfonic acid (5.0ml, 0.02mol) and deionized water (50g, 2.8mol) were heated to reflux for two hours. Toluene (1.5 l) and deionized water (410ml) were added and the mixture was heated to reflux for an additional two hours. Calcium carbonate (10g, 0.1mol) was added and the solvent was distilled until the vapour head temperature increased to 85°C. Aqueous 3 wt% potassium hydroxide (50ml, 0.27mol) was added and the water azeotropically removed using a Dean-Stark apparatus. After the reaction mixture was dry of water, reflux was continued for 8 hours, then the mixture was cooled to 50°C, and chlorodimethylvinylsilane (50ml, 0.37mol) was added. After stirring at room temperature for three days, the mixture was filtered through a Buchner funnel containing Celatom filter-aid, and the solvent removed using a rotary evaporator, giving a quantitative yield (617.6g) of a clear, colourless viscous fluid. For crosslinking, the siloxane polymers were mixed with 1wt% Lupersol 101 and heated to 150-175°C for 20-45 minutes.

4.4.2 MT Materials Cured by Platinum

Precursors to samples 21 through 25 were prepared using this technique (Dahn, 1996a). The following is the specific procedure used to prepare the polymer precursor to sample 23. Phenyltrimethoxysilane (198.0g, 1.0mol), 1,1,3,3-tetramethyl-1,3-

dihydridodisiloxane (67g, 1.0 mol), trifluoromethanesulfonic acid (2.0ml, 0.01mol) and deionized water (1.0g) were heated to reflux for two hours. The reaction was cooled, 110g of additional water was added, and the reaction was again heated to reflux for two hours. Calcium carbonate (2g, 0.02mol) was added and solvent was distilled until the vapour temperature increased to 85°C. Toluene (290g), deionized water (29ml) and trifluoroacetic acid (0.9g) were added and the mixture was heated to reflux and the water was azeotropically removed. After the reaction mixture was dry of water, reflux was continued for 2 hours, the mixture was cooled to 50°C, and chlorodimethylsilane (5g) was added. After stirring at room temperature for 16 hours, the mixture was filtered and the solvent was removed the same way described in Section 4.4.1. The polymer was then mixed with 20g of a corresponding Si-H crosslinker resin, along with 0.1g of Pt as a solution known as Karstadt's catalyst (Chandra, 1987), and heated to 150-175°C for 20-45 minutes.

4.4.3 MQ Materials Cured by Platinum

The precursors to samples 30 through 33 were made by this technique (Dahn, 1996a). What follows is a general procedure for the synthesis of organofunctional silanes.

For MQ materials with hydrogen, 1,1,3,3-tetramethyl-1,3-dihydridodisiloxane (0.74 mol equivalent), water (1.1 mol) and isopropyl alcohol (1.4 mol) were charged into a flask under cooling with an ice bath. Following the addition of concentrated HCl (0.053 mol) to the mixture, it was agitated for 30 minutes. Tetraethylorthosilicate (0.18 mol) was added dropwise into the mixture and the mixture was stirred at ambient temperature for 3 hours. The resulting reaction mixture was neutralized with 50 w/v NH_4Cl aqueous solution. The resulting organic layer was dried with Na_2SO_4 for 2 hours. The dried organic solution was filtered followed by evaporating at 50°C and further solvent stripping at 0.03 Torr and room temperature. The resultant organic solution was distilled in vacuo to obtain a major fraction at 39 to 40°C at 0.16 Torr. The yield was 40%.

For MQ materials with vinyl, 1,1,3,3-tetramethyl-1,3-dihydridodisiloxane (0.53 mol equivalent), water (0.88 mol) and isopropyl alcohol (1.0 mol) were charged into a flask while heating at 40 to 50°C. Concentrated HCl (0.051 mol) was added to the mixture followed by agitating for 30 minutes. Tetraethylorthosilicate (0.13 mol) was added dropwise into the mixture and the mixture was stirred at ambient temperature for 3 hours. The resulting reaction mixture was neutralized with 50 w/v NH_4Cl aqueous solution. The resulting organic layer was dried with Na_2SO_4 for 2 hours. The dried organic solution was filtered followed by evaporating at 50°C and further solvent stripping at 0.03 Torr and room temperature. The resultant organic solution was distilled in vacuo to obtain a major fraction at 65 to 66°C at 0.06 Torr. The yield was 50%.

The precursors to samples 30 through 33 were prepared by curing different ratios of hydrogen- and vinyl-containing MQ materials. For example, sample 31 was prepared by dissolving 35g of hydrogen-containing MQ and 36.8g of vinyl-containing MQ with 50ml of toluene. 100 ppm of a platinum solution (8.6 wt.% Pt in 1,3-divinyl-1,1,3,3-tetramethyldisiloxane) and 1000 ppm $MeSi(OC(Me_2)C{\equiv}CH)_3$ were added into the MQ resin solution. The resulting solution was left at 30°C in an oven to evaporate the toluene. The material was then cured by heating at 60°C for 2 hours followed by heating the material to 120°C at 10°C/hr with a 2 hour hold at 120°C followed by cooling to 30°C at -10°C/hour.

4.4.4 Sol-Gel Synthesis

This technique was used to make the precursors to samples 1 through 8 (Dahn, 1996a). Colloidal silica (Nalco 1034A at 34% solids) and the corresponding methoxysilane were cohydrolyzed under acidic conditions with rapid stirring. The pH of the reaction mixture was then adjusted to gel and the volatile evaporated over a 5 day period. The gels were then further dried for 16 hours in a 100°C oven and an additional 16 hours in a 250°C oven. Organic modified sol-gels can be prepared in a similar way (Dahn, 1996a).

4.4.5 Organic Modified Sol-Gels

Precursors to samples 26 through 29 were synthesized by this technique (Dahn, 1996a). By a procedure similar to one outlined elsewhere (Schneider, 1995), a variety of methoxysilane materials were cohydrolyzed with a phenolic resin with stirring for 72 hours while allowing for evaporation of the solvents. After this time the gel was dried 24 hours at 80°C and an additional 24 hours at 175°C. The reactants used in each of these materials are listed in Table 4-1, at the end of this section.

4.4.6 Silane Modified Sugars

This technique was used to make the precursors to samples 9 through 12 (Dahn, 1996b). Chlorosilanes were mixed with aqueous solutions of sugar (100g sucrose in 100g water) and stirred for 24 hours. The reaction mixtures were then heated to 300°C over a 24 hour period to form a gel and begin the decomposition of the mixture. For example, to make the precursor to sample 10, 22.4g of $MeSiCl_3$ was used.

4.4.7 Silane Modified Phenolic Resins

Precursors to samples 42 and 43 were made respectively using Georgia Pacific and Varcum 29-353 phenolic resins (Dahn, 1996b). 25g of phenolic resin was placed in a 500 ml flask and dissolved in 125 ml of tetrahydrofuran. To this was added 25g of polysilane $(Me_2Si)_{0.53}(PhMeSi)_{0.47}$ (PSS-400, Shin Nisso Kako Co. Ltd.) as a solution in 125 ml of tetrahydrofuran (THF). This mixture was then sonicated with a 400W sonicator for 15 minutes. The polymeric product was isolated by filtration and the solvent was removed by rotary evaporation. This product was not treated or heated prior to pyrolysis.

4.4.8 Polycarbosilane Modification

A polycarbosilane (PCS) was obtained from Nippon Carbon Company (NCC) which was prepared by the thermal rearrangement of polydimethylsilane. This was used as the precursor to sample 19. The precursor to sample 20 was prepared by dissolving the NCC PCS (220g) in tetrachloroethylene (2kg) in a three litre three necked flask fitted with a magnetic stirring bar, a water cooled condenser and an ebbulator tube. This mixture was then heated to 100 to 105°C and oxygen was added subsurface over a period of 12 hours. The product, $(HSi(CH_2)_{1.5})_{0.7}(HOSi(CH_2)_{1.5})_{0.3}$ was isolated by filtration and removal of the solvent by rotary evaporation. This material is soluble in most common organic solvents but crosslinks prior to melting (Dahn, 1996c).

Table 4-1. Polymer Precursors listed by the ceramic sample numbers.

Sample	Polymer Precursor Stoichiometry	Synthesis in Section
1	$(SiO_2)_{1.0}$	4.4.4
2	$(MeSiO_{1.5})_{0.1}$ $(SiO_2)_{0.9}$	4.4.4
3	$(MeSiO_{1.5})_{0.3}$ $(SiO_2)_{0.7}$	4.4.4
4	$(MeSiO_{1.5})_{0.5}$ $(SiO_2)_{0.5}$	4.4.4
5	$(MeSiO_{1.5})_{0.7}$ $(SiO_2)_{0.3}$	4.4.4
6	$(MeSiO_{1.5})_{0.9}$ $(SiO_2)_{0.1}$	4.4.4
7	$(PhSiO_{1.5})_{0.3}$ $(SiO_2)_{0.7}$	4.4.4
8	$(PhSiO_{1.5})_{0.7}$ $(SiO_2)_{0.3}$	4.4.4
9	sucrose + $SiCl_4$	4.4.6
10	sucrose + $MeSiCl_3$	4.4.6
11	sucrose + Me_2SiCl_2	4.4.6
12	sucrose + Me_3SiCl	4.4.6
13	$(PhSiO_{1.5})_{0.75}$ $(Ph_2ViSiO_{0.5})_{0.25}$	4.4.1
14	$(PhSiO_{1.5})_{0.75}$ $(Me_2ViSiO_{0.5})_{0.25}$	4.4.1
15	$(PhSiO_{1.5})_{0.5}$ $(Me_2ViSiO_{0.5})_{0.5}$	4.4.1
16	$(PhSiO_{1.5})_{0.5}$ $(Ph_2ViSiO_{0.5})_{0.5}$	4.4.1
17	$(MeSiO_{1.5})_{0.5}$ $(Me_2ViSiO_{0.5})_{0.5}$	4.4.1
18	$(MeSiO_{1.5})_{0.75}$ $(Me_2ViSiO_{0.5})_{0.25}$	4.4.1
19	$(HSi(CH_2)_{1.5})_{1.0}$ = PCS	4.4.8
20	$(HSi(CH_2)_{1.5})_{0.7}$ $(HOSi(CH_2)_{1.5})_{0.3}$	4.4.8
21	$(PhSiO_{1.5})_{0.75}$ $(Ph_2ViSiO_{0.5})_{0.25}$: $(PhSiO_{1.5})_{0.75}$ $(Ph_2HSiO_{0.5})_{0.25}$	4.4.2
22	$(PhSiO_{1.5})_{0.5}$ $(Ph_2ViSiO_{0.5})_{0.5}$: $(PhSiO_{1.5})_{0.5}$ $(Ph_2HSiO_{0.5})_{0.5}$	4.4.2
23	$(PhSiO_{1.5})_{0.75}$ $(Me_2ViSiO_{0.5})_{0.5}$: $(PhSiO_{1.5})_{0.5}$ $(Me_2HSiO_{0.5})_{0.5}$	4.4.2
24	$(MeSiO_{1.5})_{0.5}$ $(Me_2ViSiO_{0.5})_{0.5}$: $(MeSiO_{1.5})_{0.5}$ $(Me_2HSiO_{0.5})_{0.5}$	4.4.2
25	$(PhSiO_{1.5})_{0.75}$ $(Me_2ViSiO_{0.5})_{0.25}$: $(PhSiO_{1.5})_{0.75}$ $(Me_2HSiO_{0.5})_{0.25}$	4.4.2
26	Varcum phenolic resin with $Si(OEt)_4$	4.4.5
27	Varcum phenolic resin with $PhSi(OMe)_3$	4.4.5
28	Georgia Pacific phenolic resin with $Si(OEt)_4$	4.4.5
29	Georgia Pacific phenolic resin with $PhSi(OMe)_3$	4.4.5
30	$(HMe_2SiO_{0.5})_{0.8}$ $(SiO_{4/2})_{0.2}$: $(ViMe_2SiO_{0.5})_{0.8}$ $(SiO_{4/2})_{0.2}$	4.4.3
31	$(HMe_2SiO_{0.5})_{0.33}$ $(SiO_{4/2})_{0.67}$: $(ViMe_2SiO_{0.5})_{0.33}$ $(SiO_{4/2})_{0.67}$	4.4.3
32	$(HPh_2SiO_{0.5})_{0.33}$ $(SiO_{4/2})_{0.67}$: $(ViPh_2SiO_{0.5})_{0.33}$ $(SiO_{4/2})_{0.67}$	4.4.3
33	$(HPh_2SiO_{0.5})_{0.8}$ $(SiO_{4/2})_{0.2}$: $(ViPh_2SiO_{0.5})_{0.8}$ $(SiO_{4/2})_{0.2}$	4.4.3
34	$(PhSiO_{1.5})_{0.22}$ $(MeSiO_{1.5})_{0.55}$ $(Me_2ViSiO_{0.5})_{0.23}$	4.4.1
35	$(ViSiO_{1.5})_{0.77}$ $(Me_2ViSiO_{0.5})_{0.23}$	4.4.1
36	$(ViSiO_{1.5})_{0.66}$ $(MeSiO_{1.5})_{0.09}$ $(Me_2ViSiO_{0.5})_{0.25}$	4.4.1
37	$(PhSiO_{1.5})_{0.09}$ $(MeSiO_{1.5})_{0.66}$ $(Me_2ViSiO_{0.5})_{0.25}$	4.4.1
38	$(PhSiO_{1.5})_{0.38}$ $(MeSiO_{1.5})_{0.39}$ $(Me_2ViSiO_{0.5})_{0.23}$	4.4.1
39	$(PhSiO_{1.5})_{0.5}$ $(MeSiO_{1.5})_{0.23}$ $(Me_2ViSiO_{0.5})_{0.27}$	4.4.1
40	$(PhSiO_{1.5})_{0.66}$ $(MeSiO_{1.5})_{0.08}$ $(Me_2ViSiO_{0.5})_{0.26}$	4.4.1
41	$(PhSiO_{1.5})_{0.13}$ $(ViSiO_{1.5})_{0.64}$ $(Me_2ViSiO_{0.5})_{0.2}$	4.4.1
42	Georgia Pacific phenolic resin : $(Me_2Si)_{0.53}$ $(PhMeSi)_{0.47}$ (1:1)	4.4.7
43	Varcum phenolic resin with $(Me_2Si)_{0.53}$ $(PhMeSi)_{0.47}$ (1:1)	4.4.7

4.5 PITCH-POLYSILANE BLEND SYNTHESIS

Dr. Zank prepared two series of pitch-polysilane blends (I and II) by mixing pitch (Ashland Chemical A-240) with $(Me_2Si)_x(PhMeSi)_y$ (Shin Nisso Kako Co. Ltd.) at various pitch to polymer ratios (Dahn, 1996b). Here, $x = 0.80$ and $y = 0.20$ (PSS-120) for series I and $x = 0.53$ and $y = 0.47$ (PSS-400) for series II. The silane copolymers were prepared from the sodium coupling of a mixture of phenylmethyldichlorosilane and dimethylsilane. The pitch and polysilane (50 g total) were dissolved and mixed in 250 g THF containing 1% by weight Lupersol 101 (0.5 g) at room temperature. After this procedure it is believed that the silane polymer chains are in an intimate mixture with the pitch. The solid blends were then isolated by removal of the solvent by rotary evaporation, and then crosslinked by heating under argon to 200°C for 30 minutes.

The blends were pyrolysed in the same method as the polysiloxanes, as detailed in the next section. The results from this study are presented in Chapter 9 and have been partially published elsewhere (Xing, 1996b).

4.6 PYROLYSIS METHOD

These samples were pyrolysed in the same apparatus as was used in the preliminary work. The samples were placed in alumina boats and weighed and then placed inside tubular inserts (the same inserts as were used in the CVD experiments) and placed inside the furnace. Typically, four samples in separate alumina boats were pyrolysed at a time. The tube was placed in the furnace at 100°C, sealed from the atmosphere and flushed with a volume of argon (Linde, 99.999%) sufficient to fill the reaction tube 20 times. The temperature was then raised at a constant rate (between 1 and 45°C/min) to the maximum pyrolysis temperature (between 600 and 1100°C). The material was reclaimed and reduced to a powder by grinding in an automatic mortar and pestle for 20 minutes.

The first series of experiments helped to determine which heating rate to use. Various polymers were heated at rates of 45, 5, and 1°C/min. Comparative results are not presented because there was little difference between materials made at the different heating rates. However, some materials made at 45°C/min had electrochemical characteristics which were not ‘as good’ as materials made at lower ramp rates. Thus, we chose 5°C/min as a ramp rate for all the subsequent materials made in this study. Based on the previous work discussed in Section 4.2 (Wilson, 1994a; Section 8.1), we chose the maximum pyrolysis temperature of 1000°C for most of the materials. Later work investigated the effect of the maximum pyrolysis temperature on some of the ‘more promising’ precursors. Precursors were heated at 5°C/min to 600, 800, and 1100°C.

4.7 HYDROFLUORIC ACID WASHING

In an attempt to remove oxygen from one of the products of polysiloxane pyrolysis (a silicon oxycarbide glass), it was washed in a dilute solution of hydrofluoric (HF) acid. The following details how the pyrolysed polymer (sample 36) was treated to make nine samples (HF1 though HF9). The HF washing was performed by Dr. Zank, who then sent the powders to us for evaluation.

Sample HF1 was prepared by rinsing a portion of the ground silicon oxycarbide sample in distilled water. Samples HF2 through HF9 were prepared by washing portions of the ground Si-O-C sample in a dilute HF solution. HF washing was performed by immersion of the powders in a solution of HF (0.20 weight percent in H_2O) in stoichiometric excess to the oxygen present in the initial Si-O-C. After a specific period of time, varying from 15 minutes to 24 hours, the sample was recovered by filtering, and rinsed with distilled water to remove any residual HF. The results are presented in Section 8.3.2 and have been published elsewhere (Wilson, 1996c).

The results and discussion of the studies of the polysiloxanes and polysilane-pitch blends is presented in Chapters 8 and 9, respectively. The next chapter describes the experimental techniques used to characterize the materials discussed in this thesis, except the electrochemical testing, which is discussed in Chapter 6.

CHAPTER 5

EXPERIMENTAL III: CHARACTERIZATION METHODS

A number of methods were used to characterize the physical properties of the materials made. This chapter summarizes all but the electrochemical techniques, which are detailed in the next chapter.

Two very different types of materials were made (CVD and Si-O-C materials) and some of the characterization techniques were particular to the type of material. Where appropriate, this is pointed out.

5.1 X-RAY POWDER DIFFRACTION

X-ray powder diffraction was the primary method used to probe the structure of the samples. It was used quantitatively in the study of some of the CVD-I materials (see Chapter 7). The Scherrer equation was used to estimate the average size, L_a and L_c, of the ordered regions (Section 5.1.2). The differences in XRD sample holders presented some complication for subsequent data comparison. Thus, the Structure Refinement Program for Disordered Carbons, developed by Shi *et al.* (Shi, 1993a and 1993b) was used to measure d_{002} (the average distance between adjacent graphene sheets) and L_a for a few of the CVD-I materials by performing a complete refinement to the measured X-ray pattern (Section 5.1.3). In Chapters 8 and 9 it will be shown how XRD was used qualitatively in the pyrolysed polymers study. The next section outlines the experimental methods used to obtain the XRD profiles.

5.1.1 Experimental Method

Two different diffractometers were used to obtain X-ray powder diffraction (XRD) patterns (*profiles*). One was the Siemens D5000 diffractometer which employed a copper target X-ray tube and a diffracted beam monochromator. It was used in the Bragg-Brentano and flat plate sample geometry. In this configuration both the tube and detector are stepped in opposite directions, through an angle theta, while the sample remains fixed, as shown in Figure 5-1a. The slits were typically set to 0.5° divergence, 0.5° anti-scattering, and 0.6 mm receiving, providing an resolution of ~0.17°. The powders were either held in a steel well holder or, when less than 100 mg of material was available, placed on a zero background holder (ZBH). The steel well holders consisted of a stainless steel plate with a 24 mm-wide × 16 mm-long × 2 mm-deep well. The well was filled with the powdered sample and the surface was then smoothed. The ZBH was constructed from a single crystal silicon wafer cut along the {510} plane, attached to an aluminum block for support. Because of the high quality of the silicon crystal the destructive interference is nearly complete and since the structure factor for the (510) diffraction peak is zero for the diamond structure there are no peaks from the silicon in the region of interest. Thus, the appropriately named ZBH produces very low background counts. The powders were attached by making an acetone slurry which was then spread on the silicon. The powders were self-adhering, once the acetone had evaporated, and were typically less than 100 μm thick.

A Philips diffractometer employing a copper target X-ray tube and operating in the Bragg-Brentano geometry was also used. In this diffractometer, the tube, not the sample,

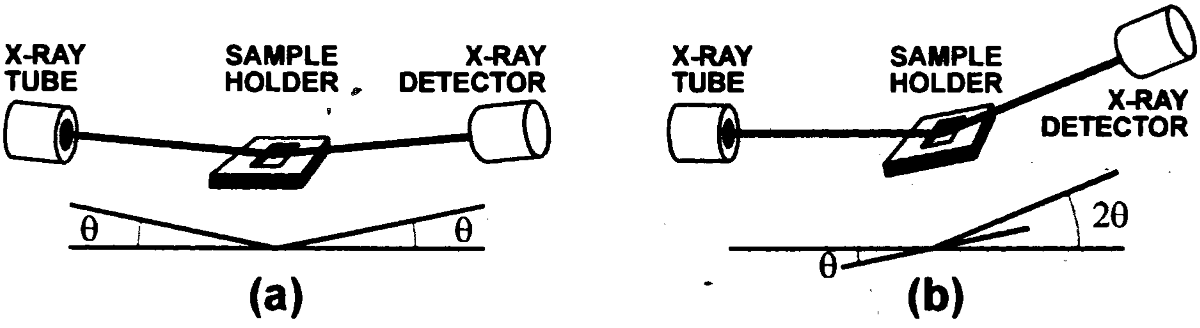

Figure 5-1. Schematics of the geometries of the (a) Siemens D5000 and (b) Philips diffractometers.

is fixed. As shown in Figure 5-1b, the sample and detector are each rotated in the same direction through angles of θ and 2θ, respectively. On this diffractometer, the slits were typically set to 0.5° divergence and 0.2 mm receiving, providing a resolution of ~0.15°. In the Philips diffractometer only well holders with dimensions 15 mm-square × 2 mm-deep were used.

5.1.2 Scherrer Equation

The XRD profile of a sample is critically dependent on imperfections within the crystal, such as finite particle size, strains and faults. The effect of particle size on the XRD pattern is the simplest and was first treated by Scherrer (Scherrer, 1918). The width of a diffraction peak is dependent on the size of the ordered region. An approximation to the Scherrer equation can be derived from Bragg's law to give:

$$L = \frac{\lambda}{B\cos\theta} \qquad [5\text{-}1],$$

where λ the X-ray wavelength, B is the full width at half of maximum of the peak in radians, and θ is the Bragg angle (Cullity, 1979). By a more exact derivation, Warren showed that the size of an organized region, L, could be described by:

$$L = \frac{K_S\lambda}{B\cos\theta} \qquad [5\text{-}2],$$

where K_S is the shape constant (Warren, 1941). Equation 5-2 is now known as the Scherrer equation. Warren showed that the constant K_S is 1.84 for two dimensional peaks (Warren, 1941) and 0.89 for three-dimensional peaks (Warren, 1990). In this thesis the value of K_S is set to 0.9. This was done for all the peaks even though the (100) and (110) peaks, in graphite, are two dimensional. The lateral extent of the crystal regions in our samples was small enough (there was sufficient disorder) that these peaks did not exhibit the asymmetric 'sawtooth' shape typical of two dimensional peaks.

The ordered regions in a disordered carbon have two discrete dimensions, L_c (the 'thickness' along the stacking direction) and L_a (the lateral extent of the graphene sheets). To estimate L_c the (002) or (004) reflections can be used. L_a can be estimated using the

(100) and (110) reflections. In this thesis, L_c and L_a were estimated using the (002) and (100) reflections, respectively.

5.1.3 Structure Refinement Program for Disordered Carbons

The Bragg law (Cullity, 1979) can be used to estimate atomic plane spacings within a crystal. However, our samples were powders of disordered carbons having relatively small crystallite sizes. By Equation 5-2, one can see that smaller crystallites result in wider peaks. In materials with significant amounts of disorder (like disordered carbons) an obvious sloping background can be observed in the XRD profile. This background can introduce asymmetry and shift the maximum of broad, weak Bragg peaks which are superimposed on it. Thus, significant discrepancies between the actual average spacing within our samples and the result from the Bragg law are expected.

Since carbons have a small X-ray scattering cross section, X-rays scattered from particles located well below the sample surface are not strongly attenuated. The contribution to the XRD profile from crystallites located 'off-axis' (below the sample surface) affects the peak position and shape. Because of this effect, thick samples exhibit asymmetric Bragg peaks (Shi, 1993b). The thickness of our samples were determined by the sample holder used (ZBH versus well holder). Thus, differences between the sample holders presented some complication of subsequent data comparison using Equation 5-2. To determine more accurate values for L_a and d_{002} in our samples, we employed the Structure Refinement Program for Disordered Carbons, developed by Shi *et al.* (Shi, 1993b).

There are two models available within the refinement program. The *double layer model* is best suited to the study of carbons prepared by the pyrolysis of soft carbon precursors at temperatures between 2000 and 3000°C. It uses two-layer packages, stacked in an *AB* registry. These packages are stacked in either *2H*, *3R*, or random configurations with various refineable probabilities for each. We used the *single layer model* which stacks single graphene layers either randomly or in one of the two possible registrations. For example, if one graphene sheet occupies the *A* position, then the choices for the next layer (and the corresponding probability of finding it) are:

1. a random shift with probability *P*,
2. occupying the *B* position with probability (1-*P*)/2, or
3. occupying the *C* position with probability (1-*P*)/2.

Clearly, this model cannot reproduce the *2H*-type stacking found in crystalline graphite. This is an appropriate model to study our materials, considering that they have essentially complete turbostratic disorder.

The single layer model of the structure refinement program also accounts for strain between adjacent stacked layers by introducing the term 'δ ' as a deviation in the spacing between layers. The spacing between layers is given as $d_{002} + \delta$ where the average value of δ is zero and the average of δ^2 is nonzero. The exact definition of this parameter is explained elsewhere (Shi, 1993b). The strain parameter delta is used with *g*, a number between one and zero which represents the fraction of low strain material. Thus, 1-*g* is the probability of finding disordered carbon (Figure 2-4). The crystallite size is described by the refineable parameters L_a and L_c, which do not represent the particle size (see Section 2.1.2, Figure 2-3).

As explained above, X-ray scattering in carbons is not strongly attenuated which can lead to an asymmetry in the Bragg peaks for thick samples. Because the sample holders we used held different sample thicknesses (the ZBH and well holders) the peaks exhibited differing amounts of asymmetry and breadth. The structure refinement program accounts for the attenuation of the X-rays in samples of differing thickness in a parameter which can be set before refinement (Shi, 1993b).

The refinement program also accounts for polarization effects and the preferred orientation of crystallites (Shi, 1993b).

The model parameters are optimized by performing a least squares fit between the measured diffraction pattern and a theoretical calculation based on the parameters mentioned above. The structure refinement program was used to determine L_a and d_{002} values for some of the CVD-I materials presented in Chapter 7.

5.2 X-RAY ABSORPTION SPECTROSCOPY

X-ray absorption spectroscopy (XAS) can be used to probe the electronic and local structure in a variety of materials. In this technique, a sample is exposed to a beam of X-rays and the absorption is measured as the X-ray wavelength is changed. The energy range corresponds to an electronic transition of a core electron to an unoccupied state above the Fermi level. Such an excitation (X-ray absorption) is shown schematically in Figure 5-2. The energy at which the onset of absorption is observed for a core level is the absorption *edge* (i.e. for electrons promoted from the *K*-level of silicon atoms this is the silicon *K*-edge). Near the edge, core electrons are not provided with sufficient energy to be excited out of the material (to the vacuum level). Rather, multiple processes involved in electrons dropping from higher energy levels to fill the vacant core level lead to the excitation of electrons from the sample.

XAS has two principal regions, defined by photon energy range, which can be used to determine different aspects about the sample. The range from the absorption edge to about 50 eV above is known as *X-ray Absorption Near Edge Spectroscopy* (XANES), also called *Near Edge X-ray Absorption Fine Structure* (NEXAFS). *Extended X-ray Absorption Fine Structure* (EXAFS) extends from the top of the XANES region to several hundred eV higher. EXAFS is used in the study of local interatomic distances in

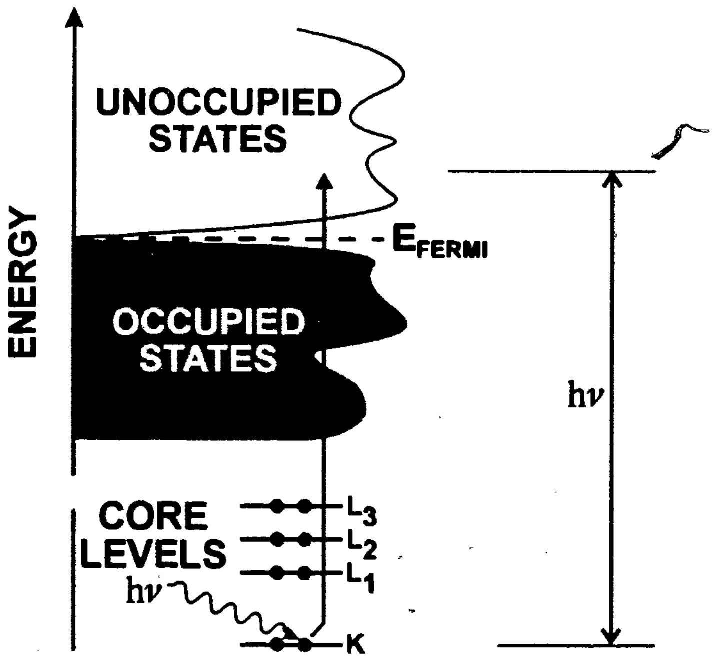

Figure 5-2. *Schematic representation of X-ray absorption near the K-edge.*

solids. Here, 'local' refers to the region surrounding atoms of the element edge being scanned. In this thesis, only the XANES region was studied.

To measure the XANES spectra, we collected electrons ejected by the sample at all energies, known as the *total electron yield* (TEY). The TEY consists mainly of electrons with energies below about 20 eV. This so-called *inelastic tail* (Stöhr, 1992) contains a significant fraction which are inelastically scattered electrons produced by an *Auger process*. These *Auger electrons* are emitted after absorbing energy from an electron of the same energy level when it drops to fill the core level vacancy, as shown schematically in Figure 5-3a. As the Auger electrons are inelastically scattered, they produce an avalanche of lower energy electrons (pictured in Figure 5-3b). While other processes contribute to the TEY, it is the Auger electrons which give the desired XANES signal (Stöhr, 1992). The electron mean free path in the solid is a function of the electron kinetic energy above the Fermi level and determines the maximum distance inside the material from which electrons can be ejected (the *electron escape depth*). This affects the penetration depth of the experiment (pictured in Figure 5-3b) and for the XANES spectra presented in this thesis it ranges between ~100 to ~1000 Å. Thus, the XANES signal is dominated by the near-surface region of the material studied.

The electronic structure around an atom is sensitive to changes in the chemical environment. Thus, XANES is a useful tool for studying the local chemical environment of

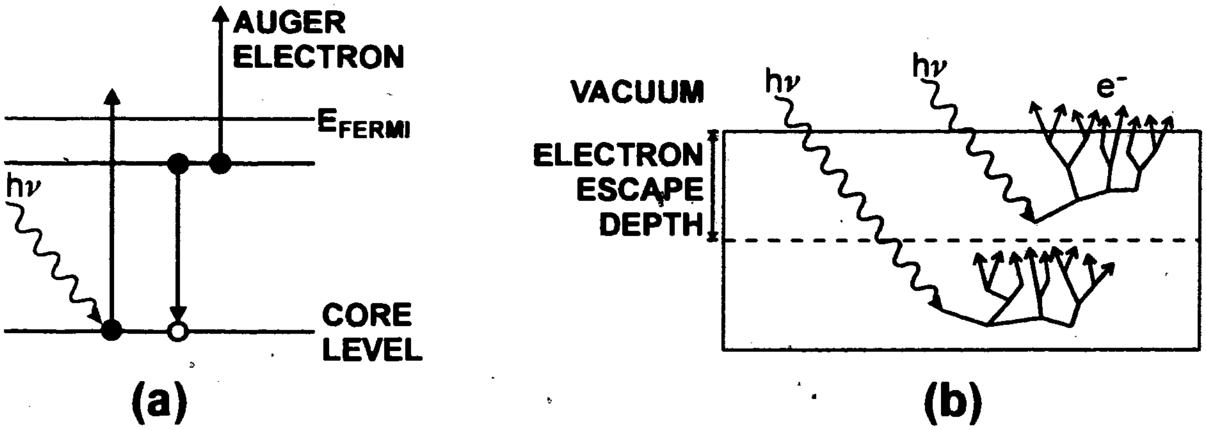

Figure 5-3. (a) A schematic representation of an Auger process. (b) A picture showing how it is the electron escape depth and not the photon penetration depth which determines a XANES signal penetration depth. Both were adapted from Stöhr, 1992.

specific elements in a series of materials. Our principal use for XANES was to study, empirically and qualitatively, differences in the local chemical environment of the silicon atoms for series of samples.

XANES spectra were measured near the silicon *K*- and *L*-edge using two different apparatus at the Synchrotron Radiation Facility (Stoughton, Wisconsin, USA). The two *beamlines* (collimated beams of synchrotron radiation emitted by electrons traveling at relativistic speeds in the *electron storage ring*) are part of the Canadian Synchrotron Radiation Facility (CSRF) which is operated by the University of Western Ontario Department of Chemistry. The *Extended Range Grasshopper* (ERG) beamline was used to measure the silicon *L*-edge for a number of the CVD-I samples. The *Double Crystal Monochromator* (DCM; named for the two quartz crystals used to produce monochromatic X-rays) beamline was used to measure the *K*-edge for many of the CVD and pyrolysed polymer samples. The next sections summarize how the measurements were performed in each device.

5.2.1 ERG Beamline Measurements

The CSRF ERG beamline employs a Mark IV "Grasshopper" grazing incidence monochromator (named after the large hinge used to align the monochromator plates which resembles a grasshopper's back leg) with an energy range of 50 to 800 eV (Tan, 1982). Because of the monochromator range, this beamline was used to study the silicon L-edge, which is located at ~98eV in crystalline silicon. The beamline is maintained at $\sim 10^{-10}$ torr, while the main chamber pressure was not allowed to exceed $\sim 3\times10^{-9}$ torr during experiments.

The TEY was measured using a multichannel plate detector (MCPD) under a small positive bias. The angle between the incident beam and the line connecting the incidence of the beam on the sample and the MCPD was 90°, as pictured in Figure 5-4. The sample could be rotated about an axis perpendicular to the plane containing the incident photon beam and the MCPD, such that an angle between the normal to the sample and the incident beam could be adjusted from 0° to 70°.

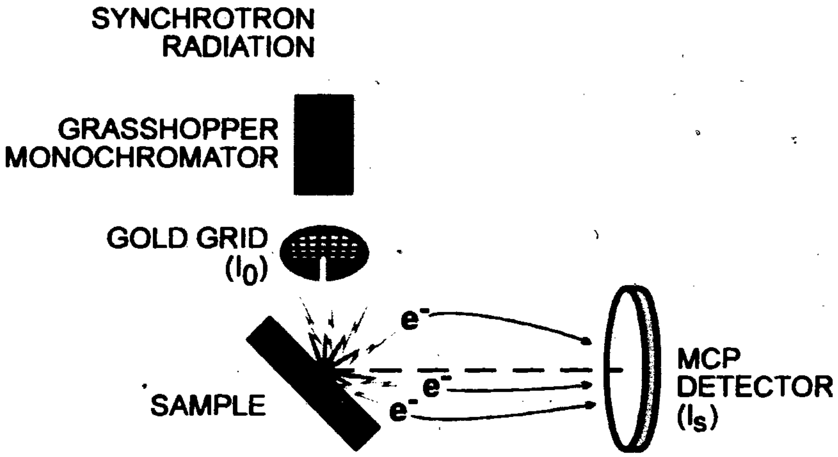

Figure 5-4. Schematic representation of the ERG beamline apparatus used to measure XANES spectra.

Because there are fluctuations in the synchrotron beam intensity (I_0), simultaneous measurement of I_0 and TEY are required. These fluctuations are caused by contaminants within the monochromator and varying current density in the electron storage ring. In the ERG beamline, I_0 is measured using a gold grid placed in the beam as it exits the monochromator. The current flow in the gold grid is measured simultaneously with the current in the MCPD (I_S). Hereafter, the ratio of I_S to I_0 is referred to as the XAS signal. In addition to measuring I_0, we also measured the absorption spectra of a thick gold foil deposited on a silicon substrate and also of clean indium foil to determine variations in the signal, caused by other impurities in the beamline.

To measure a spectrum we loaded a sample, aligned it to the beam from the monochromator and then adjusted the angle of the sample to provide a maximum signal. All of the samples were powders pressed into indium foil, which was then held onto a sample block by double sided conducting carbon tape. Indium foil was used because it contains no X-ray absorption features over the range scanned (silicon *L*-edge) and it is a good conductor. All of the samples studied were powders (i.e. not ordered films) so none of the angular dependence sometimes associated with ordered films should be observed (Way, 1995: 49). The photon energy was adjusted to a maximum absorption in the *L*-edge and the sample angle was adjusted to give the largest I_S possible.

5.2.2 DCM Beamline Measurements

The CSRF double crystal monochromator (DCM) beamline has a energy range of ~1100 eV to ~4500 eV, and was therefore used to study the silicon K-edge, which is located at 1835 eV in crystalline silicon. The operational details of the double crystal monochromator have been explained elsewhere (Yang, 1992). The beamline is maintained at ~10^{-10} torr and, as shown in Figure 5-5, is separated from the sample chamber by a 1 torr nitrogen cell equipped with beryllium windows. The nitrogen cell is used to measure the beam intensity. A few percent of the photons which pass through the cell ionize nitrogen molecules. The electrons are attracted to a current collector, biased at +67.5 V. The nitrogen ions (N_2^+) are neutralized by a ground wire. A Keithley 427 current/voltage converter measures the current flow (I_0) from ground required to neutralize the ionized nitrogen. The sample chamber pressure was not allowed to exceed 1×10^{-6} Torr during a measurement. Electrons excited out of the material were collected by a loop of wire biased at about +136 V (the *collector ring*). The purpose of the collector ring was to prevent any electrons ejected with very low kinetic energy from becoming reabsorbed by the sample. In order to maintain electrical neutrality, the sample holder is connected to ground through a Keithly 427 current/voltage converter. The electron flow from ground to the sample holder (I_S) is directly correlated to the X-ray absorption of the sample and I_0. The final XANES signal is determined by dividing I_S by I_0. X-ray absorption of clean indium foil was measured over the range of the silicon *K*-edge. Samples were powders pressed into

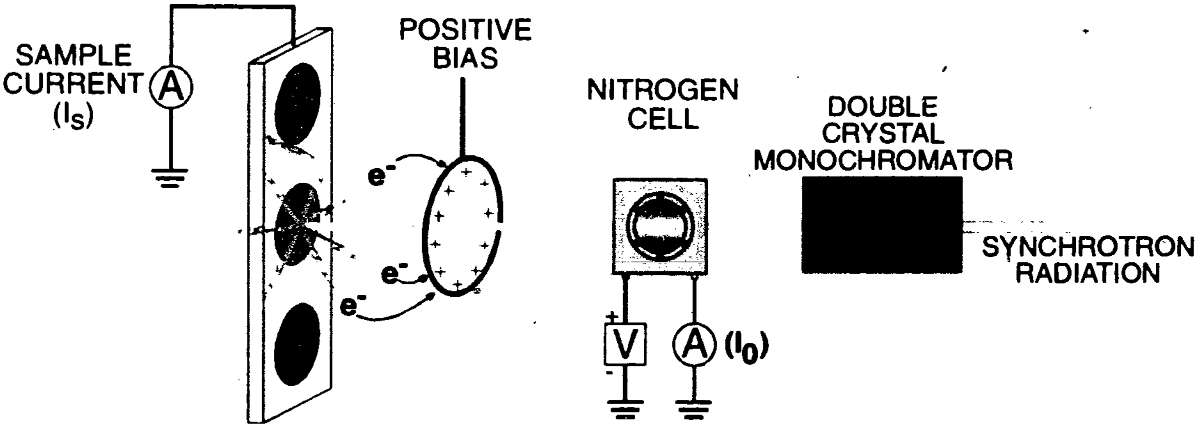

Figure 5-5. Schematic of the Double Crystal Monochromator beamline.

indium foil mounted onto stainless steel discs which were then held by the sample holder. As with the ERG beamline, indium foil was used because it has no features in the range of interest (silicon *K*-edge) and it is a good conductor.

5.3 THERMAL GRAVIMETRIC AND RESIDUAL GAS ANALYSIS

With *thermal gravimetric analysis* one studies how the weight of a material changes with temperature. It can be used to determine at which temperatures materials decompose (if there is mass lost during the decomposition) or react with the surrounding atmosphere (if there is an associated weight change). We used a TA instruments #51 thermal gravimetric analyzer (TGA) which could be connected to a Leybold Quadrex 200 residual gas analyzer (RGA; mass spectrometer).

The TGA consists of a quartz rod terminating on one end with a quartz ring, which can hold a sample pan. The opposite end of the quartz rod is connected, through a series of other joints, to an electromagnetic balance. A feedback loop is used to determine what current must be supplied to the balance to apply a force which equals the weight of the sample. When properly calibrated this current corresponds to a sample mass. A schematic of this apparatus is shown in Figure 5-6.

The next section details how the TGA was used to determine the silicon content in some of the CVD materials. Section 5.3.2 explains how the TGA and RGA were used to study the decomposition of many of the Si-O-C precursors.

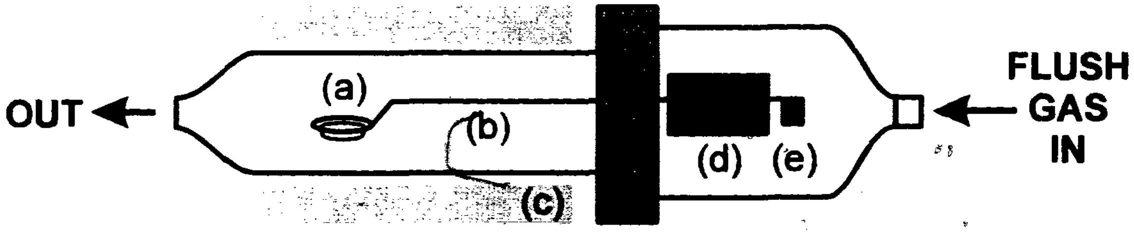

Figure 5-6. A schematic representation of the TGA where (a) is the Pt pan, held in the quartz ring, attached to (b) the quartz rod, (c) is the furnace, (d) is the electromagnetic balance, and (e) are counter-weights. The furnace and balance are controlled by a device which interfaces with a computer.

5.3.1 The TGA and the CVD Materials

The CVD materials were loaded into a platinum pan and placed inside the TGA which was then sealed from the room atmosphere. After flushing with extra-dry air (no H_2O or CO_2; Linde), the samples were heated to 950°C at a rate of 10°C/min under a flow of extra dry air. As will be shown in Chapter 7, upon heating above ~700°C, the carbon reacts with oxygen and leaves as CO and CO_2 while the silicon forms solid SiO_2. The reaction is

$$Si_zC_{1-z} + (2z + x - zx)\,O \Rightarrow z\,SiO_2\,(s) + (1-z)\,CO_x\,(g) \qquad [5\text{-}3],$$

where the average x is between 1 and 2. The initial atomic silicon content is determined by the comparison of the initial and final masses. The ratio of the final mass, m_f, to the initial mass, m_i, is, according to Equation 5-3

$$\frac{m_f}{m_i} = \frac{60.1z}{16.1z + 12} \qquad [5\text{-}4].$$

Solving for z, the silicon atomic content, we obtain

$$z = \frac{12\dfrac{m_f}{m_i}}{60.1 - 16.1\dfrac{m_f}{m_i}} \qquad [5\text{-}5].$$

The error in the calculation of stoichiometry is estimated from the standard deviation of several TGA measurements. This will be used in Chapter 7 to determine the silicon atomic content of several CVD-I and CVD-II materials. It is (as discussed in Chapter 7) only of use in determining the silicon content in materials containing only silicon and carbon in which the silicon can be fully reacted to form SiO_2 at 950°C.

5.3.2 The TGA, RGA and Decomposition of Polymers

The decomposition of various polymers was studied using the RGA connected to receive a fraction of the outflow from the TGA, as shown in Figure 5-7. Ultra-high purity argon (Linde, 99.999%) flowed at 25 cm^3/min over the polymer samples (between 50 and 70 mg) as they were heated. The argon stream exited the TGA and passed to the atmospheric pressure inlet of the RGA. A Vacoa (Vacuum Corporation of America,

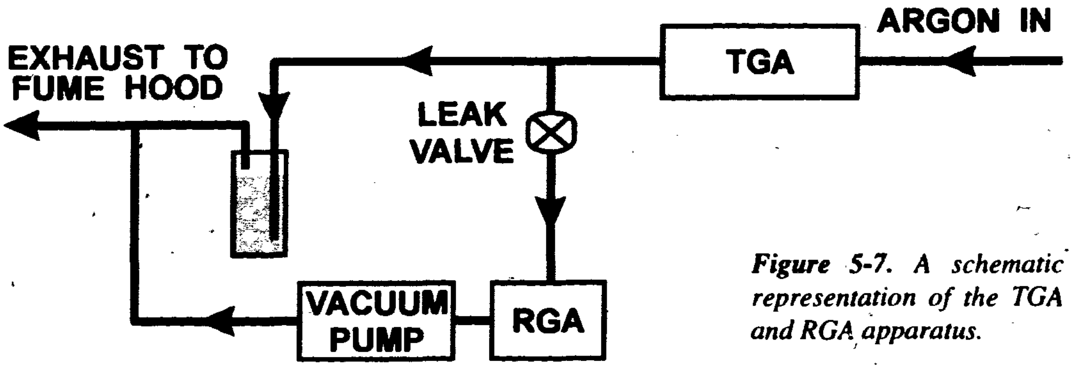

Figure 5-7. *A schematic representation of the TGA and RGA apparatus.*

Bohemia, New York, USA) leak valve was used to sample a small amount of the TGA exhaust and pass it to the mass spectrometer chamber. The base pressure of the RGA chamber is near 5×10^{-8} Torr and we operated near 3×10^{-5} Torr with the leak valve open. Thus, the signal from the gases evolved during polymer decomposition overwhelms those from the RGA chamber alone. After loading the sample in the TGA, argon was flushed through the system until the base pressure in the RGA stabilized. All gas flow lines were heated above 100°C, to facilitate the transport of evolved water, benzene, and other residual vapours which might otherwise condense in the hoses at ambient room temperature.

During the first experiments performed, to study the decomposition of PMPS and PPSS, the data were recorded manually. Later, Oliver Schilling (a Ph.D. student in the group) interfaced a computer (generic, 286 CPU) to the RGA and wrote a program to read the masses from the RGA and store them into a data file. This program was used during the extensive polymer study. Only masses between 2 and 100 atomic mass units (amu) were measured.

As will be shown in Chapter 8, for many of the materials studied it was possible to use the TGA and RGA data to estimate the stoichiometry of the resulting material, based on the stoichiometry of the starting polymer.

5.4 ELEMENTAL ANALYSIS

Many different elemental analysis techniques were used to measure the stoichiometry of the samples made. For the CVD samples, the silicon content by TGA was believed to be the most reliable. For the polymer samples, it is believed that the stoichiometries which could be calculated from the TGA and RGA results (see Chapter 8 and 9) are more reliable. Nevertheless, multiple techniques were used to estimate the stoichiometry of the materials made (which lead to the conclusion that the TGA and RGA related calculations are more reliable) so it is useful to summarize them here.

The carbon, hydrogen, and nitrogen content in many materials can be determined by the combustion of the samples in air followed by gas chromatographic analysis. This *CHN analysis* is very useful in compounds where all of the carbon, hydrogen, and nitrogen react with air to produce gaseous compounds. If, however, the samples contain significant concentrations of other elements, such as silicon, which do not react with air to form a gaseous compound at the combustion temperatures available, the results may be unreliable. As will be discussed in Chapters 7, 8, and 9, the results from the CHN analysis were not considered to be strictly accurate for carbon content because of silicon bonding to the carbon, and thus preventing it from reaching the gas phase. Nevertheless, the data is presented, for it is in rough agreement with data obtained by other methods.

Several CVD-I and -II samples and materials made during the initial polymer investigation (PPSS and PMPS) were sent to Canadian Microanalytical service (Ladner, BC, Canada) for CHN analysis.

All of the silicon oxycarbides from the extensive study were analyzed by Dr. Zank's group at Dow-Corning Corp. (Midland, MI). CHN analysis were done on a Perkin Elmer 2400 analyzer.

The silicon and oxygen analysis were performed only for the materials in the extensive polymer study. They were done by employees of Dow Corning Corp. (Midland, MI). Oxygen analysis were done on a Leco oxygen analyzer (model R0-316) equipped with an oxygen determinator 316 (model 783700) and an electrode furnace EF100. Silicon content was determined by a fusion technique which consisted of converting the solid to a soluble form and analyzing the solute for total silicon by Arl 3590 ICP-AES analysis.

Typically, (for the materials in the polymer study) the sum of the experimentally derived carbon, silicon, hydrogen, and oxygen weight percentages were within 5% of 100%. We are most confident of the carbon, hydrogen, and silicon analyses, so in the data presented in Chapters 8 and 9, the oxygen content is calculated from the difference between 100 wt. % and the sum of the carbon, hydrogen, and silicon weight percentages. We estimate that the error in any of these percentages is approximately ±3%, although this may be larger for the oxygen weight percentages presented, considering how they were determined.

5.5 SMALL ANGLE X-RAY SCATTERING

This section provides a brief summary of small angle X-ray scattering (SAX) theory and how it was used in this thesis. This section is somewhat brief because the SAX data presented in this thesis is for only one small series of materials.

5.5.1 Measurement Procedure

SAX profiles were measured by transmission in the Siemens D5000 diffractometer, as shown in Figure 5-8. Fifty to one hundred micron thick powdered samples were held in a rectangular frame with kapton windows (25 micron thick) on both sides. Data were collected between scattering angles of 0.3° and 15°. The scattering from the kapton windows in this range is very small compared to that from the samples and can be neglected. We used 0.1° incident and antiscatter slits and a 0.1mm receiving slit. The mass

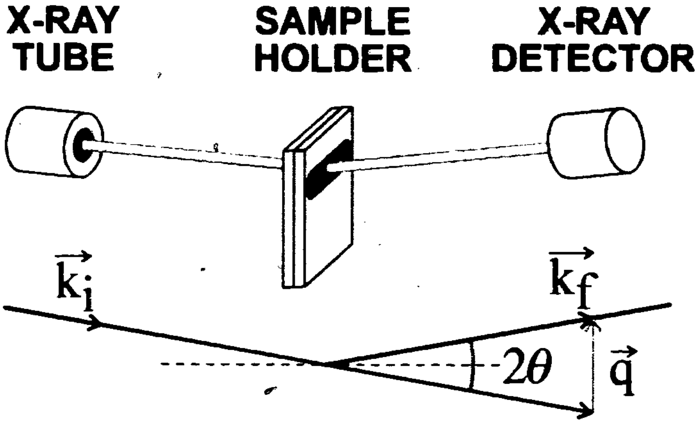

Figure 5-8. The small angle scattering apparatus (top) and a schematic showing k_i, k_f, and q (bottom).

of the sample in the frame was recorded. The attenuation of the X-ray beam by the sample was measured by comparing the beam intensity (as detector counts per second) with and without the sample in the beam path while the tube and detector were set to 0°. The holder, either empty or filled with sample, was placed in the beam path.

5.5.2 Theory and Data Analysis

The small angle scattering of X-rays by powders shows regions of differing electron density (Debye, 1957; Kaliat, 1981; Guinier, 1955). Regions with characteristic dimensions of 3 to 100Å can be examined with our diffractometer using Cu K_α radiation.

The small angle scattering results were fitted using the form proposed by Debye *et al.* and Kaliat *et al.* The intensity, $I(q)$, as a function of the scattered wave vector, q, is taken to be:

$$I(q)=\frac{A}{q^{n}}+\frac{BR_1^4}{\left(1+q^2R_1^2\right)^2}+\frac{CR_2^4}{\left(1+q^2R_2^2\right)^2}+D \qquad [5\text{-}6],$$

where R_1 and R_2 are two characteristic correlation lengths for the electron density variations. These can be associated with pore sizes by comparison to Guinier's formula (Guinier, 1955). The radius of gyration of the corresponding pores is √6 times R_1 or R_2. A, B, and C are constants proportional to the quantity of the macropores, small micropores, and larger micropores, respectively. D represents a constant background. Porod's law for a pinhole shutter gives n=4 (Porod, 1982). In cases where the slits, not pinholes, are used data is smeared and can give lower apparent values for n in our scattering angle range (Guinier, 1955; Gibaud, 1996).

In order to determine n for our system, the sample holder was filled with graphite (JMI), a material which contains no nanopores. Equation 5-6 was fitted for the graphite data with B and C set to zero, giving n=3.55. For the rest of the fits in this paper, n was set to 3.55.

5.6 SURFACE AREA ANALYSIS

The surface area of materials was measured by the Brunauer-Emmett-Teller (BET) method (Lowell, 1991), using a single point measurement on a Micrometrics Flowsorb II 2300 surface area analyzer. The surface area is determined using the BET equation (Lowell, 1991). A mixture of nitrogen in helium (30:70 mol. %) was used because, at atmospheric pressure and the boiling point of nitrogen, it provides a favourable condition for the adsorption of a monolayer of nitrogen. The samples were placed in a U-shaped holder and degassed under a flow of the gas mixture at 140°C for 10 to 15 minutes before taking the measurement. The sample and holder were then immersed in liquid nitrogen for adsorption and, after that, immersed in room temperature water for desorption. The adsorption or desorption measurements were considered complete when the change in the BET result was less than 0.05m^2/sec. The final results were taken from the desorption data.

The next chapter explains the method used in the electrochemical testing. Chapters 7, 8, and 9 present the results and discussion of the experiments.

CHAPTER 6

EXPERIMENTAL IV: ELECTROCHEMICAL TESTING

Electrochemical testing can be used to learn about the electronic and structural environments of atoms in many materials and ultimately to determine which materials are potentially useful in lithium-ion cells.

An introduction to the methods used in electrochemical testing is presented next. Section 6.2 outlines the electrochemical insertion of lithium into carbonaceous materials and Section 6.3 details cell construction and testing methods.

6.1 INTRODUCTION TO ELECTROCHEMICAL METHODS

6.1.1 Origin of the Cell Voltage

A lithium-ion cell consists of an anode and a cathode separated by an ionically conducting electrolyte, which transfers lithium ions (Li^+) but not electrons (e^-). The voltage of the cell is a direct result of the difference between the chemical potential of lithium in the anode (μ_{anode}) and cathode ($\mu_{cathode}$). The chemical potential of lithium in an electrode is defined as:

$$\mu = \left[\partial G(N,T,P) \big/ \partial N \right]_{TP}$$

where G is the Gibb's Free Energy of and N is the number of lithium atoms in the electrode, T is the cell temperature and P is the internal cell pressure

When a lithium cell is discharged a number of lithium atoms, say ΔN, in the anode enter the electrolyte as ions, travel through the electrolyte, and then enter the cathode. Simultaneously, the ΔN electrons from these atoms move through an external circuit and do work. The total change in the free energy of the cell (which combines the changes in both electrodes) is

$$\Delta G = \Delta N \cdot (\mu_{cathode} - \mu_{anode}).$$

The work done *on* the electrons in the external circuit is

$$W = -\Delta N \cdot eV \ ,$$

where V is the cell voltage and e is the magnitude of the charge on one electron. Equating W and ΔG leads to

$$V = -\frac{\mu_{cathode} - \mu_{anode}}{e}.$$

This result can also be obtained for the charge process, where the work done *on* the electrons in the external circuit is positive.

Test cells use lithium metal as one electrode and the material to be studied as the other, as shown schematically in Figure 6-1. Since the chemical potential of lithium in metallic lithium is fixed, the cell voltage is then only a function of changes in the chemical potential in the electrode material being tested.

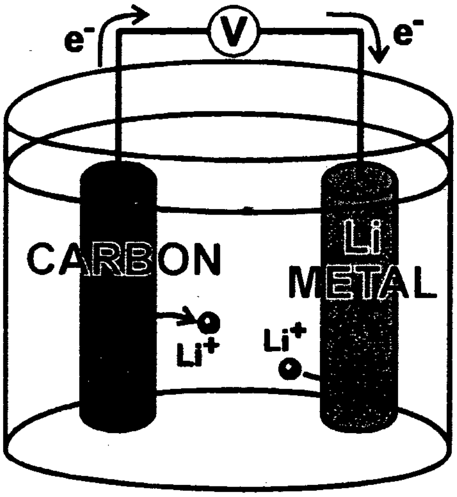

Figure 6-1. Schematic of a lithium-carbon test cell during charging.

6.1.2 Types of Electrochemical Tests

This section outlines some of the electrochemical tests commonly performed and points out which of them were used in this thesis.

6.1.2.1 Voltage Profiles

To determine a *voltage profile* the cell is kept at a fixed temperature and cycled (charged and discharged) using a constant current. The current is applied until the voltage reaches either an upper or a lower voltage *trip point* at which time the current is reversed. The cell voltage is recorded as a function of time, $V(t)$. The data can be analyzed in many ways. In compounds where the stoichiometry is well known, the voltage can be plotted as a function of the amount of lithium, x, intercalated calculated according to the formula:

$$x = {}^{t \times I}\!\big/_{C \times m} \;,$$

where t is the time in hours, I is the current in mA, m is the active mass of the electrode in grams, and C is the *magic number* of the intercalation host in mAh/g. C corresponds to the theoretical *specific capacity* for a specific change in the amount of lithium intercalated. This theoretical specific capacity can be calculated (in mAh/g) for a compound Li_xM_y which undergoes a change of $\Delta x = 1$ as:

$$C = \frac{F}{3.6 \times y \times MW} \qquad [6\text{-}1],$$

where F is Faraday's number (96480 Coulombs/mole), and MW is the molecular weight of M in grams/mole. The factor of 3.6 arises from the conversion factors of A to mA and hours to seconds (1000mA/1A × 1hr/3600s).

In this work, the nature of the lithium insertion was not known so we plotted the voltage versus the specific capacity, Q. Here, the specific capacity is calculated according to the formula:

$$Q = {}^{I \times t}\!\big/_{m} \;, \qquad [6\text{-}2],$$

where I is the applied current, t is the time, and m is the mass of the *active material* (the material into which lithium is inserted) in the electrode. We used units of mAh/g for Q.

The plots of V versus t, x, and Q all have the same shape and contain similar information. $V(Q)$ is used because it accounts for the active mass but does not require any knowledge or assumptions about the stoichiometry as $V(x)$ would.

6.1.2.2 Differential Capacity

The voltage profile of materials typically contains complex information which, depending on the materials being studied, can correspond to phase transitions and a variety of other processes. Subtle changes may not be easily observed in a $V(Q)$ plot, so the *differential capacity*, $-(\partial Q/\partial V)_T$, is calculated and plotted versus V (hereafter the subscript T is dropped). Phase transitions can be observed as plateaus in the voltage profile, as mentioned in Chapter 2 for graphite. A constant voltage would result in a divergence of $-(\partial Q/\partial V)$ but in a real cell kinetic effects result in a slight decrease in voltage during the phase transition (McKinnon, 1980) leading to a sharp peak in $-(\partial Q/\partial V)$.

Another way of visualizing the differential capacity plot is as a density of sites for intercalated atoms at various voltages. A $-(\partial Q/\partial V)$ peak corresponds to a large number of sites with the same voltage. If the chemical potential is a good measure of the binding energy of the inserted atom to the host (and is not strongly influenced by other effects such as the interactions between inserted atoms) then we can view the differential capacity as a plot of density of sites versus binding energy. The integrated area under a peak in $-(\partial Q/\partial V)$ versus V corresponds to the specific capacity over the voltage increment.

Differential capacity plots were very useful in the study of many of the materials presented in this thesis.

6.1.2.3 Cycle Life Testing

The *charge capacity* is defined as the specific capacity measured from the low to the high voltage trip points. Discharge capacity is similarly defined. Upon multiple cycles some decrease in capacity is usually observed. A plot of the discharge and charge capacities versus cycle number is called the *capacity fade curve*. Desirable materials show little capacity fading (small decreases in capacity) over many cycles and thus have a long *cycle life*.

6.1.2.4 Cyclic Voltammetry

Cyclic voltammetry involves sweeping the voltage applied across a cell, typically linearly with time, and measuring the resulting current. A plot of I versus V looks very similar to a plot of $-(\partial Q/\partial V)$ versus V. This should not be surprising if one considers that the current can be described as:

$$I = \frac{dQ}{dt} = \frac{dQ}{dV}\frac{dV}{dt}.$$

If the voltage is being changed linearly with time, then dV/dt is a constant and I is directly proportional to dQ/dV. This, however, neglects kinetic effects. If done using a two-electrode system, like a typical coin cell, the internal resistance of the cell (R_{INT}) will shift the data by $I{\cdot}R_{INT}$. Since the current is changing throughout a peak, the amount of shift is also changing. This ultimately results in deformed peaks. However, it can be a useful technique if $I{\cdot}R_{INT}$ is not significantly large. Greater accuracy can be obtained using a three-electrode system (i.e. anode, cathode, and reference), although this only removes the kinetic effects from the counter electrode. Thus, the resistance in the remaining electrode determines the shift.

Cyclic voltammetry was not used in this thesis because we could obtain more reliable, although sometimes noisy, information from differential capacity plots. It is mentioned here because it is such a commonly used technique.

6.2 ELECTROCHEMICAL INSERTION OF LITHIUM INTO CARBONACEOUS MATERIALS

Chapter 2 discussed how the different structures of carbonaceous materials affect the intercalation and insertion of lithium. The following sections present details specific to the *electrochemical* insertion of lithium into carbons and some of the associated practical considerations and complications.

6.2.1 Graphite

As mentioned in Chapter 2, the intercalation of lithium proceeds through stages. During the transition between two stages there is little change in the voltage of the cell because the sites being filled are of equivalent potential. This should be observed as a plateau in the voltage profile and as a peak in a differential capacity plot ($-\partial Q/\partial V$ or $-\partial x/\partial V$ versus V), as shown in Figure 6-2 (from Zheng, 1995b). The transitions between stages, as explained in Chapter 2, have been labeled from in-situ XRD work (where the XRD profile of a material can be measured in a cycling electrochemical cell) done by Zheng *et al.*(Zheng, 1995b). For this and all subsequent differential capacity plots the charge and discharge are respectively plotted as positive and negative. This 'standard' is

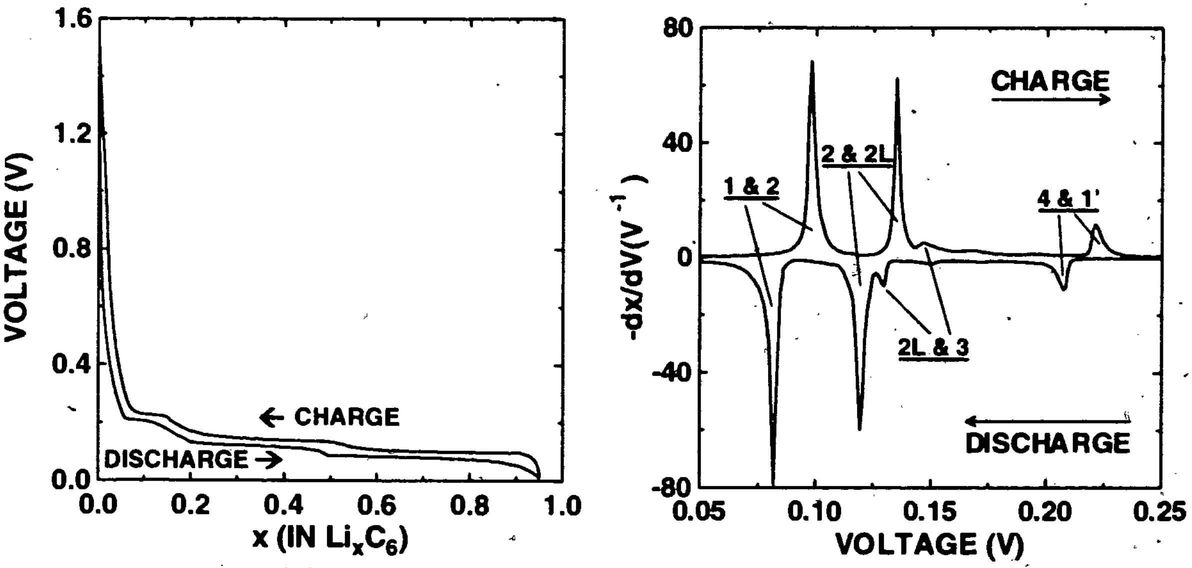

(a) (b)

Figure 6-2. (a) The voltage profile and (b) differential capacity plots for the second cycle of a lithium-graphite (JMI) cell (from Zheng, 1995b). The labels in (b) correspond to the phases which are in coexistence during the transition. 1' corresponds to a dilute stage 1 and 2L corresponds to liquid stage 2 (Zheng, 1995b).

adopted for plotting clarity, even though $\partial Q/\partial V$ is always negative.

Several chemical reactions can occur during the electrochemical intercalation of lithium into graphite. In Chapter 1 it was mentioned that lithium metal will react with non-aqueous electrolytes to form an electronically insulating, ionically conducting film known as the *solid electrolyte interphase* (SEI; Peled, 1979). The SEI grows until it reaches a thickness through which electrons can no longer pass at which time the lithium metal surface is passivated and the reaction can no longer continue. A similar reaction occurs in lithiated graphite. While carbons are stable in non-aqueous solvents, lithiated carbons, having a potential 0.1 V above lithium metal, are not. When a lithium-carbon cell is assembled the carbon contains no lithium atoms. During the first discharge, when lithium atoms first enter the carbon, some electrons will travel to the surface to combine with lithium ions which then react with the electrolyte to form an electronically insulating, ionically conducting film. As with lithium metal this *surface passivation* continues until the film becomes thick enough to prevent the passage of electrons (Fong, 1990). This reaction consumes lithium metal, and can be observed as a difference in capacity between the first discharge and charge of a lithium-carbon cell. Figure 6-3 (from Way, 1995) shows a voltage profile of a Li/graphite cell, made using Lonza KS-44 graphite and an electrolyte solution of 1M $LiN(CF_3SO_2)_3$ and 1M 12-Crown-4 ether in a 50/50 (v/v) mixture of

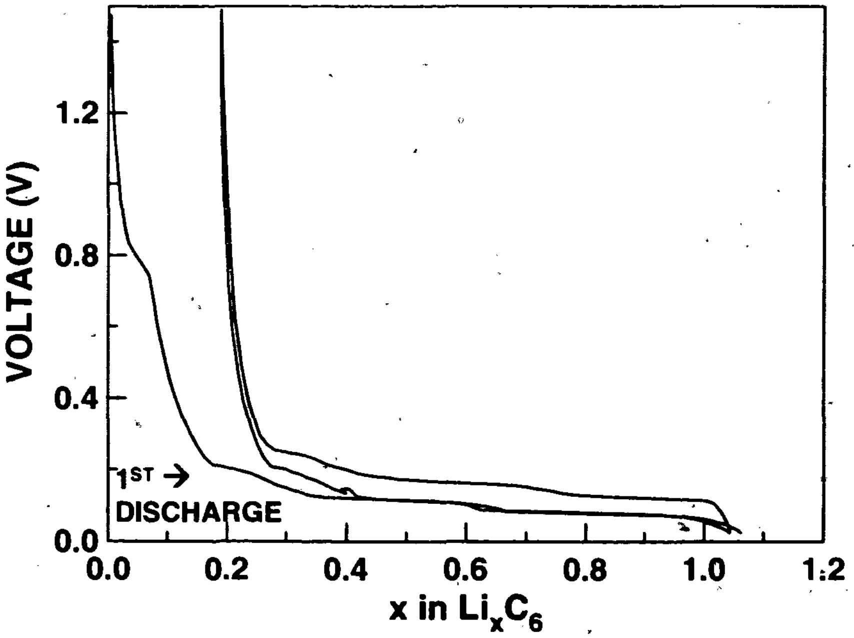

Figure 6-3. *The voltage profile of a lithium-graphite cell showing the formation of the passivation film during the first discharge (data from Way, 1995).*

propylene carbonate (PC) and ethylene carbonate (EC). The formation of the passivating film can be seen during the first discharge as "additional" capacity above 0.25 V. The lithium can only be removed from the graphite, and not the film, leading to a decreased capacity on the first charge.

This reaction is of serious consequence when making a lithium-ion cell. When a lithium-ion cell is assembled the lithiated transition metal oxide (TMO) cathode contains all of the lithium in the cell. To compensate for the lithium consumed in the formation of a passivating film, additional TMO must be added to the cathode electrode which increases the cell weight.

6.2.2 Disordered Carbons

The intercalation of lithium into disordered carbons was discussed in Chapter 2. The voltage profiles of all carbons are critically dependent on their structure. In a disordered carbon no staging is observed, because the disorder leads to slight differences in the chemical potential of most sites. Stacking faults, like turbostratic disorder, decrease the amount of lithium which can be accommodated between layers. Thus, disordered carbons which do not contain a significant number of micropores typically have smaller capacities than highly oriented graphites. Figure 6-4 shows a voltage profile and differential capacity

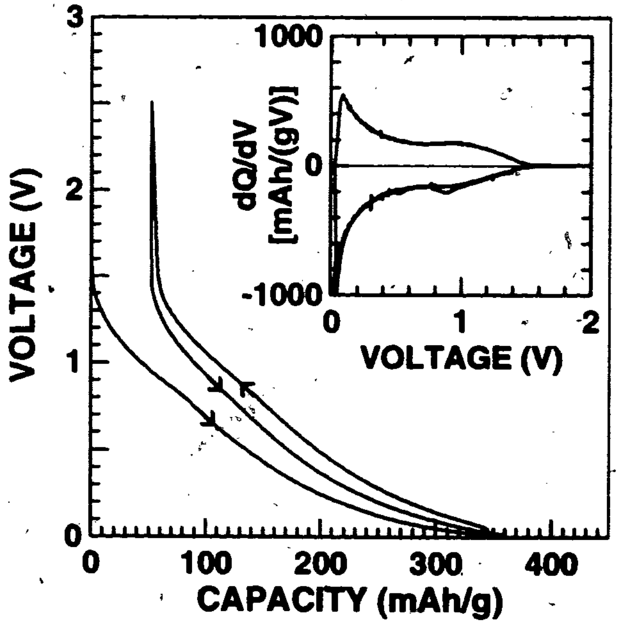

Figure 6-4. Voltage profile of a Li-carbon cell made from a (non-microporous) disordered carbon. The inset shows the differential capacity versus voltage.

plots for a 'non-microporous' disordered carbon (prepared by the CVD of benzene vapours at 950°C).

The next section details the how the cells used in this thesis were constructed and tested.

6.3 CELL CONSTRUCTION AND TESTING

This section details the construction of the coin cells used in this thesis. Section 6.3.1 describes the making of the electrodes. Section 6.3.2 describes the process used to wet the internal cell parts with electrolyte. During the course of the thesis a new electrolyte was procured, which simplified the electrolyte wetting process. There were also differences between the electrode fabrication for the CVD and pyrolysed polymer materials. Section 6.3.3 details the cell assembly process. Finally, Section 6.3.4 details the tests performed.

Some of the materials (lithium metal and electrolytes) used in the lithium test cells are reactive with the water vapour in the air and so the electrolyte wetting and cell assembly are done inside an argon atmosphere glove box.

The cells consist of a lithium electrode and a test material electrode which are kept from touching by an electrically insulating *separator*. The separator consists of a microporous polypropylene film (Celgard 2502) which can imbibe electrolyte and conduct ions through the pores but is electronically insulating. Also in the cell are a *spacer* and *spring* which are used to maintain a *stack pressure* on the electrodes and separator. These are held inside the coin cell can and cover as detailed in Section 6.3.3.

Because of the scope of the extensive polymer study and the desire to get results as quickly as possible, we opted for a division of the labour involved. To this end Weibing Xing (a post-doctoral research assistant in the lab) constructed and tested all of the cells for the polymer study.

6.3.1 Electrode Fabrication

Electrodes consisted of a thin film of *active material* (the material to be tested), Super S Carbon Black (MMM Carbon, Belgium), and binder adhered to thin copper foil. To ensure good electrical contact to all particles in the final electrode the active material was first mixed with about 5 % (by weight) Super S. Super S is a disordered carbon consisting of very fine filaments. A solution of 9.4 % (by weight) polyvinylidenefluoride (PVDF) in N-methylpyrrolidinone (NMP) is then added to the carbon mixture at ~50 % by weight. The resulting slurry is then diluted with additional NMP until it reaches the consistency of paint and can be spread onto the copper foil. After coating the electrode is dried in a convection oven at about 110°C for at least 3 hours. The NMP evaporates leaving a film (containing about 5 to 10 % PVDF binder by weight) adhered to the copper.

There were two ways used to spread the electrode slurry which depended on the amount of sample available. For the pyrolysed polymers, there was always enough sample to use the *doctor blade* method. Roughly 1g was used to make the slurry which was then spread onto the copper foil using a *doctor blade spreader*. After drying, the thickness of the coating was roughly 150μm. After pressing between flat plates at about 1000 kPa for ~1 minute, several 12 mm squares are cut. These are then used as electrodes in the lithium cells.

If not much sample was available, as was always the case for the CVD materials, the slurry was spread onto the copper foil by hand. As little as 50 mg was sometimes used to make cell electrodes. Typically, the copper foil was cut into 12 mm squares and weighed before coating. The individual copper squares were then coated using a small spatula, dried, and pressed between flat plates to ~1000 kPa for ~1 minute. The thickness of these coatings is estimated to be between 100 and 200 μm although the coatings are not as uniform as the ones made using the doctor blade spreader.

Each electrode is weighed, so that the mass of the active material can be calculated. The weight of the copper foil (if not measured prior to coating) is subtracted using an average value, obtained by cutting as many as 10 to 20 squares, weighing them, and averaging. The copper foil used with the CVD-I materials was approximately 50μm thick. Later, Moli Energy (1990) Ltd. supplied us with thinner copper foil, approximately 10μm thick. This led to a smaller weighing error associated with the cutting of electrode squares.

6.3.2 Electrolytes and Wetting

The electrodes and separator are wetted with electrolyte to ensure good ionic conductivity into the materials. The electrolyte used for the study of the CVD-I materials and the preliminary polymer pyrolysis study required a ***pressure wetting*** process. For the remaining studies, a recently procured electrolyte was used which could infiltrate the pores of the materials at room pressure.

The first electrolyte used was 1M $LiN(CF_3SO_2)_2$ dissolved in 50/50 (v/v) propylene carbonate and ethylene carbonate (PC/EC). A pressure wetting process was required in order to force the electrolyte into the pores of the electrode and separator. The electrodes and separators are anchored to the bottom of glass vials containing the electrolyte. To remove gas trapped in the pores of the materials the vials are then sealed into a pressure bomb which is evacuated with a roughing pump for about 10 minutes. The vacuum is slowly released and the bomb is filled with argon (UHP-grade, Linde) to a pressure of 830 kPa (gauge) in order to force electrolyte into the pores. After about 10 to 15 minutes, the pressure is released and the items are removed from the vials and inspected. Any uneven discoloration of the electrodes or separators implied incomplete wetting and the materials were then subjected to another round of pressure wetting.

The electrolyte used for the remainder of the thesis was 1M $LiPF_6$ dissolved in 30/70 (v/v) ethylene carbonate/diethyl carbonate (EC/DEC). This electrolyte was much easier to use because it is *self-wetting*, so pressure wetting was not required. Here, as the test material electrode and separator are added to the cell, drops of electrolyte are applied with a needle and syringe until the item evenly discolours.

6.3.3 Cell Assembly

The lithium foil is stored in a dessicator inside the glove box, to avoid any reaction with trace amounts of water vapour. It is removed and cut into 12 mm squares immediately prior to cell assembly to reduce any slight contamination to the surface of the foil.

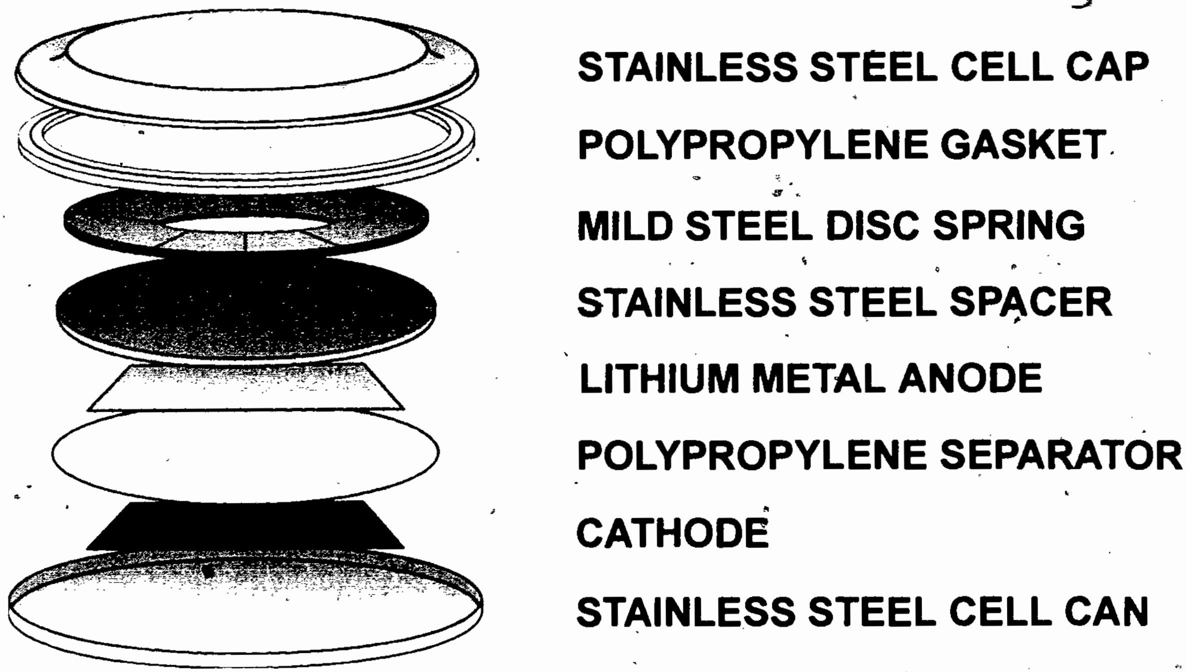

Figure 6-5. *A schematic 'exploded' view of a lithium coin cell*

All cells made in this thesis use stainless steel 2325-type (23 mm OD, 2.5 mm thick) coin cells. The cells are assembled by stacking the individual parts in the cell can, in the order shown in Figure 6-5. The test material electrode is placed, roughly centered inside the cell can. The separator is then laid on top. The lithium foil electrode is placed on top of the separator, aligned to the test material electrode. Then, in sequence, the stainless steel spacer and steel spring are added. Once the lithium foil has been added, care is taken to avoid shorting the cell, as this will cause partial discharge, obscuring some of the results. The cell cap, onto which is affixed a polypropylene gasket, is attached to the top and the entire cell assembly is sealed using a crimper, which folds the walls of the cell can onto the polypropylene gasket.

6.3.4 Cell Testing

All cells were tested by recording voltage as a function of time during constant current cycling. All cells were held at ~30°C ± 0.1°C in insulated boxes, maintained by Omega 4201A-PC2 temperature controllers employing RTDs and heating tape. Cells were cycled using a computer controlled charger system from Moli Energy (1990) Ltd.

The voltage and current set points were programmed by individual charger boards, assembled at Moli Energy (1990) Ltd. As part of this system, a Keithly 196 voltmeter measured the voltage of each cell separately, by cycling through all the cell channels (32 per voltmeter).

Before installing, the cell voltages are measured with a portable voltmeter. This is done as a check of the cell assembly process. For lithium/carbon cells good cell voltages are typically between 3 and 3.5V. 'Faulty' cells with, for example, an internal short will have lower voltages..

The CVD-I and CVD-II materials were tested with high and low voltage trip points of 2.5 and 0.01 V, respectively. The trip points of the materials in the remainder of the studies varied, but were near these values. The current used is based on the length of time one would like a single charge or discharge to take place as if the material in the electrode was graphite. That is, currents are calculated as if the active mass in the material had a capacity of 372 mAh/g. Thus, 50 and 100 *hour rates* correspond to 7.44 and 3.72 mA/g respectively. Most of the CVD-I and -II materials were tested at 50 or 100 hour rates. Tests of the pyrolysed polymers were most commonly performed at 20 hour rates (18.6 mA/g). The test current is given when specific test cells are mentioned.

The next chapter presents the results and discussion of the CVD-I and CVD-II materials studies.

CHAPTER 7

THE CVD MATERIALS

This chapter presents an overview of the CVD materials. Due to some differences in the materials produced in the two CVD apparatuses used, it is divided into sections for the CVD-I and CVD-II materials.

7.1 THE CVD-I MATERIALS

The materials presented in this section were synthesized using CVD Apparatus I. The apparatus and the method of deposition was detailed in Chapter 3, Section 3.3. From over 20 CVD-I depositions (4-6 samples were typically retrieved per deposition), five materials are discussed in detail (see Table 7-1).

7.1.1 Sample Reclamation and Characterization

Products are deposited throughout the length of the CVD reactor tube, in various forms. Near the entrance of the tube, a tar-like material is deposited, which later hardens to a dull sheen. Approaching the far end of the tube, loosely adhered fine powders, which

Table 7-1. Summary of the CVD-I samples.

Sample Label	Silicon Source	Estimated source ratio (Si source : benzene)	Deposition Temperature (°C)	Deposition Time (h)	Appearance
A	none	0:1	950	5.4	black and soft
B	$SiCl_4$	2:3	1050	4	grey and brittle
C	$SiCl_4$	2:1	950	4	black and soft
D	$(CH_3)_2Cl_2Si$	1:1	950	3	black and soft
E	$(CH_3)_2Cl_2Si$	1:1	950	3	grey and brittle

have a tendency to absorb water vapour, are deposited. Samples retrieved from the hot zone of the tube were classified into three types of materials, varying in both visual and textural properties; a black, soft, porous deposit which could be easily reduced to a powder; a grey, brittle, porous deposit which "crunched" when being reduced to a powder; and a highly reflective film which was typically well-adhered to the quartz insert. The materials deposited in the hot zone can be retrieved, without significant contamination by impurities from other regions in the tube, by removing the tubular insert. The samples obtained were ground to a fine powder.

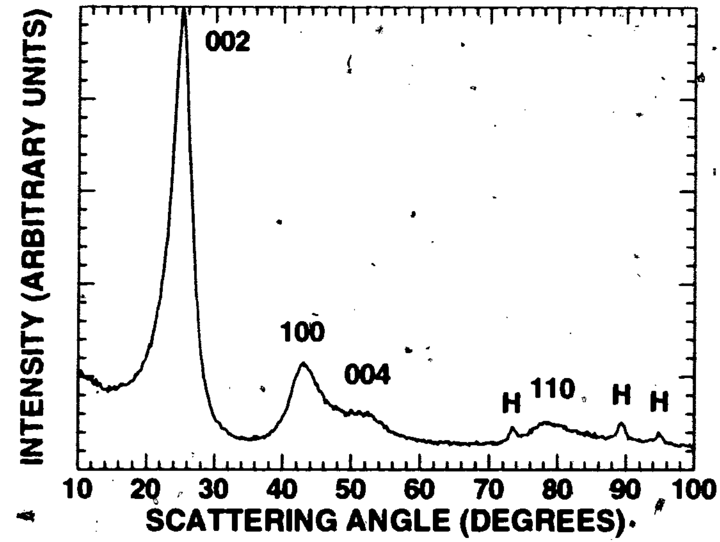

Figure 7-1. The XRD profile for sample A. The peaks labeled 'H' arise from the sample holder.

Table 7-1 contains a summary of the five CVD samples which will be discussed in detail here. Sample A is pure carbon, samples B and C were made in separate runs using the $SiCl_4$ source. Samples D and E were collected from different regions of the tubular insert for the same deposition, using the $(CH_3)_2Cl_2Si$ source.

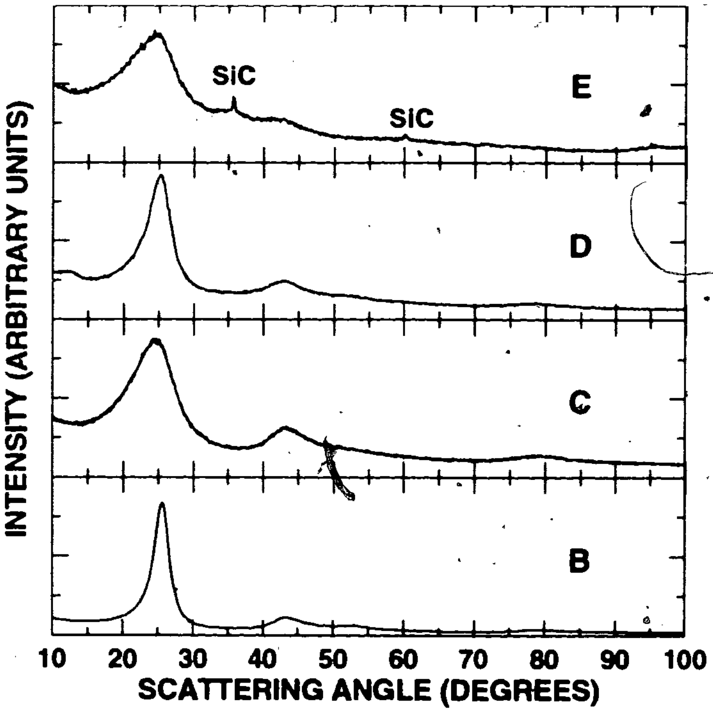

Figure 7-2. The XRD profiles for samples B to E.

Figure 7-1 shows the XRD data collected for sample A, which appears, as

Table 7-2. Summary of XRD data and analysis for the CVD-I materials.

Sample	2θ (002) (deg)	FWHM (002) (deg)	2θ (100) (deg)	FWHM (100) (deg)	d_{002} (Å) SRP*	L_a (Å) SRP*	L_a (Å) Eq.[5-2]	L_c (Å) Eq.[5-2]	XRD sample holder
A	25.1	3.4±0.2	42.8	5.4±0.2	3.51	17	13	27	2.0mm well
B	25.6	2.6±0.2	43.2	5.2±0.2	3.47	18	16	30	0.2mm on ZBH
C	24.4	6.8±0.2	43.5	5.7±0.2	3.48	15	15	13	2.0mm well
D	25.3	3.7±0.2	42.8	5.5±0.2	3.49	13	15	25	2.0mm well
E	24.7	7.2±0.2	43.0	5.0±0.2	3.49	...	16	12	0.2mm on ZBH

* SRP: Structure Refinement Program for Disordered Carbons (Shi, 1993).

expected, to be a typical pre-graphitic carbon (Warren, 1941). Surprisingly, the XRD patterns for samples B, C, and D, shown in Figure 7-2, also appear to be pre-graphitic carbons, with no evidence of silicon. Sample E shows some weak silicon carbide peaks, resulting from a minimal amount of silicon carbide in this sample. A detailed summary of the XRD patterns is presented in Table 7-2.

As discussed in Section 5.3.1, TGA (in air) was performed on each of the samples to determine the silicon content. The results are shown in Figure 7-3. The product remaining at the end of the TGA experiment was, typically, a white powder, consistent with the formation of SiO_2. This is confirmed by XRD as seen in Figure 7-4, which shows an XRD profile for sample D (indexed as SiO_2) after TGA (in air) to 950°C. The determination of

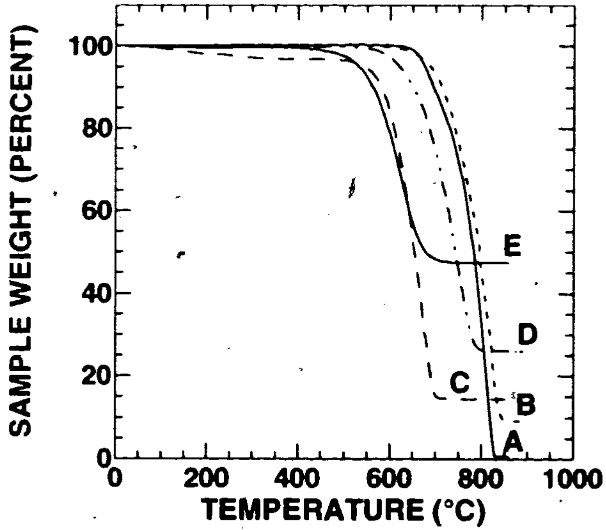

Figure 7-3. TGA data collected for samples A-E. The second plateau represents the point where the reaction described by Equation 5-3 has run to completion

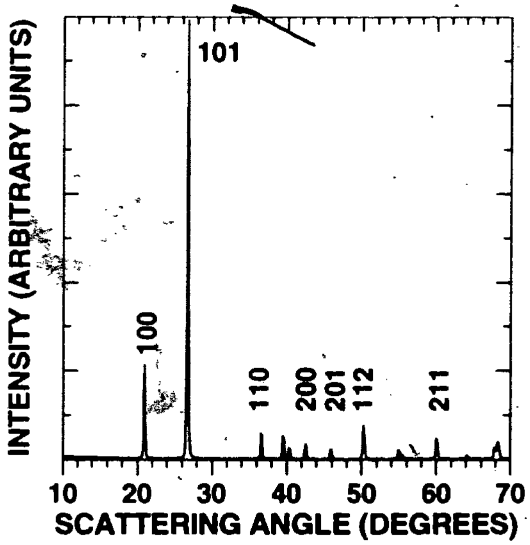

Figure 7-4. XRD profile for the product formed by the TGA of Sample D, indexed as c-SiO₂. All peaks in the pattern correspond to quartz. To avoid clutter, not all the peaks were indexed.

Table 7-3. Average TGA final masses and calculated silicon contents (using Eq. 5-5).

Sample label	Final TGA mass (% of initial)	Atomic Silicon content (%)
A	0	0
B	9	1.8±0.1
C	15	3.1±0.1
D	28	6.0±0.3
E	48	11±0.5

the silicon content was performed, according to Equation 5-5 and the results are summarized in Table 7-3. The discrepancies given are estimated from multiple TGA experiments. Note that the atomic silicon content for sample E is not strictly accurate as minimal SiC was still present after TGA, evidenced by the light grey colour of the powder. The margin of error given (0.5) does not take the presence of SiC into account.

From the TGA data it is evident that samples B, C, D, and E all contain silicon. However, the XRD profile for these materials before TGA gave no evidence of silicon content. Recall that silicon has 14 electrons and carbon only 6 electrons per atom. Since the scattered x-ray amplitude from an atom is proportional to the number of electrons it has, XRD should be quite sensitive to the silicon. This is confirmed in Figure 7-5 which shows a disordered carbon sample similar to A ground with about 4 atomic % crystalline silicon. Sample D has a significant quantity of silicon present (~6% atomic) and yet appears to have the crystal structure of a pre-graphitic carbon. It is unlikely that the silicon

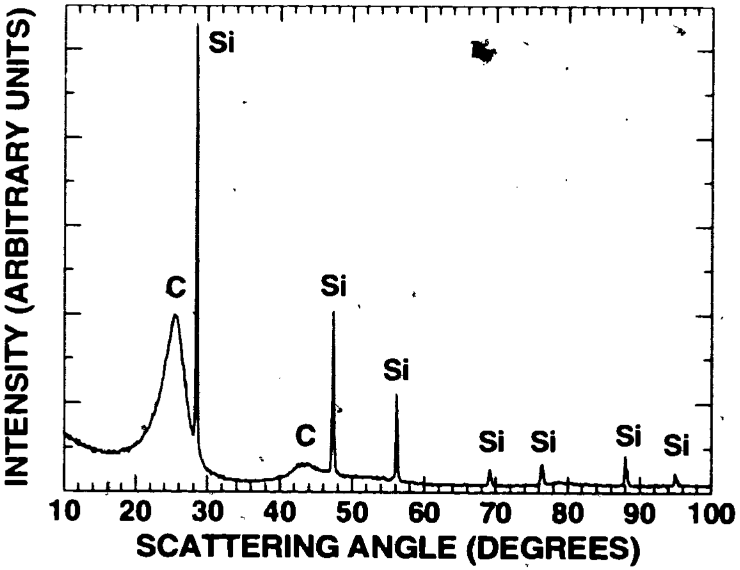

Figure 7-5. XRD profile of a mixture of pre-graphitic carbon (produced in an identical manner as sample A) and approximately 4 atomic % silicon.

in sample D is present in an amorphous phase, since this material was prepared at 950°C (Tiedje, 1994). The XRD refinement analysis shows that neither d_{002} nor d_{100} (Table 7-2; d_{100} is given as 2θ) are significantly different from that of sample A. Thus, the silicon does not affect the structure within the regions of organized carbon. Furthermore, it is extremely unlikely that silicon would form an sp^2 hybrid bond, necessary for substitutional bonding with carbon in the graphite sheets (Harrison, 1989). The presence of silicon does appear to affect the size of the ordered regions, as can be seen by examining L_a and L_c in Table 7-2. Sample E has the largest silicon content, the broadest (002) peak, and hence the smallest L_c. Also, the (100) peak for sample E is very weak. This suggests that the incorporation of silicon forces a decrease in size of the organized regions, as could be expected. This is not the only factor controlling the disorder in the material.

We have observed three principal factors which affect the degree of disorder in our materials. An increase in silicon content appears to increase disorder, as previously

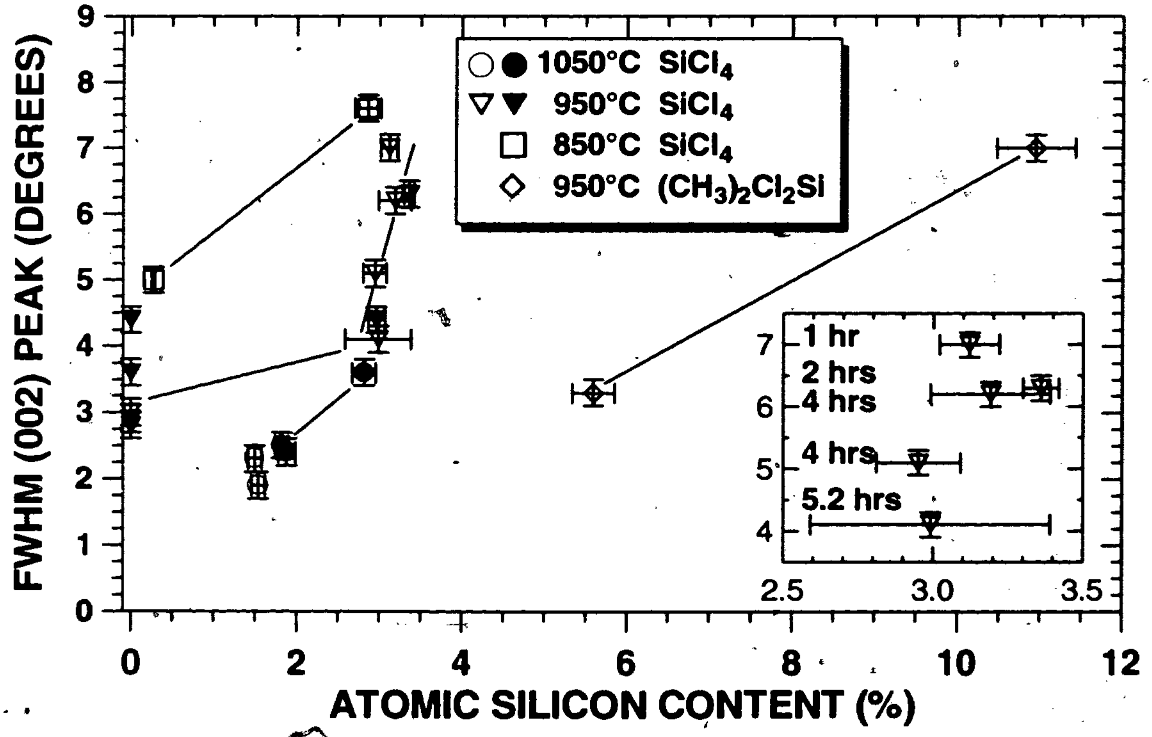

Figure 7-6. FWHM of the (002) Bragg peak vs. atomic percent silicon content for many CVD-I samples. Open and solid symbols respectively represent soft and brittle materials. Lines are only a guide to the eye. The inset shows several soft materials with similar silicon content and different deposition times. A decrease in temperature and deposition time and an increase in silicon content all increase the amount of disorder in the material.

discussed. The temperature and duration of the deposition also affect the degree of disorder in the material. Figure 7-6 shows the full width at half maximum (FWHM) for the (002) Bragg peak versus percent atomic silicon in the sample, as determined by TGA. The main graph shows data for samples deposited for times between 3 and 6 hours. The points have been arranged as 1050°C, 950°C, and 850°C depositions with $SiCl_4$ as the silicon source and as a 950°C deposition with $(CH_3)_2Cl_2Si$ as the silicon source. A higher deposition temperature produces a more ordered material. The inset shows several soft samples which were deposited at 950°C for various times, ranging from 1 hour to 5 hours, showing that a longer deposition time produces more ordered materials. Hollow and filled symbols each respectively represent soft and brittle materials. The brittle materials appear less ordered than the soft. There appears to be a maximum silicon content near 3.5% for samples made with $SiCl_4$, which may have been a limitation of CVD Apparatus I. Samples made with $(CH_3)_2Cl_2Si$ did not have this limitation, although the formation of silicon carbide in sample E suggested that at some maximum silicon content (for a given temperature) silicon carbide forms. FWHM measurements have been adjusted to compensate for peak broadening caused by well holders. A peak may broaden by as much as 0.6° when measured in a 2 mm deep well.

As detailed in Section 5.2, we used XAS to learn more about the local structure around the silicon. To remove surface oxides, samples D and E and crystalline SiC (c-SiC) were briefly washed with HF and rinsed with ethanol. Figure 7-7 shows a comparison of the silicon *L*-edge for c-SiC before and after HF washing. One can see that the surface SiO_2 contributes to the XAS spectra (resonances near 106 eV and 108 eV) and has been removed by HF washing without changing the edge position. Figure 7-8 presents a comparison of the silicon *L*-edge of samples D and E with those of crystalline Si (c-Si), c-SiC, and amorphous SiO_2 (a-SiO_2). The silicon *L*-edge positions we present in Figure 7-8 for c-Si, SiC, and a-SiO_2, are respectively in good agreement with the work presented by van Buuren *et al* (van Buuren, 1993), Waki *et al* (Waki, 1989), and Bauer *et al* (Bauer, 1980). Comparisons to the data presented by these authors show that the silicon in the Si_ZC_{1-Z} materials is bonded unlike Si in c-Si, a-Si, c-SiC, c-SiO_2, or a-SiO_2. Also, it is

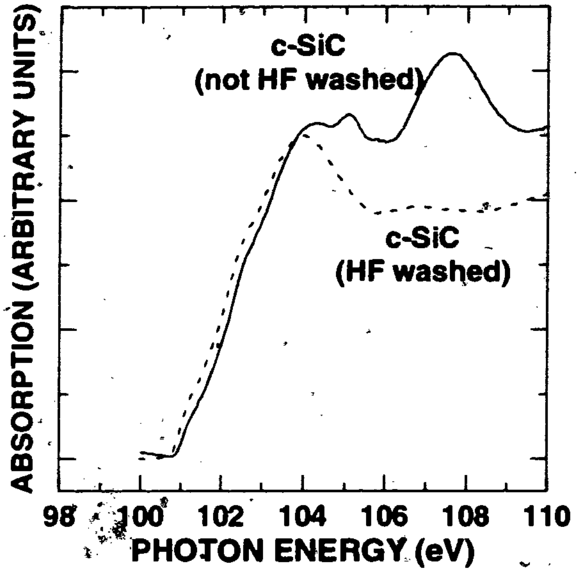

Figure 7-7. XAS profile of the silicon L-edge for c-SiC powder and HF-washed c-SiC powder. The oxide peaks have been removed without changing the edge position.

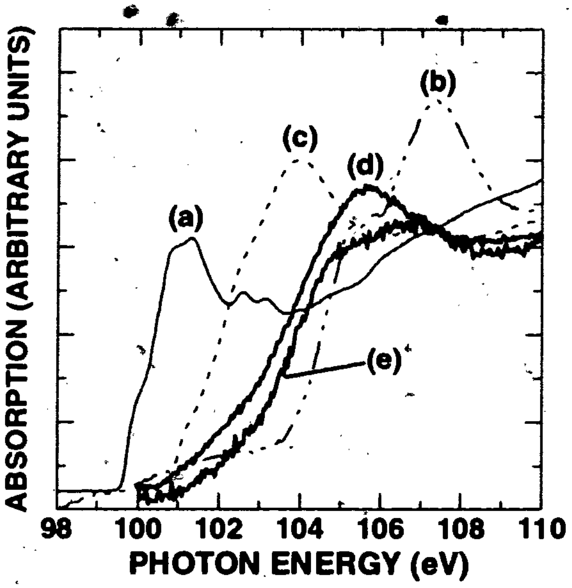

Figure 7-8. XAS profiles of the silicon L-edge for: (a) c-Si, (b) a-SiO_2, (c) c-SiC, and samples (d) D and (e) E. Samples D and E have L-edges between those of a-SiO_2 and c-SiC.

highly unlikely that either a-Si or a-SiC would form at these temperatures. In SiO_2 and SiC, the silicon donates electrons to the atoms of the other element, leading to a tighter binding of the 2p electron core level, finally resulting in a shift of the *L*-edge to higher energy. In SiO_2 each silicon atom has two oxygen atoms to donate electrons to, compared to one carbon per silicon in SiC. Also, oxygen has a larger electro-negativity than carbon and so the *L*-edge shift from silicon to SiO_2 is to a higher energy than for SiC. Figure 7-8 shows that the silicon atoms in the Si_zC_{1-z} materials have donated more electrons to carbon than the silicon atoms in SiC. We believe that it is the larger carbon to silicon atomic ratio in the Si_zC_{1-z} materials (> 8:1) compared to SiC (1:1) which gives this larger edge shift. Comparisons to the *L*-edge studies of various states of SiO by Bauer *et al.* reveal that the silicon atoms in the Si_zC_{1-z} materials are not bonded as SiO (Bauer, 1980). The silicon *L*-edge also suggests it is unlikely that large silicon clusters have formed. The silicon *L*-edge for hydrogen passivated porous silicon is near 100eV, for a silicon structure of order 2nm in size (van Buuren, 1993). Features from such clusters would be easily observed in our spectra.

Later, studies of the silicon *K*-edge confirmed much of the *L*-edge results. The silicon *K*-edge for materials B through D can be seen in Figure 7-9. For comparison, *K*-edge spectra for c-SiC and c-SiO_2 are shown in Figure 7-10. By comparing the *K*-edge profiles in Figure 7-9 to those in Figure 7-10, we conclude that there is Si-Si, Si-C, and Si-O bonding in these materials. The Si-O bonding (near 1847 eV) is believed to be due to surface oxides. The Si-Si bonding feature (near 1839 eV) is thought to support the model for small Si clusters. The features near 1844eV suggest Si-C bonding, although different from the bonding in SiC. Thus, the 'modified' Si-C features show that it is unlikely that silicon carbide clusters exist in samples B, C, or D.

The silicon *K*-edge and *L*-edge for sample D are quite different, whereas there is little difference between these for c-Si, c-SiC, and c-SiO_2. The differences are attributed to the different penetration depths in each measurement and the HF washing of sample D (for the *L*-edge measurement). The *L*-edge and *K*-edge have respective penetration depths of about ~100Å and ~1000Å. Thus, the *L*-edge is a very surface dependent measurement while the *K*-edge measures some of the bulk in the material. If sample D contains small silicon clusters near the surface (i.e. within the measurement penetration depth), it is likely

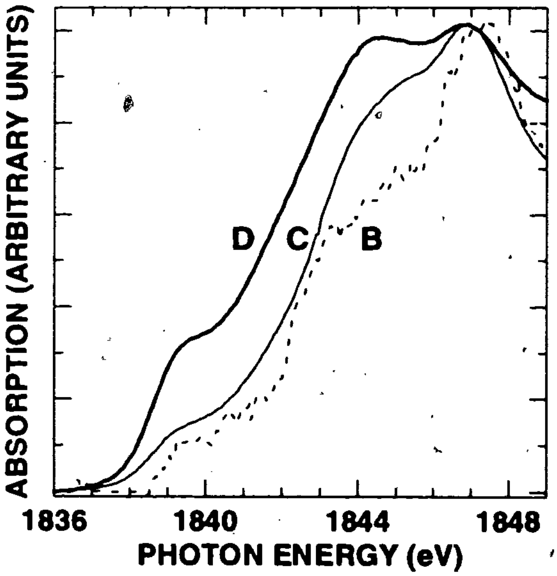

Figure 7-9. XAS profiles (normalized at 1847eV) near the silicon K-edge for samples B, C, and D.

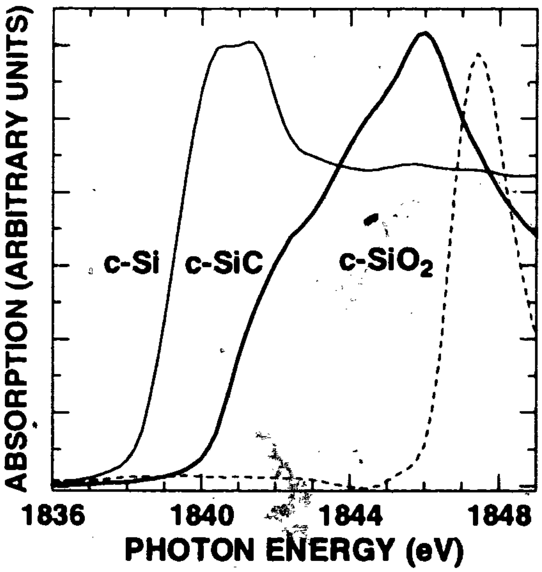

Figure 7-10. XAS profiles (normalized at 1847eV) near the silicon K-edge for c-Si, c-SiC, and c-SiO_2.

that they are at least partially oxidized. The washing with HF(done to remove the surface oxide) probably removed this oxide and thus removed any silicon clusters near the surface. Since washing with HF was not done for the *K*-edge measurement and it measures some of the bulk, it is the more reliable data.

If we have made the nanodispersed structure desired, as the results suggest, then cells made from these materials should show increased reversible capacity over pure carbons. The results from the electrochemical tests are discussed next.

7.1.2 Electrochemical Testing

Figure 7-11 shows the first discharge, charge, and second discharge of a cell made from sample A, the pre-graphitic carbon. The reversible capacity is about 300 mAh/g which is in agreement with previous work on similar samples made near 950°C (Way, 1992). The inset in Figure 7-11 is the differential capacity, dq/dV, plotted versus cell voltage.

To serve as a reference a cell containing crystalline silicon as the only active material was made. Figure 7-12 shows the first two discharges and charge for the cell made from ground silicon. While the capacity of the initial discharge (3600 mAh/g) is in good agreement with that expected for Li-Si alloys (Table 2-1), by the fourth discharge the

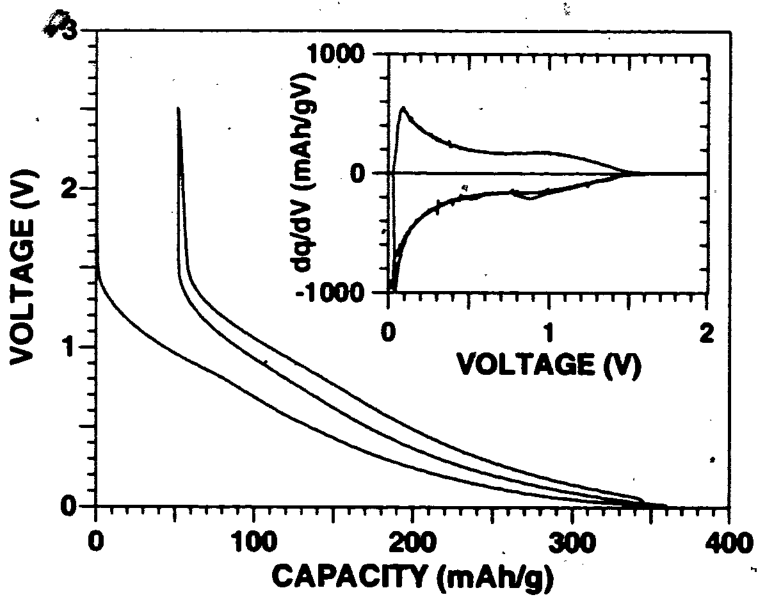

Figure 7-11. The voltage profile for a cell made with sample A. The insert shows the differential capacity versus voltage.

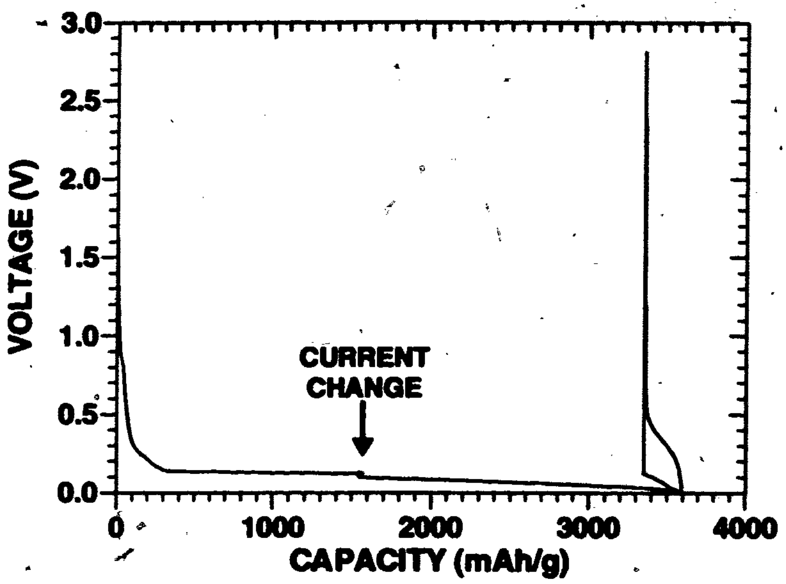

Figure 7-12. The voltage profile for a cell made with ground silicon.

capacity had dropped below 50 mAh/g. This is not surprising, and confirms what was discussed in Section 2.5.

Figure 7-13 shows the first discharge, charge, and second discharge for a cell made from sample B (solid line) compared with results for sample A from Figure 7-11 (dashed curve). There is an increase in reversible capacity to 360 mAh/g. The inset derivative curve shows that most of the capacity increase is between 0.2 and 0.5 volts.

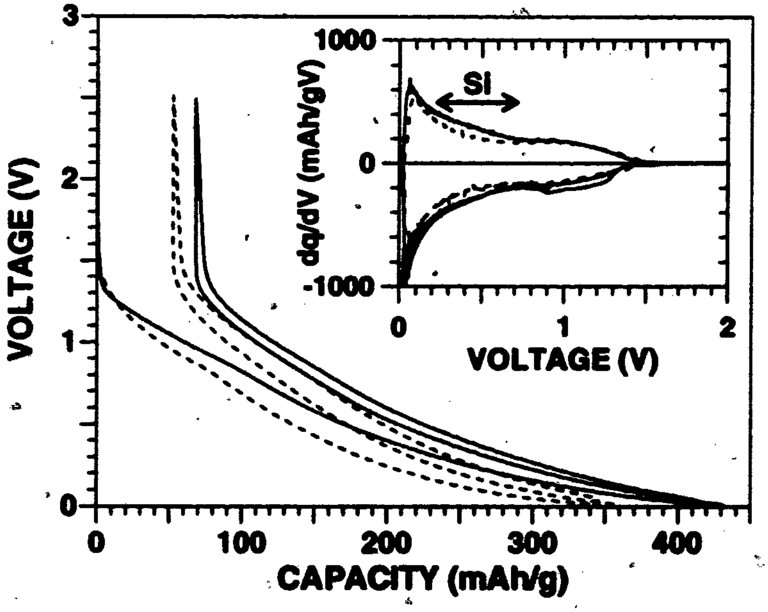

Figure 7-13. The voltage profile for a cell made with sample B. The insert shows the differential capacity versus voltage. The dashed line is the voltage profile for sample A, the CVD carbon.

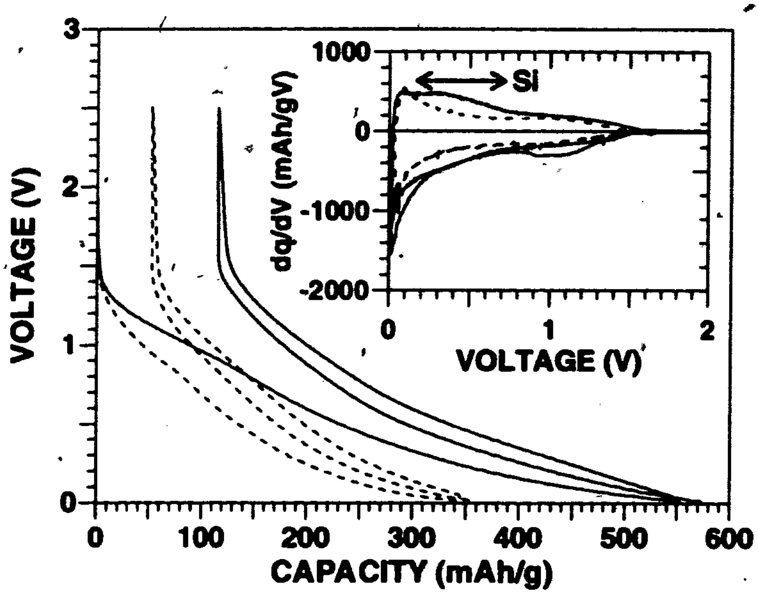

Figure 7-14. The voltage profile for a cell made with sample D. The insert shows the differential capacity versus voltage. The dashed line is the voltage profile for sample A.

Cells made from samples D and E, shown in Figures 7-14 and 15, show a dramatic increase in capacity. The inset shows that most of the additional capacity is located between 0.2 and 0.7 V (i.e. centered near 0.4V).

Figure 7-15. The voltage profile for a cell made with sample E. The insert shows the differential capacity versus voltage. The dashed line is the voltage profile for sample A.

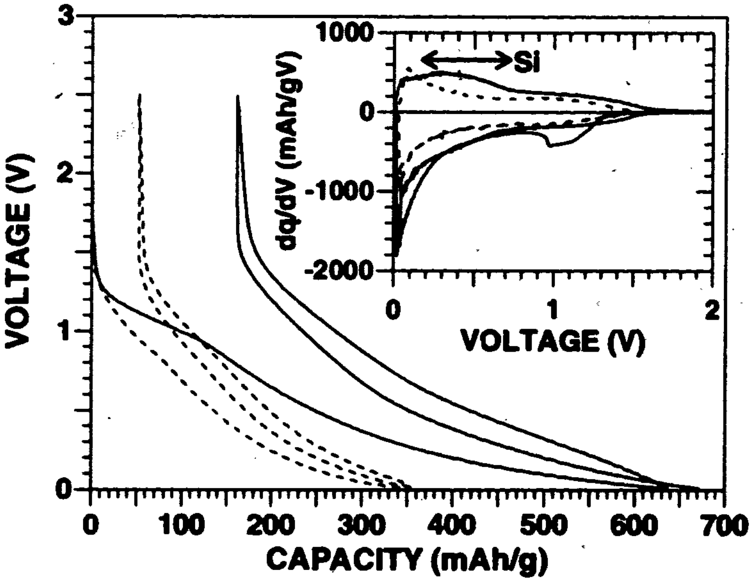

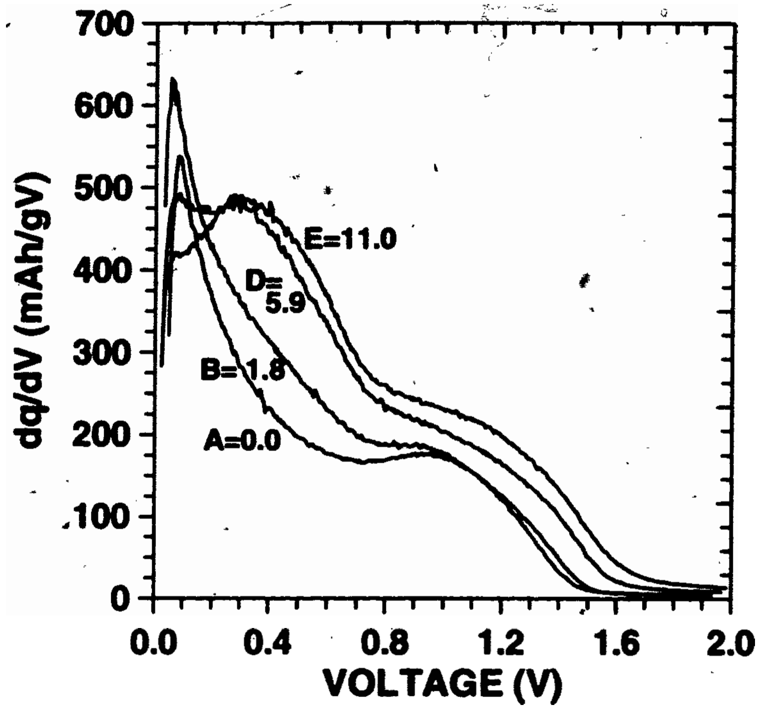

Figure 7-16. The differential capacity versus voltage (charge only) for samples A, B, D, and E. Note the additional capacity at 0.4V. The numbers indicate the atomic % silicon in each sample.

Figure 7-16 shows the differential capacity versus voltage (charge only) for samples A, B, D and E. Clearly, the bulk of the additional capacity is centered near 0.4V, corresponding to about the same voltage as the silicon in the pure silicon cell (see the plateau on the first charge in Figure 7-12).

To provide further evidence that the silicon in samples B through E is not simply distributed as small silicon crystallites, cells were made with cathodes of about 4 atomic % silicon mixed with a sample made in an identical way to sample A. Figure 7-17 shows the

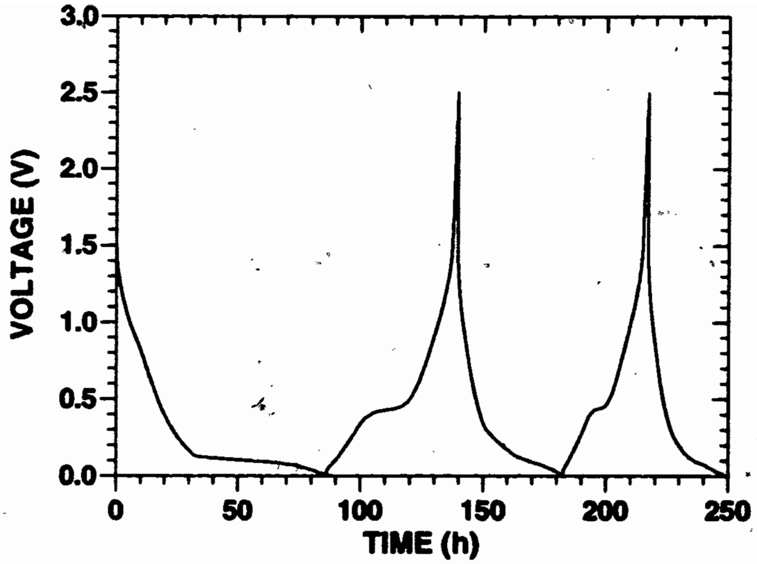

Figure 7-17. The voltage profile for a cell made from 4 atomic % Si mixed with a carbon made in an identical way to sample A.

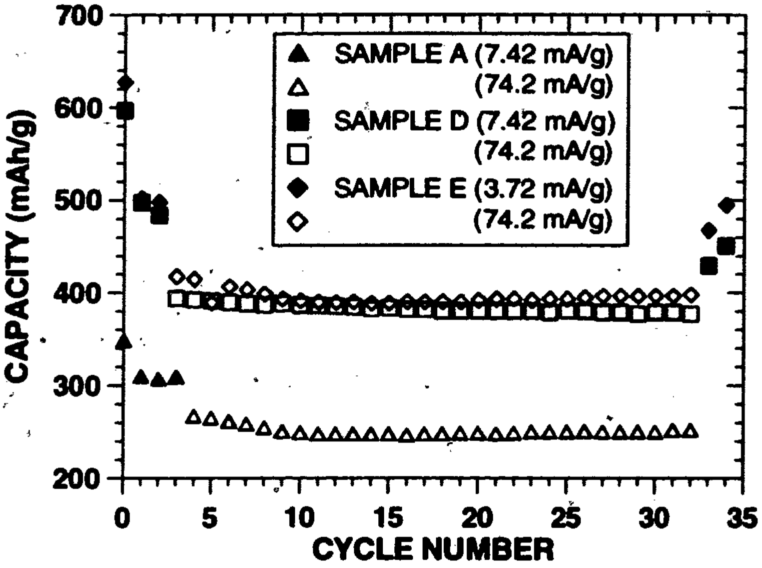

Figure 7-18. The cycling behaviour of cells made from samples A, D, and E is shown. To facilitate testing, the bulk of the cycles were run at high currents.

first three discharges and two charges for this cell where cell voltage is presented as a function of time. The initial discharge capacity is substantially greater than that of sample A (640 mA/g), although by the third discharge the silicon contribution (the plateau around 0.4V on charge) is almost completely gone.

To test the (short term) cycle life of the CVD-I materials, cells of samples A, D, and E were cycled 30 times at currents higher than the first few cycles. Once the cells completed thirty cycles they were returned to their original charge and discharge currents. The discharge capacities as a function of cycle number are compared in Figure 7-18. Very little capacity loss is observed, suggesting both that these materials are promising anodes for Li-ion cells and that the silicon exists as very small silicon clusters and possibly single atoms located in regions of unorganized carbon.

Many CVD-I samples were made and tested. Figure 7-19 shows the reversible specific capacity of most CVD-I samples, plotted versus the atomic percentage of silicon in the samples. Also included in the figure is a line which is a linear fit to the data up to 6 atomic percent silicon. The slope of this line is 35 ± 5 mAh/(g %Si). If each silicon atom in the nanodispersion is capable of reacting with 4 lithium atoms then we expect the capacity to increase with silicon content at a rate of 86 mAh/(g %Si). The observed slope in Figure 7-19 suggests each silicon is alloying with about 1.5 Li atoms. The departure of the data for

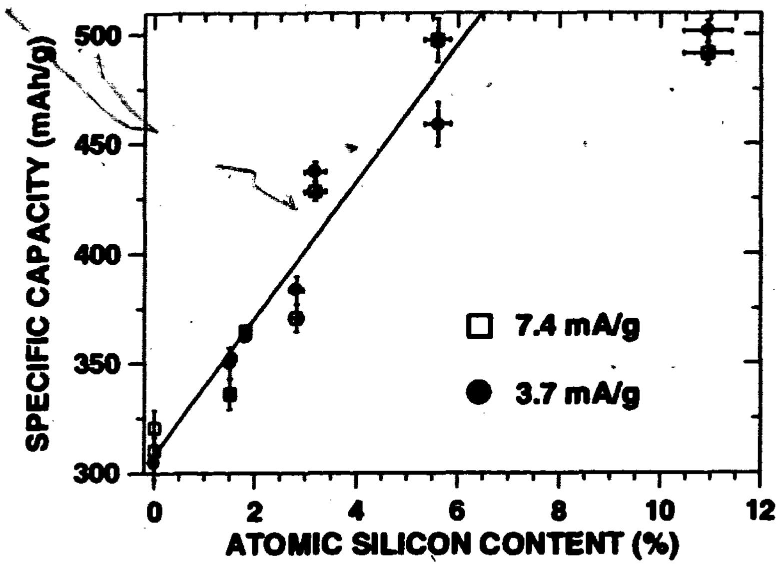

Figure 7-19. The specific capacities of cells made from many CVD-I materials plotted versus the Si content (measured from TGA) and calculated from Eq. 5-5. The line suggests that each silicon atom is alloying with about 1.5 lithium atoms.

sample E (11% Si) from the line may be due to the incorporation of some Si into electrochemically inactive SiC, as evidenced by the XRD profile (Figure 7-2).

7.1.3 Discussion

The XRD profiles and the electrochemical test results suggest that many of the CVD-I materials contain silicon either as very small clusters or single atoms bonded to carbon in a manner different than silicon carbide. The XAS profiles near the silicon *L*-edge support this view. The silicon *K*-edge profiles show that the materials contain silicon atoms which have silicon, carbon and oxygen bonds. We assume that the oxygen bonds are due to surface oxidation. But, the nature of the silicon-carbon bonds, as seen in the *K*-edge, is certainly not consistent with silicon carbide. Much of the data suggests (and none contradicts) that the CVD-I materials are what we have called a disordered (or pregraphitic) carbon containing nanodispersed silicon.

The next step was to attempt preparation of materials using the second CVD apparatus with larger silicon contents but avoiding SiC production. The next section outlines the study of the CVD-II materials.

7.2 THE CVD-II MATERIALS

Having provided strong evidence that disordered carbons containing nanodispersed silicon could be made, the goal with CVD apparatus II was to increase the amount of nanodispersed silicon and, thus, the specific capacity of these materials. As will be presented, these hopes were not realized by with this apparatus. The CVD-II material results are presented in a way which reflects this. From roughly 15 depositions only 4 materials are discussed in detail (see Table 7-4).

Table 7-4. Summary of the CVD-II samples.

Sample Label	Silicon Source	source ratio (Si source : benzene)	atomic Si:C source ratio		Deposition Temperature (°C)
F	$(CH_3)_3ClSi$	2:1	1:6	(4:24)	950
G	$(CH_3)_2Cl_2Si$	2:1	1:5	(4:20)	950
H	$(CH_3)_2Cl_2Si$	4:1	1:3.5	(4:14)	950
I	$(CH_3)_2Cl_2Si$	8:1	1:2.75	(4:11)	950

7.2.1 Sample Reclamation and Characterization

Products are deposited throughout the length of the CVD reactor tube, in various forms. Gases condense on the injection rod, which then drip into the deposition tube, forming small black pellets. Between the injection rod and the hot zone, loosely adhered fine powders are deposited. Samples retrieved from the hot zone of the tube form three principle types, varying in both visual and textural properties; a soft dark-grey porous deposit which could easily be reduced into a powder; a lighter grey brittle porous deposit which crumbled and "crunched" when being reduced to a powder; and a highly reflective film, which was typically well adhered to the quartz insert. In the *warm zone* (located downstream on the edge of the hot zone) a soft light-grey porous deposit texturally similar to the dark-grey hot zone powder was retrieved. The materials from the hot zone were retrieved, without significant contamination by impurities from other regions in the tube, by removal of the tubular insert. Unlike the CVD-I materials there was typically no clear dividing line between the hard and soft powders. Often the powder deposited appeared quite homogenous. Thus, for the CVD-II materials, no distinction is made between the types of powders. The samples obtained were ground into a fine powder.

Of all the CVD-II samples analyzed Table 7-4 summarizes the 4 which are presented here as a representative set. The Si:C source vapour ratio is calculated from the estimated vapour pressures of the source gases, as determined from the temperature of the source bottles. The vapour pressure vs. temperature curves were obtained from the CRC Handbook of Chemistry and Physics (Weast, 1986). The ratio of the atomic silicon to carbon content in the source vapour stream was calculated from the stoichiometry of the source gases and the source vapour ratio and used as a metric.

XRD data were collected and analyzed for all of the CVD-II samples. Figure 7-20 shows the XRD data collected for samples F, G, H and I. Samples F and G, with the smallest Si:C source ratios, both appear to be typical pregraphitic carbons. This is expected considering the results of the CVD-I materials. Samples H and I show evidence for silicon carbide. This might be due to the large percentage of silicon in the source vapour stream, and the different deposition conditions between CVD apparatus I and II.

TGA was performed for most of the CVD-II samples to determine the silicon content. The product remaining at the end of the TGA experiment was either a white powder, consistent with the formation of SiO_2, or a grey powder, consistent with the formation of a mixture of SiO_2 and SiC. As with the CVD-I materials, the white powders were confirmed as SiO_2 by XRD.

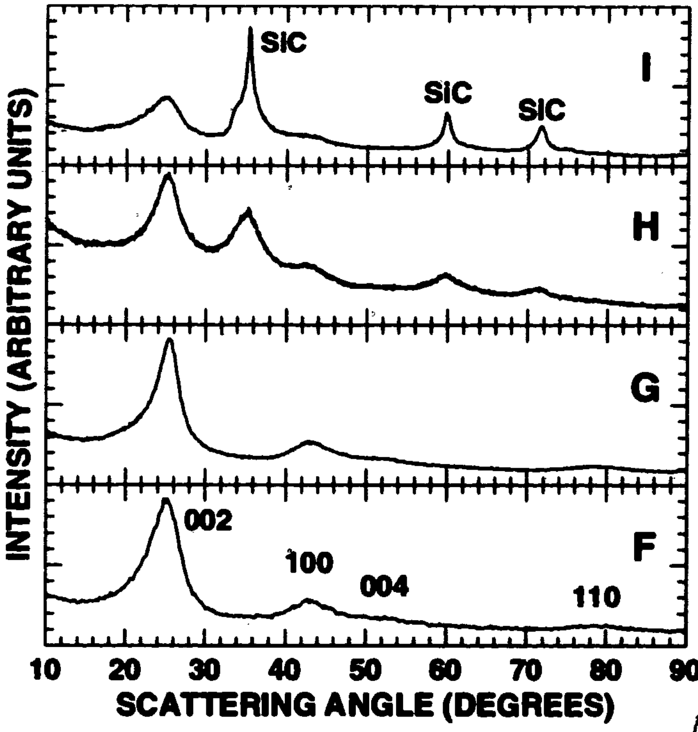

Figure 7-20. Powder XRD patterns for samples F through I. Sample F is indexed as a pregraphitic carbon. Samples H and I contain peaks identified as SiC.

The silicon atomic concentration for samples which turned 'pure' white upon TGA in air was calculated using Equation 5-5. However, the silicon content for samples which became grey upon TGA in air could not be calculated in this way as there was an unknown amount of carbon remaining as silicon carbide. Rather than undertake a different method to determine the stoichiometry of these materials, we chose to use the estimated silicon to carbon ratio in the source vapours as a metric of the carbon ratio in the product. Figure 7-21 shows the atomic percent silicon (from Equation 5-5) for samples which turned white upon TGA plotted vs. the silicon to carbon ratio in the sources. Within this range, there appears to be a linear relationship. Errors were estimated from measured drifts in the source bottle temperatures and from multiple TGA experiments. For the CVD-II materials, results are described as correlated to the Si:C ratio in the sources, rather than the atomic silicon content in the product.

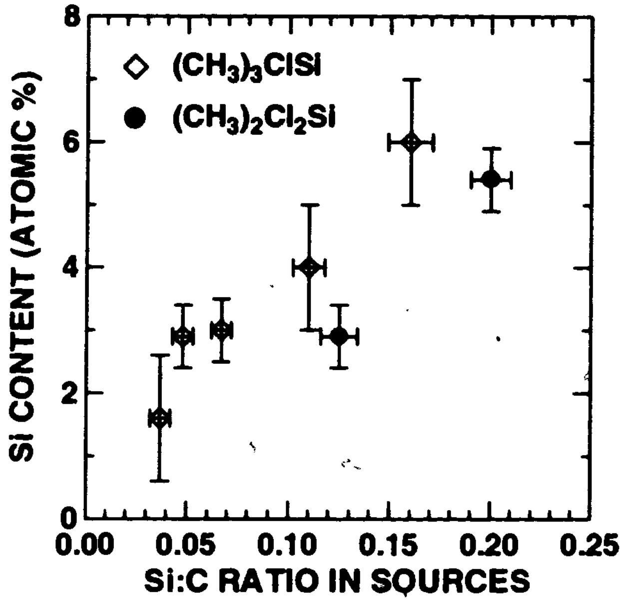

Figure 7-21. The silicon atomic % in the product plotted vs. the ratio of silicon to carbon in the sources.

The silicon *K*-edges for materials G, H, and I are shown in Figure 7-22. Samples G and H appear very similar to the CVD-I materials shown in Figure 7-9. However, the XRD profile shows the sample H contains some SiC. The XRD profile for

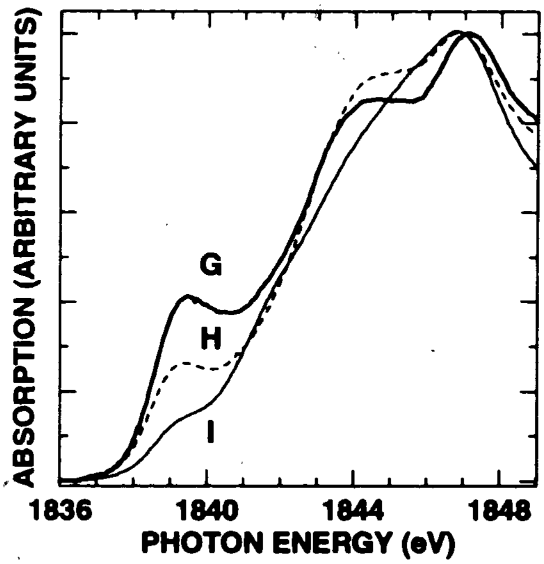

Figure 7-22. The silicon K-edges for samples G, H, and I.

sample I shows that it contains the most SiC of the materials in Figure 7-22 and has a very different *K*-edge. Sample I shows the least silicon-silicon bonding. This will be referred to again later.

7.2.2 Electrochemical Testing

The electrochemical behaviour of these samples are similar to the CVD-I materials, although the observed capacities were not as large. Figures 7-23 through 7-26 show the

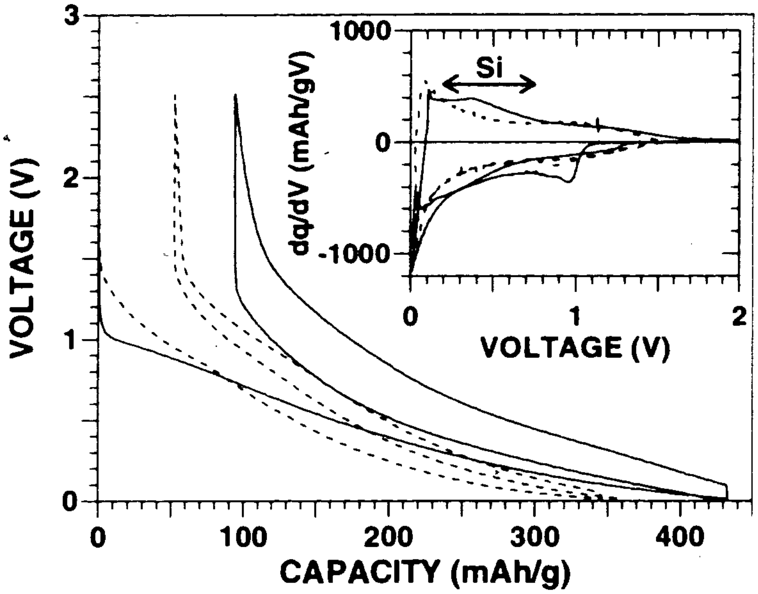

Figure 7-23. The voltage profile for a cell made with sample F. The inset shows the differential capacity versus voltage. The dashed line is the voltage profile for sample A.

Figure 7-24. The voltage profile for a cell made with sample G. The inset shows the differential capacity versus voltage. The dashed line is the voltage profile for sample A.

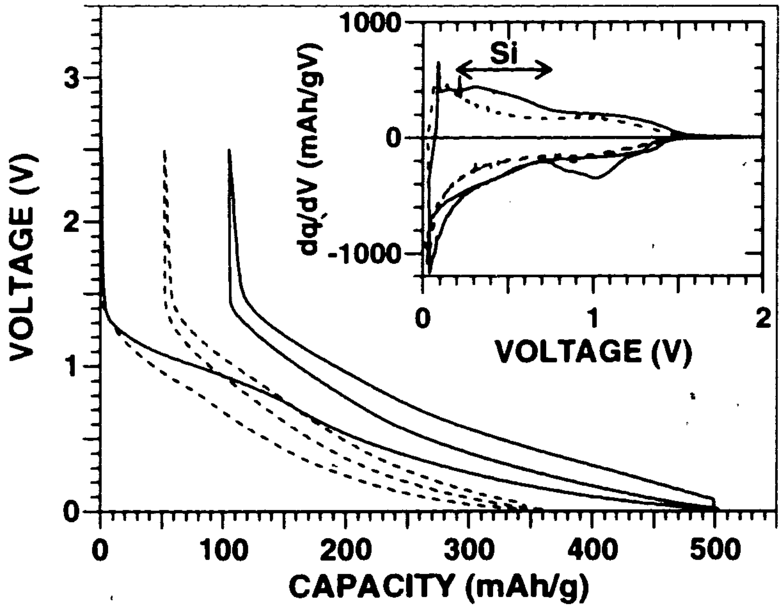

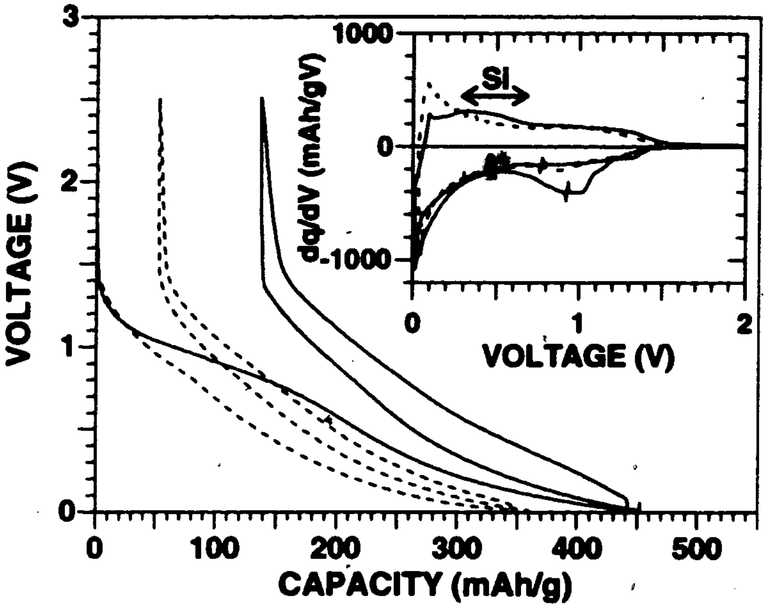

Figure 7-25. The voltage profile for a cell made with sample H. The inset shows the differential capacity versus voltage. The dashed line is the voltage profile for sample A.

first discharge, charge, and second discharge voltage profiles for samples F, G, H, and I. In each figure the differential capacity plot in included as an insert. As with the CVD-I materials the increased capacity can be observed centered near 0.4V on charge.

Figure 7-27 shows the reversible capacity plotted versus the source vapour Si:C ratio. The capacities are, where possible, averages of multiple cells. Errors in capacities have been estimated from the capacities of multiple cells. The decrease in capacity for samples H and I can be attributed to the formation of silicon carbide, evident in the XRD profiles

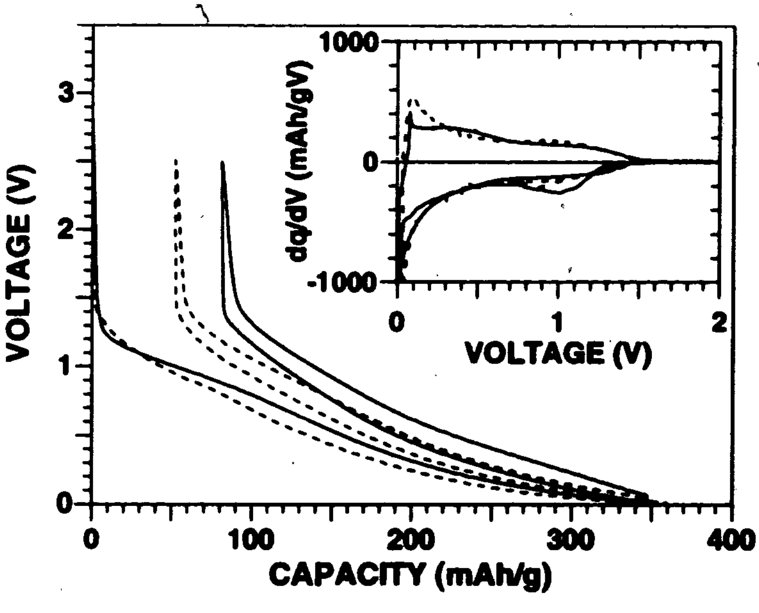

Figure 7-26. The voltage profile for a cell made with sample I. The inset shows the differential capacity versus voltage. The dashed line is the voltage profile for sample A.

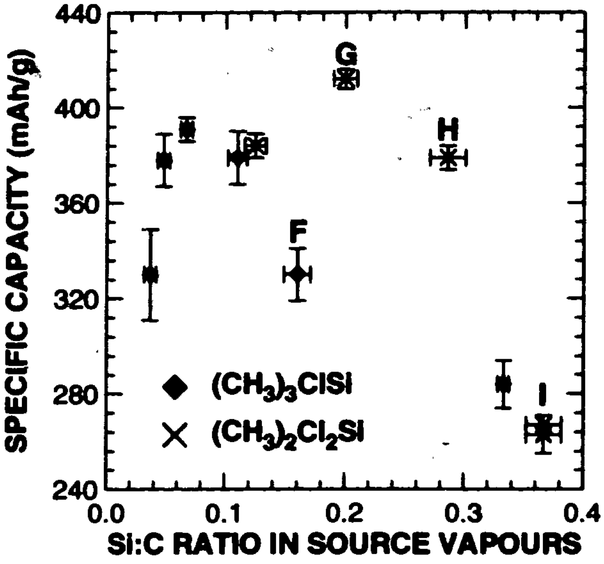

Figure 7-27. The specific capacities of many CVD-II samples versus the ratio of Si to C in the source vapours. The decrease in capacity at higher ratios is believed to be due to the production of SiC. Samples F through I are identified.

(Figure 7-21). Sample F shows a smaller capacity than other samples made using TMCS at lower Si:C ratios. However, the XRD profile for sample F shows no evidence for silicon carbide. The resulting product of sample F after TGA in air was a grey powder. Thus, it appears that much of the silicon in sample F must exist as very small silicon carbide clusters. Instead of making only nanodispersed silicon, sample F likely contains both nanodispersed silicon and nanodispersed silicon carbide.

7.2.3 Discussion

Figure 7-27 provides a concise summary of the results of the CVD-II materials. Much of the silicon in many CVD-II materials is bonded as silicon carbide, and thus not accessible for lithium bonding. The *K*-edge for samples G, H, and I (Figure 7-22) show that the materials with more evidence for silicon-silicon bonding also have higher capacities. Also, the XRD profiles (Figure 7-20) show that the samples with lower capacities also contain more SiC. There is an apparent correlation between the amount of silicon-silicon bonding and the amount of SiC in these materials. More SiC means that there is less silicon-silicon bonding.

These results appear to confirm the suspicion that the maximum nanodispersed silicon content attainable before SiC formation appears between 6 and 11 atomic % silicon.

However, none of the materials made neither met nor exceeded the specific capacity of CVD-I samples D or E. We believe that the differences between the CVD-I and -II apparatus may be the reason for this.

The kinetics of the vapours inside the reactor tube were significantly changed by the use of the injector rod. The gases are injected at 48°C into the hot zone which is at 950°C resulting in a rapid expansion of the gases (a volume increase of about 400% upon leaving the injection rod).

Materials with higher concentrations of nanodispersed silicon and thus higher capacities were not made with CVD apparatus II. It was at this time that we decided to pursue a different path towards making carbonaceous materials containing silicon. During the same time period that the last CVD-I materials were being made and the second CVD apparatus was being constructed, we experimented with the pyrolysis of siloxane polymers. The next chapter details the results of this preliminary work and the extensive polymer project.

CHAPTER 8

THE SILICON OXYCARBIDE MATERIALS

This chapter begins with a brief overview of the preliminary work done by the pyrolysis of two commercially available polysiloxanes. Section 8.2 presents the results of the main project, which focused on investigating the effect of stoichiometry on material properties. The results of the 'side projects,' which studied the polymer decomposition processes and the effect of HF washing one sample, are presented and discussed in Section 8.3.

8.1 THE PRELIMINARY WORK

As discussed in Chapter 4, two polymers, polymethylphenylsiloxane (PMPS) and polyphenylsesquisiloxane (PPSS), were pyrolysed as received. Figure 8-1 shows the

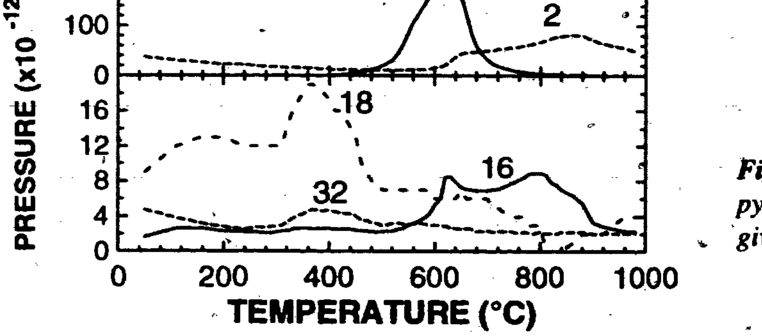

Figure 8-1. TGA/RGA results for the pyrolysis of PPSS. Mass numbers are given beside the corresponding data.

TGA/RGA results for the pyrolysis of PPSS. The small mass loss near 300°C is due primarily to the evolution of water (mass 18). Above 500°C, the polymer rapidly decomposes and benzene (mass 78) is observed as the predominant gaseous species. The peaks for masses 16 and 2 are identified as methane and hydrogen, respectively. These results suggest that the decomposition involves the loss of some of the phenyl rings, followed by the partial fusion of the phenyl rings which remain, coupled with CH_4 and H_2 loss. Oxygen-containing gas species in the decomposition stream are a minor component of the decomposition. The stoichiometry of the pyrolysis product can be estimated by assuming that the mass loss is entirely due to the elimination of benzene and hydrogen as follows:

$$C_6H_5SiO_{1.5} \Rightarrow xC_6H_6 + C_{6(1-x)}SiO_{1.5}H_y + ((5-6x-y)/2)\,H_2\,.$$

Assuming that y=0, we can used the ratios of the initial and final masses to calculate the value of x. The final mass is 77% of the initial, giving x=0.34 and an appropriate final stoichiometry of $C_{3.9}SiO_{1.5}H_y$ with y near zero. Thus, about 1/3 of the phenyl rings were eliminated during pyrolysis. After a more comprehensive study of polysiloxane decomposition, we developed a more basic and accurate method to estimate the final stoichiometry of these materials (Section 8.3.1). The above method is shown here because it was used at the time the preliminary work was done.

Similar studies of the pyrolysis of PMPS were also made. The TGA/RGA analysis showed again that benzene was primarily responsible for the weight loss. Unfortunately, we could not use the ratio of the final mass to the initial mass to help determine the

Table 8-1. List of the preliminary samples made. Their estimated stoichiometries and the method or methods used in the estimation are also included.

Sample	Precursor	Pyro. Temp. (°C)	weight % H (by CHN)	weight % C (by CHN)	Estimated Stoichiometry	Estimation Method
P1	PMPS	900	1.0	39	$C_{2.9}SiOH$	RGA, TGA, CHN
P2	PMPS	1000	.6	40	$C_{2.9}SiOH_{0.6}$	RGA, TGA, CHN
P3	PMPS	1100	.5	N/A	$C_{2.9}SiOH_{0.5}$	RGA, TGA, CHN
P4	PPSS	900	N/A	N/A	$C_{3.9}SiO_{1.5}H_{0.5}$	RGA, TGA
P5	PPSS	1000	N/A	N/A	$C_{3.9}SiO_{1.5}H_{0.5}$	RGA, TGA
P6	PPSS	1100	N/A	N/A	$C_{3.9}SiO_{1.5}H_{0.5}$	RGA, TGA
P7	sample 3	1300	N/A	N/A	N/A	--
P8	sample 3	1500	N/A	N/A	$C_{1.9}Si$	--

stoichiometry because some of the liquid evaporates before it decomposes. We relied on the chemical analysis techniques described in the experimental section to determine the stoichiometry of these samples. During this preliminary work, the RGA was not interfaced to a computer and for reasons specific to the apparatus only 6 masses could be observed and recorded manually. During the main polymer project, however, a more conclusive study of the polymer decomposition was possible and is presented in Section 8.3.1.

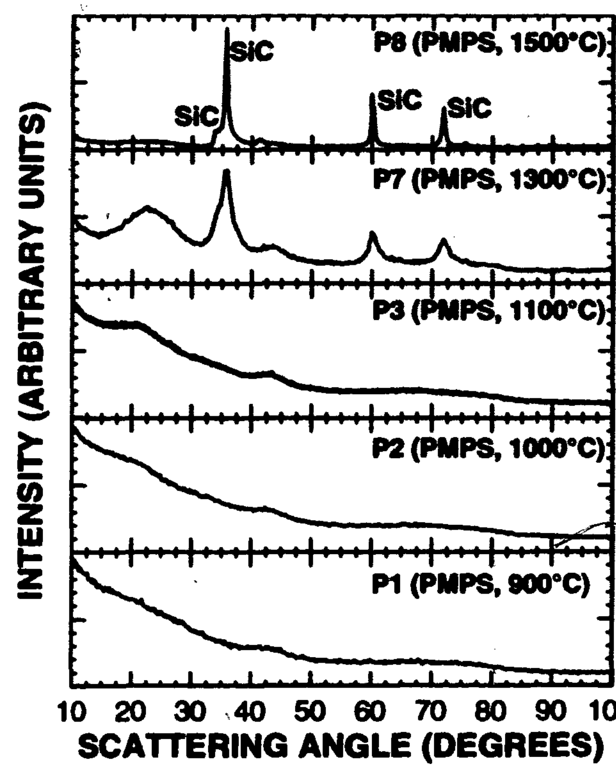

Figure 8-2. XRD profiles of samples P1, P2, P3, P7, and P8 showing the effect of pyrolysis temperature.

A variety of samples was made in the tube furnace setup. The samples and their stoichiometries are given in Table 8-1. All of these samples were black in colour. Samples P7 and P8 were made by further heating sample P3 to 1300 and 1500°C in the Centorr furnace.

Figure 8-2 shows the XRD profiles for materials made by heating PMPS to 900, 1000, 1100, 1300, and 1500°C (samples P1, P2, P3, P7, and P8). Samples P1 to P3 are amorphous while samples P7 and P8 show evidence for SiC as well as broad carbon (002) and (100) peaks near 24° and 43°. In the preparation of sample P8, 1g of sample P3 was pyrolysed at 1500°C and 0.63g of product was obtained. If all the oxygen in the sample is evolved as CO then we predict a final mass of 0.64g based on the estimated stoichiometry of sample P3. The XRD profile for sample P8 shows no evidence for oxygen-containing species and that the silicon is bonded as SiC.

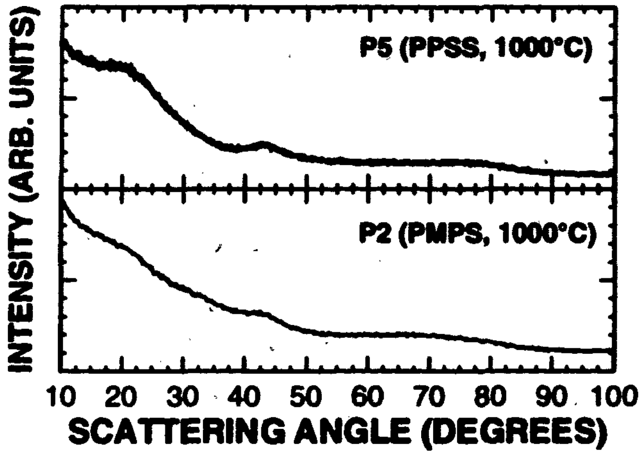

Figure 8-3. XRD profiles of samples P2 and P5.

Figure 8-3 compares the powder XRD patterns of samples P2 and P5, made from PMPS and PPSS respectively at the same temperature. Both show similar amorphous XRD profiles, even though sample P5 contains more carbon per silicon. Because of their structure and composition, these materials are commonly known as *silicon oxycarbide glasses* (silicon oxycarbide is sometimes abbreviated as *Si-O-C*).

Figure 8-4 compares the voltage profiles for lithium test cells made from samples P2 and P5. The cells were cycled using a constant current of 14.8 mA/g. The profiles are very similar, although sample P5 gives a reversible capacity near 600mAh/g, whereas sample P2 gives about 500 mAh/g. The irreversible capacities (the difference between the first discharge and charge) are about 300 mAh/g for sample P2 and about 350 mAh/g for sample P5.

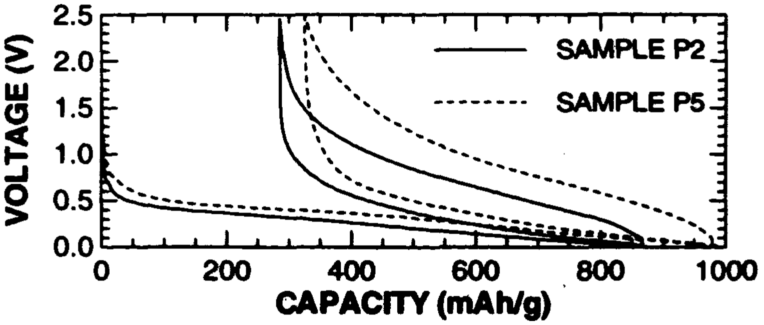

Figure 8-4. Voltage profiles for cells of samples P2 and P5.

Figure 8-5 shows the effect of heat treatment temperature on the electrochemical behaviour of pyrolysed PMPS samples by comparing the voltage profiles of test cells prepared from samples P1, P2, P3, P7 and P8. These cells were also cycled using a constant current of 14.8 mA/g. The cells show irreversible capacities of about 300 mAh/g which is slightly reduced by heating from 900 to 1100°C and then increases to about 400 mAh/g for sample P8. The reversible capacities start around 550 mAh/g and increase slightly from 900 (P1) to 1000°C (P2). The capacities then dramatically decrease at 1300 (P7) and 1500°C (P8) due to the formation of SiC.

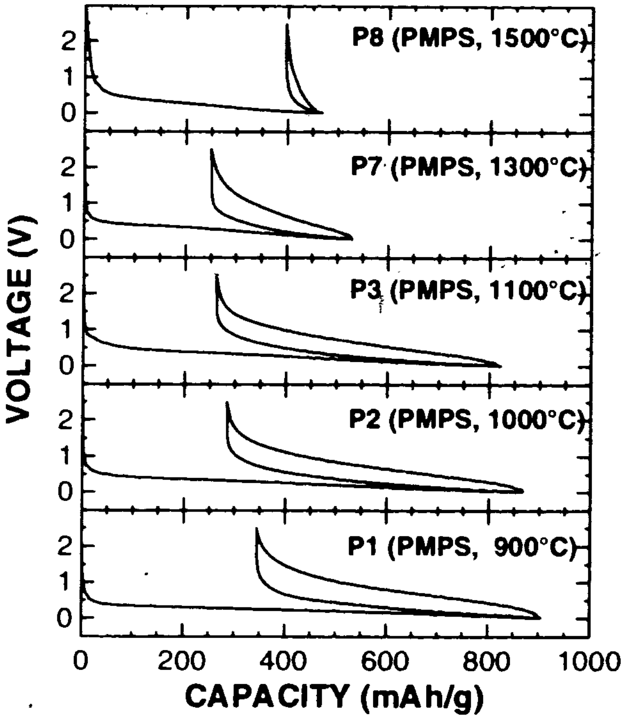

Figure 8-5. Voltage profiles of samples P1, P2, P3, P7, and P8 showing the effect of pyrolysis temperature.

After the first few cycles (at 14.8 mA/g) the cell containing sample P3 was cycled using higher currents (74 mA/g for both charge and discharge) to determine its long term reversibility. Figure 8-6 shows the cell capacity plotted versus cycle number for this cell. There can be no doubt that lithium insertion in this material is reversible. The behaviour of samples P1 and P2 under long-term testing is identical to

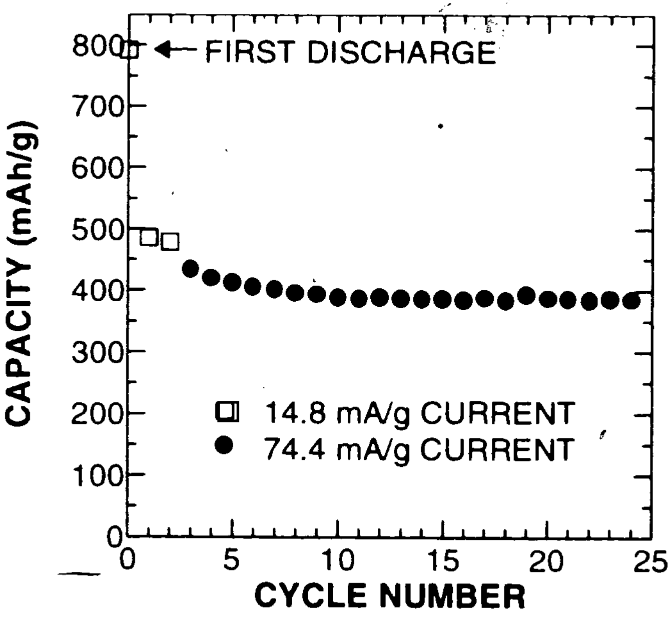

Figure 8-6. Capacity versus cycle number for the cell of sample P3.

sample P3.

At the time, these samples represented materials with the largest reversible capacities (as high as ~600 mAh/g) known for any carbonaceous material heated to above 1000°C. The reaction was reversible over at least 25 cycles. Although these materials exhibited large irreversible capacities and hysteresis, they warranted further investigation.

One possible route to follow was to attempt an understanding of where the lithium resides in these materials by using modeling techniques for glassy structures like reverse Monte Carlo structure determinations (McGreevy, 1993). Another route was to prepare and test a large number of samples over a wide range of stoichiometries. This would lend insight into the possible roles of the carbon, silicon, and oxygen in these materials as well as determine what reversible and irreversible capacities were attainable. We chose the latter path, and the results of this project are presented in the following section.

8.2 THE MAIN SILICON OXYCARBIDE PROJECT

As was detailed in Chapter 4, numerous precursors were pyrolysed to make ceramics of various stoichiometries. From the results of the preliminary work (Section 8.1) we chose the maximum pyrolysis temperature to be 1000°C for the main project (some materials in related studies were heated as high as 1100°C). We also experimented with different ramp rates (1, 5, 45 °C/min) to this maximum. We observed little difference

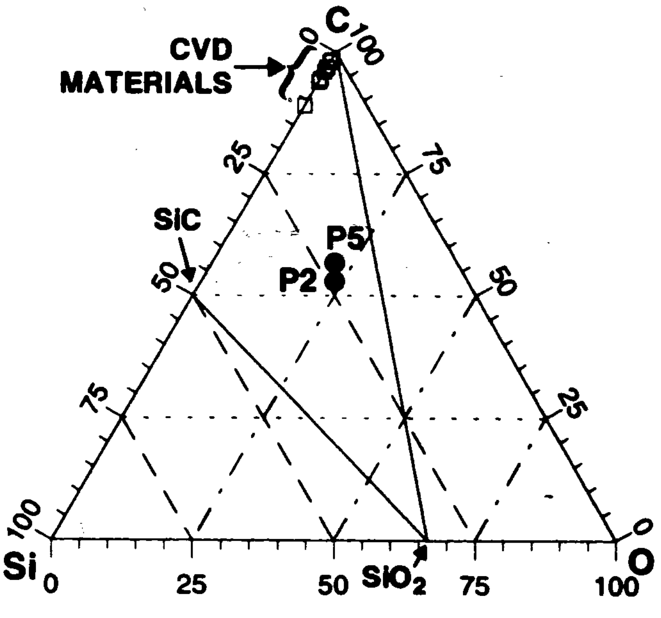

Figure 8-7. Ternary stoichiometric map showing previous CVD and Si-O-C materials represented respectively by hollow squares and filled circles.

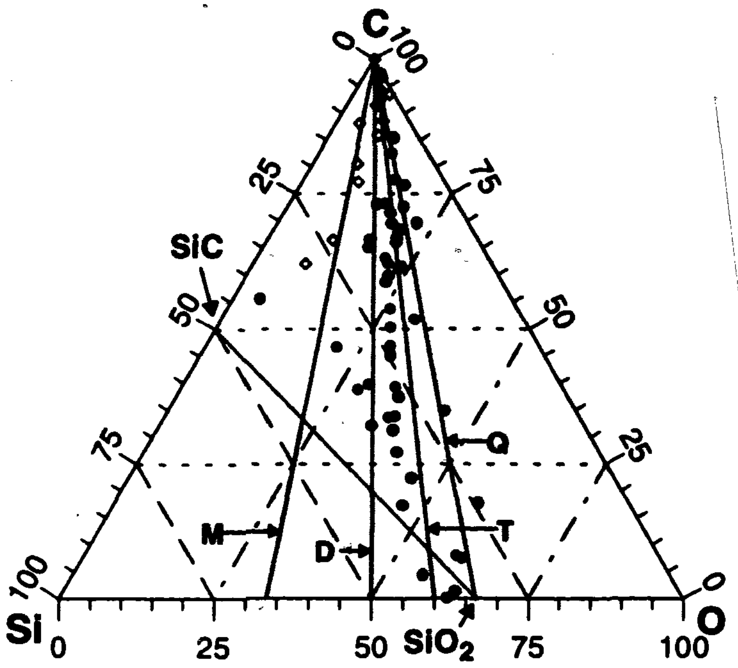

Figure 8-8. The ternary map of the stoichiometries for all samples made in collaboration with Dr. Zank. The filled circles represent the Si-O-C materials made. The hollow diamonds represent the product of pitch blend pyrolysis and will be discussed in Chapter 9.

between samples made from the same precursor at various ramp rates and chose 5°C/min to be the ramp rate for the rest of the project. The majority of the materials discussed were made at this ramp rate.

The results are presented as they correlate to the stoichiometry of the final materials. A Gibbs triangle (or ternary diagram) is used to map the atomic percentages of carbon, silicon, and oxygen in the final ceramic. Figure 8-7 shows the Gibbs triangle with the preliminary ceramics (PPSS and PMPS heated to 1000°C) and the CVD materials shown. We are primarily interested in a confined range of stoichiometries defined by the lines connecting C, SiC, and SiO_2 and so the regions of the ternary map outside this range have been shaded grey.

Figure 8-8 shows the Gibbs triangle with all of the samples made in collaboration with Dr. Zank. Note that the stoichiometries as determined by elemental analysis rarely closed on 100%. The oxygen content was adjusted such that the C, Si, and O percentages would add to 100%. The discrepancies associated with these stoichiometries is estimated to be ±3%. The samples represented with open diamonds were made by the pyrolysis of polysilane and pitch-polysilane blends and will be discussed in Chapter 9. Included on this graph are several lines along which the silicon to oxygen ratio remains constant. The *M*, *D*, *T*, and *Q* lines respectively correspond to silicon bonding to one, two, three, and four oxygen atoms (alternately, silicon:oxygen ratios of 2, 1, 2/3 and 1/2). Of particular interest are materials which lie between the D and T lines which will be presented in Section 8.2.2. The next section presents the results from 5 materials as an overview.

Table 8-2 summarizes the chemical composition and test cell properties of all the silicon oxycarbides made. Figure 8-9 shows a subset of the samples presented in Figure 8-8 with sample numbers attached. All the samples are not shown here for reasons of clarity. The samples discussed in Sections 8.2.2 and 8.2.3 are identified in Figure 8-9.

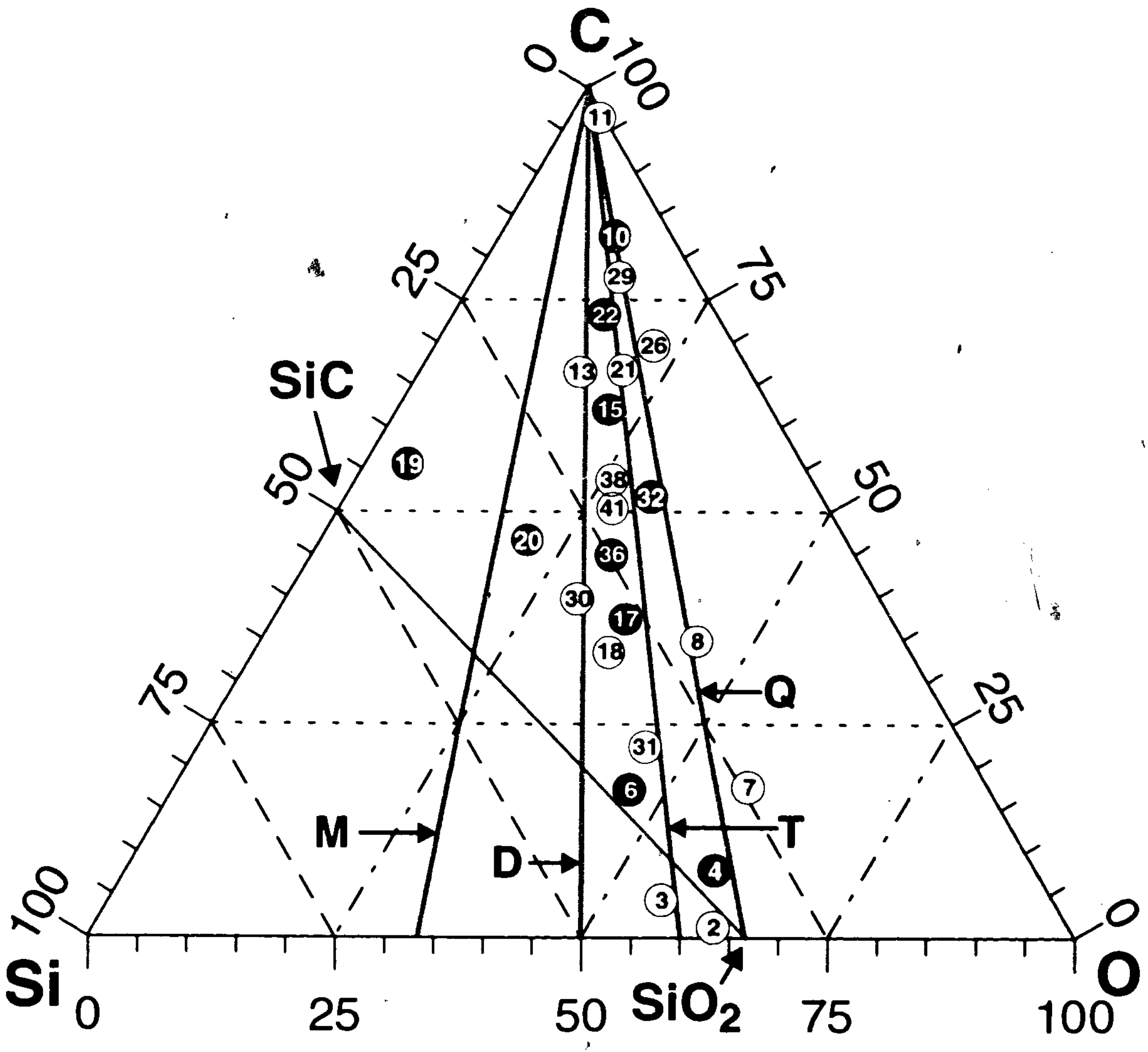

Figure 8-9. Ternary map showing the sample numbers. Results for samples marked with grey or black circles are respectively discussed in detail in Sections 8.2.2 and 8.2.3.

Table 8-2. Stoichiometry and test cell properties of Si-O-C samples.

Sample	Yield (%)	C (Atomic %)	Si (Atomic %)	O (Atomic %)	Rev. Cap. (mAh/g)	Irr. Cap. (mAh/g)	Average Charge Voltage (V)	Average Discharge Voltage (V)
1	98	0.00	37.87	62.13	22	25	0.70	0.39
2	98	1.18	35.96	62.86	10	25	0.74	0.36
3	94	4.29	39.67	56.04	13	32	0.80	0.40
4*	89	7.84	32.50	59.67	2	24	0.88	0.48
5	70	7.48	31.75	60.76	13	30		
6**	72	17.24	36.51	46.25	194	478	0.86	0.14
7	92	17.62	24.29	58.10	344	419	1.25	0.12
8	70	34.73	21.05	44.23	621	348	1.13	0.33
9	54	76.66	6.75	16.59	550	400	1.18	0.31
10*	51	82.48	5.86	11.66	400	250	0.76	0.27
11	46	96.42	0.52	3.05	320	130	0.66	0.32
12	52	97.24	0.25	2.51	310	120	0.67	0.33
13	67	66.42	17.26	16.33	561	324	0.96	0.36
14	71	61.58	14.67	23.75	770	378	1	0.34
15**	54	62.02	16.49	21.49	680	340	0.89	0.33
16	53	71.37	11.53	17.11	553	337	0.95	0.34
17**	58	37.31	27.08	35.61	728	471	1.1	0.26
18	79	33.47	30.61	35.92	751	580	1.03	0.22
19*	56	55.53	40.09	4.38	14	16	0.99	0.44
20*	64	46.61	32.40	20.98	305	124	1.07	0.49
21	73	66.69	12.80	20.52	612	357	0.96	0.36
22**	66	73.15	11.50	15.35	630	306	0.87	0.33
23	71	59.86	17.55	22.59	638	306	0.89	0.32
24	53	31.13	30.99	37.88	292	207	0.73	0.27
25	75	61.17	15.26	23.57	641	339	1.09	0.42
26	65	69.55	8.31	22.14	160	120	0.71	0.34
27	60	85.29	4.15	10.56	450	230	1.05	
28	63	72.53	8.94	18.53	420	220	1.08	0.33
29	60	77.65	7.73	14.61	404	216	1	0.34
30	55	39.70	30.71	29.59	684	344	1.1	0.26
31	85	22.34	32.44	45.22	352	759	0.85	0.16
32*	71	51.70	17.37	30.93	701	351	1.08	0.33
33	67	72.99	13.04	13.96	663	320	0.89	0.32
34	76	46.79	23.69	29.52	838	323	1.07	0.31
35	86	45.09	24.57	30.34	920	308	1.05	0.32
36**	83	44.87	24.74	30.39	890	361	1.05	0.29
37	67	39.08	26.71	34.21	758	400	1.12	0.25
38	79	53.71	20.29	26.01	800	315	1.02	0.32
39	76	58.59	18.54	22.87	790	300	0.96	0.32
40	77	63.09	16.49	20.41	740	295	0.98	0.33
41	85	50.31	21.93	27.76	660	450	1.13	0.25
42	55	65.04	18.10	16.86	600	260	0.96	0.34
43	47	69.48	12.31	18.21	620	270	0.98	0.32

* X-ray diffraction patterns and voltage profiles are plotted in Figures 8-10 and 8-11.

** X-ray diffraction patterns and voltage profiles are plotted in Figures 8-12 and 8-14.

8.2.1 An Overview of the Materials

The materials presented in this section are meant to represent the various regions of the stoichiometric map (accessed with polysiloxane precursors). The samples to be discussed in this section (19, 20, 10, 32, and 4) are identified in Figure 8-9. Results for a series of materials located between the D and T lines are presented in Section 8.2.3 and are also identified on this graph.

Figure 8-10 shows the XRD profiles for samples 19, 20, 10, 32, and 4. A small triangle which shows the approximate position of the sample in the stoichiometric map is included beside each graph. The XRD profile for sample 10 is similar to that of a disordered carbon. The 25° feature shows very little stacking of layers in a parallel fashion. The 43° peak arises from the (100) spacing in a graphene sheet. This shows that there is a significant amount of carbon present in small sp^2 bonded layers which are, for the most part, not stacked in a parallel manner. Moving downward in the figure from sample 10 to samples 32 and 4 the sample stoichiometries move from C towards SiO_2. The profile for sample 4 identifies it as amorphous SiO_2. Sample 32, located at a stoichiometry 'between' samples 10 and 4 and has an XRD profile which shows evidence for both disordered carbon and amorphous glass. The features at 43° and 65-75° are respectively attributed to sp^2 bonded carbon and amorphous glass. The feature with a maximum near 22°

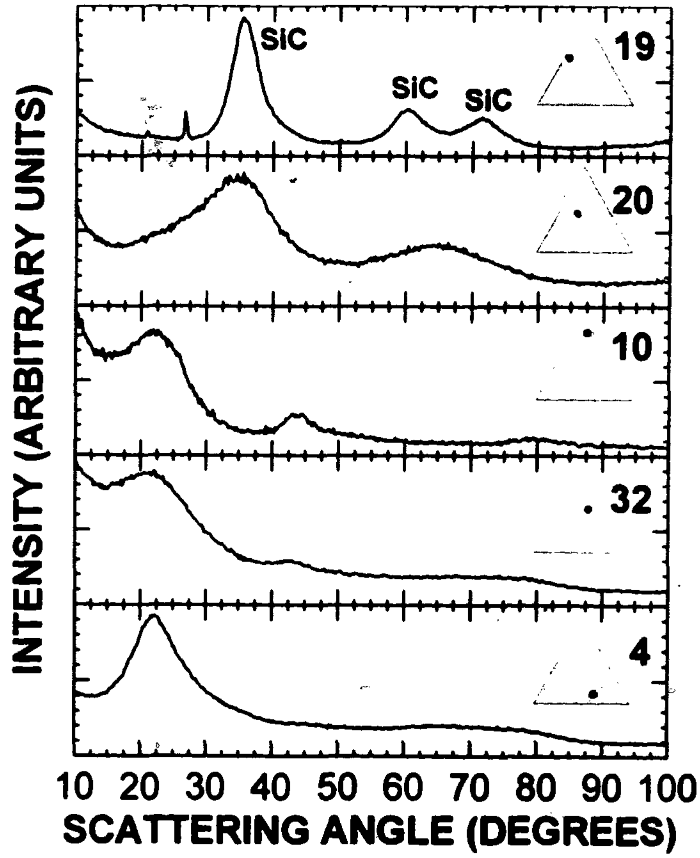

Figure 8-10. XRD patterns for the overview samples.

appears to be a combination of broad disordered carbon and glass peaks. As one moves in Figure 8-10 from sample 10 upwards, the samples move closer to the stoichiometry of SiC. The profile for sample 20 shows a very broad feature with a maximum near 35°, identified as a broad SiC peak. The presence of SiO_2 glass is evidenced by the long tail at low angle. The SiO_2 makes a contribution near 20°. The profile for sample 19 shows broad peaks identified as SiC, and one sharp feature near 27°, which is attributed to an impurity in the sample.

Figure 8-11 shows the first two discharge (1D and 2D) and charge (1C and 2C) cycles for cells made from the materials in Figure 8-10. Cells made from samples 20, 10, and 32 respectively show reversible capacities (Q_{rev}; the average of the 2C and 2D capacities) of 305, 400, and 701 mAh/g and irreversible capacities (Q_{irr}; the difference in capacity between 1D and 2D, taken near 3V) of 124, 250, and 351 mAh/g. Sample 10 has, by far, the most carbon present as disordered carbon. While sample 20 has more oxygen than sample 10, the principal difference is a smaller amount of carbon and a corresponding larger amount of silicon. In sample 20 there is evidence for SiC which is the cause of its smaller capacity than sample 10. The voltage profile for sample 32 is the most similar to the preliminary materials made (Figure 8-5) but with much larger Q_{rev} and Q_{irr}. By comparison to sample 10, the larger capacities are attributed to the presence of more Si-O-C glass in addition to the disordered carbon. Cells made from samples 4 and 19

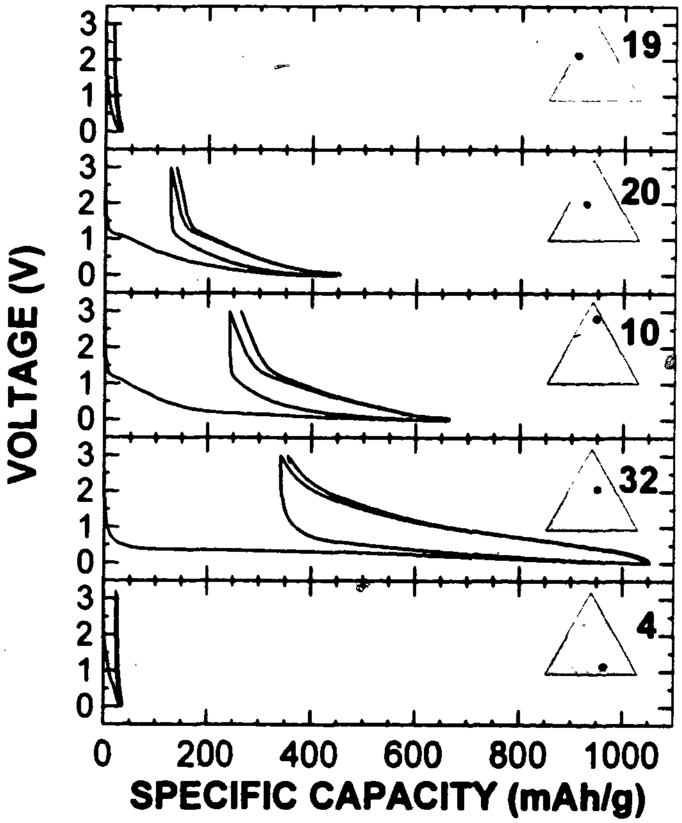

Figure 8-11. Voltage profiles for the overview samples.

both exhibit reversible capacities of 2 and 14 mAh/g, respectively. This is not surprising, considering that their stoichiometry and XRD profiles suggest that they are mostly SiC and SiO_2, both of which are electrochemically inactive with lithium.

The electrochemical results suggest that materials near the extremes of SiC and SiO_2 will not react with significant amounts of lithium. Samples 10 and 32 suggest that materials near them may be of specific interest. The next section presents the results from a series of materials between the D and T lines.

8.2.2 The D-T Line Series

Figure 8-12 shows the XRD patterns for the samples located between the D and T lines as identified in Figure 8-9. A (100) carbon peak can be seen in the XRD patterns for samples 22 (73% C) and 15 (62% C). The (002) carbon peak, however, can only be seen as a shoulder near 25° in these profiles. As was discussed in Chapter 2, this is characteristic of a hard or microporous disordered carbon with only a few graphene sheets stacked in a parallel manner. Xing *et al.* have shown how table sugar can be pyrolysed to make such a hard carbon, and its XRD pattern is shown for comparison in Figure 8-13a (Xing, 1996c). The similarities between the XRD profiles for samples 22, 15, and the sample shown in Figure 8-13a indicates that the graphene sheets in these

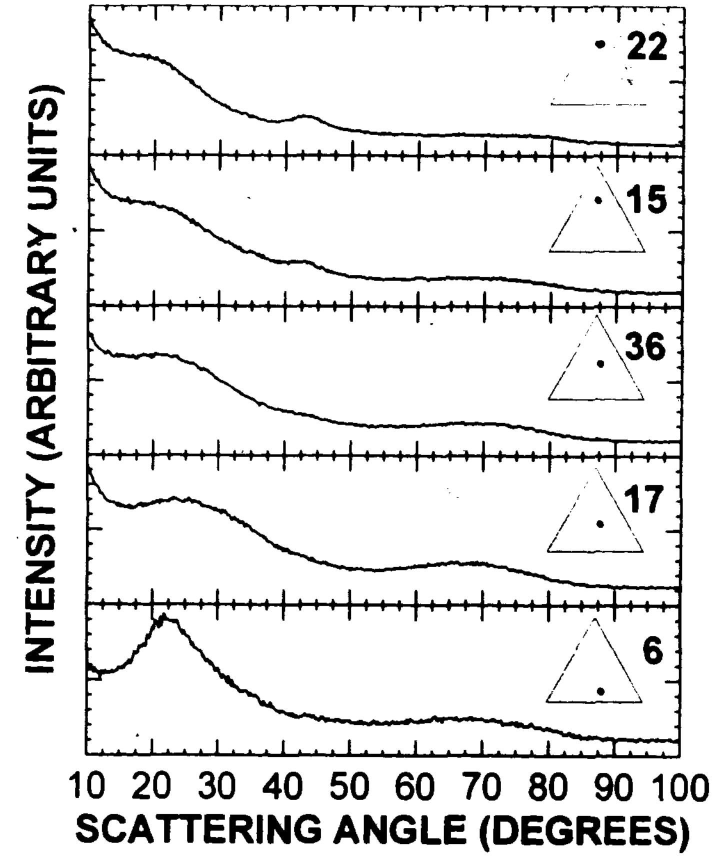

Figure 8-12. XRD patterns for the representative samples located between the D and T lines.

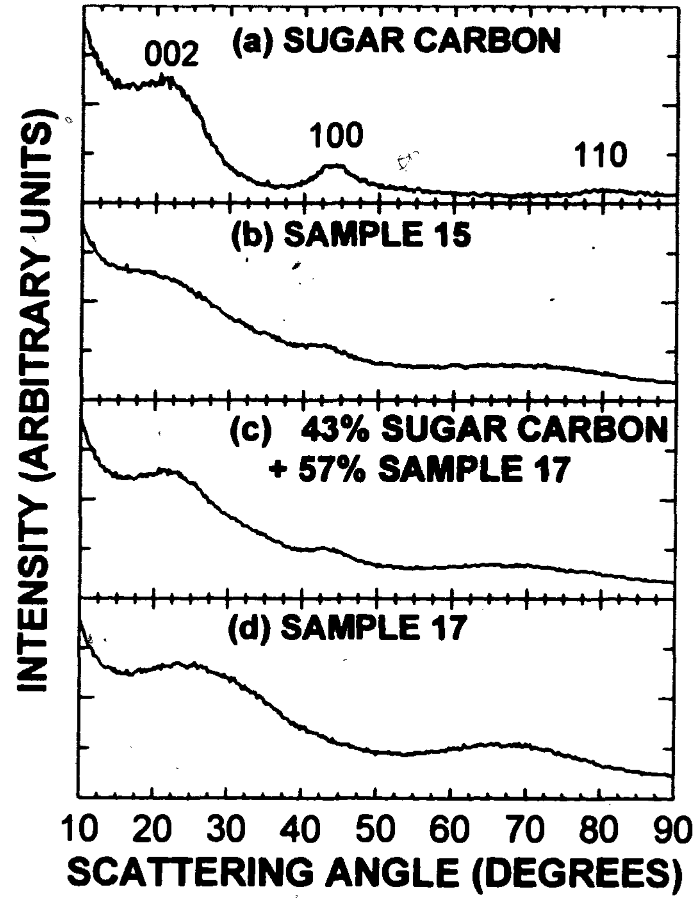

***Figure 8-13.** XRD profiles of (a) a disordered carbon (sugar precursor), (b) sample 15, (c) a calculated pattern using the sum of 43% of the sugar carbon intensity plus 57% of the intensity of sample 17, and (d) sample 17.*

materials are poorly stacked with, perhaps, only bilayer stacking and single layers (Liu, 1996). It is likely that clusters of Si-O-C glass are intimately incorporated between these carbon sheets, similar to the nanodispersions of silicon atoms in carbons for the CVD materials. This gives rise to the observed XRD patterns. The XRD profile for sample 36 (Figure 8-12) shows that when the carbon content is reduced to about 45% the (100) carbon peak is hardly observable. This suggests that only a few well-formed graphene sheets exist in this sample. Thus, in this sample the peak near 22° (Figure 8-12) arises predominantly from the Si-O-C glass and not from the stacking of carbon sheets. Moving towards the bottom of the Gibbs triangle, the Si-O-C glass structure dominates the observed patterns, as evidenced by the XRD patterns for samples 17 and 6 (and also sample 4, as in Figure 8-11).

Figure 8-13 compares the XRD pattern of sample 15 (Figure 8-13b) with that constructed by adding 43% of the XRD intensity of a disordered carbon (Figure 8-13a; from Xing, 1996c) and 57% of that of sample 17 (Figure 8-13d). The XRD patterns in Figure 8-13b and 8-13c are quite similar, suggesting that materials between the D and T lines with carbon contents between about 40 and 90% are mixtures of graphene sheets and Si-O-C glass having a stoichiometry close to that of sample 18.

Figure 8-14 shows the voltage profiles for the first two discharge and charge cycles of cells made from the materials shown in Figure 8-12. Cells made from samples 22, 15, and 36 respectively show Q_{irr} of 300, 340, and 360 mAh/g and Q_{rev} of 630, 680, and 890 mAh/g. Continuing further down the Gibbs, triangle samples 17 and 6 respectively show Q_{irr} of 471 and 478 mAh/g and Q_{rev} of 728 and 194 mAh/g. Thus, there is a local maximum in capacity near a stoichiometry of $Si_{25}O_{30}C_{45}$. The Si-O-C glass in sample 6 appears to predominantly allow irreversible lithium insertion, whereas the in samples 22, 15, and 36 the reaction appeared much more reversible. This strongly suggests that these samples (22, 15, and 36) have sufficient carbon content to form at least some disordered carbon, which allows reversible insertion.

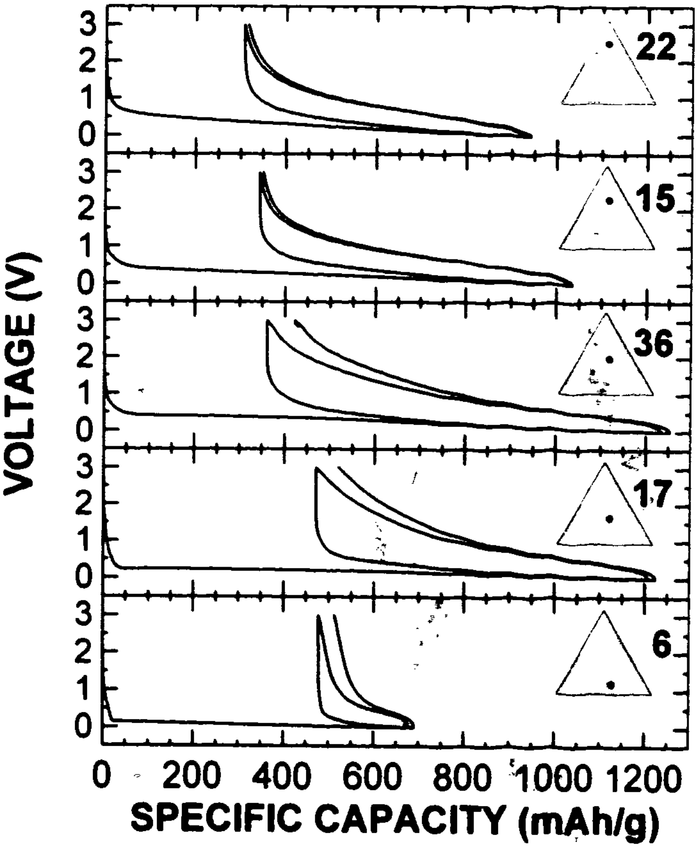

Figure 8-14. Voltage profiles for the representative samples located between the D and T lines.

8.2.3 Cell Characteristics of the Silicon Oxycarbide Materials

Figures 8-15 and 8-16 summarize the reversible and irreversible capacities in units of mAh/g for cells of the samples which were shown in Figure 8-9. Moving from the upper to the lower region between the D and T lines, the reversible capacities of materials increase dramatically to about 900 mAh/g for stoichiometries near $Si_{.25}O_{.30}C_{.45}$ and then decrease to near zero approaching SiO_2. Generally, the irreversible capacity increases with oxygen content, except for materials very near the silica composition, which are basically inactive.

Because they had similar stoichiometries, some samples are not shown in Figures 8-15 and 8-16 for reasons of clarity. In most cases, the corresponding electrochemical characteristics of these materials were similar to samples with similar compositions. This can be verified in Table 8-2 for samples 15 and 25, which are near each other in the Gibbs triangle and have Q_{rev} of 680 and 641 mAh/g, respectively. Other 'pairs' of samples are 14 and 25, 23 and 39, and the 'triplet' of 16, 22, and 43. All of these show electrochemical characteristics which do not deviate from the identified trends for the electrochemical properties. Sample 24, however, is located near sample 18 and exhibits much smaller Q_{rev} and Q_{irr} than sample 18. Since sample 18 follows the identified trend, we consider sample 24 to be an anomaly. Considering the number of samples made and the accumulation of discrepancies involved in measuring the stoichiometry and electrochemical behaviour this sample is excluded as spurious.

The voltage profiles for the materials shown in Figures 8-15 and 8-16 display a hysteresis larger than that observed for the CVD materials or for a pure carbon sample. Figures 8-17 and 8-18 respectively show the average voltages during charge and discharge for these materials in volts. These were calculated by integrating the voltage-capacity curves for the second cycle and then dividing by the measured capacity. Figure 8-17 shows that the average charge voltage generally increases with oxygen content. Figure 8-18 shows that the average discharge voltage is more or less independent of composition.

The next section describes some of the projects which were not specifically related to the electrochemical properties but did provide a further understanding of the Si-O-C materials.

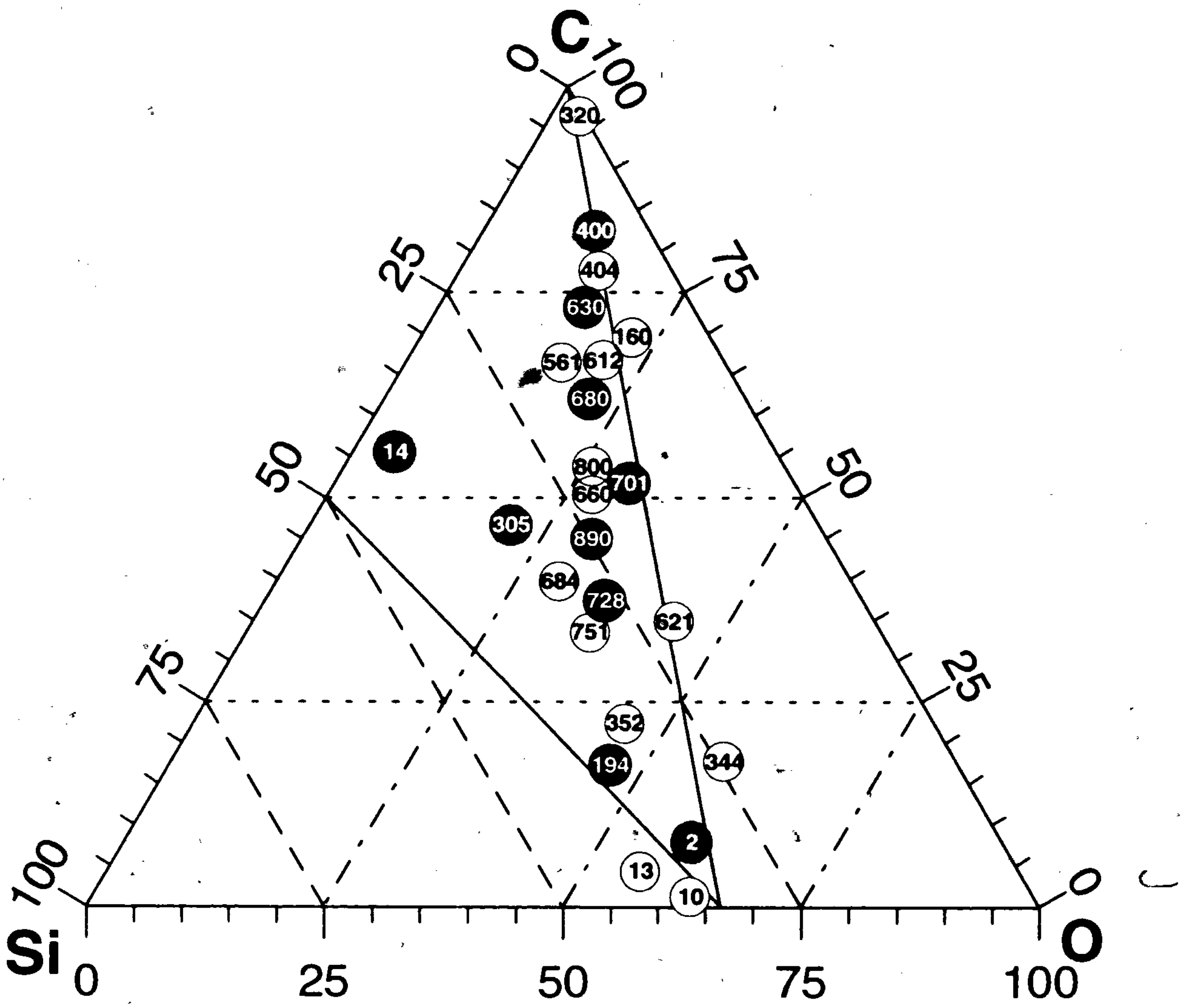

Figure 8-15. Reversible capacities (in units of mAh/g) of electrochemical test cells for the selected samples shown in Figure 8-9.

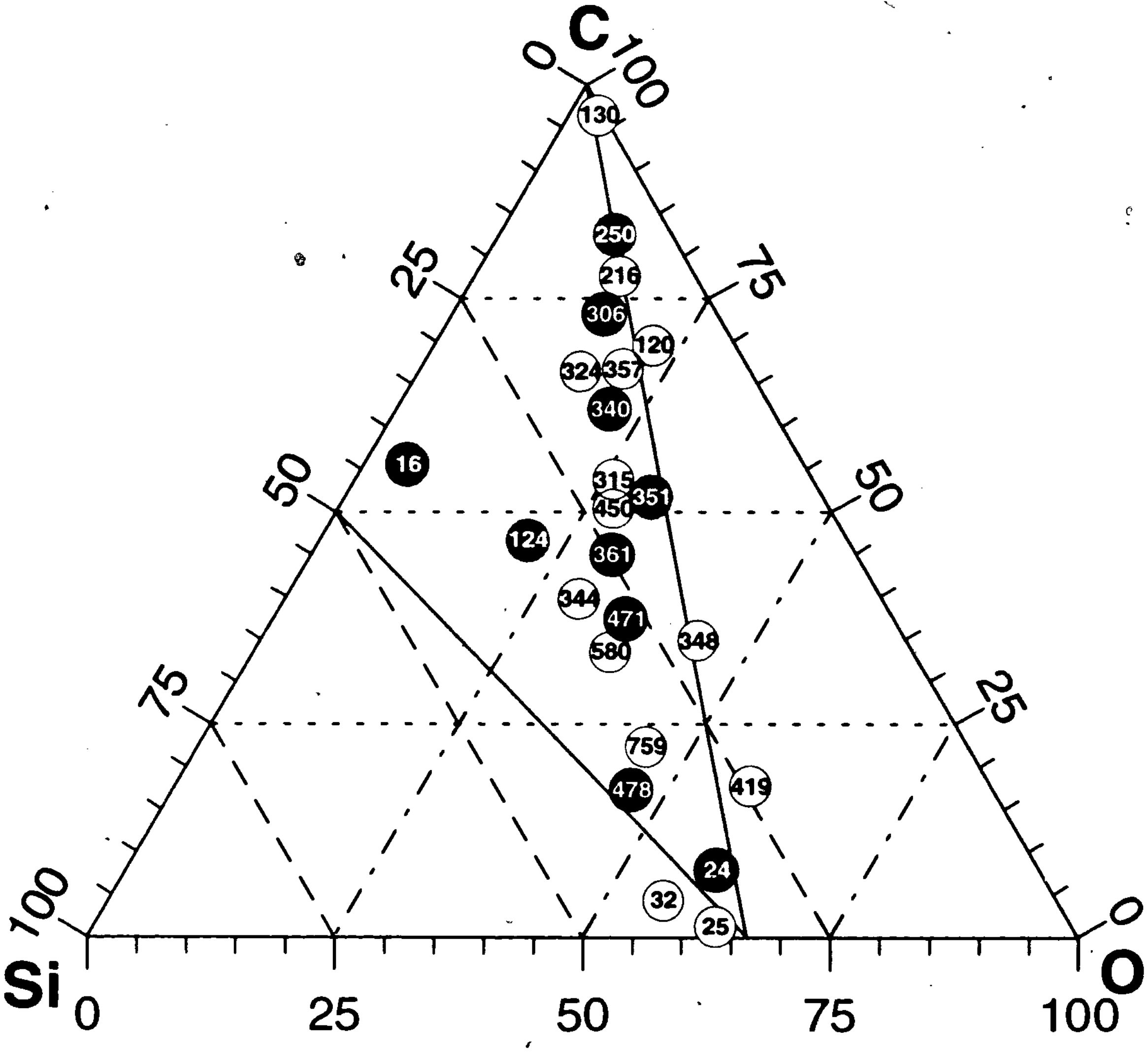

Figure 8-16. Irreversible capacities (in units of mAh/g) of electrochemical test cells for the selected samples shown in Figure 8-9.

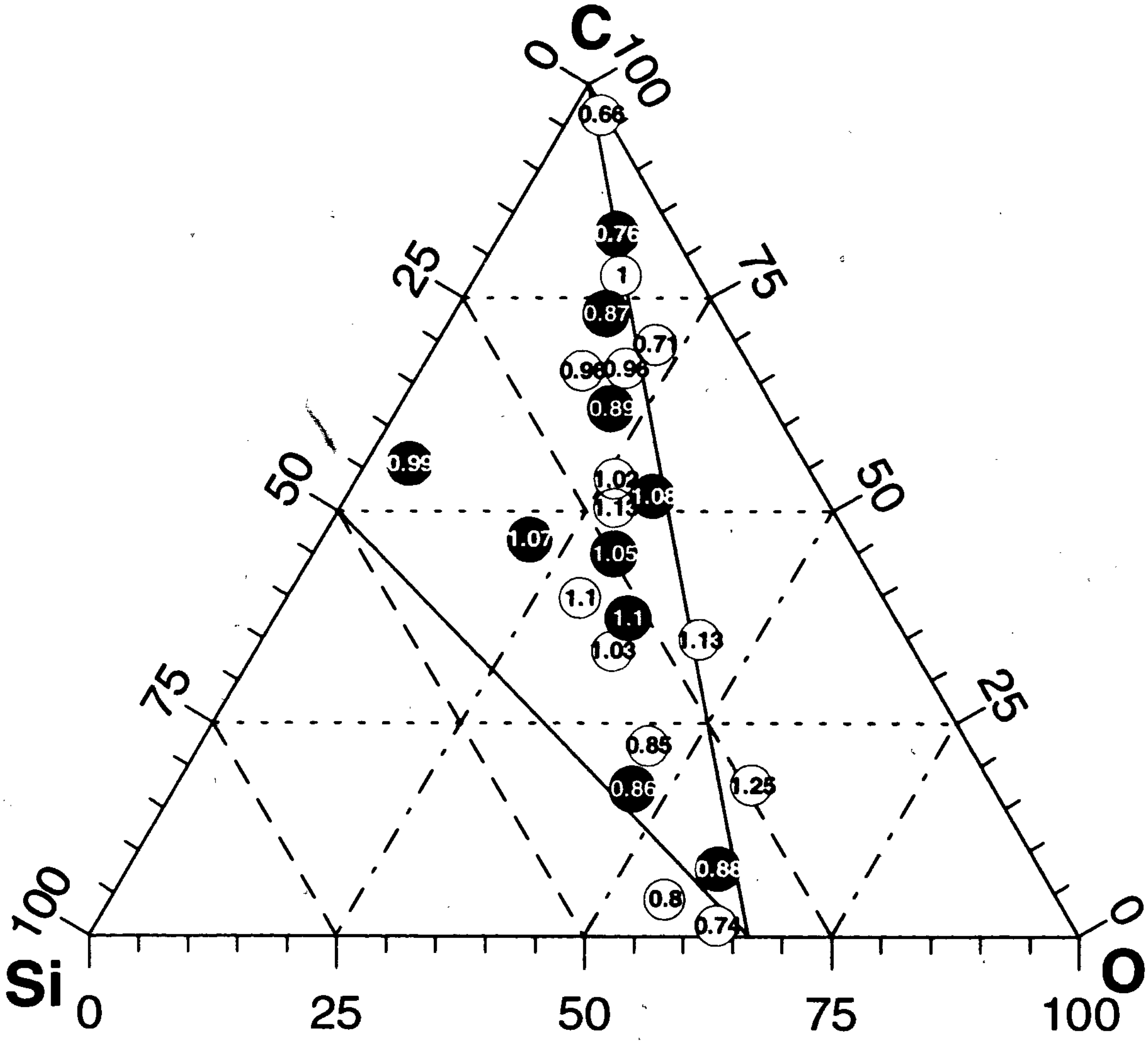

Figure 8-17. Average charge potentials (in units of volts) of electrochemical test cells for the selected samples shown in Figure 8-9.

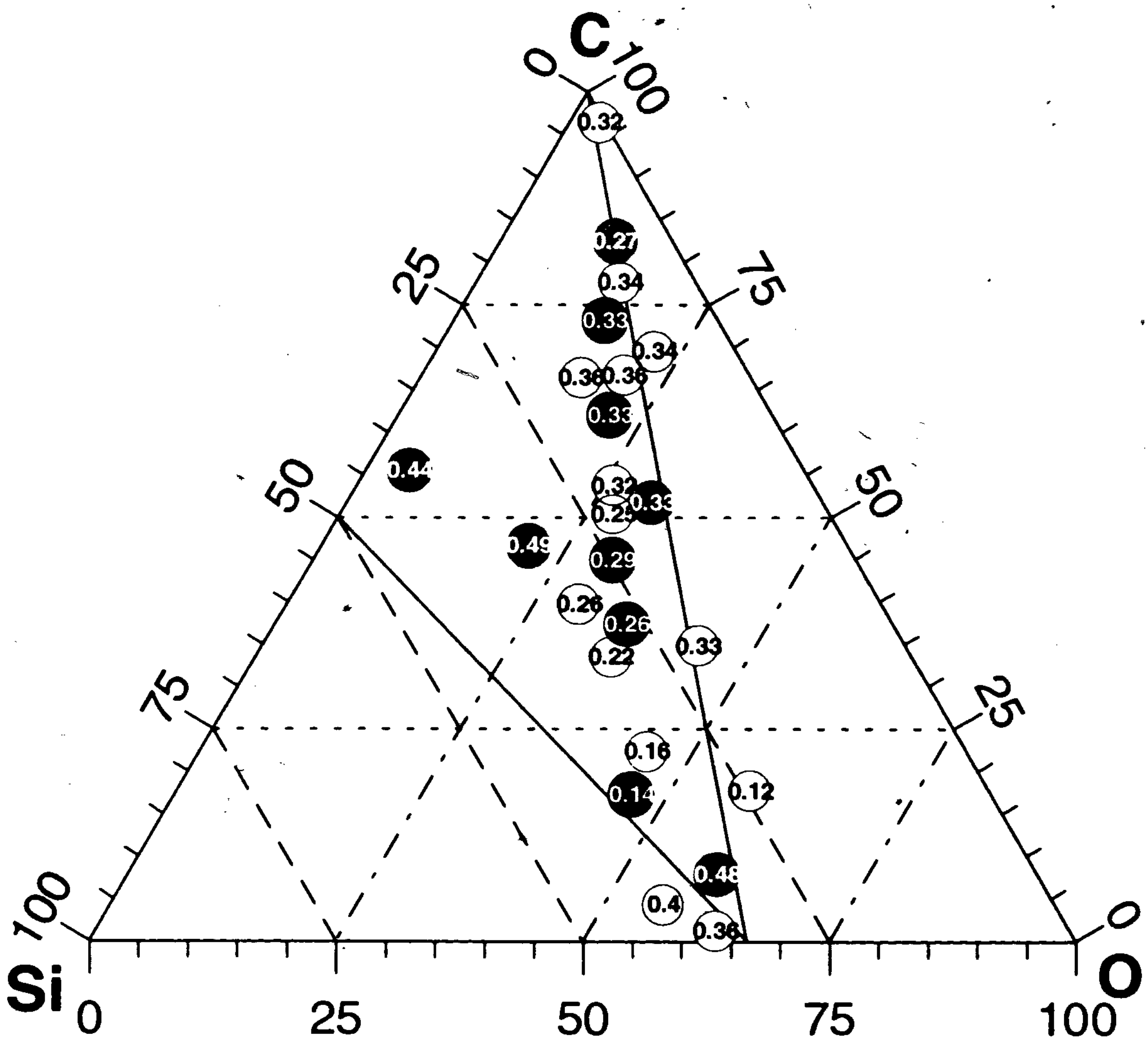

Figure 8-18. Average discharge potentials (in units of volts) of electrochemical test cells for the selected samples shown in Figure 8-9.

8.3 THE SIDE PROJECTS

8.3.1 A Study of Polysiloxane Pyrolysis

As has been discussed previously, siloxane polymers differ in the number of oxygen atoms per silicon and in the chemical composition of the ligands. Initially, it was not obvious to us how the stoichiometry and properties of the pyrolysis products should be related to that of the initial polymer. Therefore, in all previous discussion chemical analysis was used to determine the stoichiometries of the ceramic products. In this section it is shown that the stoichiometry of the pyrolysed polysiloxanes is easily estimated based on the initial polymer composition and the char yield, provided that the initial polymer is highly crosslinked or branched such that the parent backbone does not *unzip* and evaporate during heating.

Chars of the same final stoichiometry can be prepared from polymers of different initial composition. For example, phenyl-containing polymers might be expected to give chars of different properties than vinyl- or methyl-containing polymers, even if the final stoichiometries of the chars are identical. Here, we address this question as well, by examining three highly crosslinked polysiloxanes chosen, based on experience, so that they would produce roughly the same stoichiometry after pyrolysis to a sufficiently high temperature (1000°C; samples 34, 35, and 36). Other recent work (Mantz, 1996) has shown that the initial chemical environment around the silicon in a siloxane polymer is only maintained up to 500°C. As Mantz *et al.* state: "Further heating results in a scrambling of the silicon environment." Based on this, and the results presented in the previous section, one expects the three materials (prepared by pyrolysis to 1000°C) to show similar properties.

A summary of the polysiloxane precursors used is given in Table 8-3 (a subset of Table 4-1). The sample numbers correspond to the materials made after pyrolysis of the polymer to 1000°C.

Figures 8-19, 8-20, and 8-21 show respectively the decomposition of polysiloxanes 34, 35, and 36 as measured by TGA and RGA. The bottom frame in each of Figures 8-19, 8-20, and 8-21 shows the weight (as a percentage of the initial weight) and the derivative

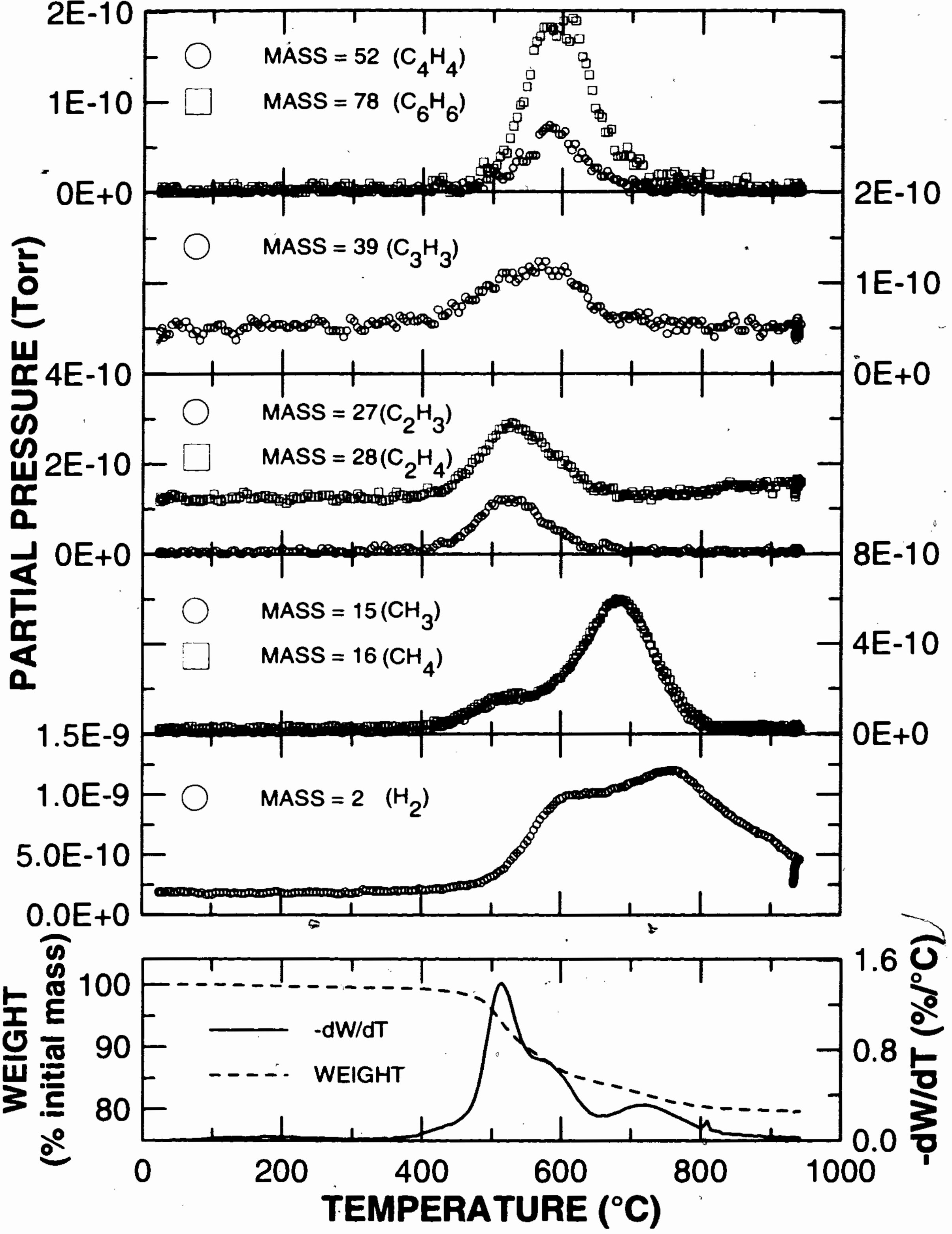

Figure 8-19. The thermal decomposition of polysiloxane 34. The TGA data is presented in the bottom panel and the upper panels are partial pressures of the masses shown, as measured by RGA.

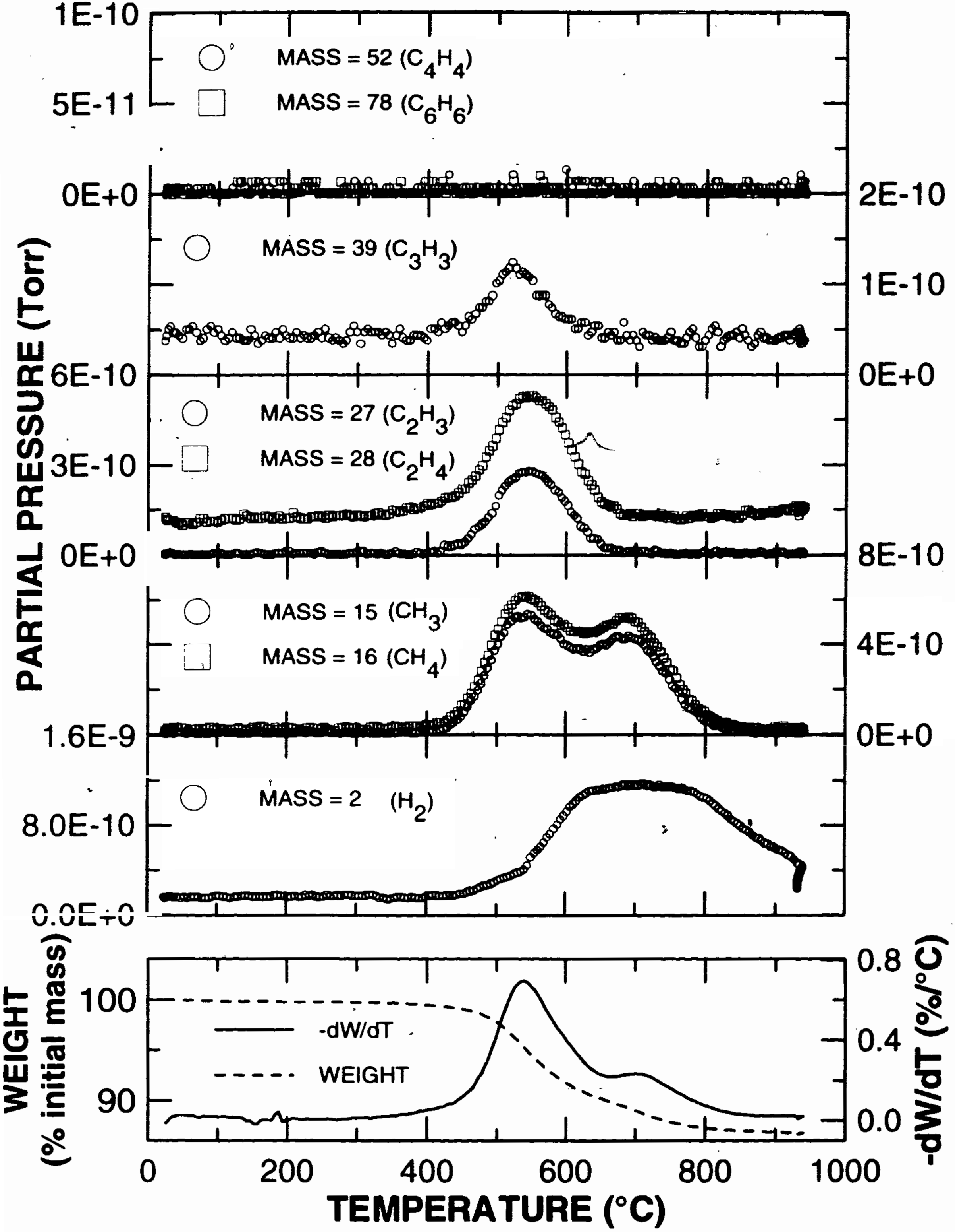

Figure 8-20. The thermal decomposition of polysiloxane 35. The TGA data is presented in the bottom panel and the upper panels are partial pressures of the masses shown, as measured by RGA.

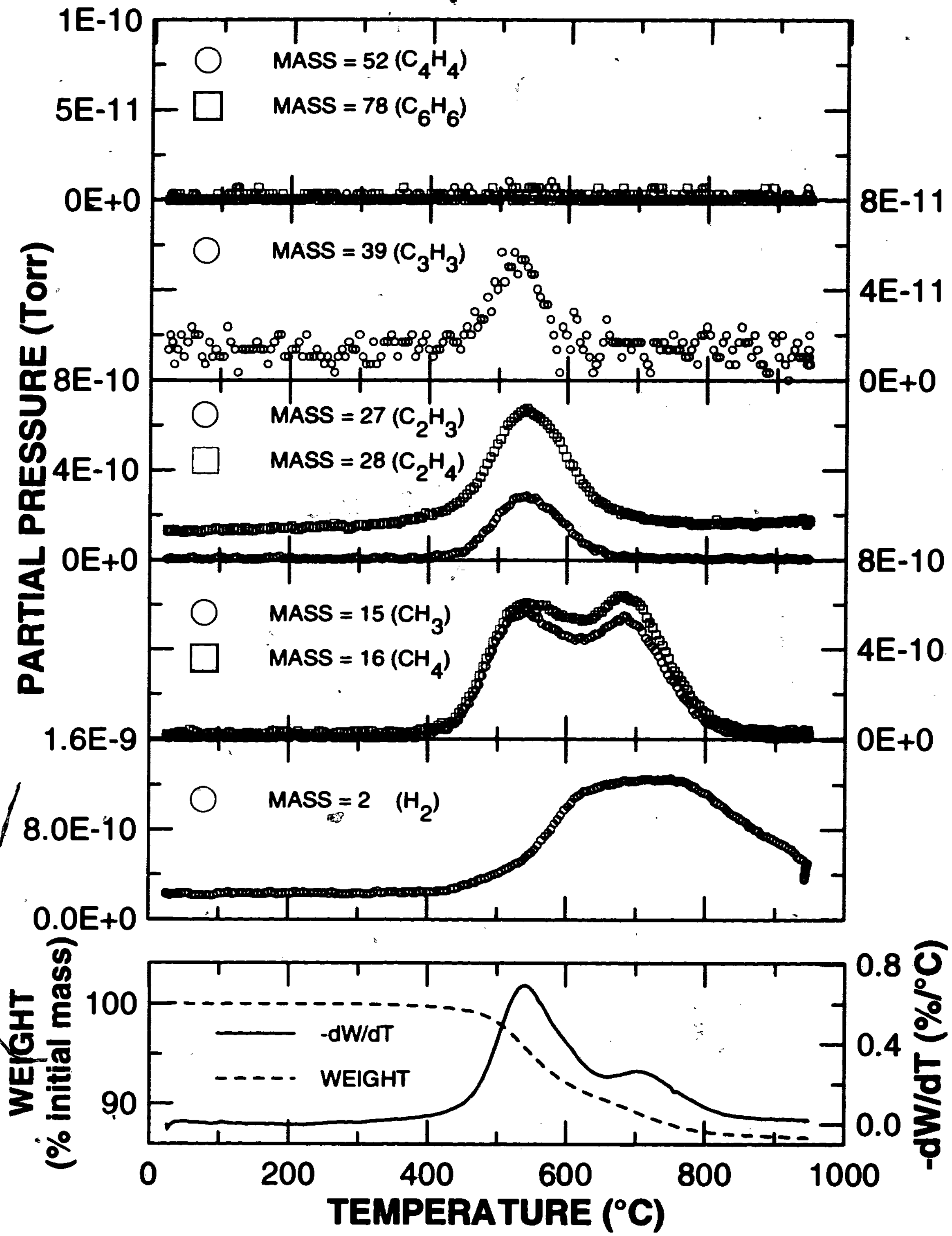

Figure 8-21. The thermal decomposition of polysiloxane 36. The TGA data is presented in the bottom panel and the upper panels are partial pressures of the masses shown, as measured by RGA.

Table 8-3. A selection of the polymers which were pyrolysed to make the samples.

Sample	Polymer Precursor Used
13	$(PhSiO_{1.5})_{0.75}$ $(Ph_2ViSiO_{0.5})_{0.25}$
14	$(PhSiO_{1.5})_{0.75}$ $(Me_2ViSiO_{0.5})_{0.25}$
15	$(PhSiO_{1.5})_{0.5}$ $(Me_2ViSiO_{0.5})_{0.5}$
16	$(PhSiO_{1.5})_{0.5}$ $(Ph_2ViSiO_{0.5})_{0.5}$
17	$(MeSiO_{1.5})_{0.5}$ $(Me_2ViSiO_{0.5})_{0.5}$
18	$(MeSiO_{1.5})_{0.75}$ $(Me_2ViSiO_{0.5})_{0.25}$
21	$(PhSiO_{1.5})_{0.75}$ $(Ph_2ViSiO_{0.5})_{0.25}$: $(PhSiO_{1.5})_{0.75}$ $(Ph_2HSiO_{0.5})_{0.25}$
22	$(PhSiO_{1.5})_{0.5}$ $(Ph_2ViSiO_{0.5})_{0.5}$: $(PhSiO_{1.5})_{0.5}$ $(Ph_2HSiO_{0.5})_{0.5}$
23	$(PhSiO_{1.5})_{0.75}$ $(Me_2ViSiO_{0.5})_{0.5}$: $(PhSiO_{1.5})_{0.5}$ $(Me_2HSiO_{0.5})_{0.5}$
24	$(MeSiO_{1.5})_{0.5}$ $(Me_2ViSiO_{0.5})_{0.5}$: $(MeSiO_{1.5})_{0.5}$ $(Me_2HSiO_{0.5})_{0.5}$
25	$(PhSiO_{1.5})_{0.75}$ $(Me_2ViSiO_{0.5})_{0.25}$: $(PhSiO_{1.5})_{0.75}$ $(Me_2HSiO_{0.5})_{0.25}$
34	$(PhSiO_{1.5})_{0.22}$ $(MeSiO_{1.5})_{0.55}$ $(Me_2ViSiO_{0.5})_{0.23}$
35	$(ViSiO_{1.5})_{0.77}$ $(Me_2ViSiO_{0.5})_{0.23}$
36	$(ViSiO_{1.5})_{0.66}$ $(MeSiO_{1.5})_{0.09}$ $(Me_2ViSiO_{0.5})_{0.25}$
37	$(PhSiO_{1.5})_{0.09}$ $(MeSiO_{1.5})_{0.66}$ $(Me_2ViSiO_{0.5})_{0.25}$
38	$(PhSiO_{1.5})_{0.38}$ $(MeSiO_{1.5})_{0.39}$ $(Me_2ViSiO_{0.5})_{0.23}$
39	$(PhSiO_{1.5})_{0.5}$ $(MeSiO_{1.5})_{0.23}$ $(Me_2ViSiO_{0.5})_{0.27}$
40	$(PhSiO_{1.5})_{0.66}$ $(MeSiO_{1.5})_{0.08}$ $(Me_2ViSiO_{0.5})_{0.26}$
41	$(PhSiO_{1.5})_{0.13}$ $(ViSiO_{1.5})_{0.64}$ $(Me_2ViSiO_{0.5})_{0.2}$

of the weight with respect to the temperature (dW/dT) plotted versus temperature. The frames above this show the RGA signal for a number of masses. There is no measurable amount of oxygen or silicon-containing gas species in the decomposition stream. Mass 28 could be CO or C_2H_4, but considering that mass 27 shows a virtually identical signal, and that no signal is observed for mass 44 (CO_2) it is likely that mass 27 is C_2H_3 and 28 is C_2H_4. The phenyl groups in polysiloxane 34 can be seen leaving as masses 78 and 52.

The RGA data suggests that only species containing carbon and hydrogen are leaving the polysiloxane during decomposition to a maximum of 1000°C. Based on the initial stoichiometries of the polysiloxanes, it is straightforward to calculate the resulting weight percentages of silicon, oxygen, and carbon that should be in the resulting silicon oxycarbide glasses. We assume that the entire weight loss is due to carbon and hydrogen and that all of the hydrogen leaves the material. As an example, a calculation for sample 34, based on the initial stoichiometry of polysiloxane 34, follows.

Sample Calculation:

Polysiloxane 34 stoichiometry: $C_{2.79}H_{5.28}SiO_{1.27}$

Weight percent carbon = 38.6%, weight percent H = 5.5%

Total weight loss observed: 19.0%

Percentage weight loss of carbon (= Total weight lost - w%H) = 13.5%

Carbon lost per formula unit = 2.79 × 13.5 / 38.6 = 0.98

Remaining carbon = 2.79 - 0.98 = 1.81

Final predicted atomic percentages:

at.%H = 0% at.%C = 44.5% at.%Si = 24.5% at.%O = 31.0%

Final predicted stoichiometry for sample 34: $C_{1.81}SiO_{1.27}$

Table 8-4 contains a summary of the atomic percentages of Si, O, and C predicted for many of the pyrolysed polymers as calculated by the method shown above. Experimental compositions (believed to be accurate to ±3%) are also given. Considering that the weight percentages by elemental analysis do not close on 100% and the discrepancy associated with that, the agreement between the experiment and the calculation is very good for all

Table 8-4. Predicted and measured stoichiometries of the samples pyrolysed at 1000°C

			Predicted			Expt.	
Sample	Yield (%)	C (At. %)	Si (At. %)	O (At. %)	C (At. %)	Si (At.%)	O (At. %)
13	67	66.3	15.0	18.7	66	17	16
14	71	57.9	18.7	23.4	62	15	24
15	62	51.0	24.5	24.5	62	16	21
16	53	66.5	16.7	16.7	71	12	17
17	60	14	43	43	37	27	36
18	79	27.2	32.4	40.5	33	31	36
21	73	68.2	14.1	17.6	67	13	21
22	66	72.1	14.0	14.0	73	12	15
23	78	57.7	21.1	21.1	60	18	23
25	75	58.2	18.6	23.2	61	15	24
34	76	44.5	24.4	31.0	47	24	30
35	86	45.1	24.2	30.7	45	25	30
36	83	44.9	24.5	30.6	45	25	30
37	75	30	31	39	39	26	34
38	79	50.6	21.7	27.6	54	20	26
39	76	54.6	20.4	25.1	59	19	23
40	77	60.1	17.8	22.1	63	16	20
41	85	48.7	22.8	28.6	50	22	28

but three of the polymers. This suggests that our model for the pyrolysis of these polysiloxanes is correct.

The experimental stoichiometries of samples 15, 17, and 37 do not agree well with the predicted values. Of these, sample 17 is the worst, and there was a black tarry material deposited at the cool end of the pyrolysis tube during its production. This suggests some evaporation of *unzipped* fragments and a breakdown of the model. On the other hand, sample 37 was observed to have fragmented violently during pyrolysis (it remained a solid during decomposition) and it could have a low yield due to our inability to recover all the fragments from within the tube. For this sample, and for sample 15, the experimental stoichiometries can be well matched if the measured yields are increased by about 11%. This treatment does not work for sample 17 at any value of the yield, presumably because of the unzipping and evaporation of molecules with stoichiometries different than that of the bulk polymer. One quick check of this hypothesis is to compare the ratio of silicon to oxygen. If poor agreement is caused by either evaporation without unzipping or an error in the yield measurement then the silicon to oxygen ratio should be the same in the polysiloxane and the ceramic. Clearly, the silicon to oxygen ratios in polysiloxane and sample 17 are different.

The XRD profiles for samples 34, 35, and 36 are shown in Figure 8-22. As discussed

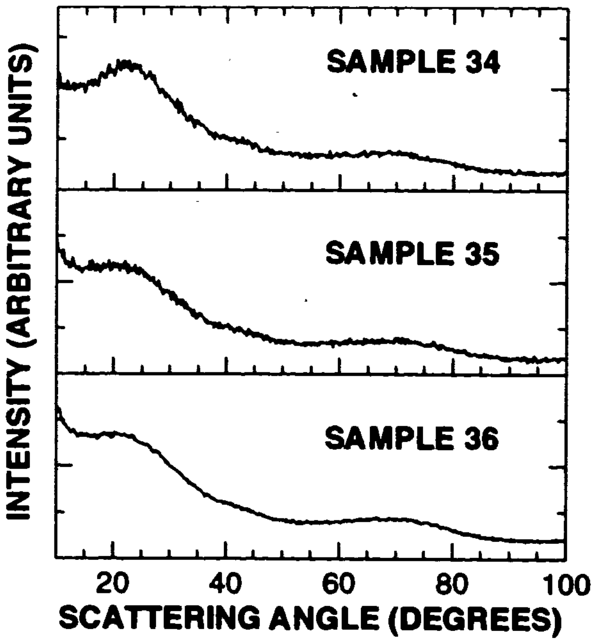

Figure 8-22. The XRD profiles for samples 34, 35, and 36. Note that there is little difference between them.

previously, the broad features identified as network glass peaks are centered near 23° and 73° and the slight feature at 43° is likely due to the presence of a small number of single graphene sheets. The XRD profiles for the samples are almost identical although the 23° peak for sample 34 is somewhat more intense and narrower.

Figure 8-23 summarizes the XAS measurements of the silicon *K*-edge for samples 34, 35, and 36. Figure 8-23a shows the profiles for the unheated polysiloxanes 34, 35, and 36. Figures 8-23b and c show the profiles for materials made by heating polymers 34 and 35 to a maximum of 600 and 800°C, respectively. The profiles for samples 40, 41, and 42 (heated to 1000°C) are shown in Figure 8-23d. For reference purposes the c-SiC and c-SiO_2 silicon *K*-edges were measured and are shown in Figure 8-21e. All the spectra (I_S/I_O) in Figure 8-23 have been normalized at 1847eV.

All the profiles in Figure 8-23a-d show features near 1845.5 eV and 1847.2eV which, by comparison to the spectra for c-SiC and c-SiO_2, we attribute to silicon-carbon and silicon-oxygen bonding, respectively. Sample 34, the only one which initially contained

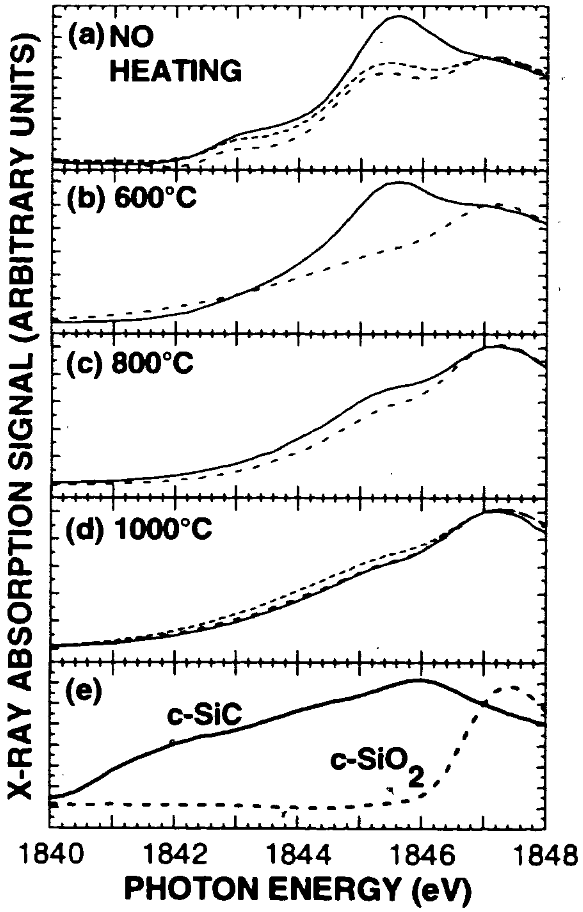

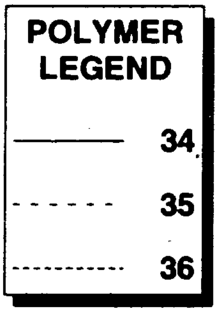

Figure 8-23. The silicon K-edge for: (a) polysiloxanes 34, 35, and 36 without any heat treatment, (b) polysiloxanes 34 and 35 heated to 600°C, (c) polysiloxanes 34 and 35 heated to 800°C, (d) samples 34, 35, and 36 heated to 1000°C, and (e) c-SiC and c-SiO_2*. All spectra were normalized at 1847 eV.*

phenyl groups, differs from the others at low temperatures. As the maximum pyrolysis treatment temperature increases the intensity of the 1845.5 eV feature decreases relative to the 1847.2 eV feature. Between 600 and 800°C, most of the labile phenyl groups leave sample 34 (see Figure 8-19) and the XAS spectrum begins to resemble that of sample 35, which did not contain phenyl groups initially. By 1000°C the spectra are almost identical, implying that the local chemical environment of the silicon atoms in samples 34, 35, and 36 is the same. If this is true, other bulk measurements should also give identical results. To confirm this, we can examine the results from the electrochemical test cells.

Figure 8-24 shows the first discharge and charge and second discharge of electrochemical cells made with materials 34, 35, and 36. The electrochemical properties for these samples (summarized in Table 8-2) are quite similar. Each of these materials reacts reversibly with over 800 mAh/g of lithium. The differences between the voltage profiles (and thus the properties summarized in Table 8-2) are within expected experimental discrepancies. Thus, the electrochemical behaviour upon the insertion and deinsertion of lithium into these materials is the same. This suggests that it is the final char stoichiometry and not the precise nature of the starting polymer which determines the bulk properties of the Si-O-C glasses.

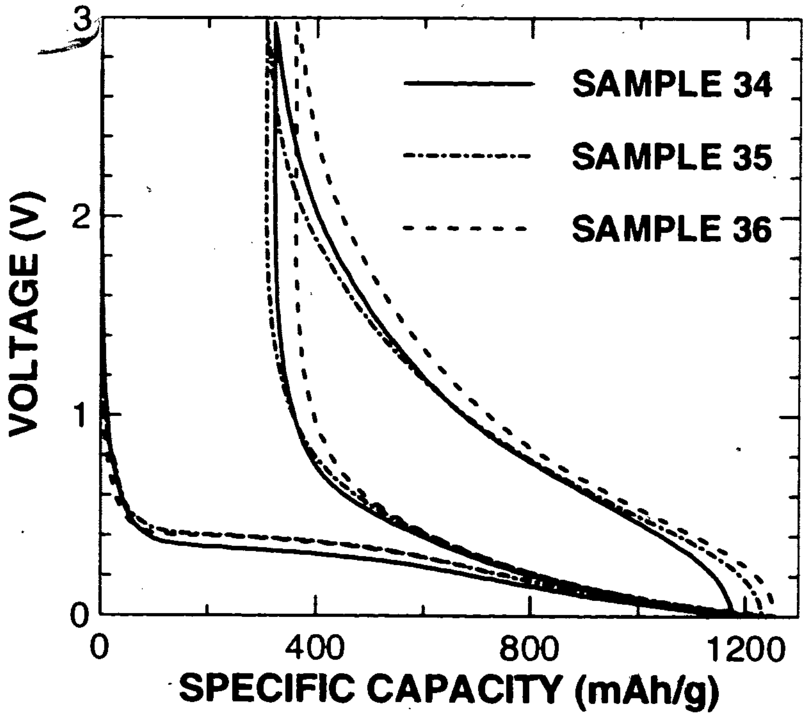

Figure 8-24. The voltage profiles for samples 34, 35, and 36 (heated to 1000°C). Note that they are essentially the same.

8.3.2 Hydrofluoric Acid Washing a Silicon Oxycarbide

As was detailed in Section 8.2, the silicon oxycarbides which showed the largest reversible capacities (~900 mAh/g) also exhibited large irreversible capacities (over 300 mAh/g). We observed that these irreversible capacities increased with the oxygen content of the material. Since hydrofluoric acid (HF) is known to dissolve SiO_2 and Si, we hoped that the oxygen content of these materials could be reduced, and consequently the electrochemical properties improved, by a room-temperature HF treatment of the Si-O-C glasses.

Sample 36 was treated by washing in HF, as described in Chapter 4 Section 4.7). Recall that 8 different samples (HF2 through HF9) were prepared by washing 1 g portions of sample 34 in HF for specific periods of time, ranging from 1 minute to 24 hours, and then filtering and rinsing with distilled water. The sample HF1 was made by rinsing and filtering a 1 g portion of sample 36 with distilled water. Figure 8-25 shows the weight change during HF rinsing as a percentage of the initial weight, versus the duration of the HF exposure in hours. Samples HF7, HF8, and HF9 show no significant change in mass, implying that the reaction has essentially stopped after 8 hours and 40 percent mass loss. Since the HF is in stoichiometric excess to the amount of oxygen present in the sample and that oxygen, by weight, makes up about 40 percent of the initial Si-O-C, it might

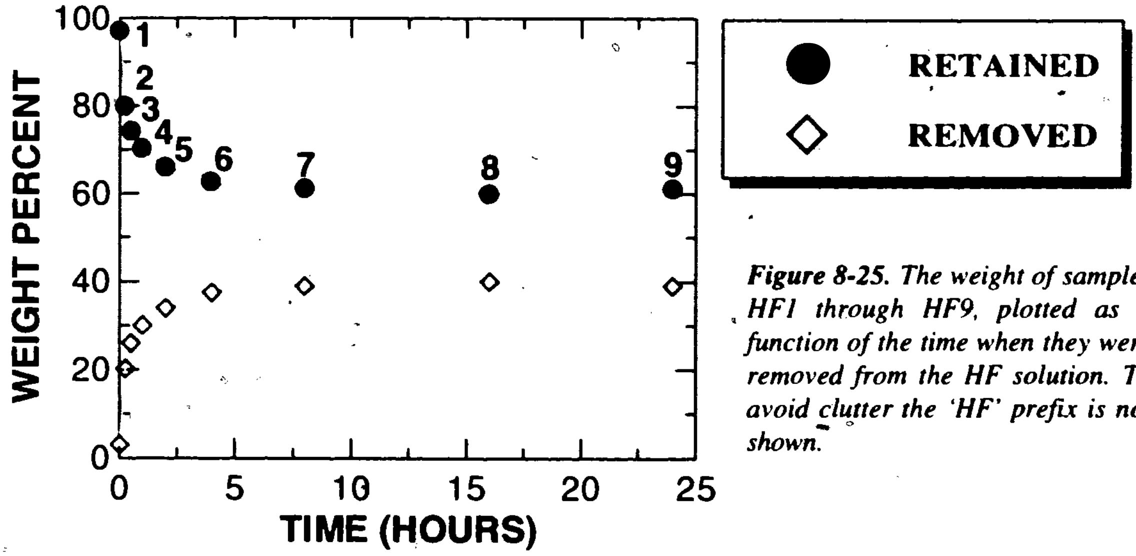

Figure 8-25. The weight of samples HF1 through HF9, plotted as a function of the time when they were removed from the HF solution. To avoid clutter the 'HF' prefix is not shown.

Table 8-5. A summary of the samples HF1 through HF9 (weight percentages by elemental analysis).

Sample	Mass (% of initial)	weight % H	weight % C	weight % Si	weight % O
36	100	0.19	28.7	38.3	33.0
HF1	97	0.01	21.7	39.8	38.5
HF2	79.8	0.07	24.8	35.5	39.7
HF3	74	0.15	27.0	34.3	38.7
HF4	70	0.01	28.3	35.8	35.9
HF5	66	0.17	30.1	34.2	35.7
HF6	62.5	0.11	30.8	34.8	34.4
HF7	61	0.51	31.2	32.1	36.7
HF8	60	0.43	31.4	31.6	37.0
HF9	61	0.55	33.4	33.6	33.0

initially appear that all the oxygen has been removed, and therefore the reaction has stopped. However, elemental analysis shows that there is a significant amount of oxygen still present. The stoichiometry by elemental analysis is summarized in Table 8-5. HF will break the silicon-oxygen bonds in these materials. However, based on the stoichiometry and weight-loss results, the breaking of these silicon-oxygen bonds must be removing not only silicon and oxygen but also some carbon from the material.

Figure 8-26 shows the XRD profiles for samples HF1 through HF9. The initial Si-O-C (not HF or water washed; sample 36) is indistinguishable from sample HF1 (see Figure 8-12) and is not shown in this figure. Differences in signal to noise are due to different counting times and are not dependent on the samples. As was discussed in Section 8.2, we believe that these materials are a mixture of graphene sheets and Si-O-C glass. The features observed in the profiles shown in Figure 8-26 have been sufficiently explained

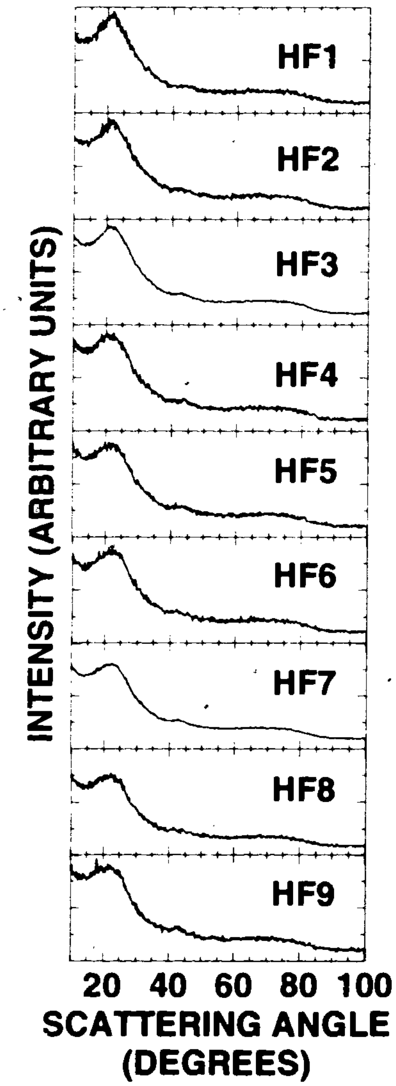

Figure 8-26. The XRD profiles for samples HF1 through HF9.

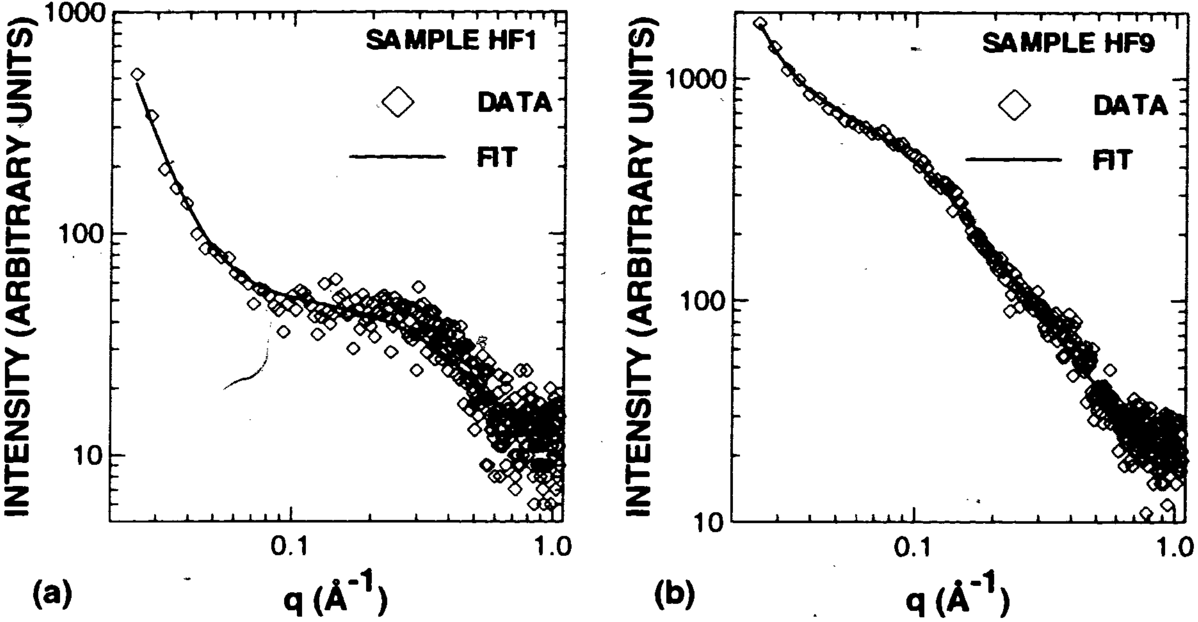

Figure 8-27. *(a) The SAX data for sample HF1 shown with the fit to the data, based on Equation 5-6 and (b) the SAX data and fit for sample HF9.*

(Section 8.2). The change in the profile from sample HF1 to HF9 is quite small, considering that the material experiences a 40 percent weight loss. The bulk of the material appears virtually unchanged by the HF treatment.

In Chapter 5 it was mentioned that small angle X-ray scattering by powders (SAX) shows regions of differing electron density. Regions with characteristic dimensions of 3 to 100Å can be examined with our diffractometer using Cu K-α radiation. We understand these materials to be a relatively homogeneous network of silicon, oxygen, and carbon atoms mixed with single graphene sheets. Thus, regions of different electron density, of the dimensions we can measure, should correspond to the presence of and absence of Si-O-C; that is to say, pores in the powder grains. While the graphene sheets must have electron densities different from the Si-O-C regions, it is believed that these differences are small enough that any contributions from the graphene sheets should be overwhelmed by the presence of pores, which are the complete absence of electrons.

Figure 8-27a shows the SAX profile for sample HF1, and a fit to this data. Figure 8-27b shows the SAX profile and fit for sample HF9. The fits to the data use Equation 5-6 and are close but not ideal. The model used to fit this data is simplified by the use of some assumptions (homogeneous, non-overlapping pores) which may not be entirely valid for these materials. Still, we believe that the trends observed are well described by the model variables. The corresponding fit variables are summarized in Table 8-6. The feature centered near 0.1Å^{-1} corresponds to micropores with a correlation length corresponding to 9Å. Figure 8-28 shows the fits (not the original data) to the SAX profiles for samples HF1 through HF9. Notice that the 0.4Å^{-1} feature does not appear to change, while the intensity of the 0.1Å^{-1} feature, absent in sample HF1, grows in intensity. An examination of the fit variables shown in Table 8-6 reveals that the initial micropore distribution, corresponding to a correlation length around $R_1 \approx$ 2Å undergoes no discernible change either in radius or number density. However, the changes in C and R_2 clearly show that the HF washing introduces micropores with larger correlation lengths, around $R_2 \approx$ 9.4Å. The number of these micropores increases with the duration of HF washing, and the correlation length of the pores decreases to around $R_2 \approx$ 6.7Å.

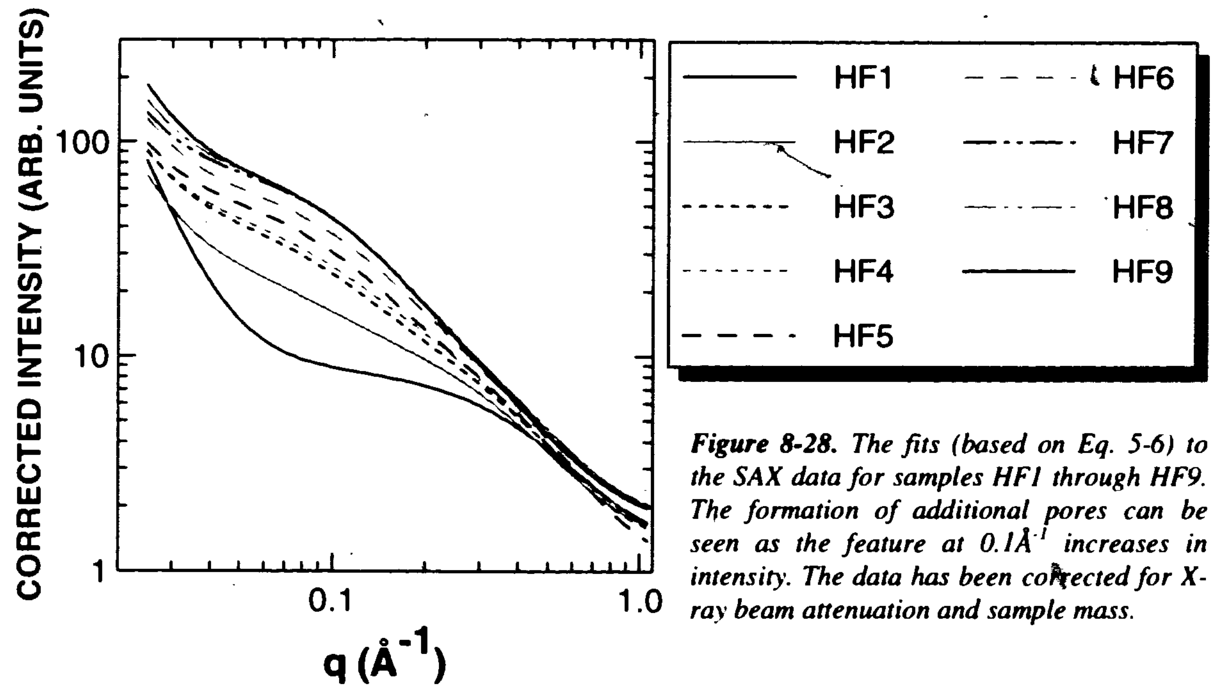

Figure 8-28. The fits (based on Eq. 5-6) to the SAX data for samples HF1 through HF9. The formation of additional pores can be seen as the feature at 0.1Å^{-1} increases in intensity. The data has been corrected for X-ray beam attenuation and sample mass.

Table 8-6. A summary of the BET measurements and the fits to the SAX data, based on Equation 5-6.

Sample	*A*	*B*	R_1 (Å)	*C*	R_2 (Å)	*D*	Surface Area (BET, m^2/g)
HF1	0.0001	0.4743	1.7615	0	0	0.8039	0.25
HF2	0.0001	0.4550	2.1830	0.0022	9.3506	1.3698	17.7
HF3	0.0001	0.4516	2.1159	0.0074	8.0137	1.2316	25.7
HF4	0.0001	0.3711	2.3254	0.0070	8.0897	1.1269	37.1
HF5	0.0001	0.6596	1.9307	0.0151	7.3441	0.9360	44.4
HF6	0.0001	0.5269	2.1549	0.0261	6.7810	1.4415	53.8
HF7	0.0001	0.4808	2.0647	0.0291	6.7768	1.5398	55.6
HF8	0.0002	0.6868	1.9124	0.0338	6.7780	1.6465	54.4
HF9	0.0002	0.5463	2.0124	0.0349	6.6890	1.6679	54.1

The BET surface area measurement results are also summarized in Table 8-6. These results show that the HF washing results in a continued increase of the surface area with mass loss. In order to determine whether the surface area results correspond to the fits to the SAX data, a simple approximation is performed. First, it is assumed that all the pores in the material are available to contribute to the surface area. Then the SAX micropore surface area can be estimated, assuming that the pores are spherical, according to:

$$SA = X\frac{4}{3}\pi\left[BR_1^2 + CR_2^2\right] \qquad [8\text{-}1]$$

where SA is the surface area in m^2/g, B, C, R_1, and R_2 are the same as the variables in Equation 5-6, and X is a scaling factor. X includes the conversion from $Å^2$ to m^2, geometrical factors involving the diffractometer, the scattering power of an electron, and

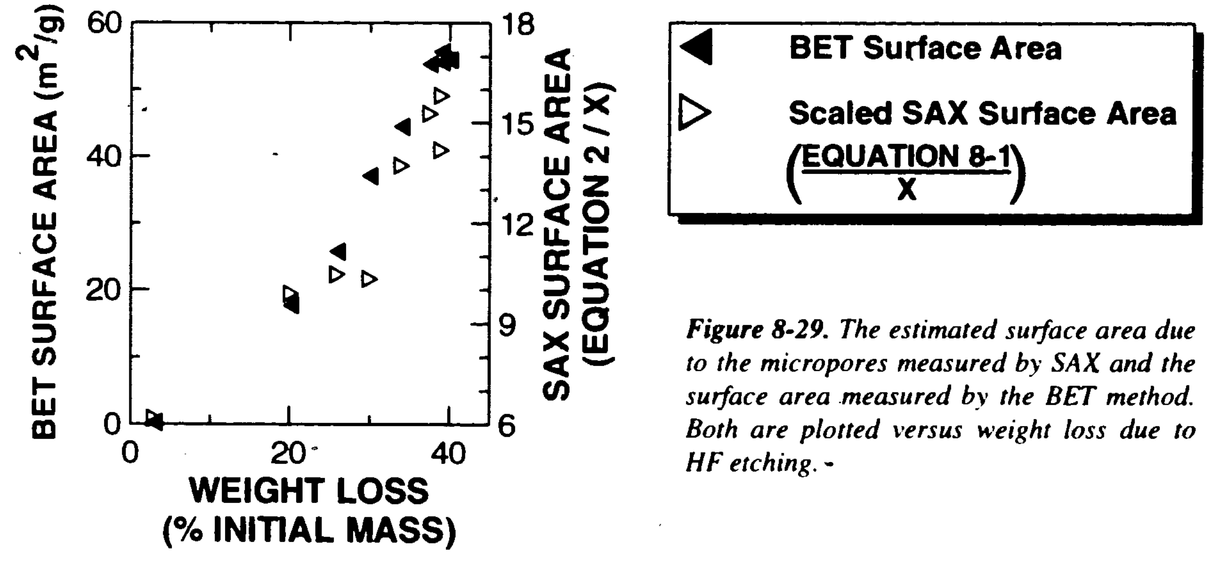

Figure 8-29. The estimated surface area due to the micropores measured by SAX and the surface area measured by the BET method. Both are plotted versus weight loss due to HF etching.

so on. This can be used to determine rough agreement between trends observed in the SAX and BET data. The results of applying Equation 8-1 to the fitted variables listed in Table 8-6 is plotted in Figure 8-29 along with the BET data. The data presented is Equation 8-1 divided by *X*, and is plotted against the right hand scale. The nonzero SAX surface area calculated for sample HF1 is due to the contributions from the R_I pores. Both the gas adsorption and small angle scattering derived surface areas show similar trends with HF etching time. This suggests that all the pores are connected somehow to the sample surface (as expected based on the fact that they were created by an etching reaction) and the micropore formation is entirely responsible for the increase in surface area.

The silicon *K*-edge XAS spectra for samples HF1, HF2, HF7, and HF9 are shown in the top panel of Figure 8-30. For reference purposes c-SiC and c-SiO$_2$ silicon *K*-edges were measured and are shown in the bottom panel of Figure 8-30 (normalized at 1847eV). The spectra (I_S/I_O) for samples HF1, HF2, HF7, and HF9 have been normalized at 1847.4eV, for comparison of the relative strength of the silicon-oxygen bonding to

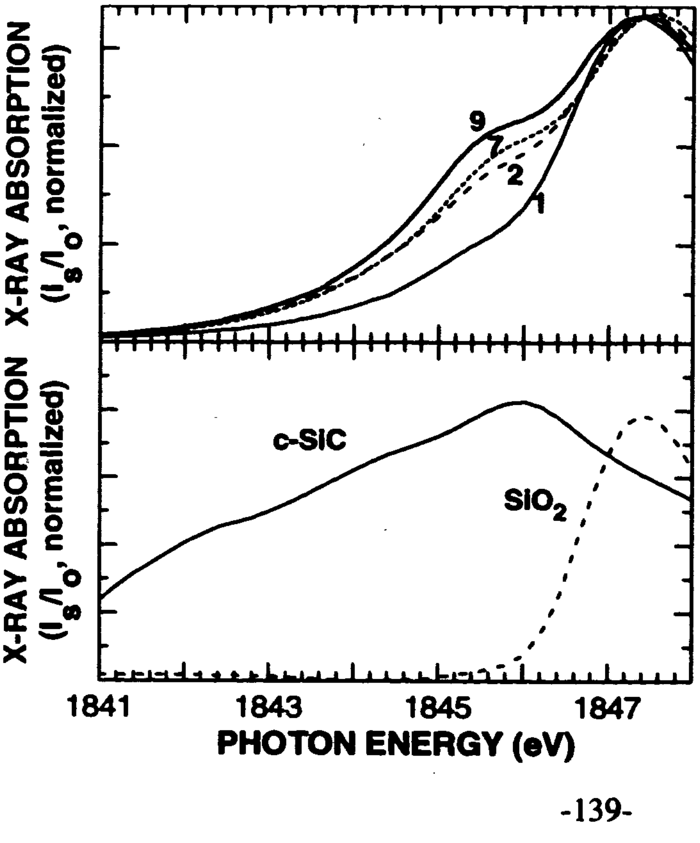

Figure 8-30. The top panel shows the Si K-edge for samples HF1, HF2, HF7, and HF9 (I_S/I_O normalized to 1847.4 eV). The bottom panel shows the Si K-edge for SiO$_2$ and SiC, (I_S/I_O normalized to 1847 eV).

silicon-carbon bonding. Samples HF2, HF7, and HF9 show a feature near 1845.5 eV, attributed to silicon-carbon bonding. This feature increases in relative intensity to the silicon-oxygen feature from sample HF2 to HF9. The stoichiometry change supports this percentage increase in silicon-carbon bonding. It is also believed that this silicon-carbon bonding increase is mainly a surface effect. The measurement has an estimated maximum penetration depth of about 1000Å. Thus, the surface of the material plays a significant role in the absorption signal. If a silicon-carbon passivating region is created on the surface of the pore walls, this would result in a changing of the relative silicon-carbon to silicon-oxygen signals in the *K*-edge. While the presence of carbon-carbon bonding in the material does not contribute to the silicon *K*-edge it may still be present, in addition to the silicon-carbon bonding.

If our view that these materials are a mixture of graphene sheets and Si-O-C network glass is true, then HF washing would only remove material from the Si-O-C regions. The SAX results show that the pores created by the HF washing reach a specific size and do not continue to increase further, implying that the surface of the pores will not further react with HF under these conditions. We believe that the F^- ions break all the silicon-oxygen bonds accessible. Thus, the HF etching reveals or creates a passivating layer. We believe it is this passivating layer which appears in the XAS *K*-edge data as an increase in silicon-carbon bonding. The decrease in silicon and oxygen content with respect to carbon content, as shown by elemental analysis, also supports this model.

The intensity of the SAX data and the magnitude of the BET surface areas suggest that these pores must be distributed throughout the bulk of the material. F^- ions are responsible for the formation of the pores and must be able to access the bulk of the material. There must be some passages which connect the micropores formed by HF etching. This is likely why Equation 5-6 was not sufficient to achieve a better fit to the SAX data. It assumes that the pores are noninteracting which is probably not the case.

Figure 8-31 summarizes the electrochemical measurements made on these materials. The first discharge and charge and second discharge are shown for cells made using materials HF1 through HF5. Included for comparison is data from sample 36, the material before any washing in water or HF. The slight differences between cells is within our error range, and should not be attributed to differences between the materials.

Despite the change in surface chemistry, pore morphology, and the slight change in stoichiometry, the voltage profile of these materials upon insertion of lithium did not change.

The conclusions concerning the results presented in this chapter will be summarized in Chapter 10. The next chapter presents the results from the pitch-polysilane blend study.

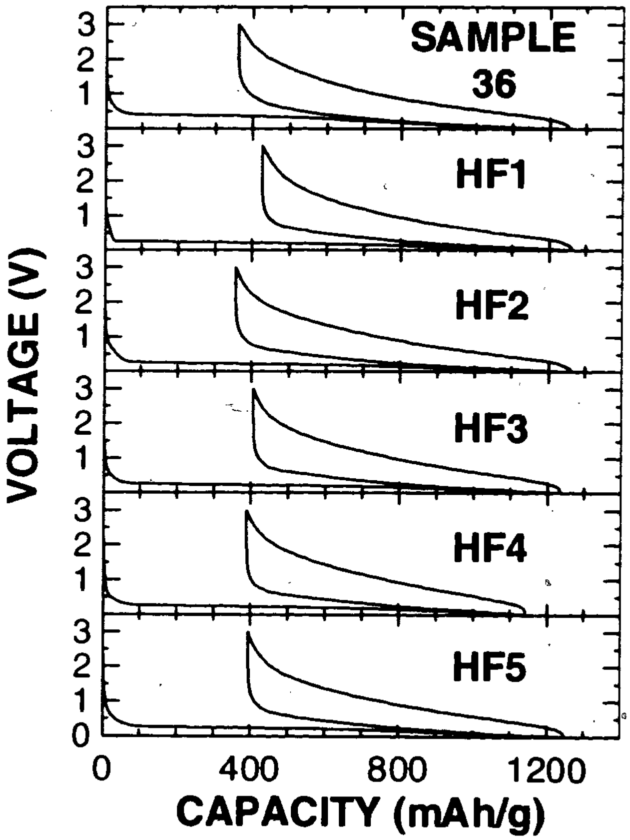

Figure 8-31. Voltage profiles for cells made from sample 34 and HF1 through HF5. Note that there is essentially no difference between the profiles.

CHAPTER 9

THE PYROLYSED PITCH-POLYSILANE BLENDS

During the course of the Si-O-C project, we also prepared materials from polysilanes. This was, in part, an effort to make the silicon nanodispersions in disordered carbon materials in an economical way. This chapter reports on the results of the various materials made in the methods described in Chapter 4.

Inspection of Figure 8-8 (open diamonds represent the pyrolysed blends) shows that these materials contain significant amounts of oxygen. This presence of oxygen was not expected and was likely introduced during the blend synthesis. Figure 8-8 also shows that the silicon to oxygen ratio is not a constant, ranging from outside the Q line to beyond the M line (<0.5 to >0.2). For these reasons, the main study of these materials (Section 9.1) uses the weight percent silicon as a metric. The effect of the oxygen is examined separately in Section 9.2. The precursors to these materials were quite different from polysiloxanes, and so another study was performed to determine the effect of changing the maximum pyrolysis temperature (Section 9.3).

9.1 THE MAIN BLEND STUDY

Figure 9-1a shows the XRD profile for a pyrolysed pitch sample. The strong (002) Bragg peak indicates that the graphene sheets are well-stacked. The (100) and (004) peaks can also be seen and although the (110) peak can barely be seen on this scale it is clearly visible on a larger scale. Figures 9-1b through 9-1g show XRD patterns for samples of series I (I1-I6), which contain the silane polymer $(Me_2Si)_{0.80}(PhMeSi)_{0.20}$ (polysilane-I or PS-I) in their precursor. Each sample has a different pitch to PS-I ratio (given as a weight ratio) in their precursor, as indicated in the figure. The derivatized pitch samples I1-5 all demonstrate characteristics of disordered carbons, indicated by broad (002) and (100) Bragg peaks in their XRD patterns. It is evident that the disorder in the materials increases

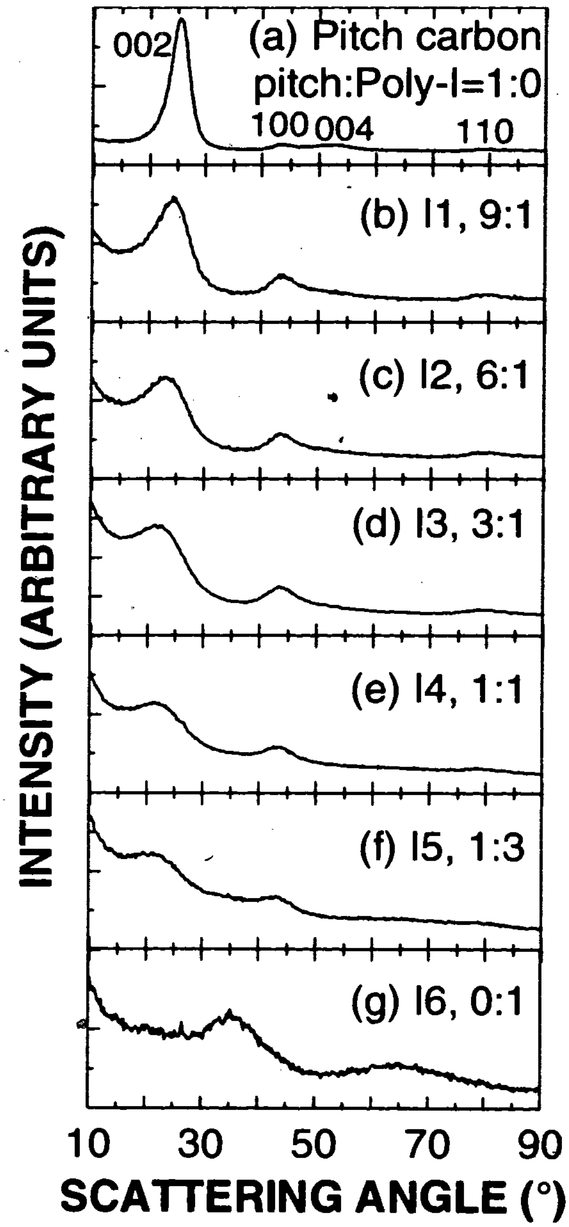

Figure 9-1. XRD profiles of heated pitch/PS-I blends as indicated on the figure. Different counting times were used, leading to different signal to noise ratios.

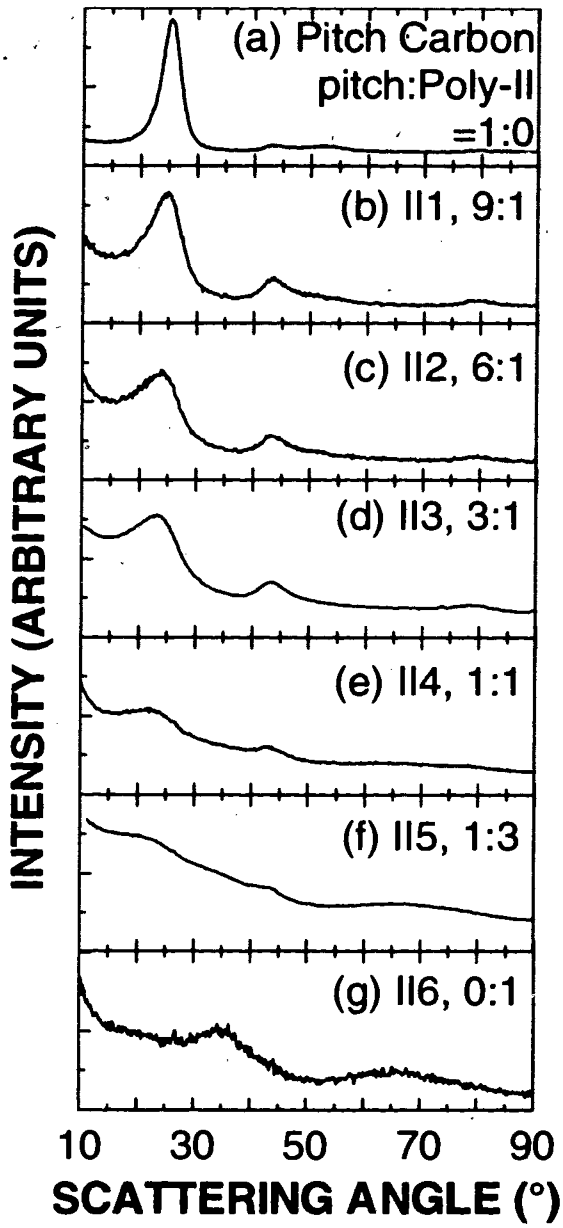

Figure 9-2. XRD profiles of heated pitch/PS-II blends, displayed as per Figure 9-1.

as the pitch to polysilane ratio decreases. There is no evidence for amorphous or crystalline silicon in the XRD profiles, suggesting that no large silicon clusters exist in these materials. Sample I6 (Figure 9-1g) is made by the pyrolysis of the polysilane alone (no pitch) and has a very different XRD profile which shows features suggesting that it may contain amorphous or highly disordered SiC. Upon close examination, the XRD profile for sample I5 may show slight features near 65° and 36°, indicative of some SiC with the disordered carbon.

Figure 9-2 shows XRD patterns for the samples in series II, which contain the silane polymer $(Me_2Si)_{0.53}(PhMeSi)_{0.47}$ (polysilane-II or PS-II). The pitch to PS-II ratios are indicated in the figure. Samples from series II have similar patterns compared to those in series I. However, because the char yield of PS-II is larger than PS-I (see Table 9-1), samples I1, I2, I3, ... respectively contain less silicon than samples II1, II2, II3 ... . Thus, the XRD profile for I5 resembles that of II4, since they have similar silicon contents. The same is true for samples I3 and II2. Since the precursors to samples II6 and I6 contain only polysilane, it is not surprising that their XRD profiles are similar. Sample II5 appears to be an intermediate between samples II4 and II6, suggesting that it may contain disordered carbon regions with silicon nanodispersions as well as amorphous SiC. The XRD data for samples I1 through I5 and II1 through II4 suggest that the silicon atoms in these materials are probably nanodispersed in unorganized regions of disordered carbon structures; that is to say, they may be similar to the CVD materials. Note, however, that the blends contain some oxygen.

Figure 9-3 shows the voltage profiles (first and second discharges and first charge) for cells of the pyrolysed pitch sample and for samples I1-I6. Figure 9-4 shows the voltage profiles for cells of the series II samples. The electrochemical properties are summarized in Table 9-1. The reversible capacities show a definite increase from the pyrolysed pitch (364 mAh/g) with a maximum of 640 mAh/g (sample II5). The irreversible capacities also show a marked increase, from 49 mAh/g for the pyrolysed pitch to 270 mAh/g for sample II5. These materials demonstrated relatively small hysteresis between charge and discharge cycles. On average, the difference between charge and discharge potentials is about 0.4V for these cells. The irreversible capacity and hysteresis are discussed further in the next section.

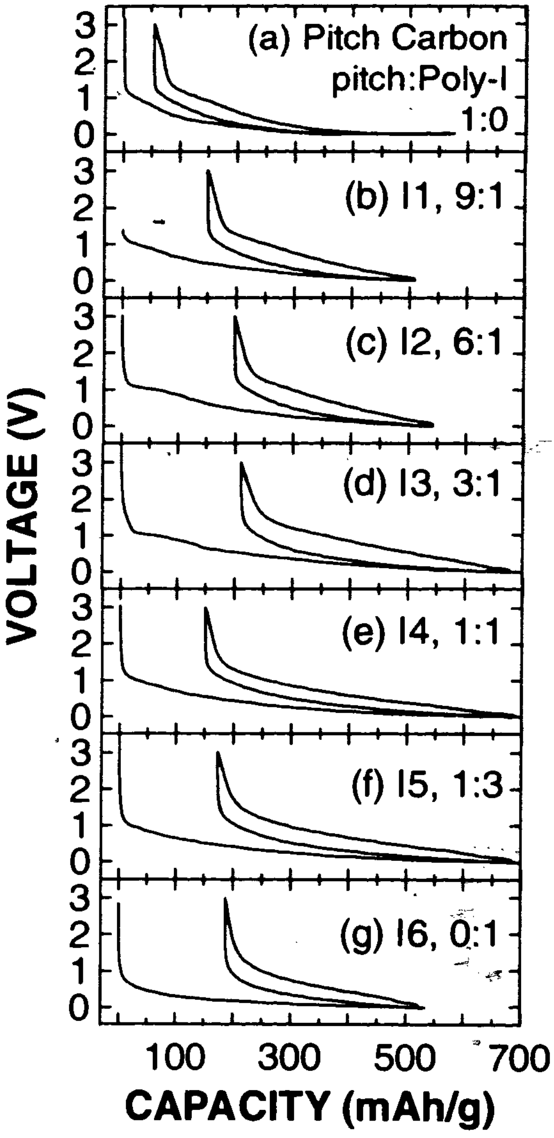

Figure 9-3. Voltage profiles of cells made from the series I samples, as indicated on the figure.

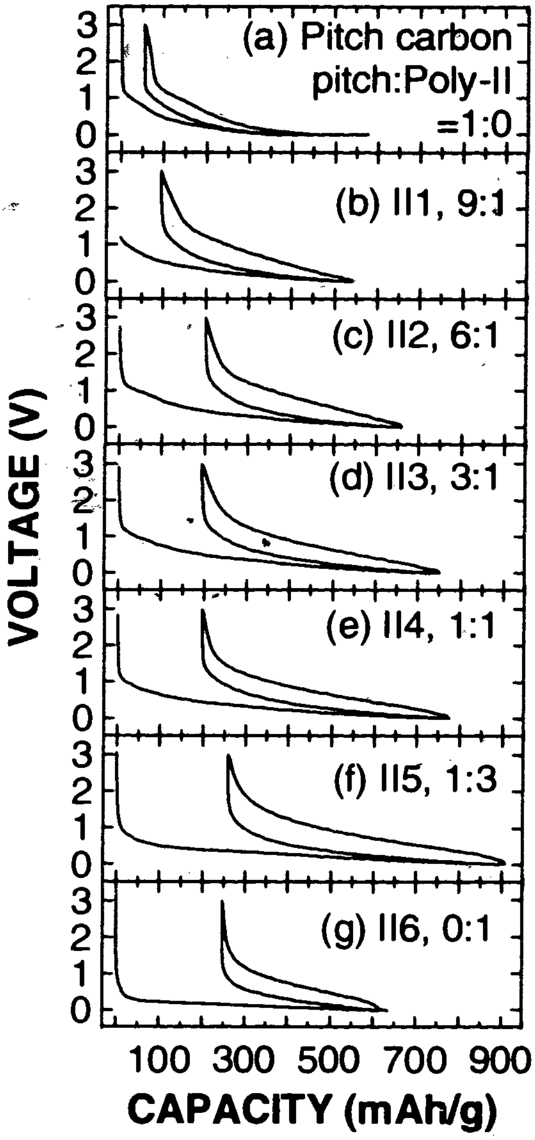

Figure 9-4. Voltage profiles of cells made from the series II samples, as indicated on the figure.

Table 9-1. Pitch to polysilane ratios, silicon weight percentages after pyrolysis, reversible (Q_{rev}) and irreversible (Q_{irr}) capacities, and char yield of the pyrolysed pitch-polysilane blends.

Sample	Polysilane	Pitch:Polymer (by weight)	Si[c] (weight %)	Q_{rev} (mAh/g)	Q_{irr} (mAh/g)	Yield (%)
pitch	--	1:0	0	364	49	45
I1	Poly-I[a]	9:1	1.8	350	150	42
I2	Poly-I	6:1	4.3	340	200	40
I3	Poly-I	3:1	8.7	470	210	34
I4	Poly-I	1:1	16.7	543	137	34
I5	Poly-I	1:3	24.2	520	180	26
I6	Poly-I	0:1	40.3	341	186	24
II1	Poly-II[b]	9:1	6.2	440	120	46
II2	Poly-II	6:1	9.2	450	210	44
II3	Poly-II	3:1	13.4	550	197	49
II4	Poly-II	1:1	26.7	577	192	58
II5	Poly-II	1:3	25.1	640	270	66
II6	Poly-II	0:1	48.8	364	246	77

[a] Poly-I = $(Me_2Si)_{0.80}(PhMeSi)_{0.20}$ [b] Poly-II = $(Me_2Si)_{0.53}(PhMeSi)_{0.47}$ [c] After heating to 1000°C

Figures 9-5a and 9-5b respectively show the differential capacity versus voltage for the first charge of some of the cells shown in Figures 9-3 and 9-4. These are similar to Figure 7-16, for the CVD-I materials. All the data shown in Figure 9-5 have been smoothed with a 5 point running average. These cells were cycled at higher currents and the data was recorded with lower precision than the cells of the CVD materials, so the differential capacity plots are quite noisy. As with those materials, we can see that there is additional capacity

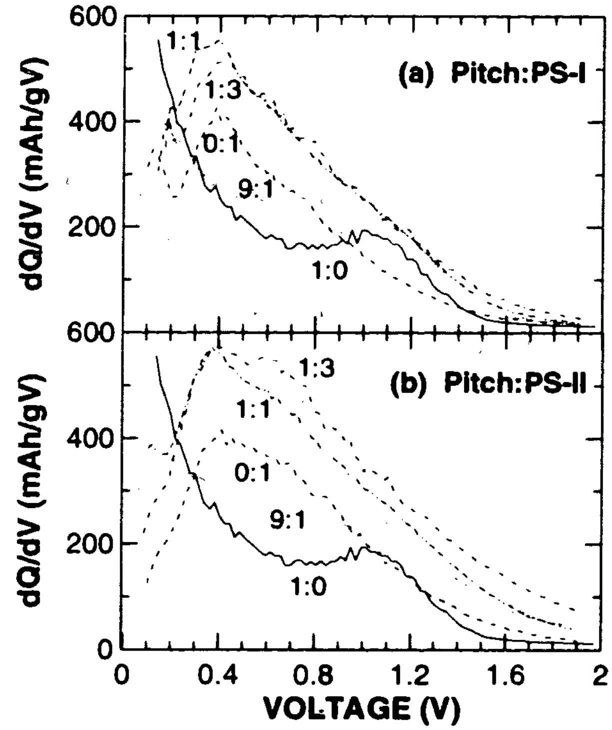

Figure 9-5. Differential capacity plotted versus voltage for the first charge of cells made from series (a) I and (b) II materials. Additional capacity is centered near 0.4V, as was the case for the CVD materials (Fig. 7-16).

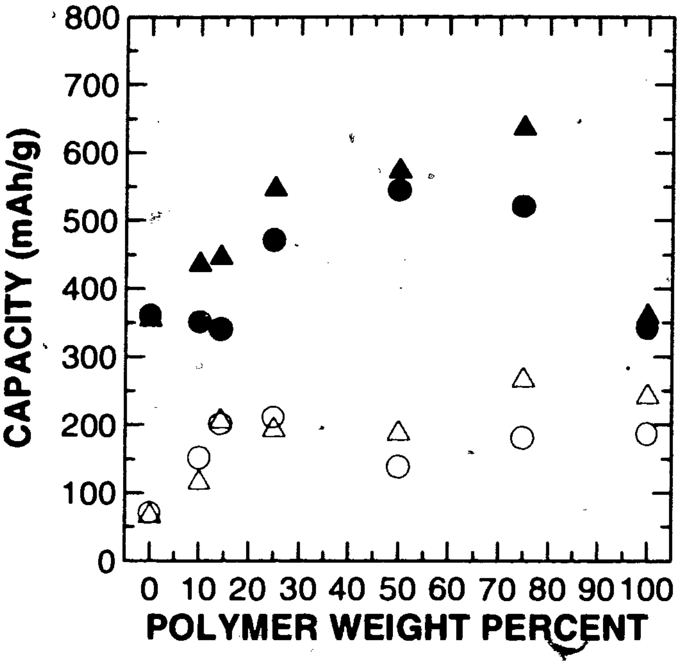

Figure 9-6. *Reversible (Q_{rev}) and irreversible (Q_{irr}) capacities versus silane polymer weight percent (before pyrolysis) for the pitch blends prepared with PS-I and PS-II as indicated by the figure legend.*

located near 0.4V. Generally, this additional capacity peak increases with decreasing pitch:polysilane ratio, with the exception of the pure polysilane (0:1). There, the peak decreases in magnitude because of the loss of capacity due to SiC. There is also an increase in capacity between 0.6 and 0.8V. With the series II materials the additional capacity near 0.6V is more pronounced and is especially obvious for sample II3 (1:3). The CVD materials (Figure 7-16) did not show this. This will be discussed in the next section.

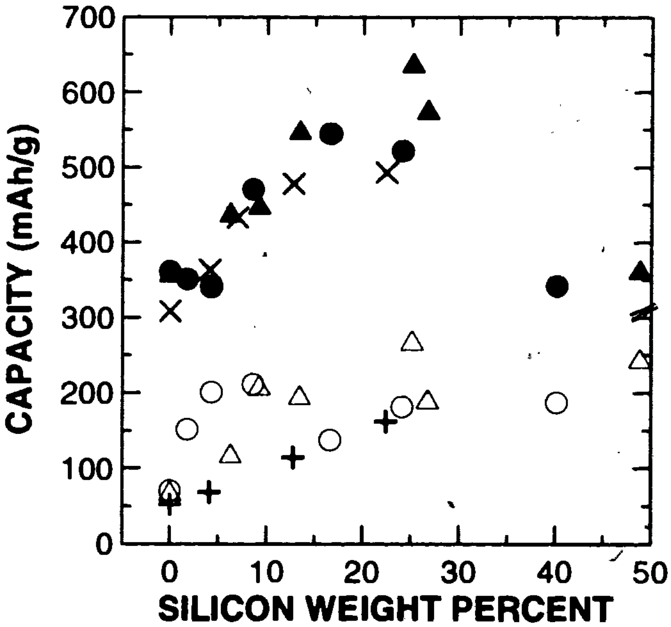

Figure 9-7. *Q_{rev} and Q_{irr} capacities versus silicon weight percent (after pyrolysis) for the pitch blends prepared with PS-I and PS-II. Also included are data for CVD-I samples.*

The effect of incorporating silicon into pitch carbons in sample series I and II are summarized in Figures 9-6 and 9-7. In Figure 9-6 the cell capacities are plotted as a function of polysilane weight percent in the blend (before pyrolysis). Figure 9-7 shows the capacity versus the silicon content (as weight percent) in the final sample. As can be seen, the reversible capacity for lithium insertion increases with the silicon content up to about 30% by weight. For sample series I, a reversible capacity of about 540 mAh/g is obtained when the polymer content is about 50% by weight, or when the silicon content is between 15 to 20% by weight. For sample series II, reversible capacities around 600 mAh/g were obtained when the polymer content is between 50 to 75% by weight, or when the silicon content is between 20 to 30% by weight. These reversible capacities are significantly larger than that of the heated pitch sample, $Q_{rev} \approx 360$ mAh/g. Figure 9-7 shows that the reversible capacities of the silicon-containing carbons increase with silicon content, but to a smaller extent than the increase observed in the reversible capacities. For most of the derivatized pitch samples, Q_{irr} increases to 150-250 mAh/g, compared with $Q_{irr} \approx 50$ mAh/g for the pitch carbon cell.

For comparison, data from some of the CVD-I materials have also been plotted in Figure 9-7. It appears that these materials follow roughly the same trend. As was detailed in Chapter 7, the initial increase in capacity seen in Figure 9-7 (silicon $\leq 15\%$ by weight) corresponds to roughly 1.5 lithium atoms per silicon atom. Thus, it appears that the inexpensive method used here can synthesize materials which duplicate the performance of the CVD materials which were initially so exciting, but not commercially viable. However, these pyrolysed blends contain significant amounts of oxygen and this will be discussed next.

9.2 OXYGEN IN THE PYROLYSED BLENDS

Because the Si-O-C samples were displayed on a ternary stoichiometric map in Chapter 8 it is useful to view the materials presented here in the same manner. Figure 9-8 shows the pitch-polysilane blend materials on a section of the ternary map used in Chapter 8. The bottom 'half' of the diagram has been removed and the resulting diagram has been enlarged to allow all the blend samples to be shown.

The oxygen weight percentages were determined by subtracting the measured silicon and carbon weight percentages from 100%. Although the error associated with the oxygen percentages is the same as the silicon and carbon (estimated to be as high as ±3%), the oxygen content was not directly measured. Oxygen data is plotted with 3% error bars attached because we are least sure of the oxygen content (it was not directly measured).

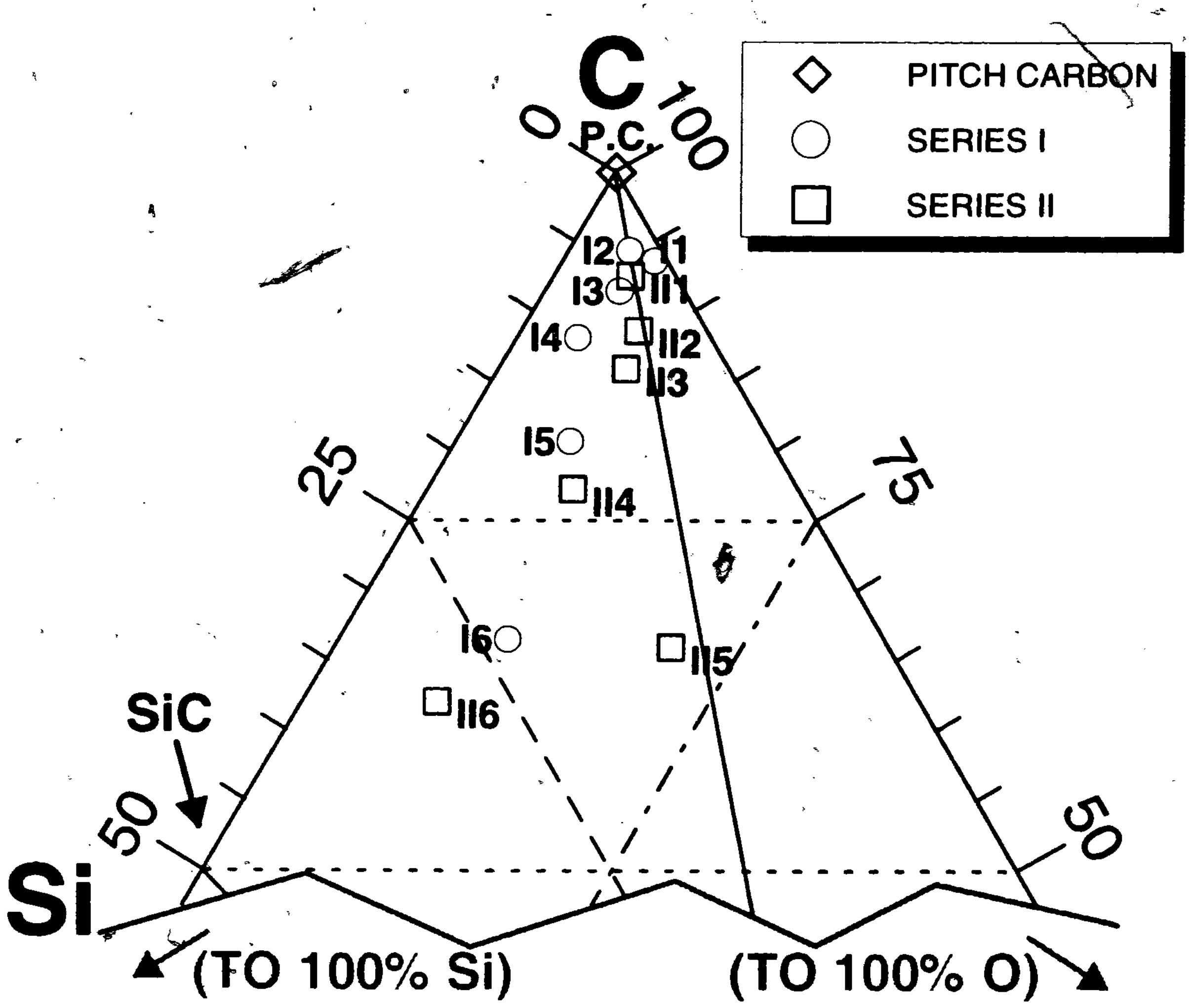

Figure 9-8. The location of each pyrolysed pitch-polysilane blend material (in atomic %) on a section of the ternary stoichiometric map used in Chapter 8.

It is clear that these materials contain oxygen and, from Figure 9-8, there appears to be no correlation between the silicon and oxygen contents. The silicon to oxygen ratio increases from less than ~1/2 to greater than ~2. Figure 9-9 shows the atomic percent silicon plotted versus the atomic percent oxygen. It can be seen that there is a slight increase in oxygen content with silicon content. However, given the large change in silicon content, there is essentially no change in the oxygen content, with the exception of sample II5 (~20% oxygen).

In Chapter 8 it was stated that the irreversible capacity in those samples appeared to increase with the oxygen content. Figure 9-10 shows the irreversible and reversible capacities, plotted versus the atomic percent oxygen. It is clear that the irreversible capacity in these materials increases with the oxygen content. In Chapter 8 it was also observed that the discharge voltage experienced little change, while the charge voltage increased. That is, the charge-discharge hysteresis increased with increasing oxygen content. Figure 9-11 shows the charge-discharge hysteresis versus

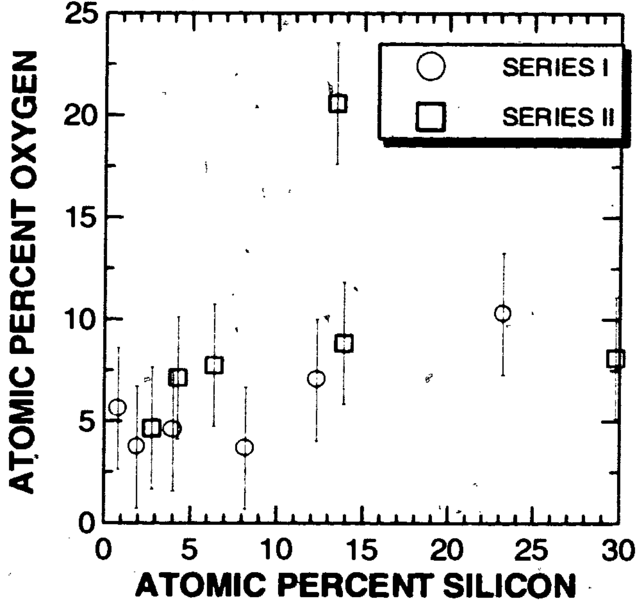

Figure 9-9. The at. % oxygen plotted versus the at. % silicon in the series I and II materials.

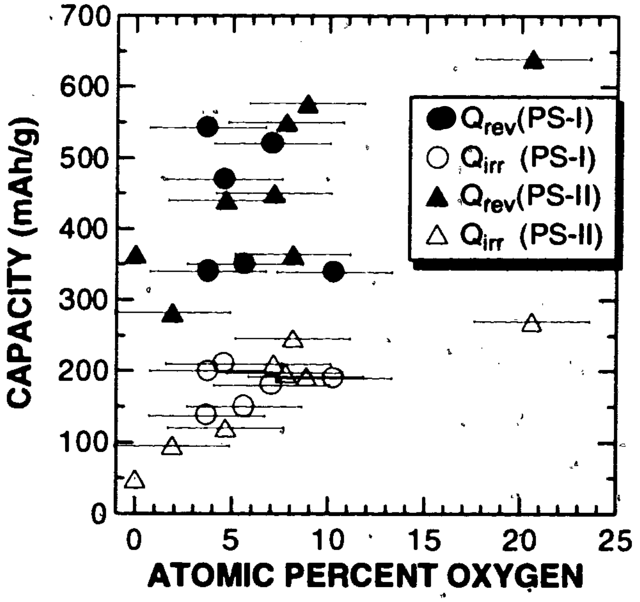

Figure 9-10. The reversible and irreversible capacities for the series I and II materials versus the at. % oxygen.

the oxygen content. Again, the trends observed for the pyrolysed polysiloxanes hold for these materials.

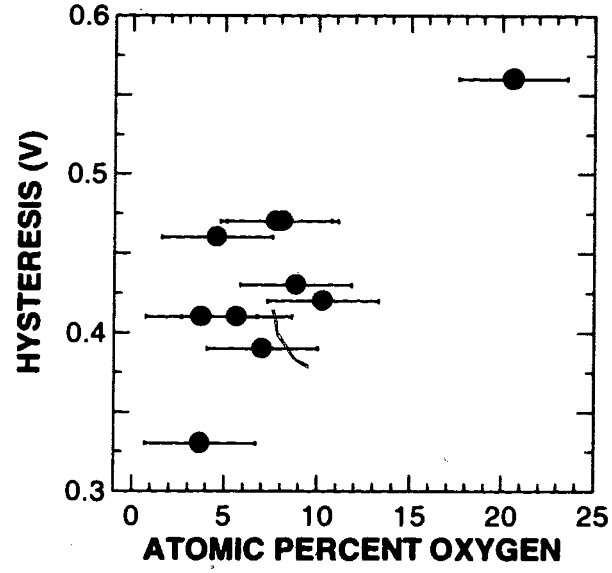

Figure 9-11. The charge-discharge hysteresis vs. the at. % oxygen.

Thus, it appears that these materials are similar to both the CVD materials and the silicon oxycarbide glasses. The electrochemical data contains additional information. As was stated in Section 9.1, there is an additional capacity (observed in differential capacity versus voltage plot; Figure 9-5) near 0.6 V for the pitch blends that was not observed for the CVD materials (Figure 7-16). Figure 9-12 shows the differential capacity plotted versus voltage (charge only) for samples A, D, I4, and II4 and the pitch carbon (P.C.). The data for Sample A (CVD of benzene alone; contains no silicon) and the pitch carbon look essentially the same. Sample D does not exhibit the additional capacity near 0.6V, which can be seen for samples I4 and II4. Figure

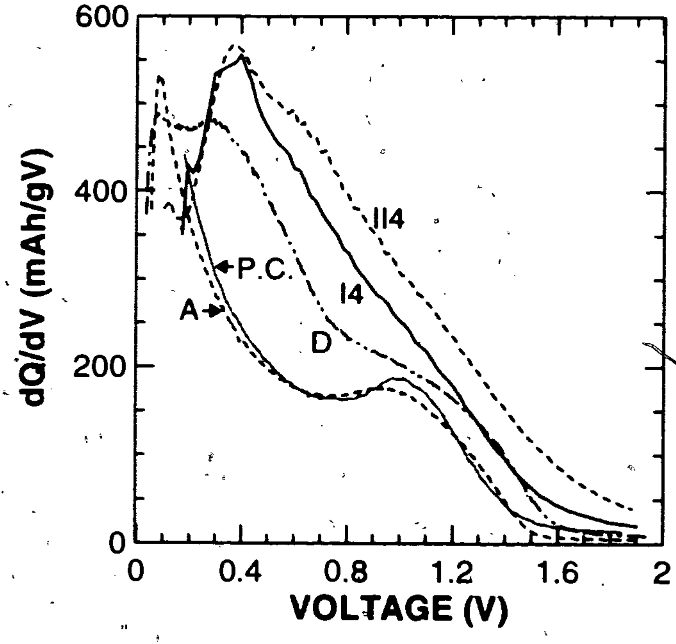

Figure 9-12. Differential capacity plotted versus voltage for samples A, D, I4, and II4, and the pitch carbon (P.C.), as indicated.

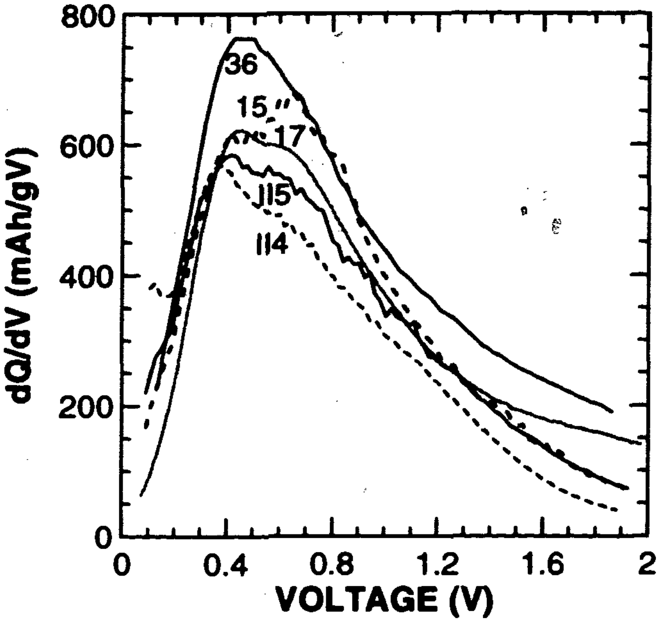

Figure 9-13. The differential capacity versus voltage for samples II4, II5, 15, 36, and 17 as indicated.

9-13 shows the differential capacity versus voltage for samples II4, II5, 15, 36, and 17. Samples 15, 36, and 17 were pyrolysed polysiloxane samples which lie between the D and T lines (Figure 8-9 and Section 8.2.2). The additional capacity near 0.6V is evident in all of these samples. Thus, the 0.6V feature appears to be correlated to the oxygen content.

Another inspection of Figure 9-5 shows that the series I samples exhibit smaller 0.6V features than the corresponding series II samples. Figure 9-8 shows that the series I samples typically contain less oxygen than the corresponding series II samples.

In an attempt to better understand the local chemical environment of the silicon atoms in these materials, XAS near the silicon *K*-edge was measured. Figures 9-14 and 9-15 respectively show the *K*-edge spectra for samples of series I and II. The top panel in each shows the unmodified total electron yield (TEY) signal plotted as a function of the incident photon energy. In the bottom panel of each the same data is shown normalized at 1847.2 eV. SiO_2, Si, and SiC reference spectra have been presented previously (Figures 7-10 and 8-30). Each sample shows evidence for silicon-carbon bonding (centered near ~1843 eV) and silicon-oxygen bonding (~1847 eV). There is no evidence for any silicon-silicon bonding (~1839 eV) as there was in the CVD-I materials (Figure 7-9). This shows that the local chemical environment of the silicon atoms in the blends is somewhat different than in the CVD materials, as suggested by the differential capacity data.

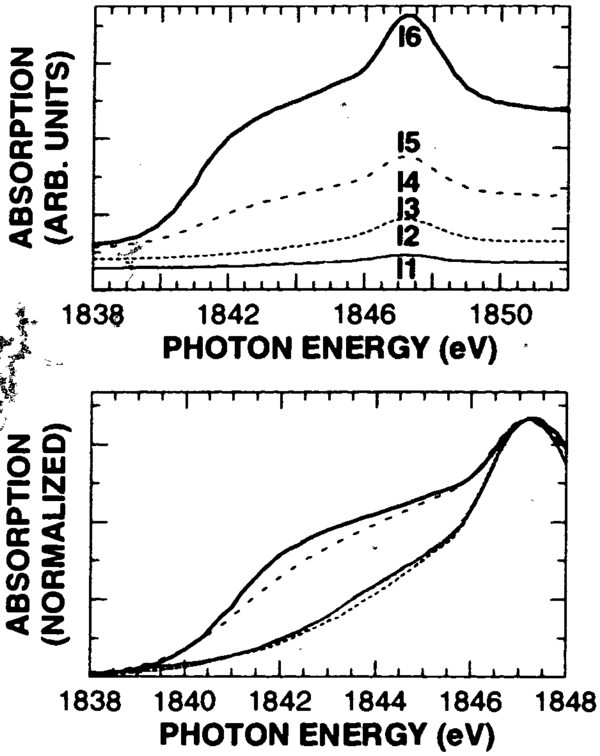

Figure 9-14. *The silicon K-edges for the series I materials. The top panel shows the absorption data (I_S/I_O) as measured. The bottom panel shows the same data normalized at 1847.2 eV.*

For both series of samples the overall intensity of the silicon K-edge increases with the silicon content. This should not be surprising, considering that the total electron yield is proportional to the amount of silicon absorbing X-rays and emitting electrons (Chapter 5).

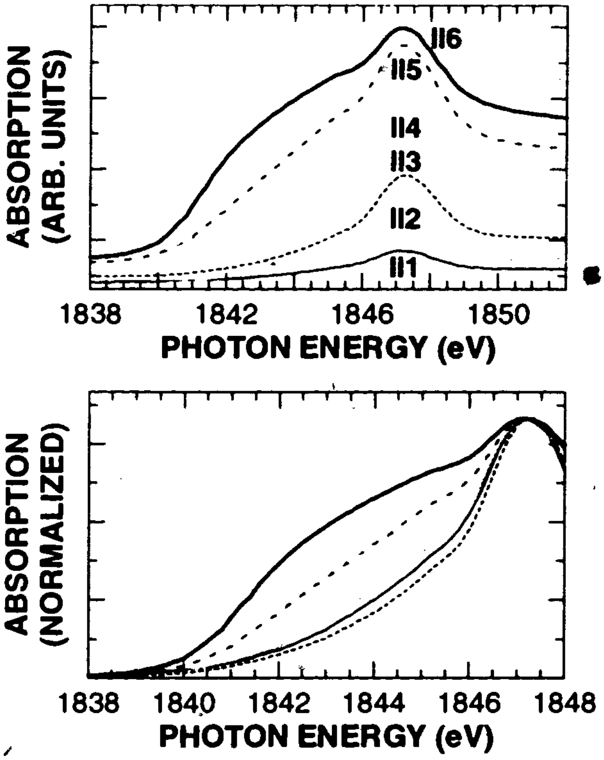

Figure 9-15. *The silicon K-edges for the series II materials. The top panel shows the absorption data (I_S/I_O) as measured. The bottom panel shows the same data normalized at 1847.2 eV.*

In the bottom panels of Figures 9-14 and 9-15 we can see the comparative intensity of signals we attribute to silicon-carbon bonding (~1843 eV) and silicon-oxygen bonding (~1847 eV). The overall trend, from the first material to the last is the same for series I and II. The magnitude of the 1843 eV feature increases (relative to the silicon-oxygen bonding feature) with the decrease of the pitch:polysilane ratio. However, there is one exception. The samples with the ratio of 3:1 (I3 and II3) show a noticeable decrease in the relative intensity of the silicon-carbon bonding feature. These slight deviations in the intensity near 1843 eV are attributed to the normalization choice (~1847.2 eV; silicon-oxygen bonding). The ~1847 eV feature should fluctuate slightly, like the oxygen content.

Comparison to Figures 8-23 and 8-30 suggests that the local chemical environment of the silicon in these materials is more like that in the Si-O-C materials than the CVD materials. The XRD and voltage profiles suggest that these materials are similar to the CVD materials. Thus, the evidence collected suggests that: materials I1 through I5 and II1 through II3 are disordered carbons containing nanodispersed Si-O-C; samples II4 and II5, contain SiC, Si-O-C, and disordered carbon; and samples I6 and II5 contain SiC, Si-O-C, and possibly some disordered carbon.

Because the materials in this study are somewhat different from the Si-O-C glasses, a heat treatment study was done on the precursor to sample I5. This study is detailed next.

9.3 MAXIMUM PYROLYSIS TEMPERATURE STUDY

To investigate how the materials change with heat treatment temperature, we pyrolysed blends at maximum temperatures of 600, 800, 1000, and 1100°C. The XRD patterns for the blend used to make sample I5 (Pitch:PS-I in the ratio of 1:3) heated to these temperatures are shown in Figure 9-16. The weak (002) and (100) peaks for the material made at 600°C shows that there are very few, small graphene sheets in the sample at low temperature. As the maximum pyrolysis temperature increases, these peaks become more well defined, although they are still indicative of a very disordered carbon with few graphene sheets stacked in a parallel fashion. Also visible at 800°C and higher is a feature near 36°, which is attributed to a small amount of disordered silicon carbide.

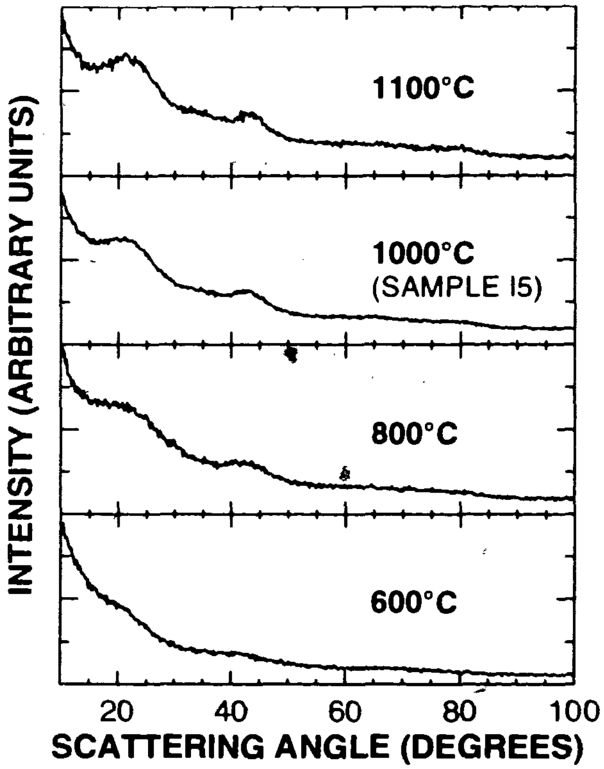

Figure 9-16. XRD patterns for samples made by pyrolyzing the pitch:PS-I (1:3) blend to various maximum temperatures as indicated on the graph.

Figure 9-17 shows the voltage profiles for the same samples presented in Figure 9-16. The 600°C sample shows essentially no reversible capacity and an irreversible capacity of about 300 mAh/g. At 800°C the material shows reversible and irreversible capacities of about 650 mAh/g and 350 mAh/g, respectively. The large hysteresis is indicative of carbonaceous materials prepared in this temperature range and, as discussed in Chapter 2, is thought to be due to the presence of hydrogen in the material (Zheng, 1996a). There is essentially no change in the material between 1000 and 1100°C. Thus, in this range the material exhibits a temperature dependence much like a pitch-based carbon, although at the higher temperatures (≥1000°C) the capacity is modified by the presence of silicon.

This completes the presentation of results. The next chapter concludes the thesis and makes recommendations for future work.

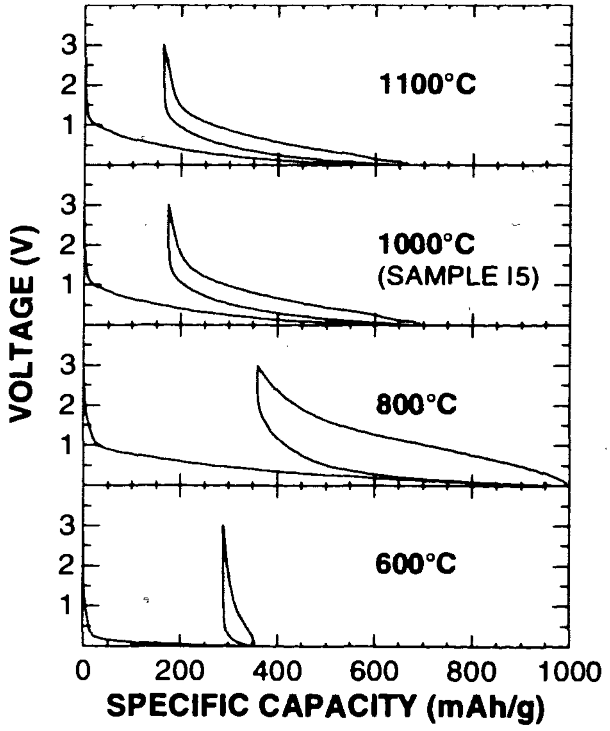

Figure 9-17. The voltage profiles for the same samples presented in Figure 9-16.

CHAPTER 10

CONCLUSION, CONTRIBUTIONS, RECOMMENDATIONS

This chapter summarizes the conclusions for the CVD, Si-O-C, and pitch-polysilane blend work presented in this thesis. The first section presents the conclusions and details the specific contributions this thesis has made. Section 10.2 outlines some recent work of relevance to this field of study. Finally, Section 10.4 makes some recommendations for future work based on the findings of this thesis.

10.1 CONCLUSIONS AND CONTRIBUTIONS

All of the work done on these carbonaceous materials containing silicon and oxygen has led us to a low temperature, structural schematic "phase" diagram. Presented in Figure 10-1, it should be viewed as an artist's conception of possible structures. For example, in the ball and stick schematics all of the bonds have been 'pressed flat' into two dimensions, although they should obviously exist in three. This was done to show, more clearly, the disorder which exists in these materials. Also, the graphene sheets have been shown to be separated somewhat from the odd shaped silicon, SiC, and Si-O-C glass clusters and not in the intimate mixture which we believe exists. This was done for practical reasons, and also to show how disorder likely exists in the graphene sheets.

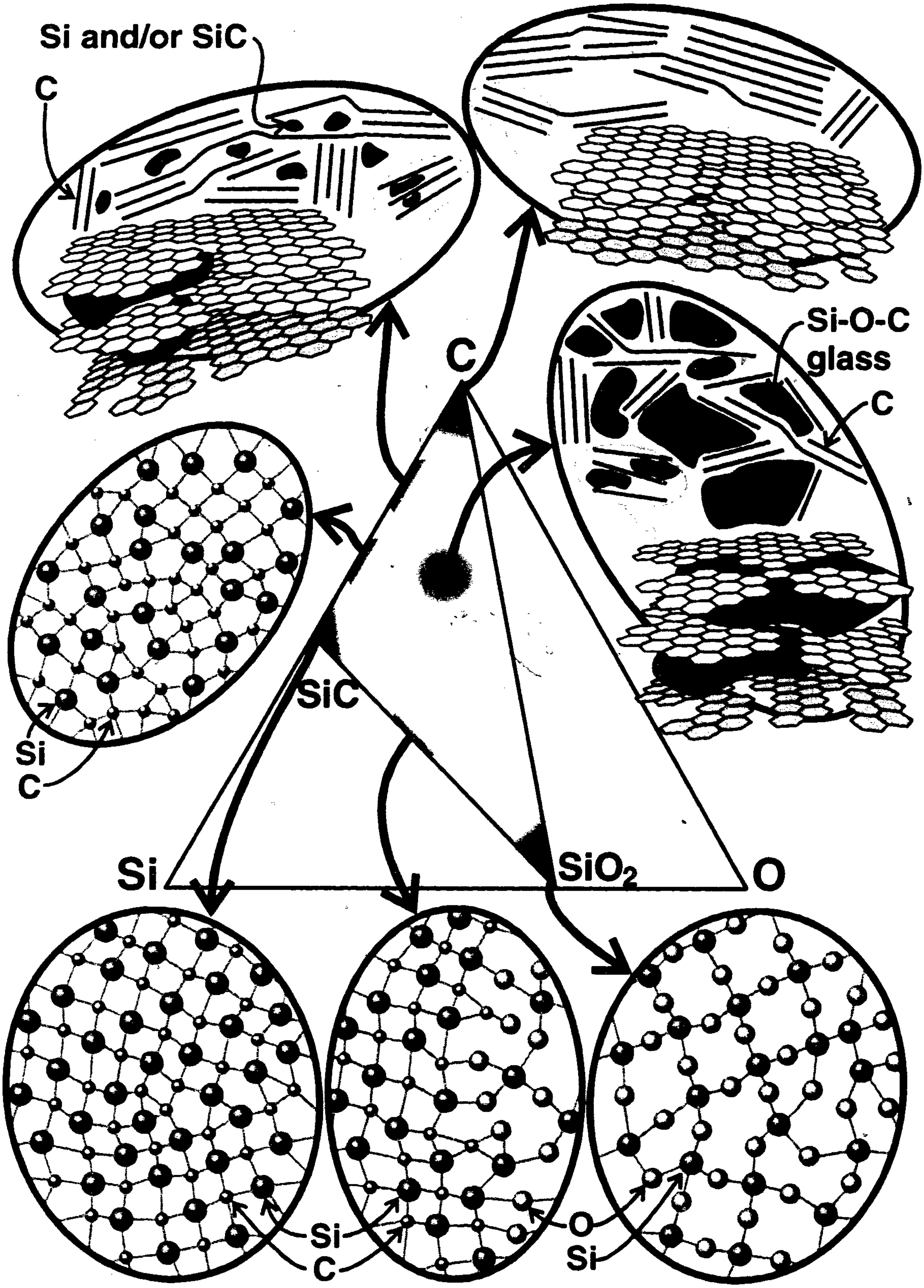

Figure 10-1. A schematic structural phase diagram based on the materials presented in this thesis. The structures shown should be treated as an artist's conception of possible structures.

10.1.1 The CVD Materials

With the first CVD apparatus we prepared silicon-carbon materials at 950°C containing up to 11 at. % silicon. Evidence has been presented which shows conclusively that the silicon does not exist as a-Si, c-Si, c-SiC, a-SiC, or a silicon oxide, nor is it contained within the regions of organized carbon. Since the carbon is disordered, we suggest that the silicon is located in the unorganized regions, as shown in Figure 2-12. If the silicon were located in these 'pockets' then it would have more carbon neighbors than in SiC and may therefore donate more electrons to these carbon atoms. The silicon *L*-edge XAS results support this. The silicon *K*-edge results suggest that some of the silicon exists in small clusters in which some silicon atoms are bonded only to other silicon atoms. This has led us to the conclusion that these materials are best described as *disordered carbons containing nanodispersed silicon.* In electrochemical test cells, the silicon performs as hoped, increasing the specific capacity (to ~550 mAh/g) of the materials beyond that of a disordered carbon prepared in the same way.

The second CVD apparatus was not successful in surpassing or even duplicating the concentration of nanodispersed silicon in the disordered carbons synthesized. The different conditions in this apparatus have made materials with similar silicon contents although their reversible capacities were lower than CVD-I materials with the same stoichiometry. When silicon concentrations are increased beyond a certain composition, the reversible capacities of the materials decrease. The XRD patterns of the samples with slightly more silicon than the material with the maximum capacity show no evidence for silicon carbide. After TGA in air these materials turned light grey, implying that there was still some carbon present as silicon carbide. It is likely that as the silicon concentration in these materials increases, nanodispersed silicon and nanodispersed silicon carbide both exist in the unorganized carbon regions. As the silicon concentration is *further* increased, silicon carbide becomes visible in the XRD profiles. Thus, the deposition conditions in the first apparatus appear more favourable for the synthesis of silicon nanodispersions in disordered carbons.

The CVD work has led to a new, and presumably metastable (since it does not appear in the silicon-carbon phase diagram (Moffat, 1990)) compound: disordered carbons containing nanodispersed silicon. We found no reports of materials like them elsewhere. From the review by Marinkovíc, it is likely that others have made silicon nanodispersions in disordered carbons although it is unlikely that they were detected (Marinkovíc, 1984).

Although the CVD materials have excellent characteristics, because of the expense of the CVD process these materials are unlikely candidates for use in practical lithium-ion cells. Still, Moli Energy (1990) Ltd. benefited from our work and patented these materials and their synthesis method internationally (Wilson, 1994b).

10.1.2 The Silicon Oxycarbides

By studying the decomposition process of many siloxane polymers, we developed a simple method for estimating the chemical composition of chars prepared from highly cross-linked polysiloxanes. The method relies on two inputs and one assumption:

1. The initial polymer stoichiometry,
2. The char yield,

and

3. That only C and H atoms evolve during pyrolysis.

Based on the model, the predicted stoichiometries for 15 of 18 chars were found to agree well with experimentally determined stoichiometries. We believe that these rules can serve as a useful "rule of thumb" for those working on chars and ceramics prepared from pyrolysed polysiloxanes.

The pyrolysed materials 34, 35, and 36 prepared from different polymers have the same final stoichiometry and were shown to have similar XRD, XAS, and electrochemical signatures. Therefore, we believe it is the final char stoichiometry, not the initial polymer structure or composition which dominates the properties of the char. This fact may have importance for those wishing to optimize the synthesis of a particular char or ceramic by moving to less expensive initial polymers which give the same char stoichiometry.

The HF washing of one silicon oxycarbide glass (sample 36) introduced micropores into the bulk of the material, which resulted in up to a 40% mass loss. Despite the presence of more than enough HF to react with all the oxygen in the material, there was little change in the ratio of silicon to oxygen, although the fractions of silicon and oxygen decreased slightly with respect to the fraction of carbon present. The lack of continued mass loss with time and the silicon *K*-edge data suggests that a silicon-carbon passivation surface is created or revealed by etching. We believe that it is this passivation surface which prevents the further etching of the material.

Despite the change in surface chemistry, pore morphology, and the slight change in stoichiometry, the voltage profile of these materials upon insertion of lithium did not change. Thus, it is the bulk, and not the surface, of these Si-O-C materials which is involved in the reversible and irreversible lithium reactions. Our initial hope of a method to change the stoichiometry of the glasses at room temperature, and their electrochemical properties, was not realized. This has shown us that, unlike with carbons, the surface of these materials does *not* play an important role in the irreversible capacity.

This work may be of interest to those developing new molecular sieves or others working with silicon oxycarbides. Dow-Corning has decided to file a patent on this pore creation process, based on our findings.

After a comprehensive study of the electrochemical properties of materials containing silicon, carbon, and oxygen, it is our opinion that the most commercially relevant materials contain very little oxygen (see Section 10.1.3). Although materials with higher reversible capacities can be found near 25% silicon, 45% carbon, and 30% oxygen, they also have higher irreversible capacities and larger charge-discharge voltage hysteresis. These negative properties appear to be linked to the oxygen content in the samples, as was shown in Figures 8-16, 8-17, and 8-18. Thus oxygen content should be minimized in order to make the most relevant materials. Perhaps some of the lithium is consumed by oxygen to make local atomic arrangements resembling those found in Li_2O. Such a reaction may be mostly irreversible.

Dow-Corning Ltd. benefited from our collaboration and decided to file for a patent based on our polysiloxane work (Dahn, 1996a). They also filed for a patent on some polysilazane work we did (Dahn, 1996d), which was not presented in this thesis for reasons of relevance (polysilazanes also contain nitrogen). Moli Energy (1990) Ltd. benefited from our preliminary work on polysiloxane pyrolysis and filed two patents based on those findings (Wilson, 1994c; Xue, 1995b).

10.1.3 The Pyrolysed Pitch-Polysilane Blends

The XRD patterns of the products from the pyrolysis of the pitch-polysilane blends showed characteristics of disordered carbons. This suggested a nanodispersion of silicon atoms in the pitch-based disordered carbon structure. Electrochemical tests showed that these materials have a roughly linear dependence of reversible capacity for lithium insertion on silicon content (≤ 20 wt. % Si). The maximum reversible capacity attained was over 600 mAh/g. For the lower polysilane weight percent materials, the XRD profiles appeared identical to the materials made by CVD. Elemental analysis showed that these materials contained significant amounts of oxygen. The electrochemical behaviour (as detailed by the differential capacity plots) shows that the pyrolysed blends are not identical to the CVD materials. The silicon *K*-edge results confirm this, showing that the local chemical environment of the silicon atoms in the pyrolysed blends is more closely related to some of the Si-O-C materials. Unlike previously made nanodispersions of silicon, these materials are probably nanodispersions of silicon oxycarbides in pregraphitic carbons. They exhibit higher reversible capacities than the materials made by CVD and can be made at a much lower cost. Dow-Corning benefited from this aspect of our collaboration also, and has filed one patent on our pitch-polysilane blend work (Dahn, 1996b) and a second on related work we did on polysilane pyrolysis (Dahn, 1996c).

10.2 RECENT WORK

Over the course of this work, others improved the performance of disordered carbons (Zheng, 1996d; Xing, 1996c). One of the major drawbacks remaining was the relatively high irreversible capacities of these materials. By a novel synthesis and cell assembly technique, Xing *et al.* were able to reduce the irreversible capacity of disordered pyrocarbons from around 200 mAh/g to about 50 mAh/g (Xing, 1996d). Typically, these carbons are made by pyrolysis under flowing argon at atmospheric pressure. In the new process these carbons are pyrolysed under vacuum and, after cooling, are exposed only to argon at atmospheric pressure. The samples are kept sealed from the room atmosphere while they are transferred into an argon filled glove box. In this way the cells are assembled without the carbon electrode ever coming into contact with the atmosphere. The irreversible capacity in carbons is typically attributed to lithium consuming reactions on the surface of the carbon (Section 6.2.1). Xing *et al.* showed that the irreversible capacity in disordered carbons was directly correlated to exposure of the material to CO_2, O_2, and air. They claim that the irreversible capacity in hard carbons arises from electrolyte decomposition on nominally clean carbon surfaces and reactions with surface groups which form on carbons when exposed to reactive gases. Thus, the amount of irreversible capacity caused by reactions with these surface groups is dependent "on the gas exposure time and involves reactions with species such as hydroxyl, carboxyl functional groups or adsorbed water" (Xing, 1996d). Now that a method has been devised to reduce the irreversible capacities in these carbons, they are prime candidates for use in practical lithium-ion cells.

Other recent advancements involve anode materials which do not contain any carbon. In a patent filed by Fujifilm Celltech Co., Ltd., Idota *et al.* describe the synthesis of hundreds of tin (and other group IV) oxides and oxide composite glasses (Idota, 1994). They claim that the reversible reaction of lithium with such oxides are intercalation reactions and do not involve the formation of tin. Electrochemical in-situ XRD studies by Courtney *et al.* on SnO, SnO_2, Li_2SnO_3, and $SnSiO_3$ have shown that metallic tin is involved (Courtney, 1996). They showed that the principal mechanism is lithium alloying with metallic tin which forms after the first discharge (initial insertion of lithium). This lithium-tin alloying process is quite reversible (possibly due to the presence of a lithia 'matrix' which helps to keep the electrode particles mechanically connected) and the tin-oxides exhibit reversible capacities on the order of 1000 mAh/g (Courtney, 1996). These materials are not only promising candidates for use in practical lithium-ion cells. Fujifilm has announced that one of these materials will be used in the 'Stal-ion' lithium ion rechargeable battery, slated for volume production in January 1997 (Fujifilm, 1996).

10.3 RECOMMENDATIONS

Chemical vapour deposition is a useful technique for making novel materials. Nanodispersions of other lithium alloying elements, such as aluminum, bismuth, lead and others might be possible, and warrants further investigation. As with any CVD, special attention needs to be paid to the deposition conditions. If carbides are unintentionally synthesized, then a changing of the vapour flow and other deposition parameters, such as pressure and temperature should be attempted. If interesting materials which appear to be useful are produced, then other techniques can be sought to make the materials in a less expensive fashion.

Further work is needed to fully understand the chemical origin of the irreversible capacity and hysteresis in the silicon oxycarbides. An understanding of the nature of the lithium insertion into these materials would be very useful. We suggested at the end of our preliminary Si-O-C work that there were two obvious paths to follow. Now that a fairly exhaustive study of the effect of stoichiometry has been done, modeling techniques for glassy structures, like reverse Monte Carlo structure determination (McGreevy, 1993), can be used to gain insight into the possible structures of these materials. Simple modeling of the silicon *K*-edge can also be done to provide one with the most likely local chemical environments of silicon atoms in these materials. These can then be used as 'seeds' to start a reverse Monte Carlo analysis of the structure. Once this work has been done, it can be applied to the electrochemical data in an effort to understand the nature of the lithium insertion. Much of the data required to do this has been collected, although time and resources (i.e. people) were not sufficient to allow a full analysis.

In-situ XRD studies of silicon oxycarbides and pyrolysed pitch blends could lend insight into the nature of the lithium insertion in these materials, as it did in the tin oxides

(Courtney, 1996). This, in turn, could be applicable to understanding the mechanisms in the silicon oxycarbides.

It was shown that the oxygen in the pyrolysed pitch blends was related to the irreversible capacities and hysteresis in these materials. Since these are undesirable characteristics, future work should focus on reducing the oxygen content in these materials. It is unlikely that the oxygen was introduced during pyrolysis. Thus, efforts should focus on different synthesis techniques which do not involve the use of oxygen-containing compounds (i.e. catalysts, solvents, pitches).

From the study of all the carbonaceous materials containing silicon, the most commercially relevant materials appear near 14 at. % silicon and 80 at. % carbon. The pitch-polysilane blend pyrolysis provides the most direct method to make these material. Note how closely spaced the samples are near 100% carbon and how much space there is between samples II4 and I6 (See Figure 9-7). More work could be done with different pitches and polysilanes to make samples located in the range of 10 to 20 atomic percent silicon. The use of different pitches and polysilanes which give stoichiometries in this range could provide even higher capacities than those already observed. Other pyrolysis methods (like the vacuum pyrolysis used to make the low irreversible capacity pitch carbons) might help to reduce the irreversible capacity in these materials (once the oxygen content has been reduced).

Although extensive studies have been completed, plenty of work remains to be done which could further improve the materials made and gain an understanding of the mechanisms of the lithium insertion into them.

REFERENCES

Abu-eid M.A., King R.B., and Kotliar A.M., Eur. Polym. J. **28**, 315-320 (1992).

Allcock H.R., and Lampe F.W., *Contemporary Polymer Chemistry* (Prentice-Hall, Inc., Englewood Cliffs, New Jersey, 1990).

Babonneau F., and Bois L., Chem. Mater. **6**, 51-57 (1994).

Bauer R.S., and Bachrah R.Z., J. Vac. Sci. Technol. **17**, 501 (1980).

Bennet P.D., Bullock K.R.,and Fiorino M.E., Interface **4**, 26-30 (1995).

Besenhard J.O., Komeda P., Paxinos A., Wudy E., and Josowicz M., Solid State Ionics **18-19**, 823 (1986).

Besenhard J.O., Yang J., and Winter M., 8th Insternational Meeting on Lithium Batteries, Nagoya, Japan, Extended Abstracts, pp 69-72 (June 16-21, 1996)

Boehm R.C., and Bannerjee A., J. Chem. Phys. **96**, 1150 (1992).

Boukamp B.A., Lesh G.C., and Huggins R.A., J. Electrochem. Soc. **128**, 725-728 (1981).

Burns G.T., Taylor R.B., Xu Y., Zangvil A., and Zank G.A., Chem. Mater. **4**, 1313-1323 (1992).

Chandra G., Lo P.Y., Hitchcock P.B., and Lappert M.F., Organometallics **6**, 191 (1987).

Colbow K., private communication via telephone on February 5, 1997.

Courtney I.A., and Dahn J.R., accepted by J. Electrochem. Soc.

Cullity B.D., *Elements of X-Ray Diffraction*, second edition (Addison-Wesley, USA, 1978).

Dahn J.R., Sleigh A.K., Shi Hang, Way B.W., Weydanz W.J., Reimers J.N., Zhong Q., and von Sacken U., "Carbons and Graphites as Substitutes for the Lithium Anode", in *Lithium Batteries*, edited by Pistoia G. (Elsevier, North Holland, 1993).

Dahn J.R., Zheng Tao, Liu Y., and Xue J.S., Science **270**, 590 (1995).

Dahn J.R., Wilson A.M., Xing W., and Zank G.A, United States Patent Application #664278, "Electrodes for Lithium-Ion Batteries using Polysiloxanes" June 11 (1996a).

Dahn J.R., Wilson A.M., Xing W., and Zank G.A, United States Patent Application #661532, "Electrodes for Lithium-Ion Batteries using Polysilanes" June 11 (1996b).

Dahn J.R., Wilson A.M., Xing W., and Zank G.A, United States Patent Application #661531, "Electrodes for Lithium-Ion Batteries using Polycarbosilanes" June 11 (1996c).

Dahn J.R., Wilson A.M., Xing W., and Zank G.A, United States Patent Application #DC4385, "Electrodes for Lithium-Ion Batteries using Polysilazanes" June 11 (1996d).

Daumas N., and Herold A., C. R. Acad. Sci. (Paris), Ser. C **268**, 373 (1969).

Debye P., Anderson H.R., and Brumberger H., J. Appl. Phys. **28**, 679 (1957).

Dorfman V.F., Thin Solid Films **212**, 267-273 (1992).

EVAA: The Electric Vehicle Association of the Americas, Press Release via the internet, http://www.evaa.org/newsflash/daily1.html (1996a).

EVAA: The Electric Vehicle Association of the Americas, Press Release via the internet, http://www.evaa.org/newsflash/nissan1.htm (1996b).

EVAA: The Electric Vehicle Association of the Americas, Press Release via the internet, http://www.evaa.org/newsflash/laauto.html (1997).

Fischer J.E., in *Chemical Physics of Intercalation*, edited by Legrand A.P. and Flandrois S. (Plenum, New York, 1987).

Franklin R.E., Proc. Roy. Soc. (London) **A209**, 196 (1951).

Fong R., von Sacken U., and Dahn, J.R., J. Electrochem. Soc. **137**, 2009-2013 (1990).

For Example, see "Cellular Phone Recall May Cause Setback for Moli", Toronto Globe and Mail, August 15, 1989 (Toronto, Canada).

Fujifilm: Dowloaded from the Fuji Photo Film Co., Ltd. WWW home page (April 22,1996).

Gat E., Cros B., Berjoan R., and Durand J., Appl. Surf. Science **64**, 345-351 (1993).

Gibaud A., Xue J.S., and Dahn J.R., Carbon **34**, 499 (1996).

Grow J.M., Levy R.A., and Bhaskaran M., J. Electrochem. Soc. **140**, 3001-7 (1993).

Guinier A., and Fournet G., (translated by Walker C.B.) *Small-Angle Scattering of X-Rays*, (John Wiley & Sons, New York, 1955).

Harrison W.A., *Electronic Structure and the Properties of Solids* (Dover, New York, 1989).

Haering R.R., Can. J. Phys. **36**, 352 (1958).

Herremans H., Grevendonk W., van Swaaij R.A.C.M.M., van Sark W.G.J.H.M., Berntsten A.J.M., Bik W.M. Arnold, and Bezemer J., Philisophical Magazine B **66**, 787-800 (1992).

Herold A., Bull. Soc. Chim. (Fr.) **187**, 999 (1955).

Hitchman M.L., and Jensen K.F., Chemical Vapor Deposition (Edited by M.L. Hitchman and K.F. Jensen) p.1-26 (Academic Press Inc., San Diego, 1993).

Huggins R.A., in *Lithium Batteries*, edited by Dey A.N., proceedings volume 87-1, p.356, (The Electrochemical Society Proceedings Series, Pennington, New Jersey, 1987).

Hurwitz F.I., Hyatt L., Gorecki J., and D'Amore L., Cerm. Eng. Sci. Proc. **8** 732-743 (1987).

Hurwitz F.I., Gyekenyesi J.Z., and Conroy P.J., Ceram. Eng. Sci. Proc. **10**, 750-763 (1989).

Hurwitz F.I., Farmer S.C., Terepka F.M., and Leonhardt T.A., J. Mater. Sci. **26**, 1247-1252 (1991).

Ibrahim K., Wilson J.I.B., Qayyum A., Henderson A.E., and Fitzgerald A.G., J. Non-Cryst. Solids **113**, 282-6 (1989).

Idota, Y., Nishima M., Miyaki Y., Kubota T., and Miyasaki T., Canadian Patent Application #2,134,053 (1994).

Kaliat M., Kwak C.Y., and Schmidt P.W., *New Approaches in Coal Chemistry*, edited by Blaustein B.D., Bockrath B.C., and FriedmanS., (American Chemical Society, Washington DC., 1981).

Kambe N., Dresselhaus M.S., Dresselhaus G., Basu S., McGhie A.R., and Fischer J.E., Mater. Sci. Eng. **40**, 1 (1979).

Linden D., Editor, *Handbook of Batteries*, 2nd edition, (McGraw Hill, New York, 1995).

Liu Y., Xue J.S., Zheng Tao, and Dahn J.R., Carbon **34**, 193 (1996).

Lowell S., and Shields J.E., *Powder Surface Area and Porosity*, 3rd edition, (Chapman and Hall, New York, 1991).

Mabuchi A., Tokumitsu K., Fujimoto H., and Kasuh T., 7th International Meeting on Lithium Batteries, May 15-20 (1994), Boston, USA, paper I-A-10, page 207 pf extended abstracts; also see Fujimoto H., Mabuchi A., Tokumitsu K., and Kasuh T., ibid, paper II-B-12, page 540.

Mantz R.A., Jones P.F., Chaffe K.P., Lichtenhan J.D., and Gilman J.W., Chem. Mater. **8**, 1250 (1996).

Marinkovíc S., The Chemistry and Physics of Carbon, Volume 19, pp. 1-64 (1984).

Matsumura Y., Wang S., and Mondori J., Carbon **33**, 1457-1462 (1995).

McGreevy R.L., J. Non-Cryst. Solids **156/158**, 2 (1993).

McKinnon W.R., and Haering R.R., Modern Aspects of Electrochemistry, number 15, edited by White R.E., Bockris J. O'm, and Conway B.E., (Plenum, New York, 1983).

Moffat W.G., *The Handbook of Binary Phase Diagrams*, (Genium Publ. Corp., Schenectady, New York, 1990).

Nalimova V.A., Guerard D., Lelaurain M., and Fateev O.V., Carbon **33**, 177 (1995).

Noguchi M., Miyashita K., and Endo M., Tanso **155**, 315 (1992).

Ovshinsky S.R., Fetcenki M.A., and Ross J., Science **260**, 176-181 (1993).

Ohzuku T., Iwakoshi Y., Sawai K., J. Electrochem Soc. **140**, 2490 (1993)

Omaru A., Azuma H., Aoki M., Kita A., and Nishi Y., paper #25, 182nd Meeting of the Electrochemical Society, Toronto, Canada (1992), Extended Abstracts of Battery Division, page 34.

Papanek P., Radosavljevic M., Fischer J.E., and Jones C.A., accepted by Chem. Mater. (1996).

Peled E., J. Electrochem. Soc. **126**(12), 2047-2051 (1979).

Qiu X.P., Liu Q.G., and Yang L.L., Solid State Ionics **60**, 351 (1993).

Renuld G.M., Prochazka S., and Doremus R.H., J. Mater. Res. **6**, 2716-2722 (1991).

Rübel H., Folsch J., Schade H., Solid State Comm. **85**, 593-6 (1993).

Safran S.A., Phys. Rev. Lett. **44**, 937 (1980)

Sanyo Canada Battery Internet Home Page: www.sanyo.ca/i_b_000.htm Downloaded and read on February 10 (1997).

Sato K., Noguchi M., Demachi A., Oki N., and Endo M., Science **264**, 556 (1994).

Scherrer P., Nachr. Göttinger Gesell, 98 (1918).

Shi Hang, Reimers J.N., and Dahn J.R., J. Appl. Crystallogr. **26**, 827 (1993a).

Shi Hang, Ph.D. Thesis, Simon Fraser University (1993b).

Shufflebotham P.K., Card H.C., and Thanailakis A., J. Non-Cryst. Solids **92**, 183-244 (1987).

Sinstead N.J., Ann. Physik. Chem., 21, **92** (1854).

Sonobe N., Ishikawa M., and Iwasaki T., 35th Battery Symposium in Japan, Nov. 14-16 (1994), Nagoya, Japan, paper 2B09, extended abstracts, page 47.

Stöhr J., *NEXAFS Spectroscopy* (Springer-Verlag, Berlin, Heidelberg, 1992).

Tadiran Battery Co. Internet Home Page: www.tadiranbat.com/rechspec.htm and www.tadiranbat.com/bro.htm. Downloaded and read on February 10 (1997).

Takahashi Y. Oishi J., Miki Y., Yoshimura M., Shibahara K., and Sakamoto H., 35th Battery Symposium in Japan, Nov. 14-16 (1994), Nagoya, Japan, paper 2B05, extended abstracts, page 39.

Tan K.H., Bancroft G.M., Coatsworth L.L., and Yates B.W., Can. J. Phys. **60**, 131-136 (1982).

Tiedje T., Private Communication (unpublished) (1994).

Tokumitsu K., Mabuchi A., Fujimoto H., and Kasuh T., J. Electrochem. Soc. **143**, 2235-2239 (1996).

van Buuren T., Tiedje T., Dahn J.R., and Way B.M., Appl. Phys. Lett. **63**, 2911 (1993).

Waki I., and Hirai Y., J. Phys.: Condens. Matter **1**, 6755-6762 (1989).

Wang Jiqiang, Raistrick I.D., Huggins R.A., J. Electrochem. Soc. **133**, 457-460 (1986).

Wang Y., Sasaki M., and Hirai T., J. Materials Science **26**, 5495-5501 (1991).

Warren B.E., Phys. Rev. **9**, 693 (1941).

Warren B.E., *X-Ray Diffraction*, p. 254 (Dover, NY, 1990).

Way B.M., Dahn J.R., Tiedje T., Myrtle K., and Kasrai M., Phys. Rev. B **46**, 1697 (1992).

Way B.M., Ph.D. Thesis, Simon Fraser University (1995).

Weast R.C. (editor in Chief) CRC Handbook of Chemistry and Physics, 66th edition, CRC press, Inc. Boca Raton, Florida (1986).

Weydanz W.J., Way B.M., van Buuren T., and Dahn J.R., J. Electrochem. Soc. **141**, 900 (1994).

Whitney T., Vancouver Sun, 'Wheels' section, page F1, Nov. 29 (1996)

Wilson A.M., Reimers J.N., Fuller E., and Dahn J.R., Solid State Ionics **74**, 249 (1994a).

Wilson A.M., and Dahn J.R., Silicon-Carbon Materials as Anodes for Rechargeable Lithium Batteries filed in Canada, May 3 (1994), #2112770; in Europe April 12 (1995) #EP95302457.7; in Japan May 2 (1995) JP07-108898 and in the U.S. April 25 (1995) US08/428,656 (1994b).

Wilson A.M., and Dahn J.R., Carbonaceous Insertion Compounds and Uses as Anodes in Rechargeable Batteries, filed in Canada, July 8 (1994) #2,127,621; in Europe August 30 (1995) EP95304410.4-2111, filed in Japan June 29 (1995) JP07-164100; in the U.S. April 25 (1995) US08/428,042 (1994c).

Wilson A.M., and Dahn J.R., J. Electrochem. Soc. **142**, 326 (1995a).

Wilson A.M., Way B.M., Dahn J.R., and van Buuren T., J. Appl. Phys., **77**, 2363 (1995b).

Wilson A.M., Dahn J.R., Xue J.S., Gao Y., and Feng X.H., Carbonaceous Materials Containing Silicon as Anodes for Lithium-Ion Cells, Proceedings of the Materials Research Society Spring Meeting, April (1995c).

Wilson A.M., Zank G., Eguchi K., Xing W., and Dahn J.R., Pyrolysed Silicon-Containing Polymers as High Capacity Anodes for Lithium-Ion Batteries, Paper I-A-5 presented at the 8TH International Meeting on Lithium Batteries. Accepted by J. Power Sources September 1996a.

Wilson A.M., Zank G., Eguchi K., Xing W., Yates B., and Dahn J.R., submitted to Chemistry of Materials, December 16 (1996b).

Wilson A.M., Zank G., Xing W.X., and Dahn J.R., to be submitted to Chem. Mater. (1996c).

Xing W.X., Wilson A.M., Zank G., Dahn J.R., accepted by J. Electrochem. Soc. (1996a).

Xing W.X., Wilson A.M., Zank G., Dahn, J.R., accepted by Solid State Ionics (1996b).

Xing W., Xue J.S., and Dahn J.R., J. Electrochem. Soc. **143**, 3046-3052 (1996c).

Xing Weibing, Dahn J.R., submitted to J. Electrochem. Soc. (1996d).

Xue J.S., Myrtle K., and Dahn J.R., J. Electrochem. Soc. **142**, 2927-2935 (1995a).

Xue J.S. , and Dahn J.R., Carbonaceous Insertion Compounds and Use as Anodes in Rechargeable Batteries, Canadian Patent Application 2,144,037, March 3 (1995b); filed in U.S. April 25 (1995); filed in Japan February 3 (1996),
(1995b).

Yang B.X., Middleton F.H., Olssen B.G., Bancroft G.M., Chen J.M., Sham T.K., Tan K., and Wallace D.J., *Nucl. Instrum. Methods A* **316**, 422 (1992).

Yata S., Kinoshita H., Komori M., Ando N., Kashiwamura T., Harada T., Tanaka K., and Yamabe T., Synth. Met. **62**, 153 (1994).

Zheng Tao, Reimers J.N., and Dahn J.R., Phys. Rev. B **51**, 734-741 (1995a).

Zheng Tao, and Dahn J.R., Synth. Met. **73**, 1-7 (1995b).

Zheng Tao, Liu Yinghu, Fuller E.W., Tseng Sheilla, von Sacken U., J. Electrochem. Soc. **142**, 2581-2590 (1995c).

Zheng Tao, Zhong Q., and Dahn J.R., J. Electrochem. Soc. **142**, L211-L214 (1995d).

Zheng Tao, Xue J.S., and Dahn J.R., Chem. of Materials **8**, 389-393 (1996a).

Zheng Tao, and Dahn J.R., Phys. Rev. B **53**, 3061-3071 (1996b).

Zheng Tao, McKinnon W.R., and Dahn J.R., J. Electrochem. Soc. **143**, 2137-2145 (1996c).

Zheng Tao, Ph.D. Thesis, Simon Fraser University (1996d).